Microstructural characterization and thermal fatigue study of a coated Incoloy 909 Superalloy

By

METTUPALAYAM BALACHANDER

A Thesis Submitted to
The Faculty of Graduate Studies
In Partial Fulfillment of the Requirements for the Degree of

DOCTOR OF PHILOSOPHY

Department of Mechanical and Manufacturing Engineering
University of Manitoba
Winnipeg, Manitoba

Abstract

This research focuses on studying the microstructure of alloy 909, its susceptibility to oxidation at elevated temperatures (~700°C) and substrate coatings compatibility with high velocity oxy fuel (HVOF) sprayed oxidation resistance coatings. The characterization work involved in studying the microstructure of Incoloy 909 at three heat treated conditions namely solution treated condition (ST), commercially recommended solution heat treated and aged condition (STA), and solution treated and over aged condition (STOA) using optical microscopy, analytical scanning electron microscopy, and analytical transmission electron microscopy. The oxidation susceptibility were investigated at elevated temperatures of bare and coated alloy 909 substrates by subjecting test materials to isothermal and thermal cycle testing.

The microstructure of alloy 909 in the ST condition showed only the presence of blocky Laves phase. The Laves phase in this alloy is a well known for its grain pinning effect that prevents excessive grain growth. In the STA condition, the microstructure revealed the presence of fine gamma prime, intergranular and intragranular Laves phase and occasionally gamma prime precipitates orienting in a platelet form ready to transition into the epsilon phase. In the STOA condition, the microstructure consisted of Laves phase in inter and intragranular locations, and a copious amount of Widmanstatten type epsilon phase.

Incoloy 909 was observed to form oxide scales in both isothermal and cyclic thermal exposures, the oxide scale consisted of distinct outer and inner scales in the micrographs. The comparison base alloy (alloyl 718) used in this study surprisingly did not show any visible presence of oxide scale after 1000 hour exposure at ~700°C. Three coatings (CoNiCrAlY, 718 , and NiAl) were sprayed on alloy 909 and alloy 718 test coupons using the HVOF process to investigate the compatibility of the coatings with the substrate. The test results points out that all the coatings were compatible with 718 substrate and only one coating (NiAl) was found compatible with the Alloy 909 substrate, indicating that the coatings that are compatible with one substrate may not be compatible with another alloy within the same family of alloys.

Acknowledgements

I would like to acknowledge my gratitude and sincere thanks to my Advisor, Dr. N.L. Richards for providing an opportunity to work on this research, and for the excellent support provided throughout these years, both in academic and in personal endeavors.

I would like to express my gratitude to my thesis committee members Dr. J.R. Cahoon, Dr.A.Shalaby for their encouragement and discussions during my qualifying exam and committee meetings. I am indebted to Dr.K.Shanker for providing constant encouragement and mentorship not limited with this research work.

I would like to thank Joe Tharayil (BAL), John Derkach (BAL), John Davies (BAL), Kerry Boucher (SAL), Casey Van Gorp (SAL), Walter Gretschmann (SAL), Melanie Mulder (SAL) and several of my previous and current co-workers for the support offered throughout this program.

I would like to express my gratitude to Dr.Krutika Vishwakarma, Dr.Binbin Tang, Dr. R Ding for the support accorded during this research. I would also like to thank technicians G. McLaren, J. Van Dorp, D. Mardis, D. McCooeye, M. Boskwick for their support.

My greatest appreciation goes to my wife Manju for her patience and also for her unwavering support. I want to express my gratitude to my parents (my dad Late. N. Arivudainambi and my mom A.Rajalakshmi) and brothers (M.A. Narayanasamy and Late.M.A. Gowthaman) for their constant encouragement and support.

There are so many other individuals and friends that I have likely failed to mention it here, I extend my gratitude to all of them for extending their support and encouragement.

Table of contents

List of Figures

List of Tables

1. INTRODUCTION

Superalloys find extensive use in high temperature components of gas turbine engines in both aerospace and industrial applications because of their excellent thermal, mechanical and surface stability at elevated temperatures. Superalloy derive high temperature strength through solid solution strengthening, and in some alloys precipitation hardening mechanisms. The robust oxidation and corrosion resistance is derived from the formation of an adherent protective oxide film that encapsulates the material, thus slowing down further oxidation and corrosion. Generally, aluminum, chromium and other elements are added in Superalloys to enhance the protective oxide forming ability. The above factors are applicable to some of the well known first generation Superalloys such as Inconel 718. However, it should kept in mind that in the last few decades a variety of Superalloys have been developed and added to the ever increasing family of Superalloys to fill the role for niche application requirements. Some of these newer alloys may not fulfill the material core property requirements of Superalloys to the same degree as envisioned in the original form.

For example, there are several classes of Superalloys, of which controlled thermal expansion Superalloys is one important class, which basically bring together the high elevated strength capability of Superalloys and low coefficient of thermal expansion from the “Invar” effect. Some of the well known controlled thermal expansion Superalloys include Incoloy 903, 907 and 909. These alloys offer a combination of excellent

mechanical properties and low coefficients of thermal expansion, approximately 40% less than the conventional Superalloys (such as Inconel 718).

The energy shortages of a few decades ago fueled the demand for increased fuel efficient gas turbine engines mainly driven by the airline industry. The unique ability to maintain close tolerances between rotating and stationary components over a range of temperatures by low coefficient of expansion Superalloys had immediate potential to enhance the fuel efficiency of the gas turbine engines. This realization evoked interest in the development of the first commercial controlled thermal expansion Superalloy known as Incoloy 903 by Special Metals Corporation (Formerly Huntington Alloys) in the early 1970s [Harner 1994]. Due to some property shortcomings, further alloy development led to the introduction of Incoloy 907 and then Incoloy 909. Incoloy 909 consists of a Fe-Co-Ni matrix, with globular AB_2 type Laves phase in solution treated condition. It was reported that in the precipitation hardened condition, in addition to Laves phase particles, gamma prime (γ'), epsilon ε (and epsilon double prime ε") and grain boundary precipitates were present [Heck et al., 1988; Larker et al., 1992; Smith et al., 1989]. Controversy exists on the presence of black and white grains on whether it is due to difference in the density of ε phase or contrast due to orientation of individual grains [Heck et al., 1988; Guo et al., 2000]. A detailed microstructure characterization in commercially precipitation hardened condition is lacking in the literature.

While Incoloy 909 exhibits attractive combinations of high strength and low expansion coefficients, the alloy exhibits poor oxidation resistance at elevated temperatures mainly due to absence of the Cr and Al. Application of protective coatings via thermally sprayed overlay coatings such as Nickel-Aluminum or MCrAlY (M=Co /Ni, Cr, Al, Yttrium) type coating is one of the most common processes used in aerospace industry. It is generally assumed that effect of CTE (Coefficient of Thermal Expansion) difference between the coating and substrate is negligible in the case of coatings such as MCrAlY coating. This assumption is based on the view that most Superalloys and coatings have similar CTE ranges under normal operating temperature [Taylor et al., 2006]. Most of the previous studies on coatings were focused on the CTE difference between the ceramic top coat and the MCrAlY bond coat in Thermal Barrier Coatings rather than bond coat to the substrate metal. Moreover, in industrial applications, process development and quality control of coatings are based on substrate family type (e.g. Superalloys) rather than optimizing for specific substrate material. In other words, if the coating meets acceptance criteria on Inconel 718, it is presumed that the coating will meet the acceptance criteria of any other alloys within the Superalloys family of materials.

Hence, this research is focused to study (1) Microstructural characterization of Incoloy 909 and (2) Viability of the application of oxidation protective coating on Incoloy 909 and to compare it with an established alloy such as Inconel 718 and (3) Selective oxidation exposure tests to confirm coating integrity.

1.1 Thesis Organization

In Chapter 2 a detailed review of the literature is provided. In Chapter 3, details of the experimental work and details of various materials used are presented. In Chapter 4 results and associated discussion are presented, in Chapter 5 a summarized conclusion on the research is provided, and in Chapter 6 suggested future work is discussed.

2. LITERATURE REVIEW

2.1 Superalloys

The development of Superalloys in the last 60 years has had tremendous impact on the progress of the aviation and land based gas turbine industry. With the growth of the gas turbine engine industry, Superalloys were able to meet the long standing demand for materials that possessed elevated temperature strength and excellent oxidation resistance. Such high strength and elevated temperature properties for the Superalloys were attributed to the use of an austenitic FCC matrix (nickel, iron or cobalt based) with small additions of precipitation hardening constituents such as Al, Ti, Nb etc., and elevated temperature oxidation resisting elements such as Al, Ti and Cr. However, the FCC matrix resulted in relatively higher thermal expansion rates compared to material that possess a BCC matrix, such as ferritic steels. Invar™ is considered to be the pioneer among the low thermal expansion alloys developed.

Guillame's extensive research with the Ni-Fe system later led to the plethora of controlled expansion alloys [Harner, 1994]. These alloys found extensive application in metrology, electronics, aerospace and the semiconductor industry. The Curie temperatures of these alloys are very important as it plays an important role in determining the useful application temperature range. The Curie temperature represents the transition from ferromagnetism to paramagnetism, above which the coefficient of thermal expansion (CTE) increased drastically. The addition of cobalt to the Ni-Fe system led to a

higher Curie temperature, with Fe-Ni-Co alloys such as Kovar™ being developed, which are extensively used for providing a strong hermetic type seals with glass and ceramic tubes [Harner, 1994]. The advent of controlled expansion Superalloys is detailed in the next section.

2.2 Low Coefficient of Thermal Expansion Superalloys

The 900 series alloys were originally developed from Fe-Ni-Co based controlled expansion alloys in the early 1970's by Huntington Alloys Ltd, now known as Special Metals Corporation Inc. Huntington Alloys developed the existing Fe-Ni-Co alloy system into a precipitation hardened alloy system by adding niobium, aluminum, and titanium. This newly developed precipitation hardenable alloy, when solution treated and aged, exhibited three times the room temperature strength than the previous Fe-Ni-Co alloys without precipitation strength with excellent controlled thermal expansion properties. The room temperature tensile properties of this alloy were comparable to the most popularly known Superalloys such as Inconel 718. The new families of alloys were later popular as Incoloy 900 series of alloys [Nakkalil 1993; Smith el at., 1989; Wanner et al., 1991]. The Incoloy 900 series consists of Incoloy 903, 907, and 909 among the low expansion alloys, the chemical composition of these alloys can be found in Table 2-1.

The first available alloy in this class was Incoloy 903, which offered attractive properties suitable for gas turbine applications. However due to the susceptibility of stress assisted

grain boundary oxidation (SAGBO), it exhibited limited elevated temperature creep rupture capability. The susceptibility to SAGBO was attributed to the absence of chromium, as any addition of chromium would decrease the Curie temperature [Symonds et al., 1986], or destroy the atomic scale magnetic interactions, thus affecting the low thermal expansion property [Smith et al., 1989]. Further research led to the development of Incoloy 907, which had better SAGBO resistance, but required a longer aging cycle (refer to Table 2-2 for detail on aging cycles), due to a lower aluminum content, which increased the heat treatment cost for the metal processors. Incoloy 909, the more recent alloy in this family compositionally differs from Incoloy 903 and 907 due to a 0.3 to 0.5 wt % increase in silicon content. The increase in silicon content improved elevated temperature creep rupture properties and reduced microstructure anisotropy after a standard precipitation treatment [Heck et al., 1990; Mannan et al., 2000].

Incoloy 909 is a Fe-Co-Ni Superalloy characterized with almost constant low coefficient of thermal expansion (CTE) below the inflection point, high modulus of elasticity and comparable high strength to alloys such as Inconel 718. The precipitation strengthening is achieved in a similar manner to that used in Inconel 718, such strengthening is possible due to the presence of required amounts of niobium and titanium. The attractive combination of excellent high strength properties and low expansion rate between ambient and 550°C makes Incoloy 909 a useful material for elevated temperature applications. The low CTE characteristics of Incoloy 909 as shown in Fig 2-1 and 2-2, makes it an attractive candidate material in gas turbine engines, as the gas leakage path between the rotating blade tips and the shrouds can be maintained within a very close

tolerances over a wide range of operating temperatures. Any reduction in the gas leakage path during the operation of gas turbine engine results in significant fuel savings. Since a major portion of the airline cost is contributed by fuel cost, there is a great deal of pressure on the gas turbine engine manufacturers to improve the fuel efficiency of the engines. The excellent elevated temperature property makes it an attractive candidate material for aerospace and industrial gas turbines. The bulk chemical composition of Incoloy 909 and Inconel 718 can be compared from Table 2-3.

Most Superalloys are characterized by a high mean coefficient of thermal expansion, hence at higher service temperature the thermal expansion increases, which partly contributes towards limited thermal fatigue properties especially in thermal shock environment. Owing to its low expansion properties, the 900 series alloys are expected to have superior thermal fatigue life when compared to Superalloys such as Inconel 718. In addition, 900 series alloys have excellent resistance to hydrogen embrittlement at high-pressure environment such as rockets used in space programs.

Table 2-1 Composition in Weight %

Alloy	Wt %							
	Ni	**Co**	**Nb**	**Ti**	**Si**	**Al**	**B**	**Fe**
903	37.7	16	3	1.75	0.20	1.0	0.007	Balance
907	38	13	4.8	1.5	0.20	0.1	0.005	Balance
909	38	13	4.8	1.5	0.40	0.05	0.005	Balance

Table 2-2 Aging time and temperature [Special Metals Corporation material data sheets]

Alloy	**Temperature**	**Time**	**Cooling Rate**	**Temperature**	**Time**	**Cooling**
903 /909	720°C	8 Hrs	55°C/min	620°C	8 Hrs	AC
907	774°C	12 Hrs	38°C/min	621°C	18 Hrs	AC

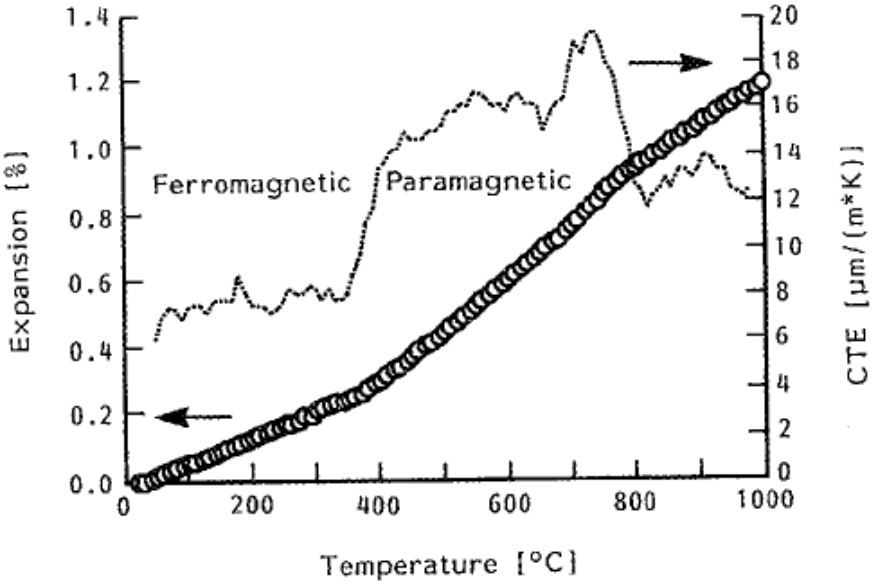

Figure 2-1 Thermal expansion and momentary CTE of Incoloy 909 [Larker et al., 1992] (Reproduced with permission from Elsevier)

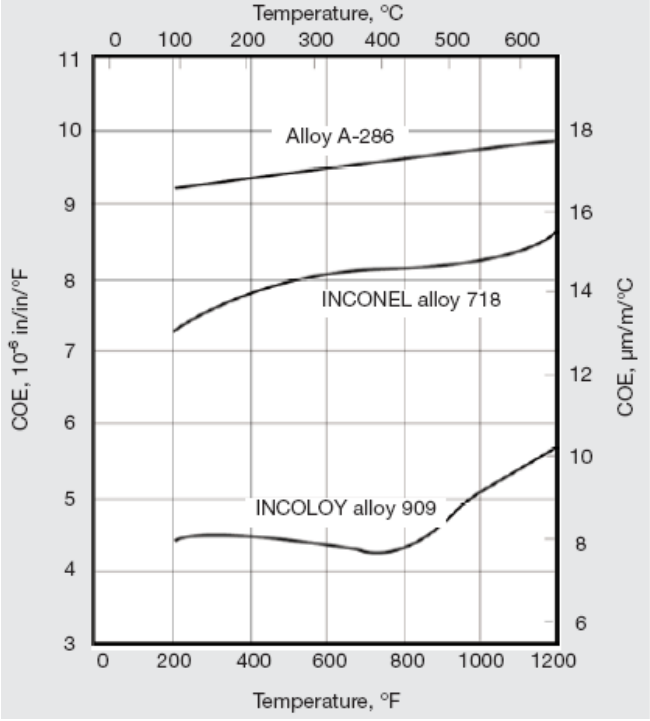

Figure 2-2 Thermal expansion rates of Incoloy 909 and other alloys [Materials 1992]. (Reproduced with permission from Special Metal Co)

Table 2-3 Comparison of Incoloy 909 and Inconel 718 bulk compositions [Special Metals Corporation material data sheets] Reproduced with permission from Special Metal Co

Alloy	**Wt %**							
	Ni	**Co**	**Nb**	**Ti**	**Si**	**Al**	**Cr**	**Fe**
909[1]	38	13	4.8	1.5	0.4	0.05	N/A	Balance
718[1]	50	1	5	1	0.3	0.5	19	18.5

[1] Does not represent complete elemental composition

2.2.1 Alloy phases present in Incoloy 909

Laves phase is an intermetallic phase first described by Fritz Laves in the 1920's. Laves phase in Incoloy 909 is an AB_2 type, characterized by closed packed layers made up of A atoms (Ni, Fe, Co) and layers consisting of B atoms (Nb, Ti, Si) and is reported to precipitate in temperature range of 800-1040°C [Heck et al., 1988]. It has been reported that Fe based Superalloys tend to precipitate phases like Laves, sigma etc., which belong to topologically closed pack structures (TCP), while Ni based Superalloys tend to favor precipitation of gamma prime, gamma double prime etc., which are geometrically closed pack structures (GCP). A modeled crystallographic structure of $MgZn_2$ type Laves Phase hexagonal closed packed structure is as shown in Fig 2-3. The presence of Nb, Si and Ti is believed to favor formation of Laves phase instead of sigma phase in Fe-Ni based alloys and the presence of relatively higher amounts of Si in this alloy favors Laves phase precipitates in Fe-Nb and Fe-Ti alloys. It is generally believed that TCP phases are deleterious due to its platelet like morphology and absence of multiple slip systems. This results in reduced ductility resulting in inferior creep rupture properties [Larker et al., 1992].

Incoloy 909 consists of Fe-Co-Ni austenitic matrix, precipitation hardenable Superalloy, deriving its strength mainly from coherent metastable gamma prime (γ') phase. Gamma prime (γ') precipitates homogeneously within the gamma (γ) matrix with an ordered FCC crystal structure in the temperature range of 538-760°C [Heck et al., 1988]. The

gamma prime precipitates found in Incoloy 909 are reported to be very fine [Larker et al., 1992;

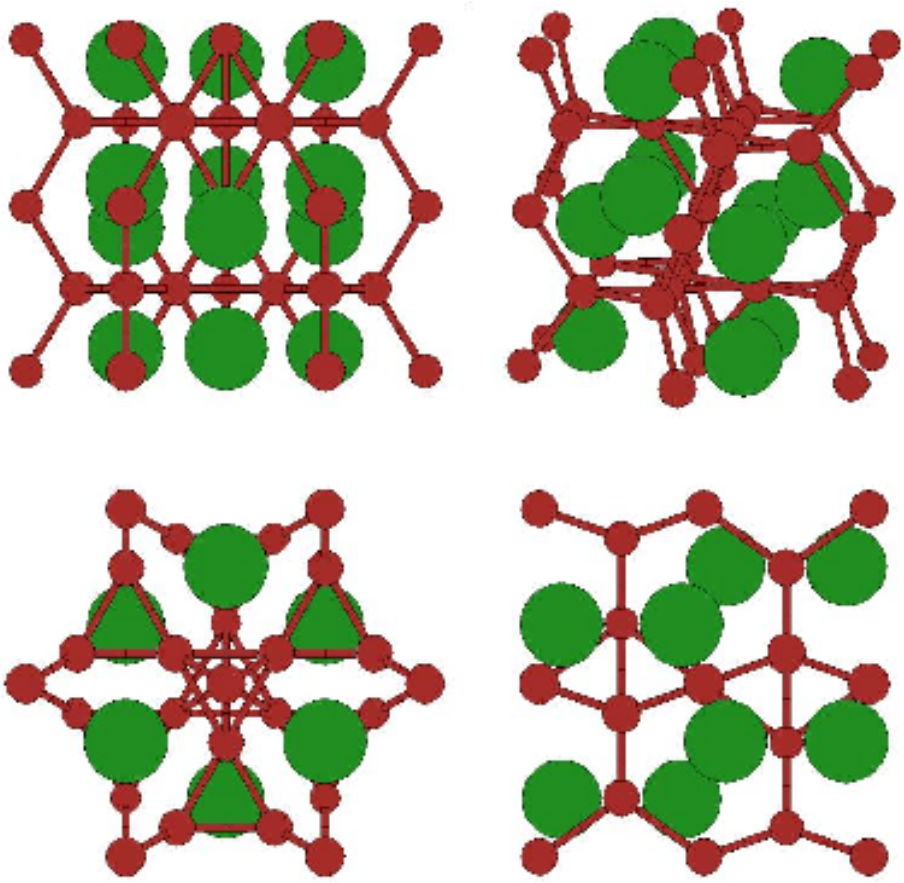

Figure 2-3 Crystallographic structure of $MgZn_2$ type Laves Phase hexagonal closed packed structure from different perspectives. Where A is the larger atom and B is the smaller atom. Pictures taken from the Crystal Lattice Structures Web page, http://cst-www.nrl.navy.mil/lattice/struk.picts/c14.s.png, provided by the Center for Computational Materials Science of the United States Naval Research Laboratory

Sato et al., 1993], but can be observed under high magnification transmission electron micrographs (TEM). Sato et al.,[Sato et al., 1993] observed that intergranular spherical gamma prime precipitates measuring approximately 10nm in diameter as shown in Fig. 2-4 using TEM.

The diameter of the spherical gamma prime precipitates ranged from 10- 20 nm depending upon the aging temperature and time that caused coarsening of these precipitates. They concluded that the maximum size of spherical gamma prime to be about 20 nm. They calculated the activation energy of gamma prime growth, based on their experimental results as 254 KJ/Mol, which is very similar to the activation energy reported for alloy 718 as 271 KJ/Mol [Han et al., 1982]. When aged 909 is subjected to continued exposure at precipitation heat treatment temperatures, the fine spherical gamma prime phase will coarsen and transition into a relatively more stable platelet, or needle like epsilon phase [Smith et al., 1989; Larker 1992]. It is believed that the negligible presence or absence of aluminum and the presence of excess amount of niobium are the main factors for the formation of this type of metastable gamma prime. At higher precipitation heat treatment temperature in the region of 770°C, a needle or platelet like epsilon phase precipitates out directly in gamma matrix without transition from the gamma prime phase. The epsilon phase is reported to precipitate in the temperature range of 700-950°C [Heck et al., 1988]. TEM micrographs of Incoloy 909 under various heat treatment conditions are shown in Fig 2-5 [Xiping et al., 2001] and Fig 2-6 shows the transitioning of gamma prime to epsilon phase.

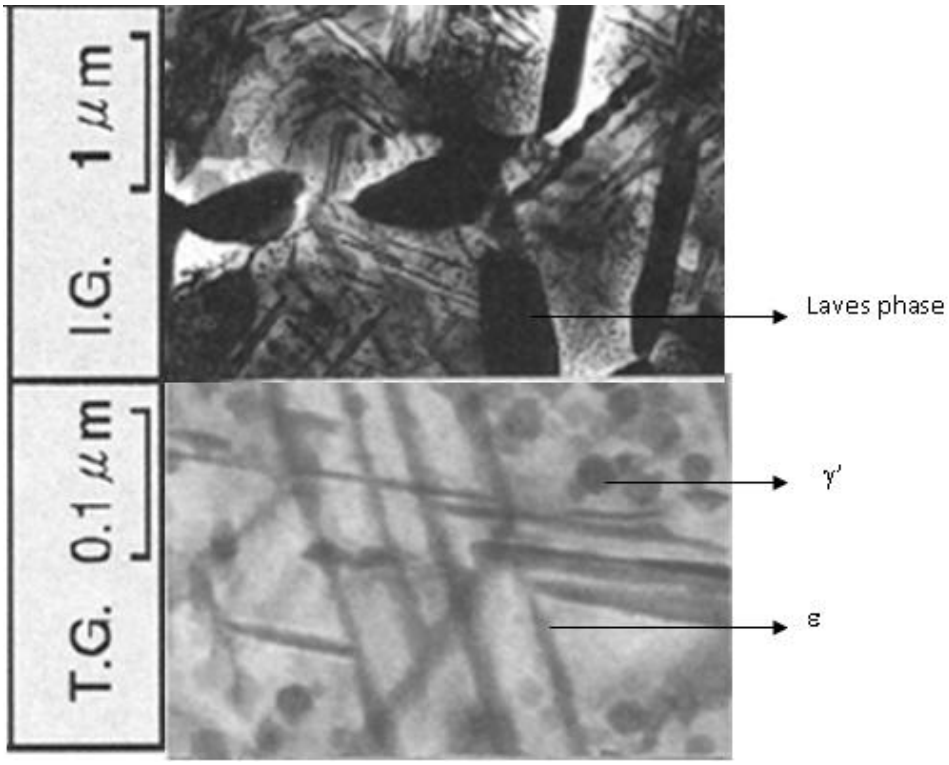

Figure 2-4 Microstructure of aged Alloy 909. IG. Intergranular: TG. Transgranular.[Sato et al., 1993]
(Reproduced with permission from Springer)

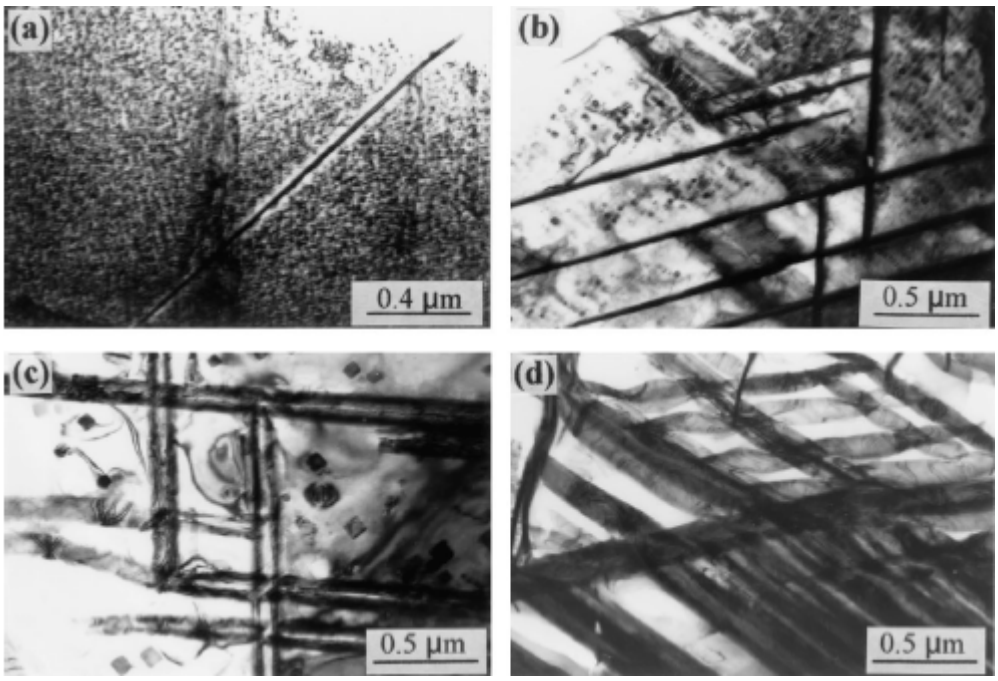

Figure 2-5 TEM micrographs of 909 showing the microstructure aged at: (a) (Gamma Prime) 720°C for 8 hours, (b) Epsilon Phase 720°C for 50 hours, (c) Epsilon Phase 770°C for 10 hours, and (d) (Eta Phase) 770°C for 42.1 hours. Beam direction is [011]. [Guo et al, 2001] (Reproduced with permission from Elsevier)

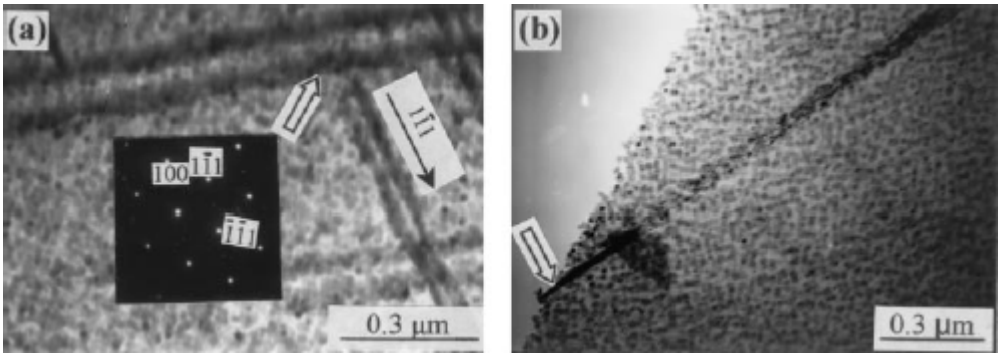

Figure 2-6 TEM micrographs of 909 showing the transition of gamma prime particles to epsilon platelets in the samples aged at 720°C for 8 hours: (a) inserted SAD pattern shows that the plates are still composed of γ', and (b) the arrow shows the end of the p [Guo et al., 2001](Reproduced with permission from Elsevier)

There seems to be a controversy in the determination of the crystal structure of epsilon phase. It was determined to be orthorhombic by Chen et al., [Chen et al., 2000]. The other investigations [Heck et al., 1988] suggested it to be HCP. Further research [Kusabiraki et al., 2000; Guo et al., 2001] confirmed the crystal structure of the epsilon phase to be HCP. Precipitation of the epsilon phase is said to result in imparting improved ductility accompanied by reduced short term mechanical strength to Incoloy 909 [Heck et al., 1988; Brown et al., 1998].

2.3 Physical metallurgy of Inconel 718

2.3.1 Introduction

Inconel 718 is Nickel-Iron based precipitation hardenable Superalloy originally developed in the 1960s with an excellent track record as the primary work-horse alloy for more than four decades. It is used extensively in gas turbine engines due to its resistance to creep and elevated temperature properties. Specific application areas include rotating components, shafts, high strength fasteners and in gas turbine engines. Also other application areas include nuclear reactor components, petroleum drilling and refinery components and marine engine components. The chemical composition of Inconel 718 (wt %) is as shown in Table 2-3.

2.3.2 Phases present in Incoloy 718

A list of phases present in Incoloy 909 and Inconel 718 is shown in Table 2-4. The main strengthening phases in Inconel 718 are (i) γ" as Primary strengthener (DO_{22} ordered)

and (ii) γ' as Secondary strengthener (LI_2 ordered). It should be noted that both of these phases are coherent with the matrix (FCC) γ. The γ" precipitate is disk shaped, predominantly made up of $Ni_3(Nb)$, a favorable and desired phase that provides strengthening mechanism upto a temperature of 650°C. Above 650°C, γ" decomposes and transitions into orthorhombic delta phase(δ). The orthorhombic delta phase (δ) precipitating in this alloy is of same composition to that of gamma double prime, but it precipitates incoherently within the gamma matrix, usually on grain boundaries. The FCC γ' is spheroidal, and is predominantly made up of $Ni_3(Al,Ti)$. It is the primary strengthener in many nickel based alloys and is relatively unimportant in Inconel 718 compared to Incoloy 909. The γ' in Inconel 718 is relatively more thermally stable compared to γ".

MC type carbide phases that precipitate inter and intra granularly during solidification, when exposed to elevated temperatures during service conditions, tend to decompose over time to more stable $M_{23}C_6$ and M_6C carbides. Also presence of trace amounts of N, B, P enhances formation of metallic nitrides, borides and phosphides along the grain boundary and increases the strength of the alloy [Xiao Huang, 1994]. However, the carbides, borides and phosphides are shown to form deleterious grain boundary films during weld solidification, thus increasing the susceptibility to weld crack formation. The presence of borides and nitrides are generally controlled by stringent materials and melting practices. The BCC ∝-Cr phases are formed in nickel depleted areas especially when there is a massive presence of intermetallic phases [Brown et al, 1998 ; Donachie 2000]. Laves Phase (AB_2) is generally not present in wrought products, however is

present in cast Inconel 718. Ni, Fe, Mn, Cr, and Si are represented by A and Nb, Mo, and titanium are represented by B. The presence of silicon, titanium, niobium in nickel based alloys promotes formation of topologically closed pack (TCP) phases such as Laves Phase.

Table 2-4: Phases present in wrought and cast Incoloy 909 and Inconel 718

Phases	**Crystallographic structure**	**Alloy**
γ”	BCC	718
γ’	FCC	Both in 909 and 718
Laves Phase	HCP	Both in 909 and 718 (Cast)
δ	HCP	718
MC	FCC	718
MN, MP and MB	FCC	718 (Cast)
η	HCP	Both in 909 and 718
σ	HCP	718
ε	HCP	909
G-Phase	HCP	909

2.4 Oxidation

Since most materials used in gas turbines are subjected to elevated temperatures and severe service conditions, the life of the component is affected by various factors, among these design engineers often accord important consideration to oxidation resistance of the material. Oxidation is defined as the chemical process in which oxygen reacts with another atom, molecule, or compound to produce a new substance called oxides. Oxidation results in the loss of at least one electron from a molecule, ion or atom. Oxide scale formation is schematically shown in Fig 2-7 and the basic steps of oxidation reaction in Fig 2-8 respectively. When a virgin surface of the metal is exposed to oxidizing conditions (presence of oxygen), during the initial stage, oxygen is adsorbed to the metal surface that results in a metal-oxygen reaction taking place at the interface. This stage leads to nucleation of oxides that result in oxide growth extending laterally so as to form a continuous film on the metallic surface. When the oxide film reaches certain threshold thickness, it separates the metal from the surrounding gas thereby resulting in slowing down of the oxide reaction. Hereafter, the oxide growth tends to follow solid state diffusion for one or more of the reactants through the oxide scale [Knoll et al., 1999].

2.4.1 Fundamentals of oxidation

Oxidation at elevated temperatures involves reactions of materials such as metals with gases such as oxygen. If the oxygen potential in the exposed area of the metal is greater than the oxygen partial pressure that is in equilibrium with metal oxide, then this will result in oxidation reaction. Two important theoretical concepts are often used to explain the fundamental aspects of oxidation. Thermodynamics explains the factors that contribute for the oxidation reaction to take place and kinetics explains at what rate the reaction would take place.

The applicability of thermodynamics theory for oxidation process can be represented by the expression for Gibbs free energy,

$$G = H-TS$$

Where H – Enthalpy; S- Entropy; and T – Temperature

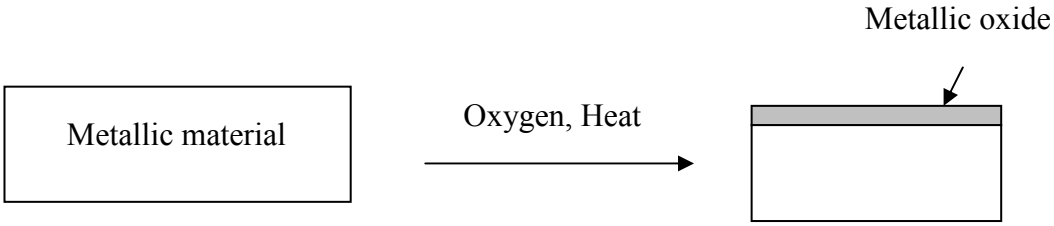

Figure 2-7 Schematic of oxide formation on an alloy

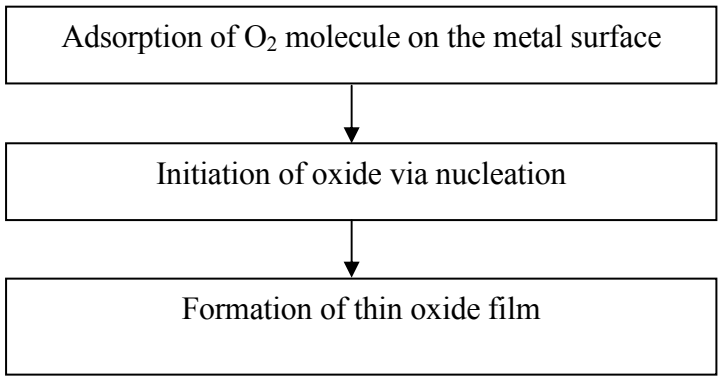

Figure 2-8 Basics of formation of an oxide scale

Any small changes in the system at constant temperature can result in changes in free energy, which can be represented by

$$\Delta G = \Delta H - T\Delta S$$

Where ΔG – change in Gibbs Free Energy , ΔH- change in Enthalpy , T- Absolute Temperature , ΔS- change in Entropy

Free energy change determines in which direction the process will proceed, e.g.,

$$4Cr + 3O_2 \rightarrow 2Cr_2O_3$$

In other words, at certain temperature chromium reacts with oxygen to form chromium oxide, this is accompanied with decrease in free energy (ΔG negative). Hence, thermo-dynamics provide the direction in which the process will proceed based on the following conditions. If ΔG is negative, a spontaneous reaction will take place; If $\Delta G = 0$, the system will be in equilibrium; and If ΔG is positive, no reaction takes place;

An Ellingham diagram is shown in Fig 2-9 which is often used to compare the standard free energy of formation of oxides as a function of temperature. This diagram can be used to compare the relative stability of various oxides. Based on the Ellingham diagram, the oxidation partial pressure of oxygen equilibrium with the oxide can be determined by the following equation,

$$pO_2 = \exp(\Delta G^\circ/RT)$$

Where ΔG- Change in Gibbs Free Energy , R- Gas Constant , T- Absolute Temperature in Kelvin, pO_2- Partial Pressure of Oxygen

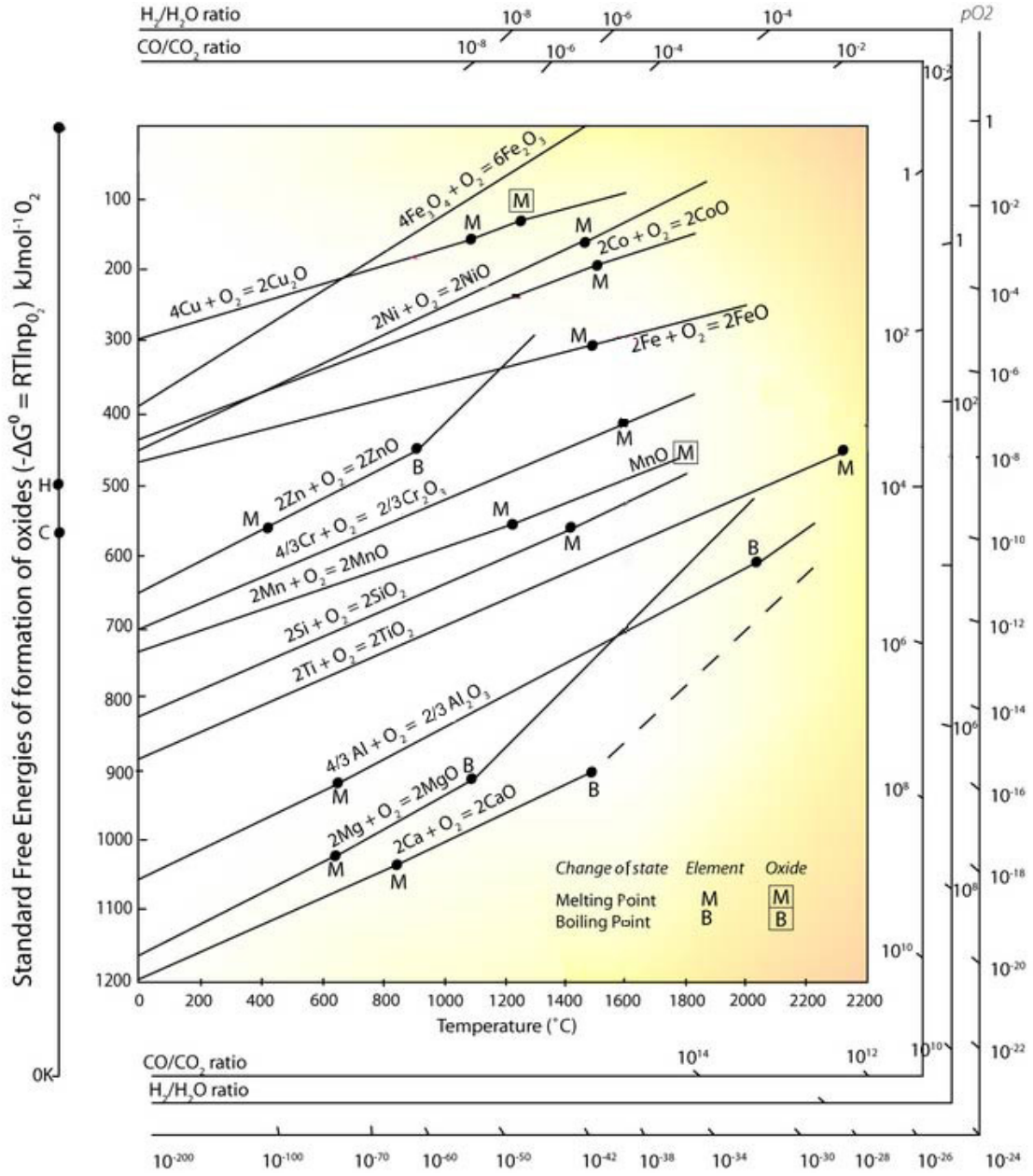

Figure 2-9 Ellinghan Diagram (Reproduced with permission from university of Cambridge) [Ellingham 1944].

A simple oxidation reaction can be represented by following reactions [Bose., 2007].

$$M \rightarrow M^{2+} + 2e \quad [\text{ Metal – Oxide Interface}]$$

$$M^{2+} + 1/2O_2 + 2e \rightarrow MO \text{ [Oxide – Gas Interface]}$$

$$1/2O_2 + 2e \rightarrow O^{2-} \text{ [Oxide – Gas Interface]}$$

$$M + O^{2-} \rightarrow MO + 2e^- \text{[Metal – Oxide Interface]}$$

As further oxidation process can take place only through the oxide layer, which is limited by the diffusion of reactants across the oxide scale, the rate of isothermal oxidation can be expressed as

$$x^2 = Kt \text{ for protective oxide scale}$$

x – oxide scale thickness; K – Rate constant; t – time in minutes

Since oxidation process is dependent on temperature, the diffusion rate exponentially increases with temperature, the Arrhenius relationship is represented by,

$$D = D_0 \exp(-\Delta H/RT)$$

D-Diffusivity factor; D_0-Constant; R-Gas constant; T-Temperature in Kelvin, and

ΔH- change in Enthalpy

2.4.2 Kinetics

Kinetics enables one to attempt to evaluate the rate of oxidation reaction. Kinetics can provide information on why one type of oxides will grow faster than the other in certain conditions. This is very useful for design engineers, as they often choose material for a certain component based on specific service environment, as they can estimate the

design life based on oxidation growth rate models. Using kinetics, individual steps involved in oxidation mechanism are addressed. The steps involved in a simple oxidation process are illustrated in Fig 2-10. The following steps are involved in an oxidation reaction,

A – Oxygen molecules are adsorbed and / or absorbed to the metal surface

B – Oxygen molecules breaks down into atomic oxygen

C – Oxygen atoms ionizes and reacts with metal atoms

D – Reactive elements are transported across the oxide scale

E – Metal ions are transported in the metal substrate towards the metal – oxide interface by diffusion phenomenon

Thus oxygen and metal ions continue to diffuse through the oxide scale for continued growth of oxide scale.

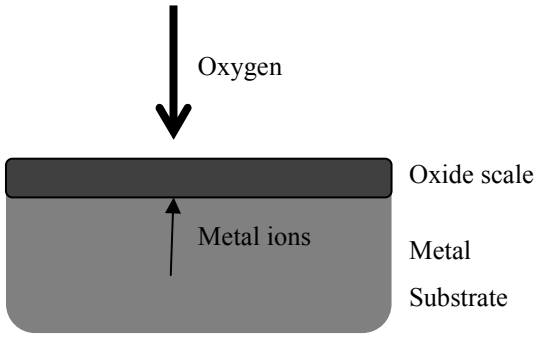

Figure 2-10 Illustration of steps involved in oxidation process

2.4.3 Oxidation rates

The oxidation growth rate depends on various factors such as chemical composition of the substrate, total surface area exposed to the environment, temperature of the environment, type of gas and its composition. Oxidation growth rate is greatly influenced by the method of heating, two of the most common types employed by researchers to measure oxidation studies are isothermal and cyclic oxidation tests.

The isothermal approach is very popular to characterize oxidation scale growth or mass gain as a function of time conducted at various temperatures. On the other hand, cyclic oxidation tests are often used to simulate the actual service conditions that involve rapid heating and cooling conditions. Since, most oxide scales are brittle in nature with considerably lower coefficient of thermal expansion (CTE) compared to the underlying substrate, they tend to crack or spall under cyclic conditions.

Isothermal oxidation scale growth rates are often expressed as one of the rate equation models. These rate equations are generally classified as logarithmic, parabolic and linear.

It should be noted that these models represents only ideal cases, it is not uncommon to notice deviations between the actual oxidation growth rate and the growth rate calculated based on rate equations. In the subsequent section, some of the most common rate models used to predict high temperature oxidation are briefly described.

2.5 Parabolic, logarithmic and linear growth rates

2.5.1 Parabolic growth rate

The expression for parabolic growth rate of oxide scale is expressed as

$$x^2 = k_p t + C,$$

Where,

x = weight change (mg/cm^2); k_p = Parabolic rate constant; t = time; an C = initial oxide scale thickness.

Most metals at elevated temperature exhibit parabolic oxidation growth rate [Smialek et al., 1987]. When the square of the specific weight change is plotted against time, a resultant linear trend line will confirm the parabolic nature of the oxidation growth rate, which is illustrated in Fig 2-11. The oxidation growth rate of some of the well known oxide scales exhibiting parabolic growth rate [Smialek et al., 1987] is as shown in Fig 2-12.

2.5.2 Logarithmic growth rate

In thin films (thin oxide scale), the oxygen atoms adsorbed to the surface react with the metal atoms resulting in an electric field across the thin oxide film. Continuation of oxidation takes place by transportation of metal atoms through the oxide scale by an electric field.

The expression for logarithmic growth rate is expressed as

$$x = x_0 + k\ln(t)$$

Where,

x = weight change or scale growth; x_0 = initial scale thickness when t=0; k = rate constant; and t = time taken.

Logarithmic growth of oxidation is generally observed in many metals in the lower temperature region (below 400°C) or during the early state of oxidation, where the transportation of electrons or ions are dominated by the electric field until a continuous scale or a stable form of oxide is formed. Lipkin et al [Lipkin et al., 1997] during investigation of oxide scale growth characteristics of NiAl at 1100°C for various exposure time ranging from 0.25-2.0 hours observed that initially metastable polymorphs of Al_2O_3 formed which progressively transformed to stable α-alumina scale. They concluded the kinetics of scale growth during the transformation phase was logarithmic, but the overall oxidation kinetics of the alloy as a whole based on thermogravimetric results confirmed to parabolic growth rate.

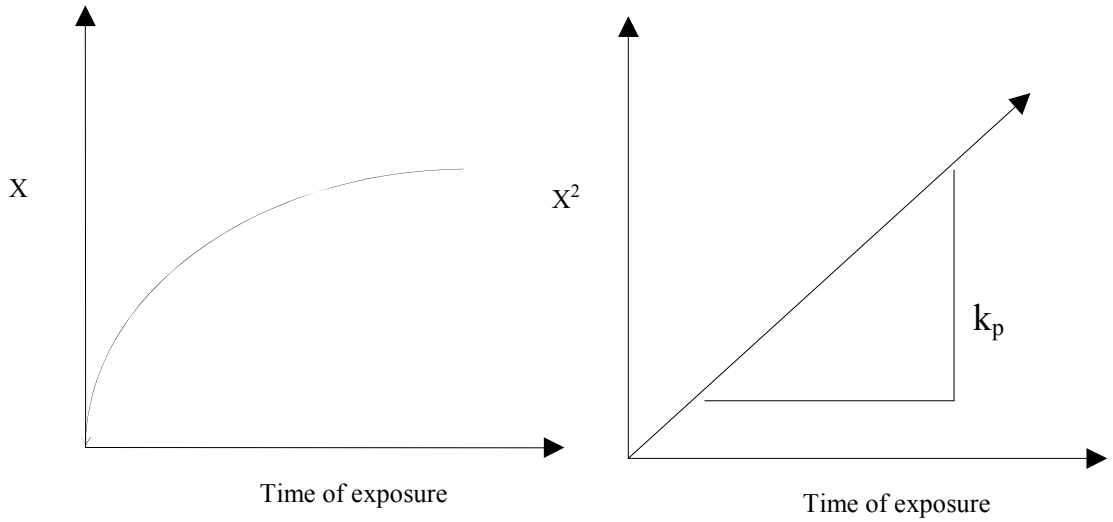

Figure 2-11 Illustration of parabolic oxidation growth rate

(Where x is the specific weight gain in mg/cm^2)

2.5.3 Linear growth rate

Linear growth rate of oxide scale growth is often common were non-protective nature of oxide scale formation. The non-protective nature of the oxide allows continuation of rapid oxidation reaction leading to a linear growth rate, expressed by

$$x = x_0 + k_0 t$$

where, x = weight change or scale growth; x_0 = initial scale thickness when t=0; k_0 = rate constant; and t = time taken

Fig 2-13 illustrates various growth rate models that provide the differences between parabolic, logarithmic and linear growth rates.

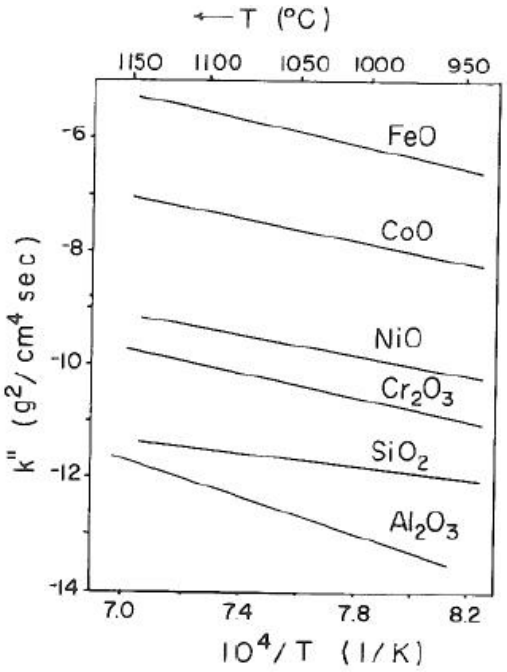

Figure 2-12 Oxidation scale growth rate of some of the alloying elements used in the manufacturing of alloys used in gas turbine engines [Smialek et al., 1987] (Reproduced with permission from Wiley & Sons)

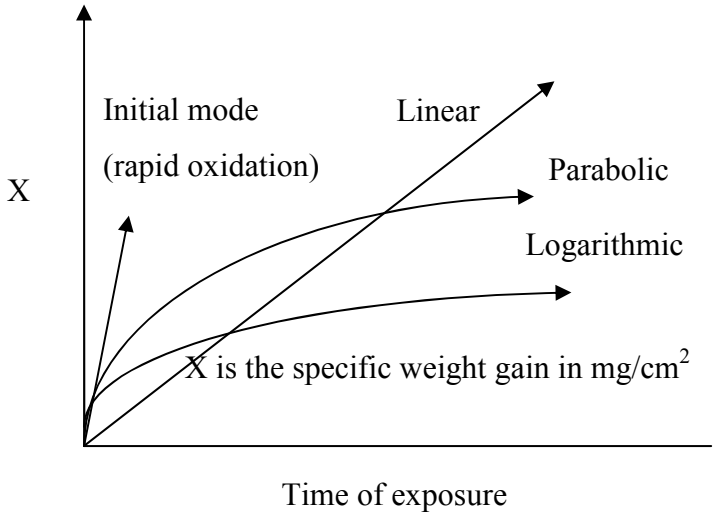

Figure 2-13 (L) Illustration of oxidation growth rate modes

2.5.4 Breakaway oxidation

Some of the oxidation scales tend to spall or crack more often, which causes rapid oxidation, exhibiting linear (initial mode) growth rate until the scale is completely rehealed. When the oxide scale is protective in nature until further spallation, the scale growth rate exhibits parabolic growth rate. This behavior of mixed mode oxidation growth mechanism is illustrated in Fig 2-14.

2.5.5 Wagner's Theory

Wagner's oxidation theory is an important cornerstone in the fundamental understanding of elevated temperature oxidation of metals [Douglass 1995]. When a bare metal is exposed to elevated temperature, rapid oxidation takes place and a transient scale is formed, with a protective scale slowing down the rate of scale growth. Wagner first proposed that the scale growth would depend on the diffusion of ions or electrons across the scale, making certain assumptions such as i) The oxide scale is always coherent and adherent to the substrate ii) Diffusion of reactants or ions takes place only by lattice diffusion iii) The growth of oxide is stable and in uniform thickness. Wagner's theory predicted short-term oxidation of simple metal alloys e.g. binary metals (two component system) but failed to predict multi component complex alloys, for example, a Ni or Fe based Superalloy. However, it remains as a basic guide in the understanding of elevated temperature oxidation growth. It has been shown that for more complex alloys [Atkinson 1985], Wagner's theory is not applicable due to effects such as grain boundary diffusion, alloying element segregation, effect of minor elements such as Yttrium etc.

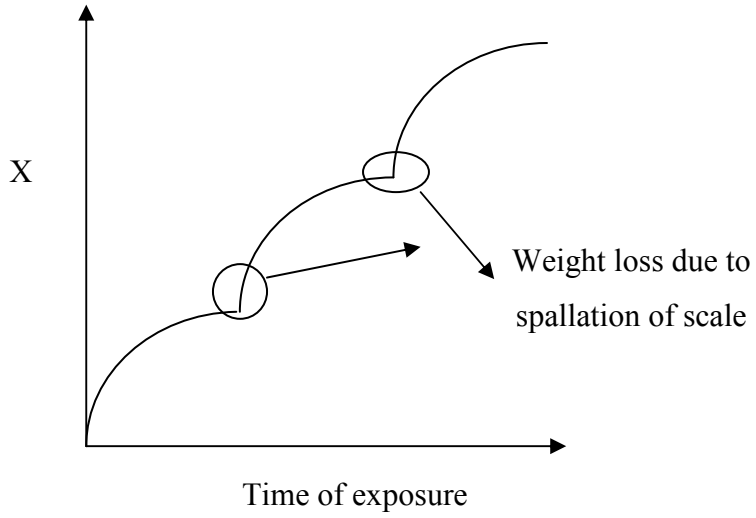

Figure 2-14 Oxidation growth of oxide scale that spalls frequently there by exhibiting both parabolic and linear growth modes

2.5.6 Elements and their effect on Oxidation in Superalloys

Aluminum: is an excellent and preferred choice in most high temperature alloys to improve oxidation resistance. However, alumina scales are not the best choice when used in corrosive atmosphere. Aluminizing is a well known process in many high temperature applications and extensively used by many coating methods in gas turbines and other industries [Whittle 1978].

Chromium: An excellent choice below 950°C, having a synergistic effect with the presence of aluminum. It is preferred in many high temperature materials as it also offers better hot corrosion resistance [Whittle 1978].

Silicon: Silicon can be used to improve oxidation resistance at elevated temperatures similar to aluminum. Excess addition of silicon tends to cause brittleness and precipitation of deleterious brittle phases along with the beneficial oxidation resistance. The main protective oxide is due to formation of SiO_2, which is an excellent protective oxide that can reduce the oxidation scale growth rate. However, SiO_2 tend to vaporize much more easier than alumina or chromia scales. There are commercial coatings enriched with silicon (up to 5%) available such as Sermalloy J™, which finds extensive application in gas turbine engines.

Titanium: In many precipitation hardenable alloys, small additions of titanium are made to form high temperature strengthening phases such as gamma prime in Ni based alloys. It has been known that titanium promotes formation of chromium oxide in Ni-Cr alloys. It has been reported that titanium reduces the scale adherence thus being detrimental to oxidation resistance on Ni base alloys [Bose 2007]. Titanium at elevated temperatures (600°C –1000°C) forms oxide scales conforming with the parabolic rate law for growth rate. However, it should be noted that any model should consider the rate of combination of oxidation scale growth and oxide dissolution in the metal to accurately predict the life of this material. It is known that similar behavior is exhibited by other metals such as Zirconium and Hafnium [Birks et al., 2006].

Nickel: Nickel is extensively used in many high temperature alloys used in the gas turbine engines. Nickel readily forms nickel oxide (NiO) at high temperatures and this scale does not provide stable oxide that can prevent further oxidation. Nickel helps forming transient oxide during the initial phase of oxidation, however without presence of oxidation resistance elements such as aluminum, chromium, it does not protect the underlying alloy substrate from subsequent oxidation. [Bose, 2007]

Cobalt: Cobalt is used in many solid solution strengthened and precipitation hardened alloys which are used in the gas turbine industry. Cobalt can form two types of cobalt oxides (Co.O) and (Co_3O_4). It is similar to nickel oxide as it forms porous and fast growing outward oxide scale. The cobalt oxide growth rate is generally observed to be greater than nickel oxide scale in many alloy systems [Bose, 2007].

Iron: Iron is used in several Superalloys for cost considerations. Iron forms Fe.O, Fe_3O_4, and Fe_2O_3, all are porous and fast growing oxide scales. At temperatures below 570°C, FeO does not form, but expected to form two layer oxides consisting of Fe_3O_4 (Inner layer) and Fe_2O_3 (Outler layer). When the temperature is above 570°C, it promotes formation of FeO along with other two types of iron oxides. Hence, it generally results in a three-layer oxide with FeO being the inner most scale adhering to the substrate metal [Birks et al., 2006]. Due to undesirable scale properties, it is often not preferred in many high temperature Superalloys especially from an oxidation perspective. [Birks, 2006]

Boron: It has detrimental effect in many nickel based Superalloys, as boron strongly supports formation of nickel oxide instead of protective alumina scales.

Manganese: It has beneficial effect of promoting formation of chromia scales in Ni-Cr based alloys and formation of alumina scales in Fe-Al alloys [Bose, 2007].

Niobium and Tantalum: Nb is known to form oxides at elevated temperatures by inward diffusion of oxygen transported across the scale. As the scale tends to increase in thickness, they tend to crack thereby allowing rapid linear oxidation growth. Ta is used upto 7% in many modern high temperature alloys to improve oxidation properties [Birks et al., 2006].

Sulphur: It is known that even a very small amounts of sulphur can have deteriorating effect as it can lower the oxide scale adhesion, thereby leading to premature spallation of protective scales. Addition of yttrium has shown to help in tieing up sulphur by forming sulfides or complexes, thereby improve oxide scale adhesion. [Bose, 2007]

Reactive elements: Yttrium, Hafnium, Cerium and other such elements are used for several years and have been known to improve the scale adhesion properties and also to reduce the oxidation scale growth rate. Many high performance coating materials such as MCrAlY materials are composed of about 0.5-1 weight percentage of such materials to improve the oxide scale characteristics. [Bose, 2007]

2.5.7 Oxidation of Alloys

Most metals used for engineering applications are made up of alloys to obtain superior structural strength, which is one of the most important properties among other desired properties such as oxidation resistance, corrosion resistance, etc. Oxidation mechanisms in alloy systems are more complex as it involves formation of multilayered oxides, bi-modal oxides, internal oxides and spalling, etc.

The oxidation mechanism in Superalloys has been described [Smialek et al., 1987] using two different scenarios. In the first one, in an alloy made up of major element A, which is more resistant to oxidation and minor element B that is susceptible to oxidation. When element B is present below a threshold atomic fraction, oxygen diffuses into the alloy, reacts with element B forming a dispersed oxide BO in surrounding A. The BO formed in this alloy is called as internal oxidation. This is illustrated in Fig 2-15a.

If BO is stable, the depth of oxidation can be expressed as

$$x(t) = [2N_0(s)\, D_0\, t / N_B(0)]1/2$$

If element B is present above a certain critical amount, oxygen would react with B more easily forming external continuous oxide as illustrated in Fig 2-15b. The expression that can be used to calculate the critical amount of element B required for external scale formation is

$$N_B^{(Critical)} >= [0.1\ \pi\ N_0(s)\ D_0\ V_m / D_B\ V_{ox}]^{1/2}$$

Where,

$N_0(s)$ = Atomic fraction of oxygen;

D_0 = Diffusivity of oxygen in alloy AB;

V_m = Molar volume of metal;

D_B = Diffusivity of element B in alloy AB;

V_{ox} = Molar volume of oxide formed

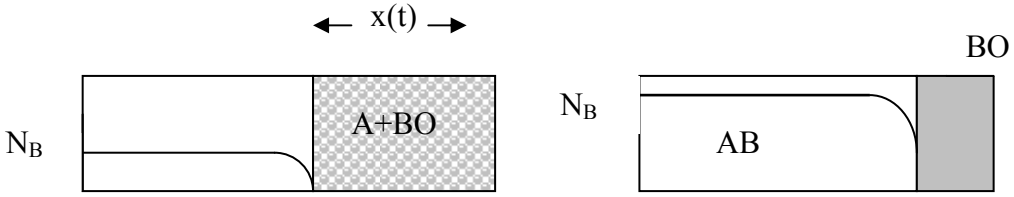

Figure 2-15 Cross sections and concentration of profiles for oxidation of an alloy AB, where A is a noble metal and B is a reactive metal (a): Minimal amounts of B in A resulting in internal oxidation of B in A; (b) Sufficient amount of B in A resulting in continuous Reproduced with permission from Cambridge publications [Birks et al., 2006]

In the second scenario, both A and B form oxides AO and BO, where oxide scale BO is more stable than oxide scale AO. When the element B is present in below critical concentration level, internal oxidation takes place resulting in subsurface precipitation of BO in A and this enveloped by an external oxide scale AO as shown in Fig 2-16a. However, if B is present in higher concentration (above critical level) an external BO scale will result as shown in Fig 2-16b. This shows when sufficient amount of B is

present, oxidation favors formation of a stable oxide that results in slow down of further oxidation, thereby exhibiting parabolic growth rates. This is important for designing alloys with sufficient amount of alloying elements that can protect the substrate from rapid oxidation attack. Some AO type oxide will likely form during the transient state, ie., during the initial discontinuous oxide scale on the bare alloy surface. However, continuous formation of external scale of type BO, depletes the alloy of element B, thereby finally resulting in inability to form further protective scale resulting in rapid oxidation growth rates leading to structural failure of the substrate.

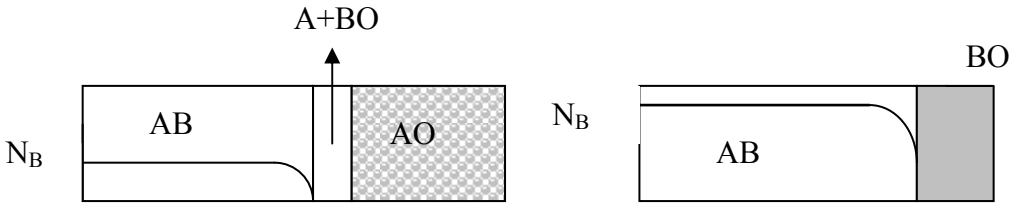

Figure 2-16 Cross sections and concentration of profiles for oxidation of an alloy AB, where A is a noble metal and B is a reactive metal (a): Minimal amounts of B in A resulting in internal oxidation of B in A; (b) Sufficient amount of B in A resulting in continuous Reproduced with permission from Cambridge publications [Birks et al., 2006]

The transition from slower desired parabolic oxidation scale growth to more deleterious rapid scale growth rate depends on several factors such as initial concentration of protective scale forming B, diffusivity in alloy, diffusivity in oxide, geometry of the part etc. Other factors that needs to be taken into account are stability of oxide (some of the oxides such as Cr_2O_3, SiO_2 are volatile under certain unfavorable conditions), spallation of oxide scale from the substrate due to internal stresses, erosion or mechanical wear of

oxide scale, stressed developed in between the oxide scale and underlying substrate due to thermal expansion mismatch during heating and cooling etc. The coefficient of thermal expansion (CTE) of various oxides and their substrates is tabulated in Table 2-4, showing the substantial difference between the thermal expansion characteristics of oxide scale and the substrate alloying material. This is generally exacerbated when the component is subjected to rapid cyclical heating and cooling cycles. The illustration in Fig 2-17 shows the difference between the rate of weight gain / loss for isothermal and cyclic oxidation conditions.

2.5.8 Protectiveness of the oxide scale - Pilling-Bedworth Ratio

The protectiveness of the oxide scale depends upon the opaqueness to oxygen permeation that would help in conserving the oxide forming elements in the substrate for longer period of time. One of the common indications used to define the protective nature of the oxide scale is by Pilling Bedworth Ratio (PBR). The PBR can be used to express the ratio between the volume of oxide formed to the volume of metal consumed. The various nature of oxide formed and the consequence on the metallic substrate is illustrated in Fig 2-18. When PBR≈1, a protective oxide scale close to the desired ideal condition results. When PBR >>1, the volume of oxide formed is more than the metal consumed, thereby resulting in compressed oxide scale that tend to buckle or spall easily. This leads to the in exposure of unreacted metal surface to service environment thereby resulting in rapid oxidation. When PBR <<1, the volume of oxide scale formed will be insufficient to completely cover the underlying substrate metal, this will result in

continued oxidation due to non-protective nature of the scale. The Pilling-Bedworth ratios for some of the well-known oxide scales are tabulated in Table 2-5. It can be seen that a protective oxide like Al_2O_3 exhibits a value close to 1 and non-protective oxide scale like MgO exhibits a value less than 1.

Table 2-4 Coeffcient of thermal expansion of metals and oxides [Birks et al., 2006]

Metal-Oxide	Substrate CTE $X10^{-6}$	Oxide CTE $X10^{-6}$
Fe - FeO	15.3	12.2
Ni-NiO	17.1	17.6
Cr-Cr_2O_3	7.3	9.5
Cu-CuO	9.3	18.6

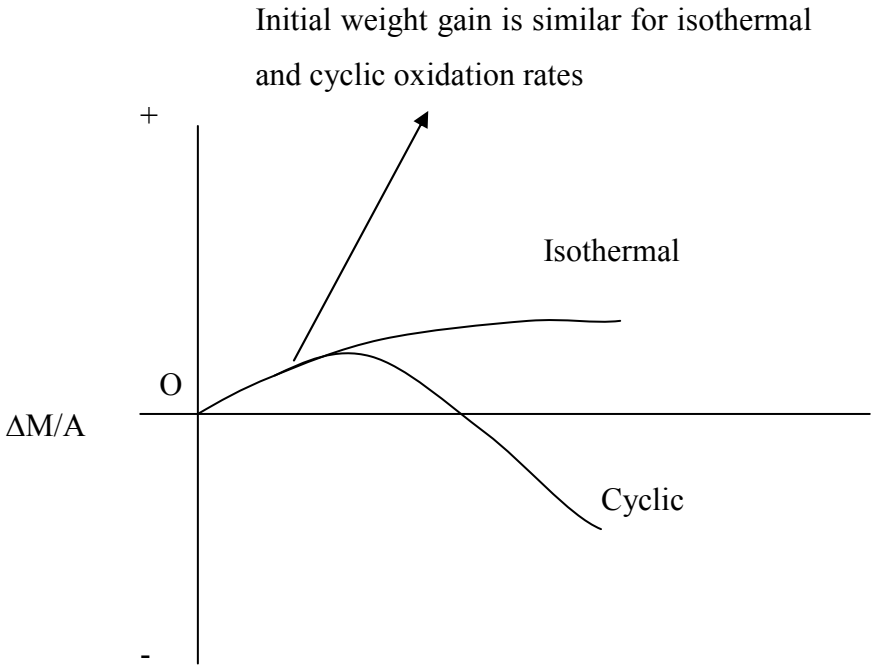

Figure 2-17 : Difference of oxidation scale weight gain for isothermal and cyclic oxidation mechanisms

2.5.9 Oxide Scale failure due to stresses

The thermal stresses generated during heating and cooling cycles can result in one or more of the following: i) crack formation in the oxide scale, ii) spallation of the oxide scale, and iii) plastic deformation of the oxide and scale to accommodate the relieving the internal stresses [N.Birks, 2006]. The above mentioned mechanisms are illustrated in Fig 2-19. It is believed that the growth stresses on the oxide scale tend to cause spallation during cooling cycle, where the growth stresses tend to be compressive in nature. When the elastic strain energy of the oxide scale exceeds the interfacial fracture resistance, it will result in spallation of oxide scale. Evan et al., [Evan et al., 1984] proposed the expression for failure criterion as

$$(1-\gamma)\sigma^2 h / E > \text{Gc}$$

Where,

E is Young's Modulus

γ is Poisson's ratio

h is oxide scale thickness

σ is biaxial residual stress in the oxide scale

Gc is the interfacial fracture resistance

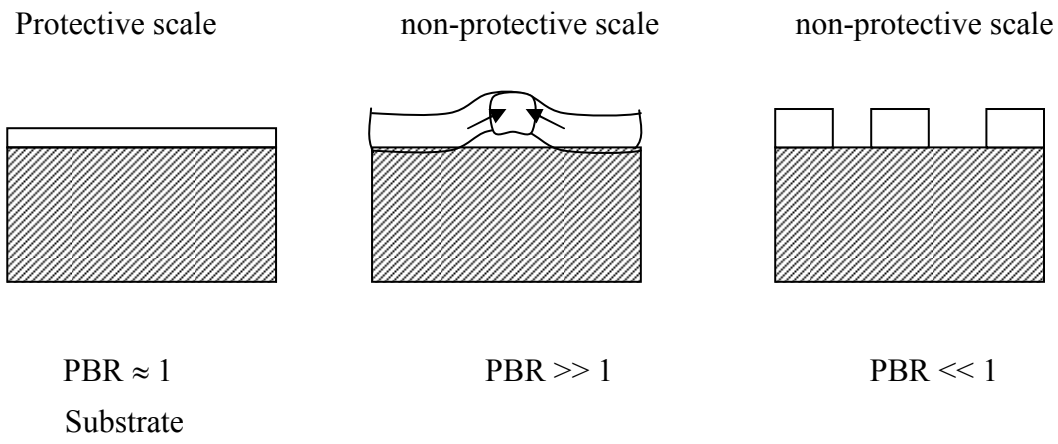

Figure 2-18 : Illustration of Pilling-Bedworth protective and non-protective scales Reproduced with permission from Elsevier [Bose, 2007]

Table 2-5 Pilling-Bedworth ratios for some well known oxide scales Reproduced with permission from Elsevier [Bose, 2007]

Oxide	**PBR**	**Nature of the oxide**
V_2O_5	3.19	Non Protective
Al_2O_3	1.28	Protective
Cr_2O_3	1.99	Protective
SiO_2	2.15	Protective
MgO	0.81	Non Protective

This expression shows that if any increase in scale thickness, stress in the oxide scale, and interfacial free energy can increase the risk of failure. It has been shown [Evan et al., 1984] that development of a wedge crack or increase in buckling instability along with the compressive stresses to result in spallation failure. Buckling of a thin oxide scale

under biaxial compression with a buckle radius a will occur, when the critical stress σ_c given by,

$$\sigma_c = 1.22\left[\frac{h}{a}\right]^2 \frac{E}{1-\gamma^2}$$

The buckle will be stable and will not result in separation of oxide scale, unless the strain energy release rate satisfies above equation as illustrated in Fig 2-19a. If the scale thickness increases, buckling may not be possible resulting in shear or wedging failure of the oxide scale as illustrated in Fig 2-19b. If Gc is very high and the substrate alloy is weak and ductile, the compressive stresses can cause deformation of the scale and substrate without any scale failure as illustrated in Fig 2-19c.

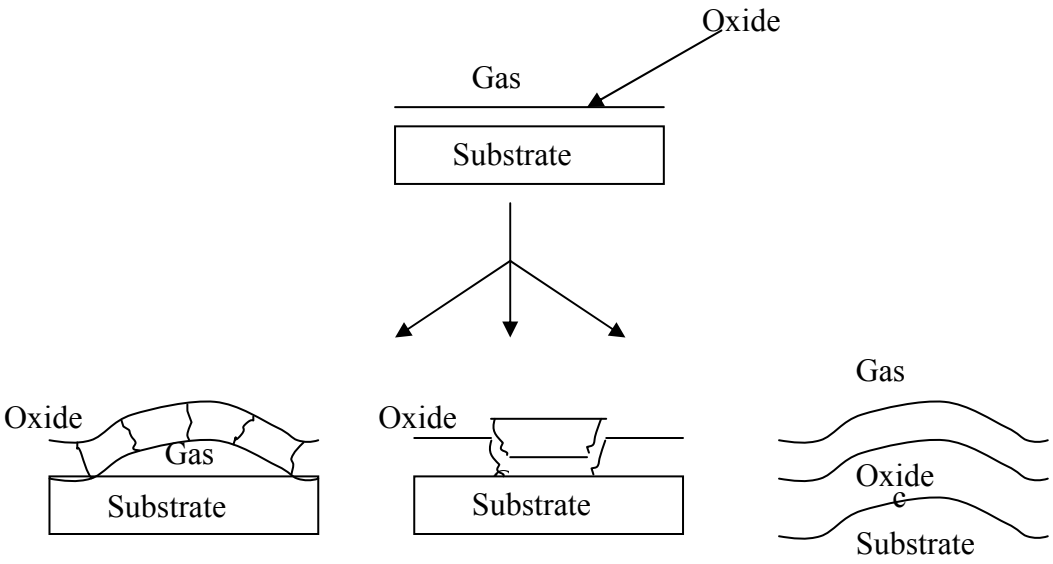

Figure 2-19 Illustration of oxide scale response to stresses, a) Buckling of oxide scale, b) Shear failure of oxide scale, and c) Plastic deformation of the oxide scale and the alloy Reproduced with permission from Cambridge publications [Birks et al., 2006].

2.5.10 Hot Corrosion

In addition to oxidation, several components in gas turbine engines are also subjected to corrosion as combustion of fossil based fuels leave a residual deposit of sulphates, vanadates etc., on the surface of the alloy components. Further salt deposits such as Na_2SO_4 at certain conditions as been shown in many studies could result in severe "Hot corrosion" attack resulting in catastrophic failures. The deposit induced high temperature reaction (Hot corrosion) depends on various factors such as operating environment, gas composition, service temperature, thermal cycling characteristics, substrate chemical composition, type of salt deposit and erosion. [Sims et al., 1987].

There are two type of hot corrosion Type I and Type II. Type I pertains to high temperature corrosion in the region above 800°C, generally common in aircraft gas turbine engines resulting due to sulphide deposits. This type of hot corrosion is often studied in laboratory environment using Na_2SO_4 deposits. Type II pertains to hot corrosion at relatively lower temperature regime in the region of 600°C, generally of more significance in marine based gas turbine engines. This type of hot corrosion is commonly studied in laboratory environment using sulphur dioxide or sulphur trioxide gas. The Fig 2-20 illustrates high temperature oxidation and the two types of hot corrosion in gas turbine engines.

In this research, the focus is limited to high temperature oxidation, hence the literature provided here is a brief introduction with information on the difference between high

temperature oxidation and corrosion. A detailed summary on hot corrosion studies can be found elsewhere [Roberge 2000; Schütz 2000; Donachie 2000]

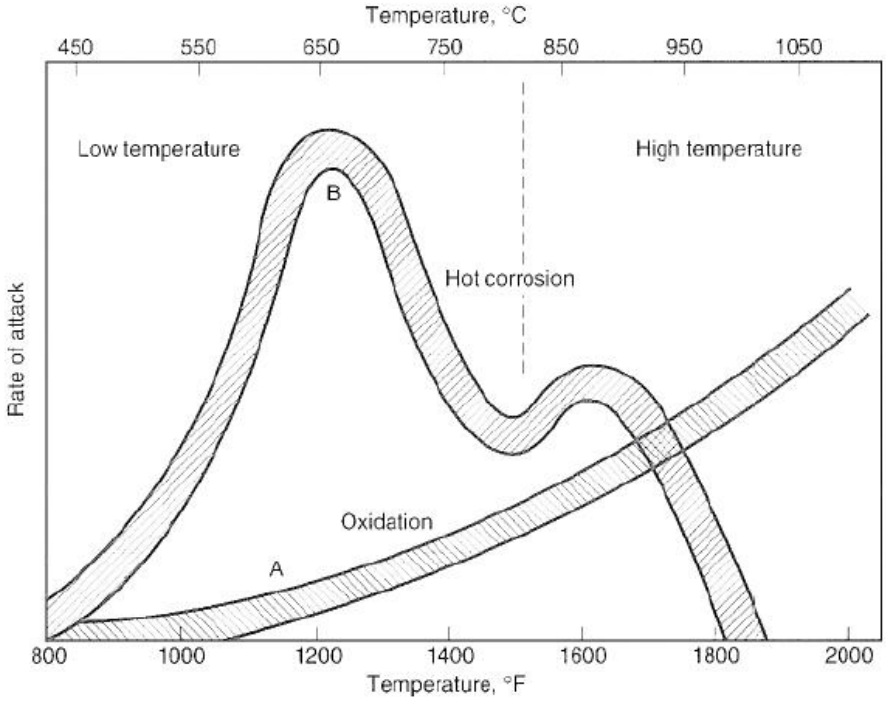

Figure 2-20 Expected rate of attack (A) vs actual rate of attack from test rigs and engines for a nickel based superalloy turbine foils (Reproduced with permission from ASM International [Donachie, 2000])

2.6 Oxidation characteristics of Incoloy 909

While Incoloy 909 possess excellent mechanical and attractive low coefficient of thermal expansion properties, the one drawback is poor oxidation resistance at elevated temperatures due to the absence of protective scale forming elements such as chromium in this alloy [Symonds et al., 1986; Smith et al., 1989; Material Data Sheet of Incoloy 909 1992; Mannan 2000; Sato et al., 1993]. The addition of 0.4% silicon improved the SAGBO resistance dramatically in Incoloy 909 which is likely due to increased resistance to block oxygen diffusion along the grain boundaries [Heck et al., 1988].

Bricknell et al., [Bricknell et al., 1981] reported SAGBO resistance can be improved with additions of Boron, which showed excellent improvement in elevated temperature creep rupture properties in Incoloy 903. The general oxidation resistance still remained poor due to the absence of chromium and lack of significant amounts of aluminum, the two most important constituent elements that can provide significant improvements to oxidation resistance.

During the development of low CTE alloys it was observed that any increase in chromium to provide significant oxidation resistance degraded the attractive low CTE property. This is due to a reduction in lowering the Curie temperature. Also the presence of significant amounts of aluminum (1%) in the alloys 903 and 907, affected long term stress rupture properties at elevated temperatures due to poor SAGBO resistance, which resulted in continued efforts in the development of better low CTE Superalloys [Smith et al., 1989; Wanner et al., 1991]. Thermo-gravimetric analysis is one popular and simple

test to compare the oxidation resistance at elevated temperatures. Fig 2-21 shows significant rate of weight change on Incoloy 909 compared to negligible changes to Inconel 718. These results are based on cyclic oxidation test carried out at 650°C, with 15 minutes hold time at temperature, followed by cooling using air blast for 5 minutes.

Smith et al., [Smith et al., 1991] investigated effect of cyclic oxidation on thermal barrier coated Incoloy 909 pins as shown in the Fig 2-22. Each test cycle consisted of heating at 1375°C for 45 minutes followed by cooling under ambient condition for 15 minutes. After several cycles, they observed the coated surface on the external diameter acted as an oxygen barrier thereby preventing any oxidation of the substrate. However, the cooling holes used for inserting Inconel 600 tubes were found oxidized as no protective coatings were present on those surface.

2.6.1 Stress Accelerated Grain Boundary Oxidation and Dynamic Embrittlement oxidation

Embrittlement oxidation

Fe-Co-Ni alloys are as earlier reported susceptible to notched stress rupture testing in exposed air environment due to failures in relatively short time compared to vacuum environment in the temperature range of 540 –650°C. These fractures were characterized by intergranular failures with grain boundaries exhibiting oxide wedges. It was thought that oxide penetrated onto the grain boundaries due to the application of stress. As the failures occurred intergranularly and as the parted grain boundaries contained oxide wedges, this phenomenon was termed as stress accelerated grain boundary oxidation

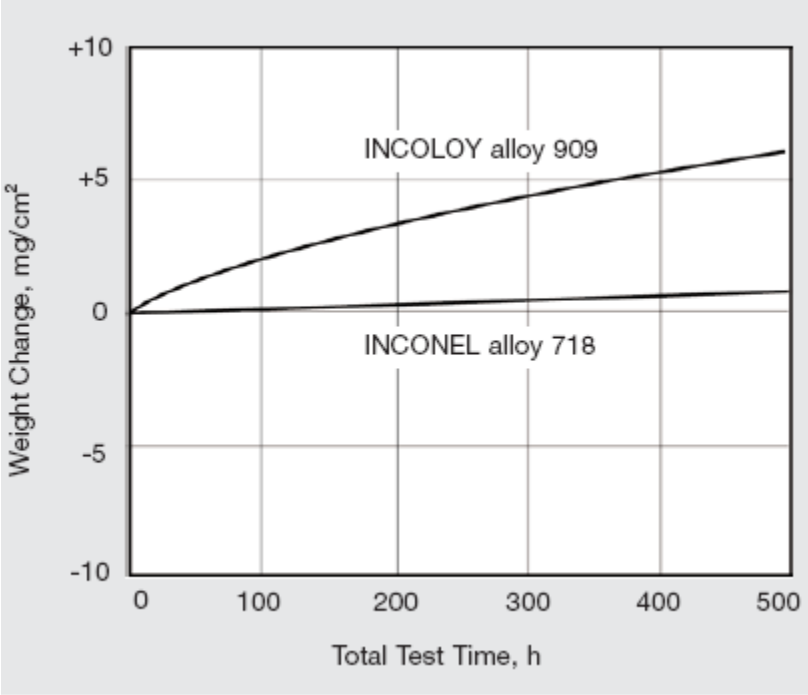

Figure 2-21 Thermogravimetric results of cyclic oxidation test carried on Incoloy 909 and Inconel 718. [Material Data Sheet of Incoloy 909 1992] (Reproduced with permission from Special Metal Co)

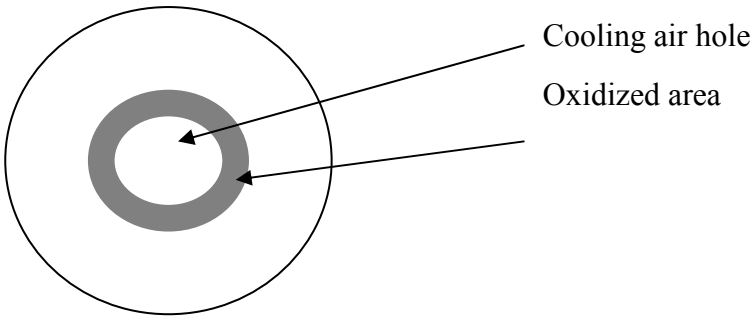

Figure 2-22 Illustration of oxidized region in the near the unprotected cooling air passage located in the test Incoloy 909 pin

(SAGBO). These failures were thought to have occurred by the penetration of oxide along grain boundaries perpendicular to tensile load axis. Controversy exists on whether Fe-Co-Ni alloys are susceptible to SAGBO, where continuous oxide formation leads to failure or susceptible to dynamic oxygen embrittlement failures, where oxygen diffusion along the grain boundaries causing a transition from ductile to brittle failures. The later is reported [Woodford 1981] to be common in pure nickel and some nickel based alloys.

Bricknell et al., [Bricknell et al., 1981] investigated Incoloy 903 to understand the primary cause of reduction of ductility in notched elevated temperature tests, concluded that oxygen diffusion along the grain boundaries was the primary reason for reduced stress rupture time. They suggested that presence of oxide wedges in the grain boundaries of failed test specimen indicate that oxidation likely took place after primary failure due to oxygen embrittlement. Furthermore, Bricknell et al [Bricknell et al., 1981] graphically explained the difference between SAGBO and Oxygen embrittlement effect as shown in Fig 2-23.

.

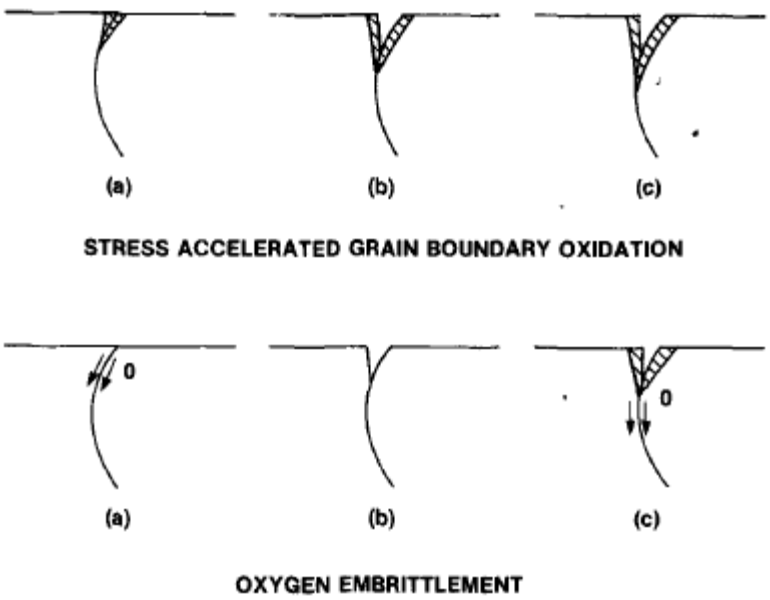

Figure 2-23 Comparison of stress accelerated grain boundary oxidation ((a):oxide wedge forms preferentially on grain boundary, (b):oxide cracks due to tensile load, (c) oxide grows along grain boundary and process continues until complete failure) and oxygen embrittlement [Bricknell et al., 1981](Reproduced with permission from Springer)

2.6.2 Oxidation characteristics of Inconel 718

Inconel 718 is a traditional Ni-Cr-Fe based Superalloy shown to have exhibited excellent oxidation resistance in its aging temperature range ie., below 650°C. This is attributed due to the presence of copious amounts of chromium (17-19%). In addition to chromium, the presence of various other elements such as nickel, titanium, aluminum and niobium likely plays a role on elevated temperature oxidation resistance for this class of superalloys due to complex interplay among alloying elements [Donachie 2000]. It has been reported that chromium oxide (Cr_2O_3) scale forms and grows by counter current diffusion of chromium and oxygen [Basu et al., 1991].

During an investigation of oxidation of Inconel 718, [Jian et al., 2000] researchers studied oxide film formation after heat treating test coupons in air at 580°C with a hold time of 3000 hours, however, no noticeable formation of oxide film or scale was observed. However, when the temperature was increased to 620°C, a thin oxide film measuring about 5μm formed after an exposure of 3000 hours as shown in Fig 2-24. Jian et al., predicted using the parabolic law, that the scale would grow into about 18μm thick oxide layer after exposure of 40000 hours, assuming the process was still controlled by solid state diffusion. Deadmore et al., investigated [Deadmore et al., 1977] the effect of ΔT on oxide spallation behavior and subjected Inconel 718 test coupons to thermal cycles consisting of 60 minutes exposure to 1100°C, followed by 30 minutes at lower temperature to achieve various ΔT temperatures ranging from 0°C to 1030°C. Here ΔT is the difference between the oxidizing temperature(high temperature) and the cooling

temperature used in the cyclic oxidation test. They characterized the resulting oxide scale using X-ray diffraction.

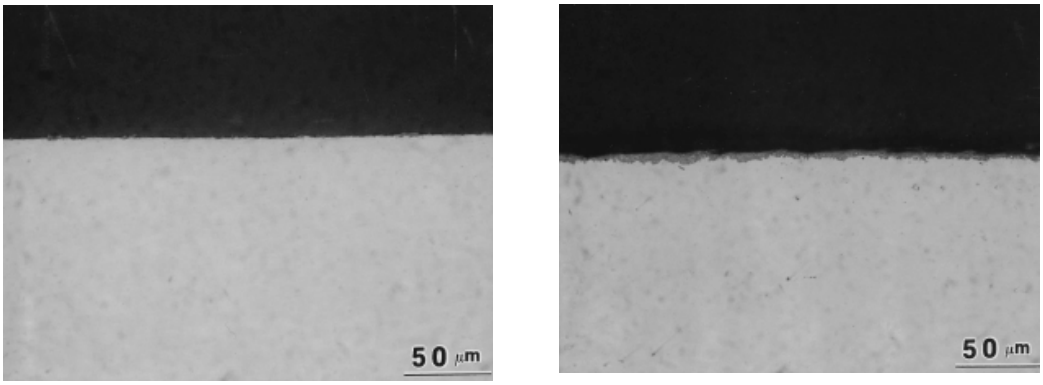

Figure 2-24 Inconel 718 exposed to 580°C (Left) and 620°C (Right) to oxidant atomosphere[Jian et al., 2000] (Reproduced with permission from Elsevier)

It was reported that the presence of chromium oxide (Cr_2O_3), tapiolite [$Ni(Nb(Nb,Ta)_2O_6$] occurred under all ΔT conditions except some $NiCr_2O_4$ was also observed after ΔT = 1030°C testing. They noted that these oxides were sensitive to spallation with a ΔT of as low as 560°C, while Hosking 875, a Fe-Cr-Al alloy which solely formed aluminum oxide (Al_2O_3) scale, resisted spallation up to a ΔT=1400°C. These investigators attributed the spallation resistance of Al_2O_3 oxide scale to its low CTE especially in the temperature range of 25-1200°C.

While investigating the oxidation of Inconel 718 [Greene et al., 2001] in air at high temperatures, it was reported that below 900°C, Inconel 718 alloy forms a transient oxide for approximately during the initial 24 hours. However, continued exposure at this temperature did not result in any measurable growth in oxide scale. Such initial oxidation was rapid due to the absence of a barrier between oxygen and the metal surface; however, scale formation slowed down oxidation scale growth. Hence most protective scales are thought to exhibit parabolic growth rate.

Trindade et al., [Trindade et al., 2000] reported on the mass gain of Inconel 718 exposed to laboratory air at 1000°C at various intervals for up to 90 hours. The mass gain growth rate agreed with a previously reported parabolic behavior by Greene et al. The mass gain was noted to be 2.5 mg/cm^2 after exposed to 1000°C for 90 hours. The parabolic growth rate constant was calculated to be kp = 0.374 $mg^2cm^4h^{-1}$. Some intragranular attack was

also reported with formation of Al_2O_3 precipitates at the grain boundary closer to the exposed surface.

2.7 Why coatings are needed

In the previous sections it was evident that the high temperature oxidation can have deleterious effects on alloy substrates. Several researchers have confirmed that presence of protective scale forming elements, in sufficient quantities, are essential in the underlying substrate alloy to weather elevated temperature oxidation.

Most alloys used in gas turbine engines are selected based on desirable properties such as elevated temperature strength that includes creep and fatigue strengths, better strength to weight ratio, low coefficient of thermal expansion, ease of fabricability etc. Having these requirements in consideration, material designers cannot improve the oxidation resistance of the substrate metals, as any addition of excessive scale forming elements can drastically impede other properties such as strength. The oxidation resistance can be improved by selective deposition of an alloy enriched with protective scale forming elements. Hence, using a coating becomes an important option as it can effectively improve the surface protection from severe oxidation, while the substrate metal can have better elevated temperature mechanical strength.

There is an increasing demand on surface engineering technologies to meet various specific needs at affordable cost. This has led to the development of numerous coatings, which have played an important role in the protecting substrate metals from the severity

of elevated temperature oxidation. Candidate coating materials are often tailored to suit the substrate alloy, in which several factors shall be considered which includes coating deposition method, material properties such as Young's modulus, thermal expansion rate, Poisson's ratio, ductility, thermal conductivity, density, specific heat and other factors for both coating and the substrate [Stern 1996].

As discussed previously, depletion of scale forming elements in the substrate alloys due to continuous consumption of these elements for scale formation, also takes place within the coating. The formation of an oxide layer on the surface results in consumption of elements like aluminum and chromium from the coating. When the oxide film is eroded or spalls, a new oxide film grows on the exposed area maintaining continuous growth of oxide film. This phenomenon can continue until oxide-forming elements can continuously diffuse from the underlying coating material. This continuous depletion can result to a point where the coating cannot supply any more oxide forming elements thus resulting in coating failure.

The coatings generally exhibit fine-grained microstructure when compared to the substrate alloys with similar chemistry. The diffusion coefficients can be ranked as follows,

$$D_{Surface} > D_{Grain\ boundary} > D_{Volume}$$

Based on the above, the diffusion rates in the coatings can be substantially different (faster) compared to the substrate material as coatings are present on the surface and

tend to be characterized with small grains compared to the substrate. Hence for most Superalloys used in extreme conditions, using a coating is an economically feasible solution, and when the oxide forming elements are depleted, the coating can be stripped and the component re-coated thereby extending the life cycle of the component. A thriving industry is dependent on such type of component repair often called as maintenance repair and overhaul business within the aerospace industry. As shown in Fig 2-25, some of the relevant coating processes frequently used in application of coating on gas turbine engine components are illustrated. Brief introductions of these processes are presented in this section.

As detailed in the previous sections, there are many coating deposition techniques available, and choosing the best process depends on the functional requirements, (size, shape, and metallurgy of the substrate), adaptability of the coating material to the technique intended, level of adhesion required, and availability and cost of the equipment.

2.7.1 Chemical Vapor Deposition

Diffusion coatings enriched with oxide scale forming elements consisting of aluminum, chromium, silicon or combination can react with the substrate alloy surface and form intermetallic compounds with excellent scale forming properties. Nickel aluminide is one of the most commonly used diffusion coatings on nickel based Superalloys. In high temperature applications, aluminides are often used, which on exposure to service conditions will form protective alumina scale. In gas turbine engine components such as

blades and nozzle guide, vanes aluminide coatings, often with platinum or chromium inter layers are added to improve the hot corrosion resistance along with oxidation resistance.

The basic process consists of generating vapors of scale forming elements and exposure of the substrate material to these vapors at specific conditions conducive for reaction of these vapors with the substrate surface. There are several variant in this process such as pack process, out of pack process, slurry process and chemical vapor deposition. [Siva-kumar at el., 1989; Krishna et al., 1998; Warnes et al., 1997; Bose 2007]

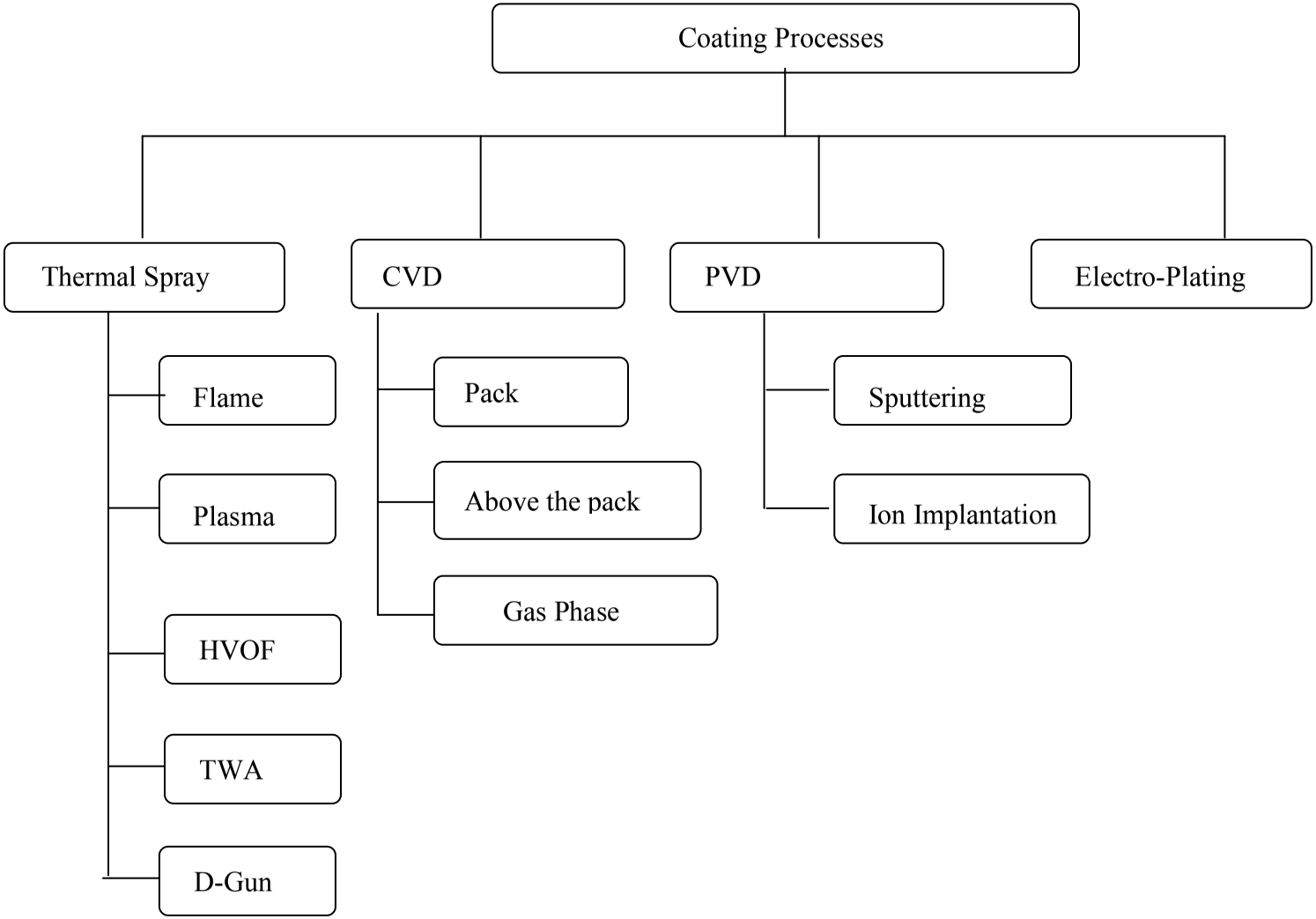

Figure 2-25 Types of selected coating processes used for oxidation resistance in gas turbine engine components

2.7.2 Physical Vapor Deposition

Physical Vapor Deposition is a line of sight process, which include techniques such as ion plating, evaporation and sputtering capable of forming coatings characterized by both amorphous and crystalline microstructure. At lower pressures the most difficult materials can be vaporized easily and then they undergo deposition onto the substrate by collision less transport in the chamber. Electron beam assisted PVDs are often used in aerospace industry to coat turbine blades with thermal barrier coatings. The coating spallation due to stresses generated by variation in coefficient of thermal expansion between the ceramic coating and the substrate metal is reported to cause relatively less damage to columnar type structure due to the natural ability to expand and contract without causing cracking [Nichols et al., 2001].

2.7.3 Electroplating

High temperature oxidation resistance coatings such as proprietary Tribomet™ can be deposited using advanced electroplating process. Taylor et al., [Taylor et al., 2006] have investigated the thermal expansion characteristics of thermally sprayed MCrAlY and electroplated equivalent Tribomet™ coatings. They reported that the electroplated coating exhibited about 7% higher expansion rates compared to thermally sprayed coating in the temperature range of 525°C – 825°C. The relative difference in CTE between these coatings were attributed to the differences in phase content between these coatings.

2.7.4 Thermal Spray Process

Thermal spraying is one of the widely used, extremely versatile coating deposition techniques used in dimensional build-up on worn-out components using overlay coatings [Ishikawa et al., 1993]. In thermal spraying the raw feed stock material can be of the form of rod, wire, or powder, which is heated generally to a semi-molten to molten condition and then imparted a velocity thereby projecting onto a desired substrate surface. The classification of thermal spray processes is as shown in Fig 2-26(a) and illustration of coating process in Fig 2-26(b).

2.7.5 HVOF

The combustion flame spray process is a matured technology and is used to deposit coatings for more than 5 decades. The HVOF process is an advanced combustion flame spray technology and it is regarded as a "Milestone" in coating process technology [Heath et al., 1998]. The high velocity oxygen fuel (HVOF) process basically utilizes fuel and oxygen, which is combusted in an internal combustion chamber to produce a ontinues supersonic gas stream with a velocity over 2000 m/sec and the flame temperature is about 2650°C, a schematic of Praxair Tafa JP500 HVOF gun is shown in Fig 2-27. The initial development of this technology was reported to be developed at the Thayer School of Engineering, Hanover [Browning 1981], NH, USA and by Browning Engineering, West Lebanon, NH, USA in the early 1980s.

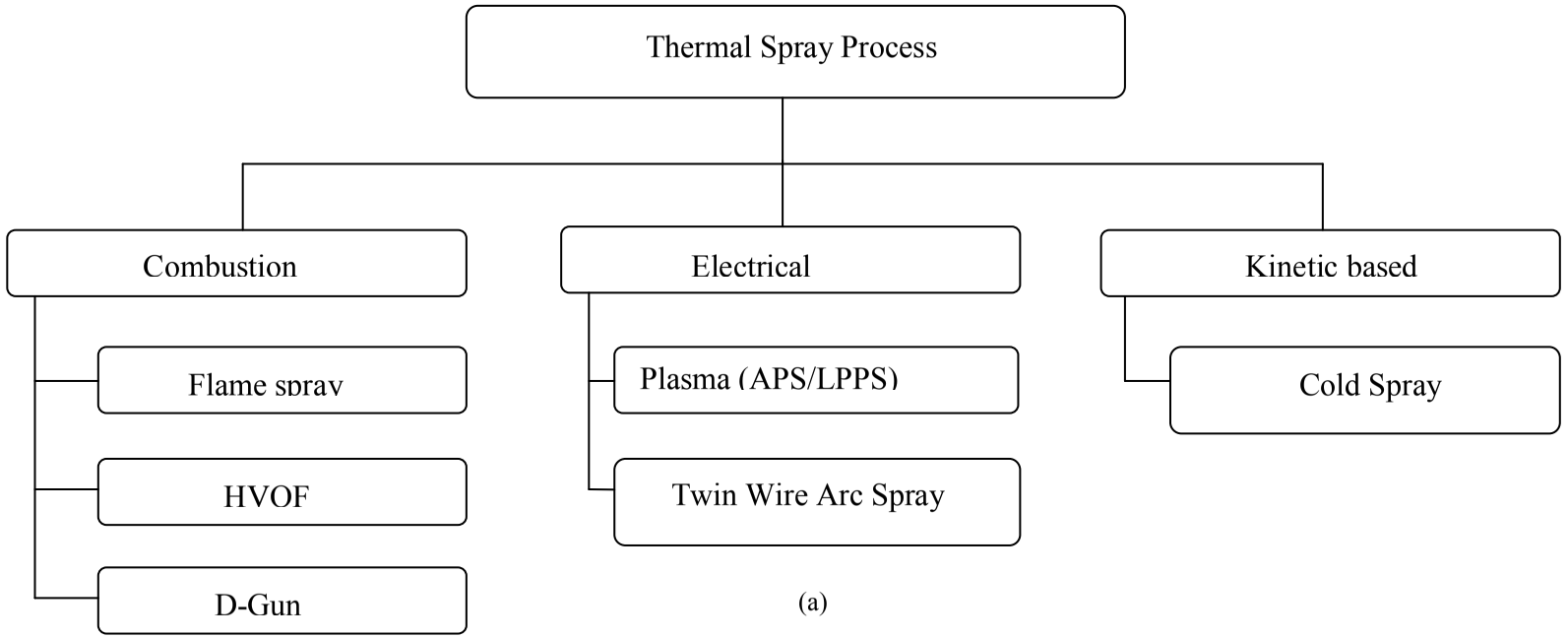

Figure 2-26 (a) Types of thermal spray coating process (b) Schematic of thermal spray coating deposition process

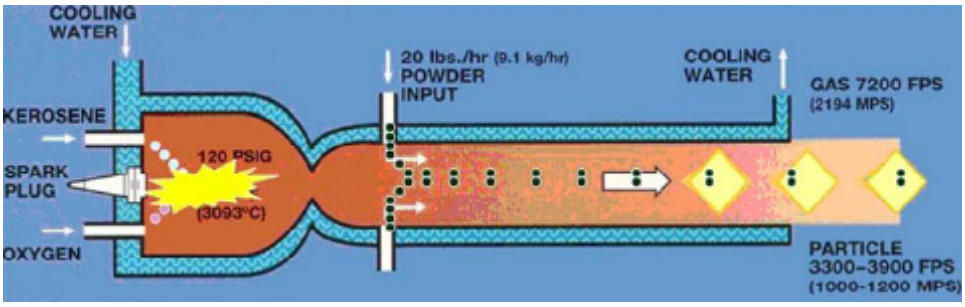

Figure 2-27 : Schematic of the Praxair TAFA JP5000 HVOF gun[Feuerstein et al., 2008]
(Reproduced with permission from Springer)

The HVOF process revolutionized the application of dense hard coatings in several smaller thermal spray shops across the world, as some of these coating can be applied only by D-Gun(detonation gun). D-Gun process is a patented and licensed process by Praxair Surface Technology Co. which offers the coating services but does not sell the equipment. The growth of HVOF technology was fuelled by low operating cost, low capital cost and flexibility that allow easy integration to an existing thermal spray facility.

These coatings are usually characterized by attractive features such as low void content, low oxides and excellent adhesive and cohesive bond strength. These features allow HVOF coatings to be preferred in wear resistance and corrosion resistance applications. HVOF equipment is also available in portable units, which allows to carry out field repairs in industries such as petrochemical plants, refineries, chemical storage vessels, valves which are subjected to aggressive corrosive and erosive (mechanical wear) conditions. It has been reported coatings such as Inconel 625, AISI-316-L and C-276 Hastalloy coatings are widely used for such applications. [Sidhu 2005].

There are numerous HVOF systems available, generally they can be categorized based on first and second generation systems. In the first generation systems, such as Jet-kote®, and Diamond Jet® systems, the combustion pressure ranges between 0.3-0.5 MPa, the gas jet attains supersonic velocity while exiting the nozzle. The particle size preferred for this application is (–45+10)μm and the particle velocity range from 300-450 m/sec. In the second generation systems such as JP-5000®, Top Gun K®, the

combustion pressure range between 0.6-1.0 MPa, the gas jet attains supersonic velocity in the combustion chamber itself [Korobov 2006]. The heat transfer rates are much better and hence higher particle velocities in the order of 800 m/sec are possible. Also the HVOF systems can be classified based on fuel types 1) Gaseous fuel HVOF and 2) Liquid fuel HVOF. Some of the popular gas fuel torches are DJ2600 (Sulzer Metco), DJ2700 (Sulzer Metco), Jet Kote (Stellite), Top Gun (IBEDA) and the popular liquid fuel torches are JP5000 (Praxair), Wokajet (Sulzer Metco) etc. Some of the popular gaseous fuels used in HVOF process include propylene, propane, hydrogen, acetylene, methane, MAPP (sort for methylacetylene propadiene) , CNG (compressed natural gas) and kerosene is the most popular liquid fuel used in the HVOF [Sidhu 2005]. The benefits of using HVOF coatings are as tabulated in Table 2-6 [Stokes 2003] and Fig 2-28 illustrates the classification of various processes based on particle temperature and velocities [Korobov 2006].

The feed stock powder is fed internally into the high velocity gas stream, which in turn heats and propels the semi-molten material against a target resulting in a coating [Thorpe 2003]. Zhang et al have modeled the temperature profile of such particles as shown in Fig 2-29. The particles as it exits the nozzle can be molten, semi-molten or solid depending upon the melting point of the feed stock material and the flame temperature. Temperature and velocity of the flame are the two important parameters that have direct effect on the coating microstructure and mechanical properties. The particle upon impingement flattens out and forms a splat as shown in Fig 2-30. Hence, optimal

balance between various parameters are key to get acceptable coating quality as it can depend on the substrate properties, coating material melting point, particle size, etc.

Table 2-6 Benefits of using HVOF coatings

[Adapted from J.Stokes, theory and application of HVOF, Ireland, TS Sidhu]

Coating benefit	**Causes for this benefit**
Dense coating (lower porosity)	High velocity transfer produces dense
Excellent wear resistance	Dense coating with retained hard phases
Better corrosion resistance	Low porosity in the coating
Higher coating cohesive strength	Improved particle bonding
Low oxide formation within coating	Fast in-flight transfer and less exposure to
Less globular particles in the coating	Higher impact force results in better splats
Better integrity and phase retention	Reduced time at high temperature
Thicker coatings (per pass and total)	Compressive residual stresses
Smoother as-sprayed surfaces	Finer particles and higher transfer velocity

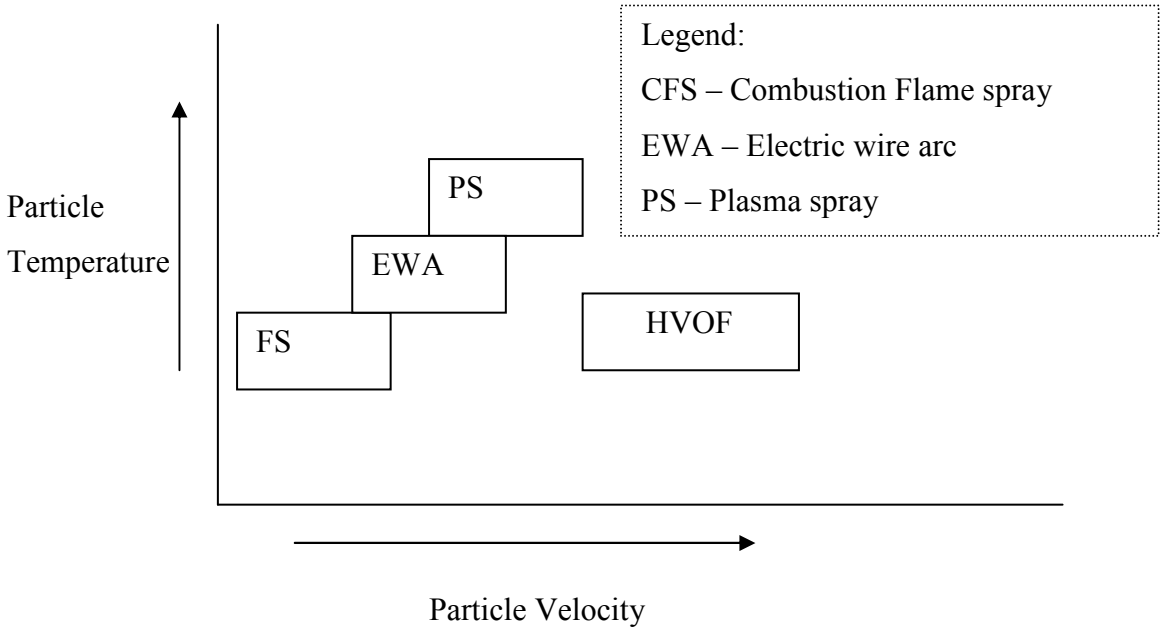

Figure 2-28 Particle temperature and particle velocities for various thermal spray processes

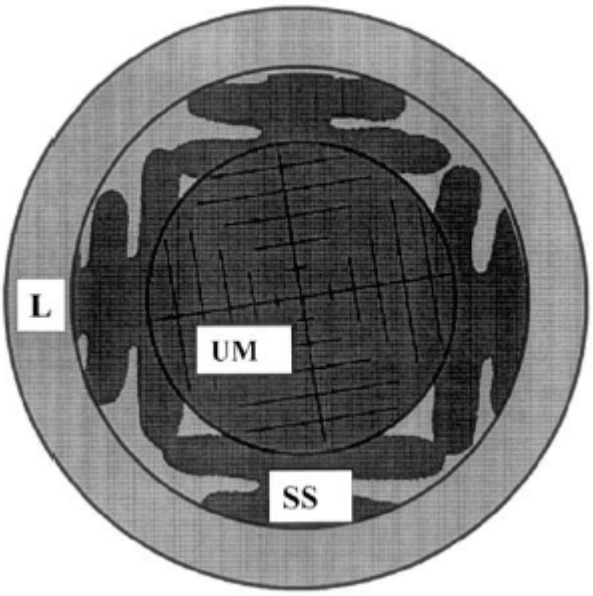

Figure 2-29 Schematic illustration of the structure of a partially melted powder particle during spraying with three zones as follows: unmelted core, UM; solid plus liquid (semi-solid) region, SS; fully melted, liquid shell. [L. D. Zhang et al., 2003] (Reproduced with Permission from Elsevier)

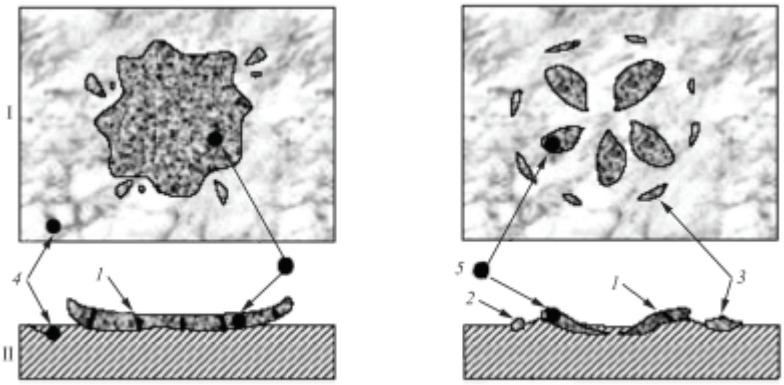

Figure 2-30 Splat formation, Splat microstructure pancake and star [Sidhu et al., 2005]
(Reproduced with Permission from Elsevier)

As splats rapidly solidify, it is believed to form a columnar structure within each splat or a brick work like structure [Sidhu et al., 2005]. Each gun pass over the substrate material results in a layer of coating composed of few to several lamellae thick deposit. In practice, the desired coating thickness is achieved after several gun passes over the substrate. As the coating cools, thermal stresses develop which can potentially result in problems such as cracking or interface separation resulting in coating failure.

Application areas that include aircraft engine parts, landing gears, oil drilling equipment and process equipments such as paper rollers. In addition to offering, faster coating rates, operators are not exposed to carcinogenic hexavalent chrome as in hard chrome plating process. In recent times, HVOF process is also found to be attractive alternative in other areas such as depositing Metallic (dimensional build-up), MCrAlY (Oxidation resistance) and ceramic protective overlay coatings (thermal insulation). These coatings can be deposited to a thickness of about 200-300 μm thick on the surface of the parts that

operate under high temperatures but internally cooled by air. This allows increasing the firing temperature, as the thermal barrier coating is capable of providing thermal insulation [Stern 1996; Pawlowski 1995].

The operating characteristics for various types of HVOF systems using gas and liquid fuel with heat content are shown in Table 2-7. A comparison of HVOF and other type of thermal spray process based on operation characteristics and coating properties are shown in Table 2-8.

Table 2-7 Comparison of Operating Characteristics for Gas and Liquid Fuel HVOF Torches and Heat content of fuels and typical fuel flow rates [Rusch, Sulzer Metco]

Fuel	Heat Content (kJ/liter 0°C)	Typical Fuel Flow (l/min 0°C)	Total Heat Available (kJ/min)	Stociometric Ratio (O_2/Fuel by volume)
H_2	11.307	613	6766	0.5
CH_4	36.524	189	6903	2
$C_{12}H_{26}$ (Kerosene)	35306.575	0.3785	13358	2034

The power output of the HVOF gun can be expressed as

Power(KW) = Fuel flow rate (S^{-1}) X Stochiometric ratio (Fuel to O_2)X ΔHc

Where, ΔHc is heat of combustion of fuel [Hearley et al., 2000]

Table 2-8 Coating characteristics of various thermal spray processes

Process	Oxide Content (%)	Porosity (%)	Bond strength(MPa)	Particle Velocty(m/s)
Flame	5-15	5-20	10-25	50-100
Wire Arc	5-20	5-15	30-60	100
Air Plasma	1-10	2-10	20-70	150-300
HVOF	1-3	1-2	65-80	400-800

Legoux and others [Legoux et al., 2002] evaluated kerosene and gas fuelled HVOF guns using WC 10% Co 4% Cr cermet coatings. They used a DPV-2000 gun diagnostic system to monitor the velocity and temperatures of the in-flight particles. They concluded that particles reached highest velocity at lower temperatures with the kerosene fuelled guns compared to gas fuelled guns. They concluded that coatings sprayed with kerosene-oxygen gun resulted in relatively denser coatings (very low porosity or void content) compared to gas fuelled guns.

The HVOF system when compared to Vacuum plasma spray (VPS) and Electron beam physical vapor deposition (EB-PVD) process involves coating deposition in an oxidizing environment, hence the HVOF coatings tend to exhibit oxide scales on the splat boundaries. The smaller the particle size, the larger will the surface area exposed to oxidizing environment, thus oxidation is expected to increase with decrease in the particle size of the coating material [Li et al., 2003].

Studies showed that the effect of various HVOF [Lugschider et al., 1998] process parameters on oxygen content of the sprayed coatings. They observed that spray distance, oxygen fuel ratio, and powder feed rate were the parameters among several other HVOF parameters that directly affected the oxygen content of the coatings. It is known that HVOF coatings exhibited lower void content, high bond strength, low surface roughness with relatively low thermally induced effect compared to plasma sprayed coatings. Knight et al [Knight et al., 1993] reported compressive residual stress of (-)200Mpa for a 0.2mm coating thickness. It was reported that grit blasting [Brandt 1995] with a coarser (F22) grit particles prior to coating deposition reduced the endurance limit under fatigue conditions compared to grit blasting with finer grit particles (F60).

2.7.6 Coatings Types

In the previous section a brief overview of coating application methods applicable to high temperature oxidation related with this research work is presented, while in this section the focus shall be the on coatings used in the gas turbine industry for high temperature oxidation resistance. Overlay and diffusion coatings are two important coating systems used in protecting high temperature oxidation in gas turbine engines. Diffusion coatings differ from overlay coatings, in which the interaction of the coatings and the substrate are substantial, as it becomes part of the coating formation. In the overlay coatings system, the substrate exhibit limited interaction with the coating, as it is limited to providing a base for the bonding of the coating [Bose 2007]. Most overlay coating system allow easier removal, as the component can be repaired and then new

coating can be applied thereby saving component replacement cost. While diffusion coating can also be repaired, the extent is limited, as removal of coating will entail removal of part of the substrate, as it becomes an integral part of the substrate. One of the primary advantages of overlay coating is the flexibility to incorporate elements such as yttrium, hafnium that are difficult to deposit using diffusion coating methods [Birks et al., 2006]. In Fig 2-31 classification of coating types and application methods used are presented. Since, this research focuses on metallic overlay coatings, the discussions will be limited to coating systems based on MCrAlY, Superalloy powders (Alloy 718) and Nickel – Aluminum.

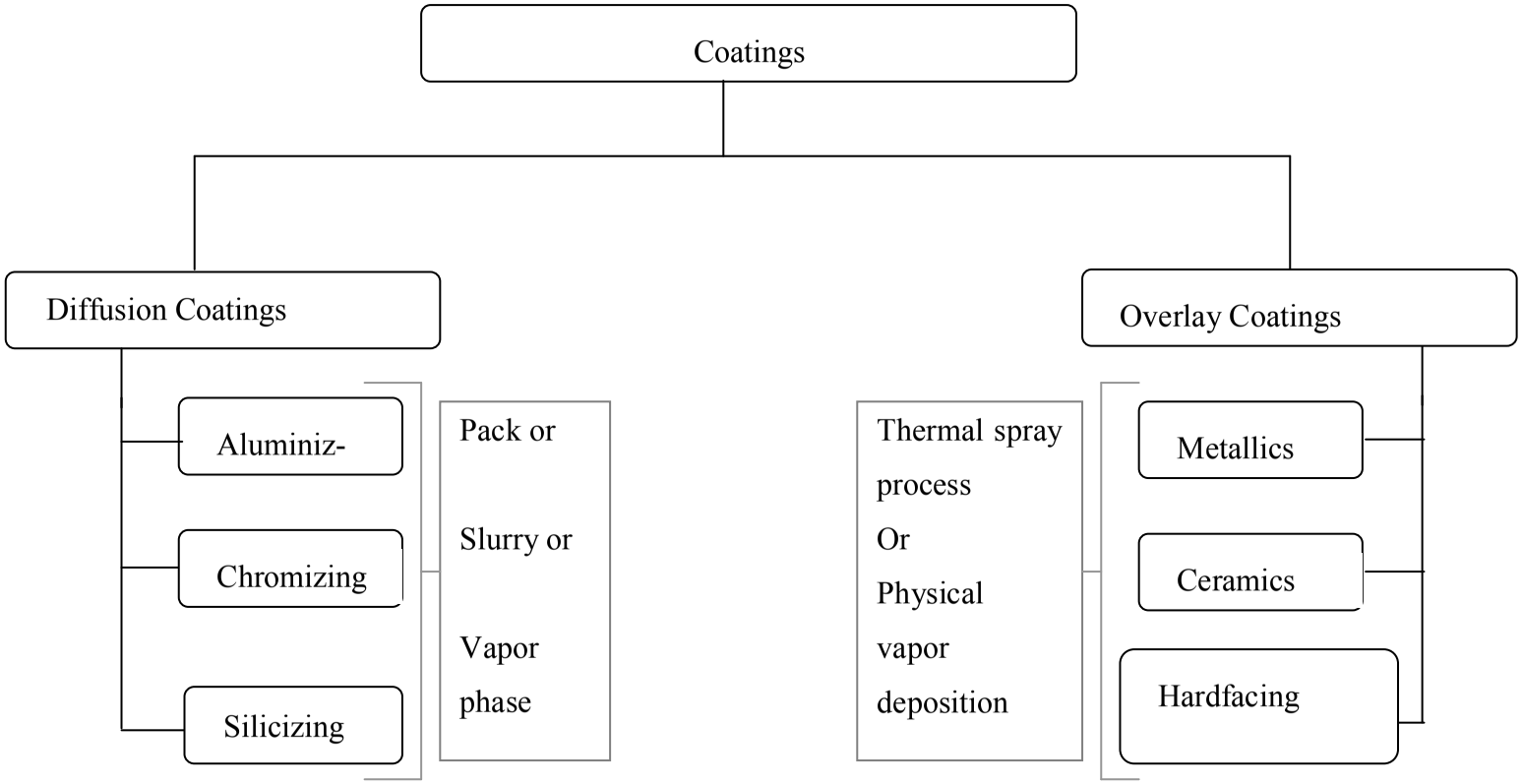

Figure 2-31 Types of coating used in gas turbine engine for high temperature oxidation resistance

2.7.7 MCrAlY

MCrAlY stands for Metal (Ni or Co or Fe or combinations)+Chromium+Aluminum+ Oxygen reactive elements such as Yttrium), are well known protective materials deposited on substrates to protect the surface from elevated temperature oxidation and hot corrosion. These coatings are known to provide a surface enriched with aluminum, chromium, and other elements those that are capable of resisting high temperature corrosion and oxidation by developing an adherent protective oxide scales. These scales are thermodynamically stable, and exhibit slow oxide growth rate. A slow-growing oxide layer is desirable because the scale failure due to cracking and spallation depends strongly on oxide thickness. The oxidation behaviour of the coating can be highly influenced both by the coating properties such as porosity and by the oxidation of the MCrAlY constituents during the HVOF deposition process. It is desired to have coating sprayed with minimum amount of porosity to lower the oxidation rate. MCrAlY type coatings used in aerospace industry are applied using one of the following process i) Electron Beam – Physical Vapour Deposition ii) High Velocity Oxy Fuel and iii) Plasma Process (Air Plasma and Vacuum or Inert Plasma). HVOF process in recent times emerging as a preferred application method due to the excellent coating quality at an affordable cost [Itoh et al., 2000]. The MCrAlY powders are produced by gas atomization, that involves rapid solidification in an inert gas environment. The resulting particles are spherical in morphology consisting of (Ni,Co)Al precipitates dispersed in a CoNiCr solid solution matrix. An EPMA photomicrograph showing 47.8Ni-21.7Co-17.2Cr-12.6Al-0.6Y particle is as shown in Fig 2-32.

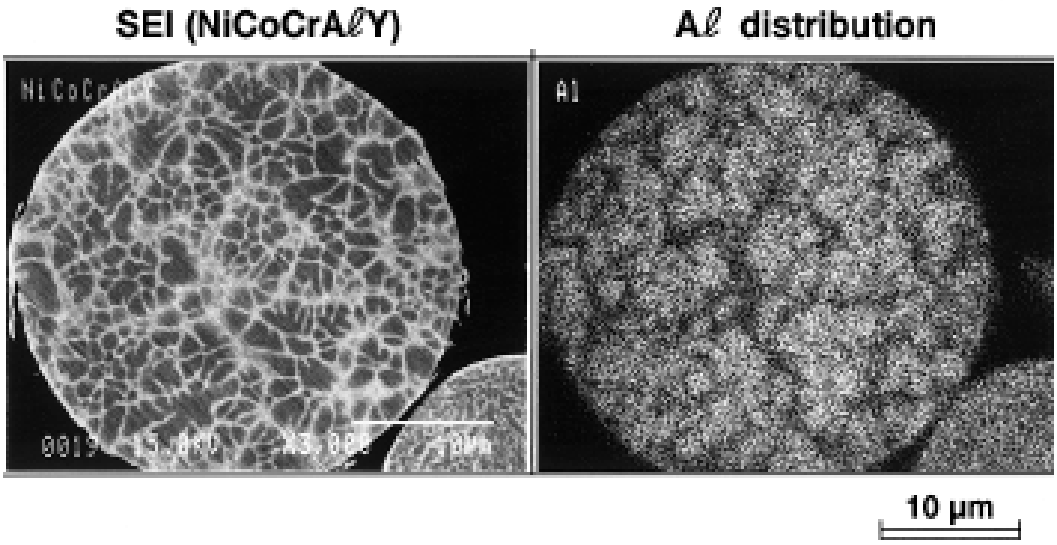

Figure 2-32 EPMA photomicrograph showing 47.8Ni-21.7Co-17.2Cr-12.6Al-0.6Y particle and distribution aluminum within the particle. [Itoh et al., 2000]

(Reproduced with permission from ASME)

Itoh et al., [Itoh et al., 2000] compared MCrAlY coatings deposited by various processes, and noted that Vacuum Plasma coatings were superior in terms of Young's Modulus and bending strength in as sprayed condition. The difference in modulus and bending strength decreased and become negligible when HVOF coatings were subjected to a diffusion heat treatment. The as sprayed HVOF coating consisted of porosity (4%), oxides and some poorly melted particles. The diffusion heat treatment transformed the coating into a more dense coating with about 3% reduction in porosity and also resulted in an uniform microstructure consisting of two phases i) (Ni,CO)Al precipitates and ii) CoNiCr solid solution matrix. The amount of Cr and Al depletion with HVOF was slightly more comparable to VPS sprayed coating, however the overall coating integrity were similar.

Poza et al., [Poza et al., 2006] used CoNiCrAlY powder supplied by Praxair™ (CO-210- 24), one of the powders used in this research work. They reported the powder characteristics with particle size distribution confirming to the range 45 ± 20 μm, with a mean particle diameter close to 34 μm. The as-gas atomized powder consisting of two-phase microstructure, with β particles dispersed in γ matrix. Based on XRD and EDS results, they identified the crystal structure of Co rich γ phase as FCC with a lattice parameter of 0.358 nm, and (Co, Ni)Al β phase as an ordered B_2, BCC, with a lattice parameter of 0.286nm.

Saiedi et al [Saiedi et al., 2009] reported that VPS deposited coating consisted of single phase, while the HVOF as sprayed coating consisted of two phases similar with starting feed stock material. However when they carried out diffusion heat treatment, both coatings looked similar with a two-phase structure. The researcher reasons that due to very high temperature involved with VPS spray process, the particles were taken into solution and then during rapid cooling, the precipitation reaction in the splats were restricted due to the limited time at which precipitation reaction will take place. In the HVOF process the maximum temperature of the flame is around 2700°C, with the particle temperature substantially cooler, the two phase structure in the coating is basically similar to the original composition due to limited phase transformation during the short resident time in the flame.

2.7.8 Ductile Coatings

Ni-5%Al coatings are traditionally used as a bond coat material for many years. It has proven in many years due to dependable coating offering excellent adhesion to a variety of substrates, ability to be sprayed with a variety of thermal spray processes that includes combustion flame spray, plasma, electric wire arc, HVOF and even non-thermal spray processes such as PVD and cold spray processes [Sampath et al., 2004; Ding et al., 1997]. Ni-5% Al powder for thermal spray process is available as clad and pre-alloyed material [Al coated Ni particles using an organic binder]. The excellent bond strength exhibited by this coating was originally thought to be due to exothermic reaction of Ni and Al during the spray deposition (in flight) process [Technical data Bulletin, Metco

450NS]. However, Sampath [Sampath 1989] have conclusively reported that an oxidation mechanism as the likely reason behind the exothermic reaction.

Ni-Al intermetallic compounds are reported to exhibit excellent high temperature oxidation resistance upto (1000°C) [Sampath, 1989]. Previous studies have shown that these intermetallic –compounds (IMCs) form adherent continuous protective Al_2O_3 scales at elevated temperatures [Doychak et al., 1994].

Hearley et al., [Hearley et al., 2000] investigated effect of HVOF spray parameters on the Ni-Al coating properties using Ni-Al powders with particle size distribution of 15-45 micrometers. Hearley observed that by optimizing oxygen to fuel ration to 80% stoichiometry and using a spherical gas atomized powder were able to obtain a coating with low porosity in the order of 2% and a high modulus of 281 GPa. The hardness and modulus obtained with the optimized HVOF coatings were reported to be similar to the values exhibited by bulk Ni-Al.

Mahesh et al [Mahesh et al., 2009] investigate HVOF sprayed Ni-5%Al coatings on 3 different Superalloy substrates equivalent to the Hastealloy X, Inconel X-750 and Inconel 800. They observed the coatings on all the substrates exhibited excellent integrity with the porosity less than 2%. The average hardness of the coating was 240HV15, the surface roughness (Ra) in the range of 9.22-9.45 micrometers and average bond strength 42MPa. Ni-Al intermetallic compounds reported to exhibit high melting

point (1911K), excellent thermal conductivity 970$Wm^{-1}K^{-1}$) and low density (5890 Kg/m^{-3}).

The reason and mechanism involved for superior adhesion have been investigated for several years. One well known theory [Technical data sheet of Metco 450, Sulzer Metco] dating few decades ago was the intermetallic exothermic reaction that was supposed to take place between the Ni and Al during the spray process, which was said to enhance the bonding strength for this coating. In the early days, the original form of Ni-5 wt.% Al powder was composite or clad material, the nickel core was cladded with aluminum on the outer surface with the aid of an organic binder. However in recent times, the preferred route of manufacturing this material is by inert gas atomization, which results in pre-alloyed Ni-Al powder. Although, the pre-alloyed material does not possess any free aluminum, still the coating provided excellent bond strength similar to the clad material thereby conflicting the original theory of exothermic reaction during the spray process. One reference [Sampath, 1989] in the literature concluded that exothermic reaction is not the reason as such reactions are not possible at atmospheric conditions. However, no conclusive evidence exist to date on any one particular mechanism but several factors such as wettability, surface tension and splat/substrate interface interaction etc., are said to be some factors that are likely to play a role for the resultant bond strength. NiAl coating is a versatile coating typically applied using various different thermal spray processes including HVOF process. However, HVOF sprayed NiAl coatings are superior due to high particle velocity and relatively lower temperature compared to electric wire arc, air plasma process as shown in Table 2-9. In addition to

this, they observed HVOF applied NiAl coating exhibited the highest elastic modulus. [Sampath et al., 2004].

Table 2-9 In-flight particle velocities and temperatures noted during spraying of Ni–5 wt.%Al [Sampath et al., 2004](Reproduced with permission from Elsevier)

Process	Velocity (m/sec)	Temperature (°C)
APS	121	2340
EWA	87	2330
HVOF	612	1819

2.8 Quality control requirements of thermal spray coatings

Quality control of thermal spray coatings in aerospace industry is usually accomplished by evaluating test coupons. The most popular tests include evaluating for microstructure, hardness and tensile bond strength.

2.8.1 Metallographic Examination

As shown in Fig 2-33 there are several microstructural features that play an important role in coating quality control. One of the most popular quality control used in the industry is to evaluate the microstructure of the coatings under optical microscope and compare it with standard micrographs. The aspects that are considered as a part of microstructural characterization are interface separation, interface contamination, porosity, oxides and oxide clusters, unmelts or globular particles, cracks (transverse and longitudinal), and integrity.

Interface separation: A separation or horizontal defect is associated with physical bonding between the substrate and the coating. Good surface preparation, absence of oxides on the substrate surface and residual stress of the coating are some of the importance factors that influence interface separation problems. Superalloys tend to form refractive type oxides on the surface especially when exposed to elevated temperatures, hence it is a generally a good practice to deposit the coating soon after grit blasting (surface preparation) process.

Interface contamination: The residual embedded grit, contaminants like foreign materials such as remnants from wipe, oxides, or previous coating present on the interface area that can potentially impede coating adhesion or prevent direct contact between coating and the substrate surface. It is expressed as a percentage either in each "Field of View" or in the total length of the coating that is made up of several "Field of Views".

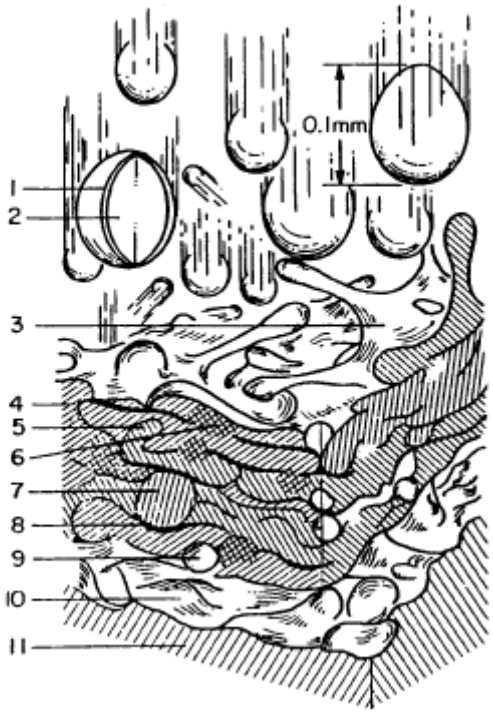

Figure 2-33 Schematic cross section of the microstructure of thermally sprayed coatings. 1, partially sectioned oxide layer formed on a metal droplet in flight; 2, metal particle with its center still in the liquid state; 3, impinging metal droplet, partially splats[Lin et al., 1994]

Porosity: It has been reported for corrosion and oxidation resistance coatings, that the presence of higher amounts of voids present in the coating is considered to have debilitating effects on the life and performance of the coatings. In general most thermal

coatings are mounted in vacuum impregnated cold or hot curing epoxy, so that the original voids or pores when interconnected can be back filled to prevent further damage or pullouts during grinding and polishing steps. However HVOF sprayed coatings are considered to be robust and its microstructure do not change drastically when hot press mounted under higher pressures. Porosity is expressed as a percentage and when present, it is preferred to be spread out uniformly throughout the coating. Any concentration of porosity in specific area of the coatings may lead to coating failures thus exposing the substrate to deleterious environment in gas turbine engines.

Oxides and oxide clusters: The hot inflight particles that comes in contact with atmospheric air during transit from the nozzle exit to the part will get oxidized on the surface depending upon the sensitivity of the coating material. These oxidized particles when deposit as splats on the substrate, the oxides becomes part of the coating. There are various type of oxides such as stringers (inter splat linear oxides), oxides associated with porosity or massive oxides usually referred to as cluster oxides and uniformly distributed oxides. The definition of cluster oxides is applicable based on the size of the cluster, in practice cluster greater than 0.75mm in diameter are considered to be deleterious. In some coatings, it has been reported that it is hard to distinguish between oxides and porosity and the original coating porosity to the induced coating pull out based porosity. Researchers to some extent successful used fluorescent dye penetrants during mounting of the coated sample and then later used ultraviolet light to illuminate the penetrant. The resulting photomicrographs or images can be used with image analysis software to calculate the percentage or area of voids present in the coating.

Cracks: Cracks usually appear perpendicular to the substrate. Brittle coatings are sensitive to cracking, hence careful metallographic preparation is very important to prevent induced damage to the coating.

Delaminations : Usually propagates along or parallel to the base metal interface are commonly (but not always) a result of mechanical damage.

Integrity: It is the measure of overall quality of the coating.

2.8.2 Residual Stresses

It is well known that increased residual stresses at coating substrate interface can affect the adhesion of the coating, thereby resulting in the coating spallation [Lyphout et al., 2008; Stokes et al.,2004; Clyne et al., 1996; Sampath et al., 2004; Bansal et al., 2006]. Due to increased kinetic and thermal energy involved during high velocity oxy fuel (HVOF) deposition of coatings, and due to significant differences in the thermo mechanical properties between the coatings material and the substrate, it is important to understand the effect of residual stresses. The stress caused due to grit blasting of substrate, peening stress (HVOF deposition of coating), quenching stress (contraction take place when splats cool to ambient conditions), and thermal mismatch stress caused due to differential thermal expansion characteristics of the coating and the substrate, all contribute to the final state of residual stress at the coating substrate interface.

There are different methods to measure residual stresses, both qualitative and quantitative test methods. One of the simple method is an Almen arc deflection method, which finds extensive practical application as a quality control tool in aerospace industry for processes such as shot peening [SAE J433]. The presence of compressive stress at the coating substrate interface was commonly known to inhibit the formation of coating separation and said to be beneficial for better coating adhesion strength [Clyne et al., 1996]. There are analytical methods, such as X-ray stress evaluation (XSE), Neutron diffraction, and high energy X-ray diffraction. The residual stress calculation is dependent on the accuracy of mechanical properties of coatings and substrate material, as well as the accuracy of the unstressed lattice parameter "d_o" used in the calculation [Lypout et al., 2008]. Several researchers [Sampath et al., 2004; Bansal et al., 2006; Lypout et al., 2008] have shown that HVOF coatings, where particle velocity reach as high as 400 – 600 m/s and tend to exhibit larger compressive stresses compared to APS (air plasma spray process), where the particles are accelerated to lower velocity in the order of 100-200 m/s. The lower velocity spray deposition process tend to exhibit tensile residual stresses at the coating surface, thereby limiting the adhesion bond strength between the coating and the substrate. Due to the peening action involved during the HVOF spray process, the compressive stress region is reported to extend into the substrate by few millimeters [Bansal et al., 2006].

2.8.3 Adhesion Bond Strength

The failure modes of a coating under tensile adhesion test (TAT) conditions are (1) interfacial failure, which occurs along the coating/substrate interface, (2) cohesive failure within the coating, and (3) mixed-mode failure, which is a combination of the first two modes. Fig 2-34 shows schematic of coating deformation during testing. However, HVOF coating generally exhibits very high bond strength, hence most failure are confined within the epoxy glue material rather than the coating failure. In other words, the glue wafers that hold the test coupon together usually fail during testing, leaving the coating intact. The bond strength acceptance is based on coating exceeding ~65MPa (adhesive strength), which would meet most aerospace standards for HVOF sprayed coatings. It is usually assumed that failure is controlled only by the magnitude of the applied tensile force, and therefore the average failure stress is measured. However, the highly defective nature of a thermal spray coating gives rise to stress singularities within the coating during tensile testing.

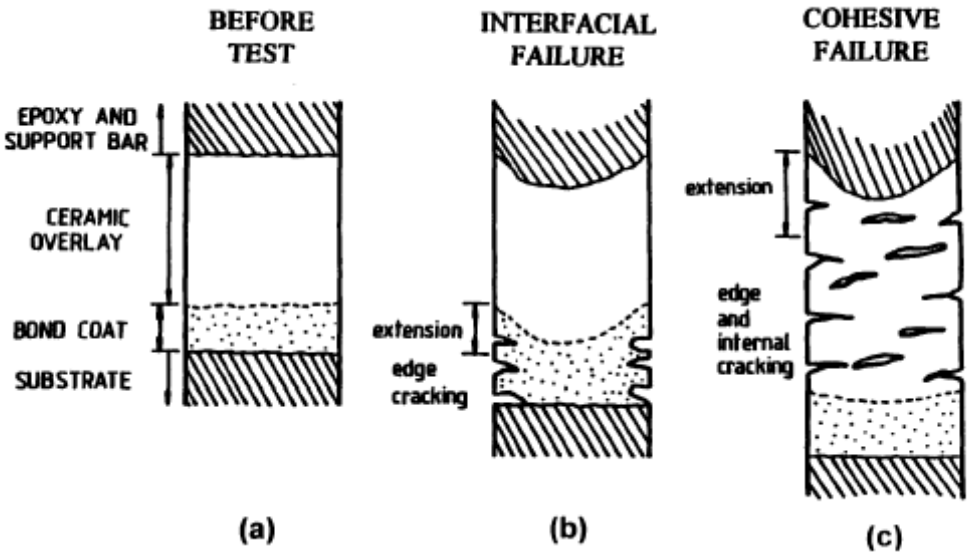

Figure 2-34 Schematic illustrating the coating deformation response during the interfacial and cohesive failure modes. (a) Original specimen setup. (b) Interfacial failure mode. (c) Cohesive failure mode [Lin et al., 1994] (Reproduced with permission from Springer)

2.8.4 Weldability Studies

Weldability is an important criterion for most Superalloys as it is a primary joining process employed during manufacturing of various components for industrial applications. Most nickel based Superalloys are considered to be susceptible to HAZ cracking, due to liquation of phases i.e., MC, γ', and segregation of deleterious elements such as boron, phosphorus, and sulphur. Other common weld cracking factors include strain age cracking due to rapid γ' precipitation. The presence of certain percentage of Al and Ti can have significantly impact on the weldability in nickel base alloys as they tend to promote precipitation of gamma prime phase. However, it is not possible to generalize this effect on all the alloys.

Wrought Inconel 718 is considered to posses excellent weldability among most nickel based Superalloys, due to the sluggish precipitation reaction of its primary strengthening gamma double prime phase.

2.8.5 Scope of this research

In summary, low CTE Superalloys have attracted a great deal of interest from the gas turbine engine and other industry since the development of such alloys in 1970s and 80s. These alloys offered potential design advantages hitherto not available with then existing alloys. Among these low CTE Superalloys, Incoloy 909 offered attractive low CTE, excellent strength, at the same time used similar joining and heat treatment schedules as applicable to the then existing alloys. This alloy also posed challenges with elevated oxidation resistance due to absence of well known protective scale forming elements such as chromium. The presence of unique phases present in Incoloy 909 has attracted interest from the research community. However, research data available in the literature is limited on the microstructure of Incoloy 909 at various heat treated condition but information is lacking in the commercial recommended solution treated and solution heat treated condition. Although it was known that Incoloy 909 have only moderate elevated temperature resistance, information on oxidation resistance at the useful service temperature range and preventive measure with application of coatings is not available in the literature.

Keeping this background in view, the present research was carried out to acquire comprehensive understanding of the microstructure, mechanical, oxidation and oxidation preventive measure with application of coatings was studied. Application of protective coatings using HVOF process is extensively studied but coating process requirements are assumed to identical for all substrates within the same family of (Super)alloys. As a part of this research the feasibility of using various protective coatings such as CoNi-CrAlY, 718, and Ni-Al coatings on Incoloy 909 and to compare it with a conventional Superalloy Inconel 718 was undertaken.

3. EXPERIMENTAL METHODS

3.1 MATERIAL

Sixteen mm diameter bar wrought Incoloy 909 and Inconel 718 were obtained from Precision Metals Corporation, USA for use in this study. The required heat treatments were undertaken as detailed in the subsequent section.

3.1.1 Heat treatment condition

The Incoloy 909 bar was received in solution treated and aged (STA) condition, while the Inconel 718 was obtained in solution treated (ST) condition. To characterize the microstructure of Incoloy 909 in the solution treated (ST), solution treated and aged condition (STA) and solution treated and over aged conditions (STOA), heat treatments were carried out as shown in Table 3-1. Inconel 718 was used in this study for comparison purpose only, heat treatments as shown in Table 3-2 was used to obtain solution treated and aged condition (STA).

3.1.2 Chemical composition

The chemical composition based on the certificate of conformance accompanied the material is as shown in Table 3-3 for Incoloy 909 and Table 3-4 for Inconel 718 respectively.

3.1.3 Grain Growth Study – Incoloy 909

As a part of an investigation on the effect of time and temperature on grain growth, heat treatments were carried out to understand the grain growth process. The times and temperatures used for this study are tabulated in Table 3-5.

Table 3-1 Heat treatment time and temperatures for Incoloy 909 to obtain various conditions

From Condition	To Condition	Temperature (°C) and Time (Hours)
STA	**ST**	982°C, 0.5 Hrs, AC
ST	**STA**	718°C/ 8Hrs/ FC for 2 Hrs to 621°C/8Hrs, AC
ST	**STOA**	770°C, 17 Hrs, AC

Table 3-2 Heat treatment time and temperatures for Inconel 718 to obtain various conditions

From Condition	To Condition	Temperature (°C) and Time (Hours)
ST	**STA**	718°C/ 8Hrs/ FC for 2 Hrs to 621°C/8Hrs, AC

AC – Air cooled or Gas fan quenched, FC – Furnace cooled

Table 3-3 The bulk chemical composition in weight percentage for Incoloy 909

Alloy	Ni	Co	Fe	Nb	Al	Ti	Si
Incoloy 909	38.2	13	42.4	5.1	0.1	1.5	0.4

Table 3-4 The bulk chemical composition in weight percentage for Inconel 718

Alloy	Ni	Cr	Fe	Nb	Ti	Al	Mo	Trace
Incoloy 718	52	19	18.4	5	1	0.8	3.8	B, C

Table 3-5 Effect of Time and Temperature on Grain Growth

Time			**Grain size in μm**		
Time in Hrs	**Time (Mins)**	**Log(Hrs)**	**980F**	**1030F**	**1080F**
0	0		**X**	**X**	**X**
1	60	0	**X**	**X**	**X**
4	240	0.60	**X**	**X**	**X**
32	1920	1.51	**X**	**X**	**X**
152	9120	2.18	**X**	**X**	**X**

3.1.4 Weldability Characterization

Solution heat treated coupons were welded by EBW (Electron Beam Welding) at Magellan Aerospace, Winnipeg using bead on plate methodology (autogenous welds), the parameters used were 79 mA Current, 44 KV Voltage, sharp focus and 152 cm/min traverse speed. The weldability was assessed by measuring the total crack length and maximum crack length in five metallographic specimens of weld cross sections perpendicular to the welding directions.

3.1.5 Coatings

Three coating materials were used in this research work to improve the surface oxidation resistance of Incoloy 909, 1) Gas atomized Praxair™ CO-210-24 (CoNiCrAlY) powder and 2) Gas atomized PAC™ 718 Class B (Inconel 718) powder and 3) Diamalloy™ 4008 (Ni-Al). The chemical composition of Praxair CO-210-24, PAC 718 Class B and Diamalloy 4008 powder are given in Table 3-6, Table 3-7 and Table 3-8 respectively.

The powder produced by gas atomization process usually results in spherical form with few satellites attached to it as shown Fig 3-1. Since this process is carried out with an inert gas such as argon, the amount of oxidation during the atomization process is kept to very minimum levels. The powder size distribution requirements for Praxair CO-210-24 (CoNiCrAlY), PAC 718 Class B and Diamalloy 4008NS powders are as tabulated in Table 3-9, Table 3-10 and Table 3-11 respectively.

Table 3-6 The nominal bulk chemical composition in weight percentage for CO-210-24

Powder	Ni	Cr	Al	Y	Co
CoNiCrAlY	32	21	8	0.5	Balance

Table 3-7 The nominal bulk chemical composition in weight percentage for PAC 718 Class B

Powder	Nb+Ta	Cr	Fe	Mo	Ni
PAC 718	5	19	18	3	Balance

Table 3-8 The nominal bulk chemical composition in weight percentage for Diamalloy 4008

Powder	Ni	Al
Diamalloy 4008	95	5

Table 3-9 Powder size distribution for Praxair™ CO-210-24 gas atomized powder

Mesh Size	Size
-325mesh + 11 um	- 44+ 11
Hall Flow, s/50g	N/A
Apparent Density, g/cc	4.2

Table 3-10 Powder size distribution for PAC™ 718 Class B gas atomized powder

Mesh Size	Size
-325mesh + 11 um	- 90+ 45
Hall Flow, s/50g	14
Apparent Density, g/cc	4.5

Table 3-11 Powder size distribution for Diamalloy™ 4008 gas atomized powder

Mesh Size	Size
-325mesh + 5.5 um	- 45+ 5.5
Hall Flow, s/50g	14
Apparent Density, g/cc	4.5

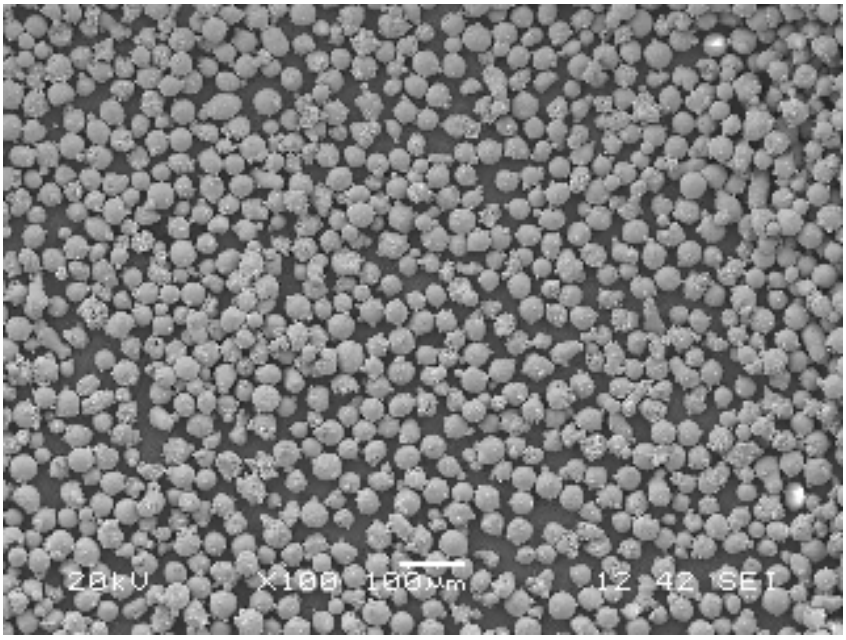

Figure 3-1 Typical shape of gas atomized CoNiCrAlY powder

3.1.6 High Velocity Oxy Fuel Spray Deposition Process

MCrAlY and Superalloy coatings such as 718 are used in gas turbine and other industries for imparting surface protection for various components at elevated temperatures. Generally, these overlay coatings can be deposited by APS (Air Plasma Process), LPPS (Low Pressure Plasma Process) or by HVOF (High Velocity Oxy Fuel) processes. In this research work, HVOF process was used to spray deposit the coatings on the substrates, a schematic of the HVOF gun is as shown in Fig 2-27. The surface preparation for substrate material solvent wiping to remove any oil residues and other contaminants. Then the substrate rods were manually grit blasted using 60 grit white aluminum oxide at 100-125 mm stand-off distance at an approximate impinging angle of 70-80° in a suction type grit blast cabinet using a pressure of 2.7- 4.2 bar. The grit blasted surface

was then acetone wiped with a low lint wipe and then dried under clean filtered dry compressed air. Coating application was carried within one hour of surface preparation. A kerosene-oxygen based HVOF system at Standard Aero was used to spray CoNiCrA-lY, 718 and Ni-Al coatings using parameters listed in Table 3-12.

3.2 METALLOGRAPHIC EXAMINATION

The heat treatments as tabulated in Table 1 were followed to obtain ST and STA conditions for Incoloy 909. The as received wrought Incoloy 909 billet exhibited a fine grain microstructure with average size of 10 μm (Certificate of Conformance: ASTM 10). To study the microstructure of Incoloy 909 at various heat treated conditions, standard metallographic techniques were employed, swab etching was performed using 65 grams $FeCl_3$-$6H_2O$, 200mlHCl, 5mlHNO_3 etchant. Etching time of 3-10 seconds was used to reveal various precipitates present within the microstructure. Microstructure examination were carried out using optical microscope, a scanning electron microscope (SEM) and a Transmission Electron Microscope (TEM).

Table 3-12 HVOF Spray Parameters

Parameters	CO-210-24	PAC 718
Fuel LPH[i]	13.2	14
Oxygen LPH	28.3	27
Standoff Distance M[ii]	0.165	0.170
Surface Speed M/Min[iii]	50	50
Feed Rate G/Min[iv]	60	50
Thickness/Pass μm[v]/Pass	30-35	30-35

[i] LPH – Liters Per Hour,

[ii] M –Meters,

[iii] M/Min - Meter Per Minute,

[iv] G/Min – Grams / Minute,

[v] μm – Micrometer,

3.2.1 Optical Microscopy

The microstructures of bare and coated samples were studied using an inverted reflected light microscope (NIKON) equipped with Clemex vision 3.0 image analyzer software.

3.2.2 Scanning Electron Microscopy

The microstructures of samples heat treated to ST, STA and STOA, were examined on a JEOL-5900 scanning electron microscope (SEM) equipped with an Oxford (with ultra thin window detector) energy dispersive X-ray spectrometer (EDS). The SEM was used in secondary electron (SE) mode and back scattered electron (BSE) mode. X-ray line scan and area mapping were done on the samples using Inca software. A Hitachi S-3600N SEM equipped with EDAX energy dispersive spectrometer (EDX) using Genesis software located in StandardAero was also used.

3.2.3 Transmission Electron Microscopy

The microstructure of the Incoloy 909 in various conditions was further examined by a JEOL-2000FX transmission electron microscope. X-ray microanalysis in TEM, and selected area diffraction analysis were performed on constituents extracted on carbon extraction replicas and on those present in thin foils, using Genesis thin-film analytical software. Camera length calibration was carried out using a pure aluminum sample deposited on a copper grid. Thin foils were made from 3mm rods that were machined by wire electro discharge machining. Disks of 150-200 micrometer thickness were sectioned from these rods again using wire electro discharge machining and then manually

polished to 70-80 micrometer thickness. These thin disks were further thinned using twin-jet polishing with 10% percholoric acid in 90% methyl alcohol at –30 to -35°C temperature, using a current of 1.5 – 2.0 A and voltage of 2 V. Electro-polishing of a thin disk resulted in a thin film around the perforation, these areas were suitable for viewing under TEM. Sometimes these coupons were further processed using Ion-milling for 2-4 hours in Gatan Duomill using an accelerating voltage of 4.5KeV at a vacuum of $1X10^{-5}$ Torr with an angle of incidence maintained between 5°-10°.

3.3 MECHANICAL TESTING

3.3.1 Tensile Test

An Instron tensile tester model 4208 with a PC based data acquisition system supplied by United Testing Corporation, Canada located in Standard Aero(Winnipeg) was used in this study. Tensile tests were carried out to characterize yield strength, ultimate tensile strength and % elongation for wrought Incoloy 909 in ST, STA and STOA conditions. All the tests were carried out at room temperature using, round test coupons manufactured in accordance with ASTM E8. The test specimen used is as shown in Fig 3-2 and the test matrix is as given in Table 3-13. The test frame was equipped with a ±50 KN calibrated load cell. The strain rate was maintained at 0.75mm/min for all the test specimens. At each condition three test specimens were tested and the average values of yield strength, ultimate strength and % elongation were reported.

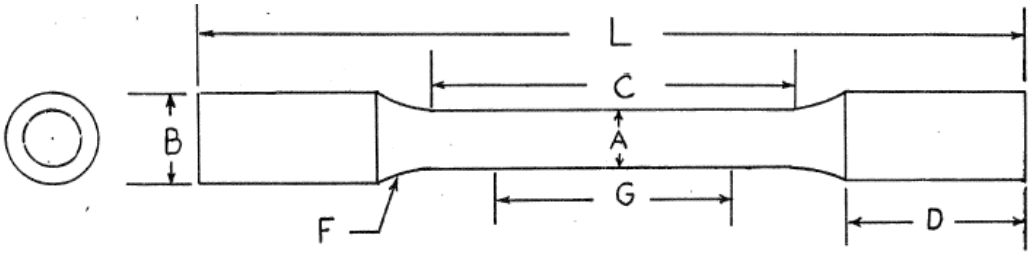

Figure 3-2 Dimension of tensile test coupon

A Diameter at center 6.35±0.125 mm
B Thread at grip end 9.53 mm
C Min. length of reduced section 28.58 mm
D Grip length 15.875 mm
F Fillet radius 4.572 mm
G Gauge length 25.4 mm
L Total length 76.2 mm
Cross sectional area Area of Cross section (mm2) 32.26 mm

Table 3-13 Tensile test matrix

Material	**Condition**
Incoloy 909	ST
	STA
	STOA

3.3.2 Hardness Test

Microhardness measurements of each coating were performed using a hardness tester (Leitz GMBH, Germany) equipped with a Vickers micro-indenter with a load of 300g test, five measurements were performed and average value was reported.

3.3.3 Four Point Bend Test

For the evaluation of comparing the ductility of the coatings, four point bend tests were carried out. Fracture toughness is generally used for bulk materials, due to wide variations between the microstructure and inherent coating defects, there is a need to characterize this property for thermal sprayed coatings as bulk property could be very different from the coating property. Bend testing determines the ductility or the strength of a material by bending the material over a given radius. The bend testing was carried out using a Instron tensile testing machine on which a 4-point bend testing apparatus was mounted. The tensile testing machine was used in the compression mode with the lower jaw in stationary position, the load was applied on the inner span of the 4-point bend test apparatus.

Aluminum 6061 plates 60mmX12mmX1mm were deposited with coating as shown in Table 3-14. Four samples were tested at each condition until coating failure under tensile condition. The crosshead speed of the tensile test machine was 2.5 mm/min for all samples. The force applied was measured using a load cell installed on the Instron tensile testing machine and deflection was measured using the position sensor readings, via data acquisition device monitored by a computer. The force and the deflection measured during the tests were

transformed, after the completion of the tests, to stress and strain values using the following equations for four point bend tests:

Table 3-14 4 point bend test matrix

Coating	**Coating thickness in mm on aluminum 6061 plate substrate**		
CO-210-24	**0.125**	**0.250**	**0.38**
PAC 718	**0.125**	**0.250**	**0.38**
Diamalloy 4008 (NiAl)	**0.125**	**0.250**	**0.38**

$$\text{Stress (MPa)} = 1.5F\,(L_2-L_1) / (bh^2) \quad \text{[Voyer at al., 2003]}$$

$$\text{Strain \%} = 436Dh/ L^2_2$$

Where F is the force applied in Newtons, L_2 and L_1 are the outer and inner span of the 4-point bend test apparatus in millimeters.; b is the sample's width in mm, h is the thickness of the sample, and D is the deflection of the sample at mid-span in millimeters.

The width and thickness of each tested sample were measured using a vernier caliper prior to perform each bending test. The modulus of elasticity of a sample can be calculated from the curve force displacement obtained during a typical bend test.

$$\text{Modulus of Elasticity} = 11\ L_2^3\ X\ \Delta\ /\ 64bh^3$$

Where delta is the slope of the linear section of a typical curve force displacement and the other variables have been explained in the previous two equations.

3.3.4 Coating Bond Test

Tensile bond test is widely used to characterize the adhesive or cohesive strength of thermally sprayed coatings. This test finds prevalent use as a quality control tool in many aerospace and industrial specifications.

The test method used was adapted from ASTM C633, A test specimen diameter of 16mm pins was used instead of the recommended 25 mm since the original material was purchased as 16mm rod. The test specimens consisted of 16mm diameter discs of thickness ranging from 5.6 – 6 mm. One side of these discs was deposited with HVOF sprayed coating to the three thicknesses as given in Table 3-15. At each condition 3 test coupons were tested. The coated thin discs were later adhesively bonded to the pins using FM1000 epoxy composite material cured at 170°C for 2 hours prior to testing. A typical bond strength testing set-up is illustrated in Fig 3-3.

An Instron (Model 4208) screw type machine with a load cell capable of measuring loads upto 100 KN was used for testing. The crosshead speed during the pull test used was 0.76 mm/min. The bond strength of the coating was calculated based on the fracture load and cross sectional area of the coated surface.

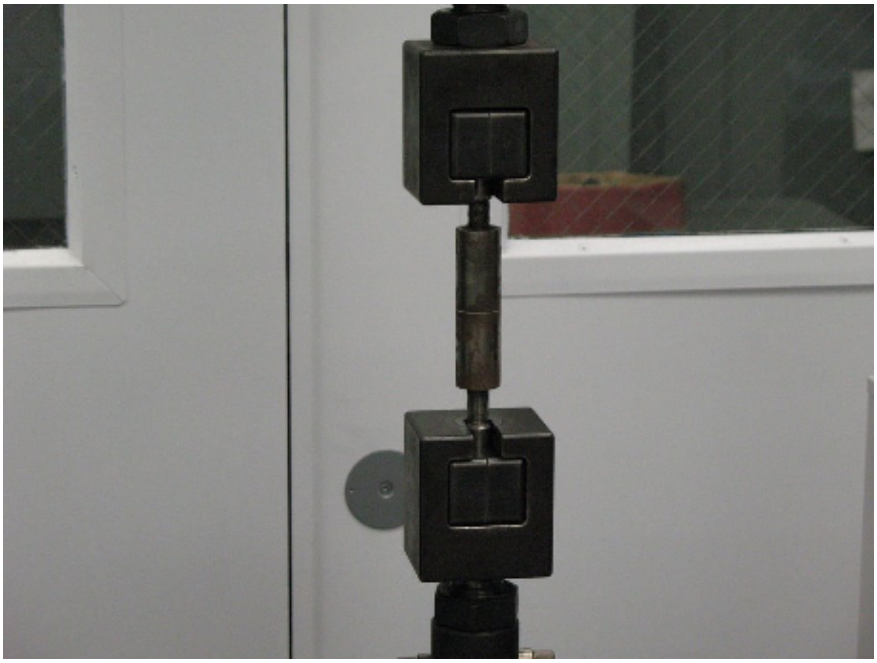

Figure 3-3 Typical thermal spray bond test set-up

Table 3-15 Coating thickness on bond test coupons

Coatings	**Thickness (mm)**		
CO-210-24 (CoNiCrAlY)	**0.125**	**0.250**	**0.38**
PAC 718 (718)	**0.125**	**0.250**	**0.38**
Diamalloy 4008 (NiAl)	**0.125**	**0.250**	**0.38**

3.4 OXIDATION TESTING

Isothermal and thermal cycle testing was carried out to study the oxidation resistance of coated and bare Incoloy 909 and Inconel 718.

3.4.1 Constant Temperature Testing

Isothermal high temperature testing were carried out in StandardAero box type furnaces. All isothermal exposures of test coupons were sectioned (dimension of ϕ16mm X 10mm Length) using electric spark erosion or using diamond saw carefully to avoid any crack formation during the preparation process. The test coupons were abraded using 400 grit aluminum oxide sand paper to remove any oxides present on the surface of the test coupons prior to placing into furnace. The test matrix used for the isothermal testing is as shown in Table 3-16.

3.4.2 Thermal Cycling using Burner Rig Testing

The cyclic thermal testing were carried out in burner rig located in StandardAero, the test set-up is shown in the Fig 3-4. The test coupons used for thermal cycling test were ϕ16mm X 50mm. The test matrix used is as shown in Table 3-17. The test coupons were abraded using 400 grit aluminum oxide sand paper to remove any oxides present on the surface prior to testing. Each cycle consisted of 3 minutes continuous heating and 2 minutes cooling using cold air blast.

Table 3-16 Isothermal Furnace Testing

Temperature	**Time**			
	250 Hrs	**500 Hrs**	**750 Hrs**	**1000 Hrs**
704°C	X	X	X	X
Conditions: 909, 909+CoNiCrAlY, 909+718, 718, 718+CoNiCrAlY, 718+718				

Table 3-17 Thermal Cycling Using Burner Rig Testing

Temperatures	**909 (bare)**	**909+CoNiCrAlY(coating)**	**909+718 (coating)**	**718 (bare)**	**718+CoNiCrAlY (coating)**	**718+718 (coating)**
704°C	X	X	X	X	X	X

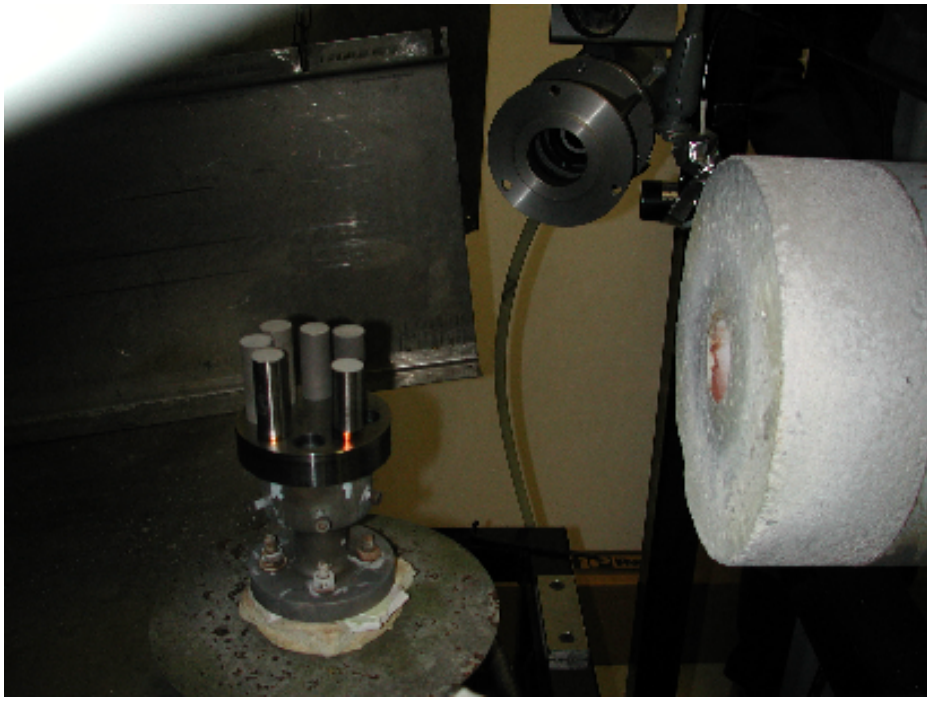

Figure 3-4 Arrangement of Burner Test Rig (Courtesy: Standard Aero Ltd)Cycles: 1000,Heating Time: 3 Mins, Cooling Time: 2 Mins (Blast of cooling air)

3.4.3 Almen Deflection Test

The Almen strip deflection test is a quality control test that is prevalent in Aeropace and other industries to quantify indirectly the internal stress imparted during a process by measuring the relative deflection. A schematic of the Almen strip set-up is as shown in Fig 3-5. The Almen strip tests were performed using commercially available steel strips (N), on two different coatings with cooling air blast and without any cooling as shown in Table 3-18. To ensure repeatability 3 strips were coated at each condition.

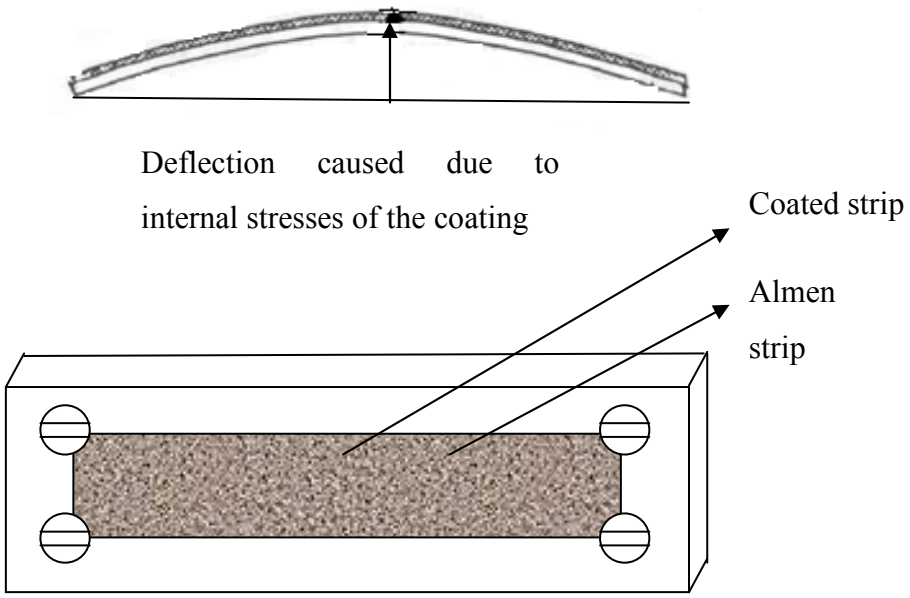

Figure 3-5 Illustrates typical Almen strip fixture, strip prior to coating deposition and after coating deposition (Adapted from J.P Sauer et al, 2001)

Table 3-18 Almen strip deflection test matrix

Alloy	**Coating Thickness (mm)**		
CO-210-24	**0.125**	**0.250**	**0.375**
PAC 718	**0.125**	**0.250**	**0.375**

3.4.4 Secondary Ion Mass spectrometry

Secondary ion mass spectrometry often referred to as "SIMS", is a well known versatile instrument used in surface analysis with the ability to detect elemental composition with excellent accuracy and repeatability. The elemental detection limits of SIMS is generally specified in nanograms per gram range and depth resolution in the range of nanometers. SIMS finds extensive application in the semiconductor industry for analyzing and quantifying impurities and dopants in various substrates. SIMS measurements were performed using Cameca IMS-7f instrument at the University of Manitoba. A Cs^+ primary ion beam of 15 keV impact energy was employed. The beam current was 120 nA, and the beam was scanned across an area of 180 ×180 μm^2. The negative secondary ions, originating only from a 60 μm region in the centre of the crater, were directed towards the mass spectrometer. The vacuum pressure in the analysis chamber was maintained at ~ $1 \cdot 10^{-9}$ Torr. The secondary ions of H, C, O, Ti, Fe, Ni, Co and Nb in the sample were monitored and detected in the depth profiles.

To investigate the effect of HVOF heating in the formation of thin oxide scale on the substrate surface (909 and 718), test panels were polished with 600 grit SiC paper and then subjected to HVOF without powder injection at the same gun traverse rate and overlap distances during actual spray process for one and 10 times. Then these panels were compared against the panels that were not exposed to any HVOF flame using secondary ion mass spectroscopy in depth profiling mode.

Hence the focus of this test is to obtain a SIMS chemical make up of surface layer as a function of sputtering time. It is possible to indirectly get chemical composition as function of depth by measuring the crater depth using a stylus profilometer after the total sputtered time. However, it is assumed that the ions are bombarded out at a constant rate, which is an approximation as the erosion rate decreases when the crater depth increases in practice. The erosion rate can be calculated by:

$$E = \text{Total Depth/Bombardment time.}$$

The SIMS analysis method and crater creation on a test panel is illustrated using line drawing as shown in Fig 3-6 In this study the erosion depth for 718 and 909 alloys after 5 mins of sputtering resulted in

$$\text{Erosion Depth } 718 = 208.3 \pm 2.5 \text{ Å}$$

$$\text{Erosion Depth } 909 = 217.6 \pm 3.7 \text{ Å}$$

The depths were based stylus profilometer measurements based on 5 mins sputtering time and the depth values reported are not absolute values as the crater surface usually are rough when exposed to ion beam rastering. The stylus profilometer measurements are similar to the research carried out by Bardi et al [Bardi et al., 2005], as shown in Fig. 3-7. Hence, depending upon the stylus profile it is difficult to probe the absolute deepest area of the pit esp., when surface profile is rough. The secondary ions of H, C, O, Ti, Fe, Ni, Co and Nb in the sample were monitored and detected in the depth profiles, but primary importance was given to the detection of presence of O.

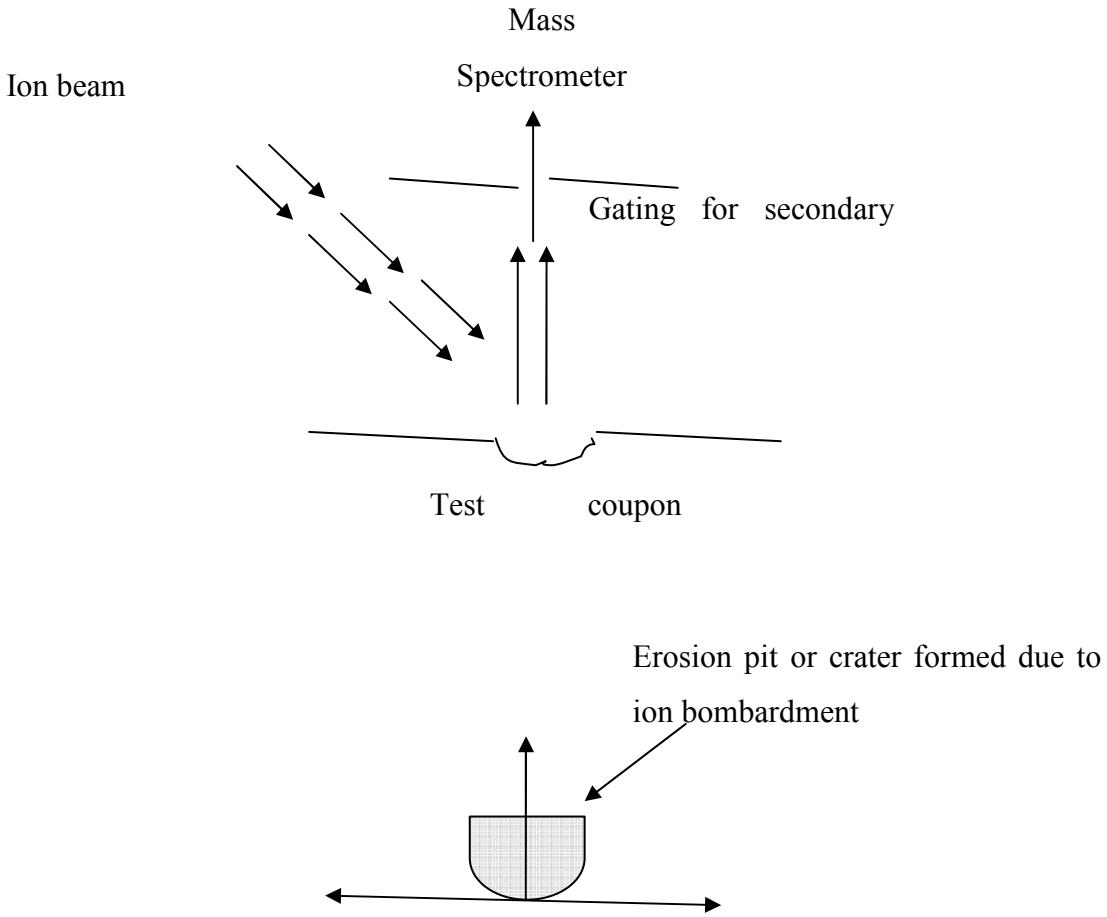

Figure 3-6 Illustration of SIMS in depth profiling analysis and resulting crater formed due to ion bombardment

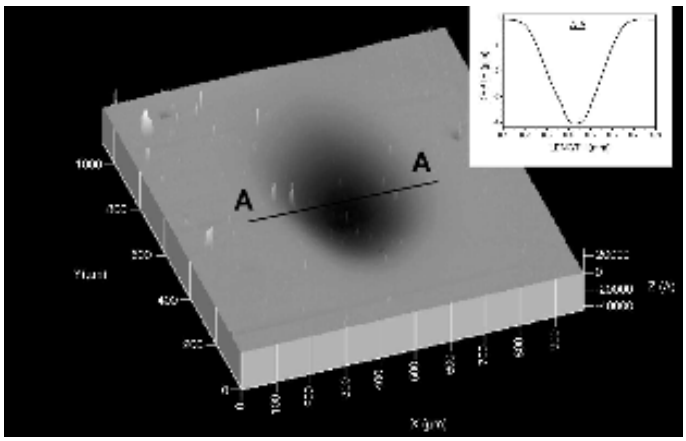

Figure 3-7 3D image of the eroded crater measured by a stylus profiler (inset depicts a cross-section of the crater along the line A-A).

3.4.5 Coefficient of Thermal Expansion

Among various techniques available for characterizing coefficient of thermal expansion, Dilatometry is the one that was used in this research. It is a technique for measuring expansion or contraction (shrinkage) of variety of materials by subjecting it to a controlled heating or cooling rate. The thermal expansion data obtained using this technique is valuable in characterizing important material properties such as glass transition, phase transition, densification range, optimize sintering parameters and to measure thermally induced stress. However, in the current research the dilatometry is used only to characterized thermal expansion data from materials of interest pertaining to this research.

To investigate the effect of differential thermal expansion rates between the substrates and the coating, coefficient of thermal expansion rates for 718, 909, and CoNiCrAlY were characterized using a dilatometer in Dalhousie University. Sample test coupons with

dimensions ϕ6mm X 25mm length with parallel faces were carefully machined and sent to Dalhousie University.

The linear thermal expansion studies were characterized using a Netzsch dilatometer model 402, operating with flowing argon and using a 10°C/ min programmed heating rate from ambient to 760°C. The test coupon cyclinder were carefully clamped and constrained in within an alumina tube, the instantaneous expansion rates were continuously measured and recorded along the cylinder axis.

3.4.6 Differential Scanning Calorimeter

The DSC analysis instrument (NETZSCH DSC 404C) was used to identify Laves phase dissolution temperature using 5mg discs (about 3mm diameter) of Incoloy 909 cut using wire electro discharge machining, followed by careful removal of oxide scales by sanding with 400 grit silicon carbide paper. The equipment was calibrated in accordance with ASTM E967-03 standard using indium, aluminum, silver, gold and nickel at 2.5°K/min, heating rates. The heating was conducted to 1300°C, and the heat flow data was acquired by via computer interfaced with the analysis instrument as a function of temperature.

4. RESULTS & DISCUSSION

4.1 Composition and microstructure of as received 909 material

The mill test report composition in weight % is shown in Table 4-1. To confirm this composition, Electron Dispersive Spectroscopy (EDS) analysis was performed in the raster mode on areas measuring about 50 μm X 50 μm at five different random locations on the polished mounts prepared from the as received material. The scatter between individual measurements was found to be negligible except for lighter elements such as Si. The analyzed composition in Table 4-1 was found to be consistent with the bulk chemical analysis supplied by the material supplier.

The as received material was supplied in solution treated and aged condition by the supplier rather than solution treated condition, using the commercial heat treatment schedule as presented in Table 3-1. Since the manufacturer performed this heat treatment in vacuum, the bar was bright with no indication of any oxide scales. From Fig 4-1, it is evident that the microstructure consisted of a fine grained microstructure with a blocky globular phase dispersed within the matrix, observed at both inter and intragranular locations.

4.2 Microstructure of Incoloy 909 in Solution Treated condition

4.2.1 Commercial Solution Heat Treatment

The specimens after solution heat treatment at 980°C as detailed in Table 3-1 were investigated by optical and scanning electron microscope with the aim of identifying the phases retained after this heat treatment. It is evident from the optical micrograph in Fig 4-2 that globular phase particles are dispersed throughout the matrix. However, in the electron micrograph in Fig 4-3, the contrasts between the dark and bright grains can be clearly viewed.

The solution treated grain structure consisted of fine grains with an average size of about 10μm. It is thus evident that the grain sizes have been largely unaltered and have retained the prior as received grain sizes to a large extent. This effect is associated with the grain pinning effect provided by globular or blocky phase particles with this heat treatment.

The blocky globular particles sizes ranged from submicron to about 3 microns, the particles being found on both intergranular and intragranular locations. Although the blocky particles were uniformly dispersed and to a great extent ranged below 3 microns, some particles were as large as 5 microns. Occurrences of larger particles are likely thought to be originated at the manufacturing stage of this material.

Table 4-1 Composition of the as received Incoloy 909 material based on supplier provided certification and SEM- EDS based analysis

Elements	Weight % (Mill certificate)	Weight % (SEM EDS Analysis)
Iron	Balance	39.2
Cobalt	13.01	13.3
Nickel	38.2	40.2
Niobium	5.1	5.8
Titanium	1.5	1.2
Silicon	0.4	0.3
Aluminum	0.04	0
Carbon	0.008	N/A
Boron	0.002	N/A

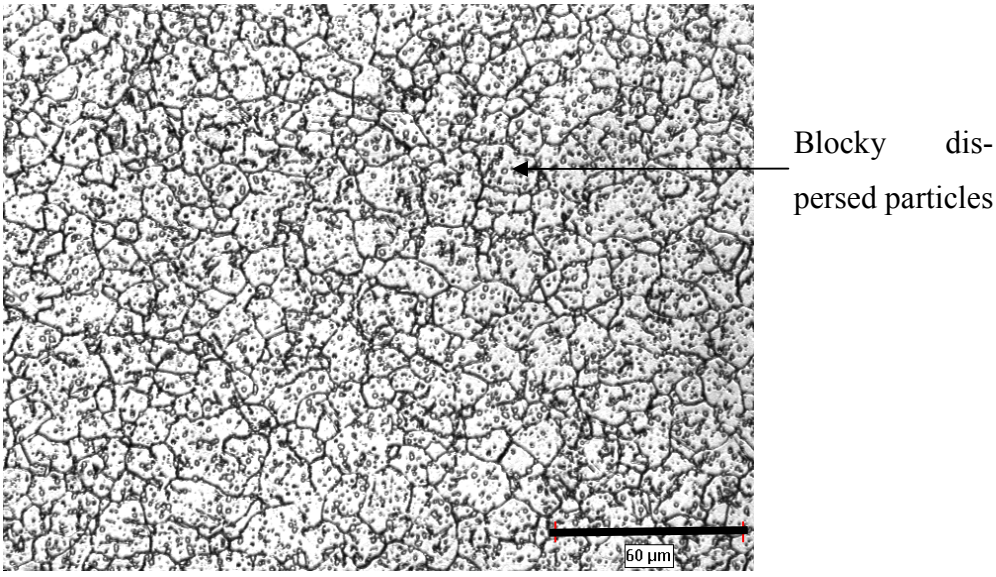

Figure 4-1 Optical micrograph, as received, Incoloy 909 in STA condition

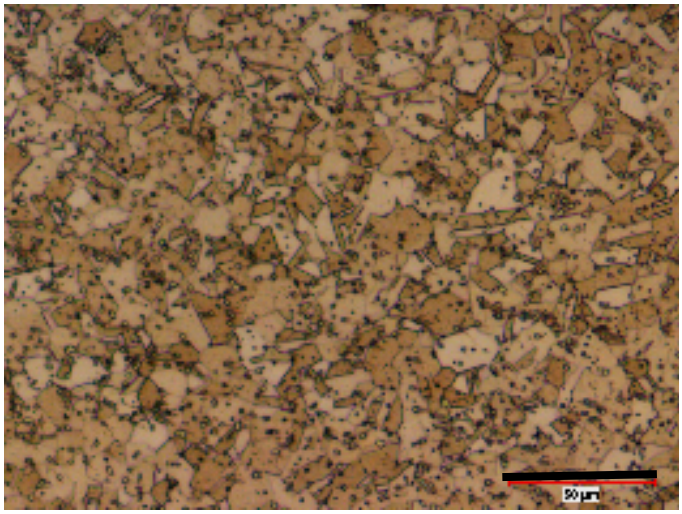

Figure 4-2 Optical micrograph of Incoloy 909 in solution treated condition

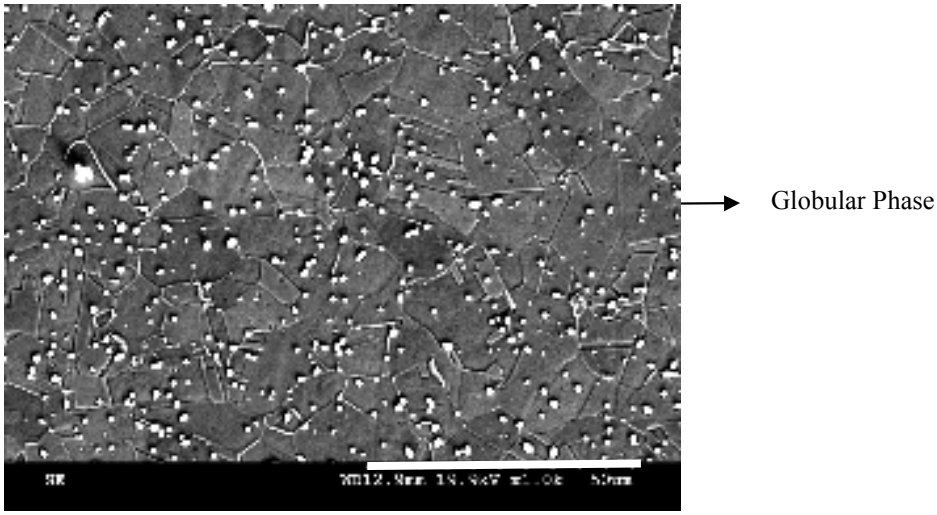

Figure 4-3 SEM micrograph of Incoloy 909 in solution treated condition

The chemical composition of the matrix was attempted using semi-quantitative analysis using SEM-EDS on an etched surface as shown in Fig 4-4. The blocky precipitates were

also analyzed using SEM-EDS that confirmed it is rich in Nb and Si, indicating that it is likely the AB_2 Laves Phase. In addition, it is also known that the resolution in SEM-EDS is limited to about a few micrometers laterally as well as in depth. Therefore, it was decided to confirm using TEM-EDS analysis method as this method is considered to provide more accurate composition notably for smaller and thinner phases present in a thin foil.

Figure 4-5 shows the microstructure of Incoloy 909 in solution treated condition (982°C) obtained from thin film using transmission electron microscope (TEM). The absence of superlattice reflections from the matrix (not shown) also supported by complete absence of gamma prime particles confirming earlier reports [Heck et al., 1988; Kusubiraki et al., 1997] that these precipitates cease to exist above 760°C. As shown in Fig 4-6, TEM/EDS analysis was performed on the globular phase in the spot mode, with the composition being expressed as $(FeCoNi)_{0.63}$ $(SiTiNb)_{0.37}$. It can be seen that this is consistent with the ratio expressed as $MgZn_2$ type or AB_2 type Laves phase by previous researchers, implying agreement with the literature [Heck et al., 1988], where A represents Fe, Co, Ni and B represents Si, Ti and Nb. The presence of niobium, silicon and titanium as well as high occurrence of Ti/Si ratio are known to promote intermetallic Laves formation in Iron-Nickel based alloys [Larker et al., 1992]. In many alloy systems, the presence of Laves phase is undesirable due to a variety of reasons including reduction of ductility, formation of brittle deleterious segregated phases leading to cracking during welding process [Nakkalil 1993]. Though Laves phase is considered to be undesirable in most Superalloys, it is found beneficial in Incoloy 909 in restraining grain growth at the elevated temperature heat treatment [Larker et al., 1992; Chen et al., 1993; Heck et al., 1990; Smith et al., 1981].

It is known that both metal carbides and intermetallic compounds such as Lave phases improve grain growth resistance in Superalloys. However, the presence of fine discrete carbide particles along the grain boundary is desirable compared to intermetallic compounds as they offer relatively improved resistance to grain growth and averts grain boundary sliding or grain boundary migration [Jena et al, 1984]. Sufficient presence of carbon and presence of carbide formers like Cr, Nb, Ti and Ta are said to promote formation of stable metal carbides in Superalloys [Huang 1994]. In spite of sufficient Nb, Ti and Si present in this alloys, negligible presence of carbon (0.008 wt. %.) is the likely reason behind the absence of any metallic carbide phases in its microstructure. On the contrary, previous researchers have found sufficient amounts of metallic carbide phases in Incoloy 903 [Nakka-lil 1993] and Incoloy 909 [Lin 1991].

.

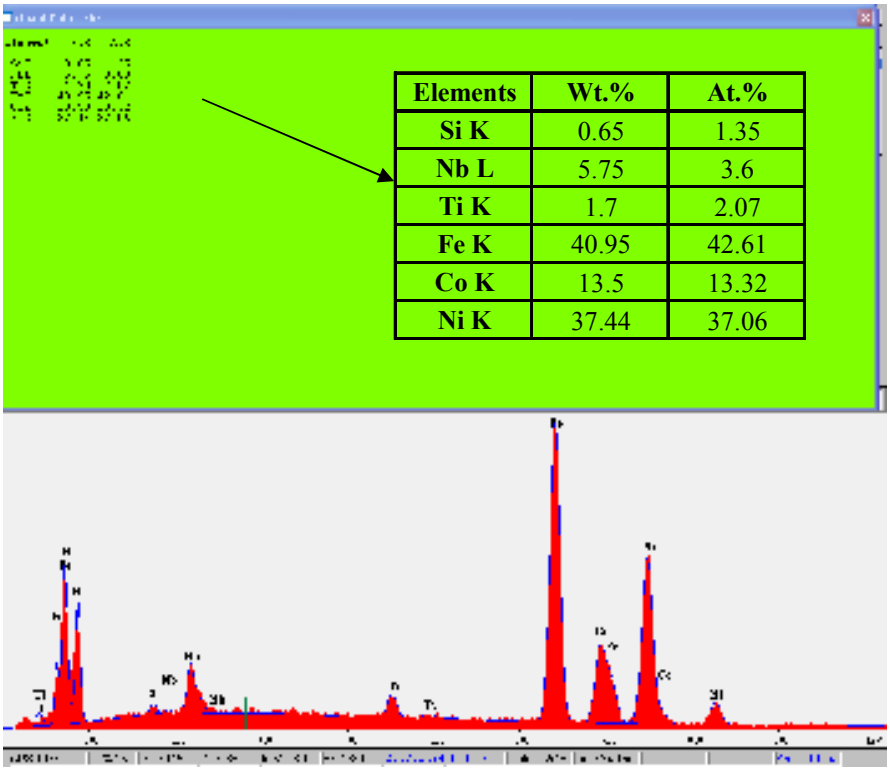

Elements	Wt.%	At.%
Si K	0.65	1.35
Nb L	5.75	3.6
Ti K	1.7	2.07
Fe K	40.95	42.61
Co K	13.5	13.32
Ni K	37.44	37.06

Figure 4-4 SEM-EDS matrix of Incoloy 909 in solution treated condition

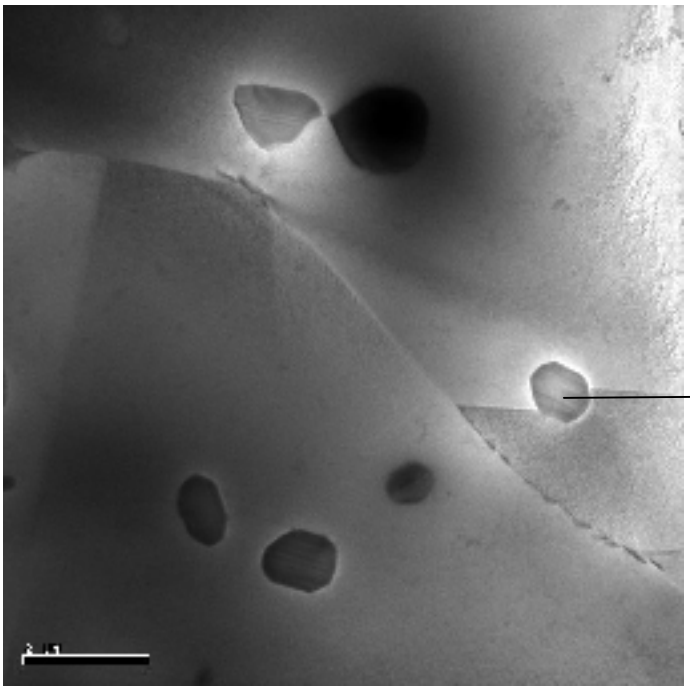

Figure 4-5 TEM micrograph of Incoloy 909 in solution treated condition

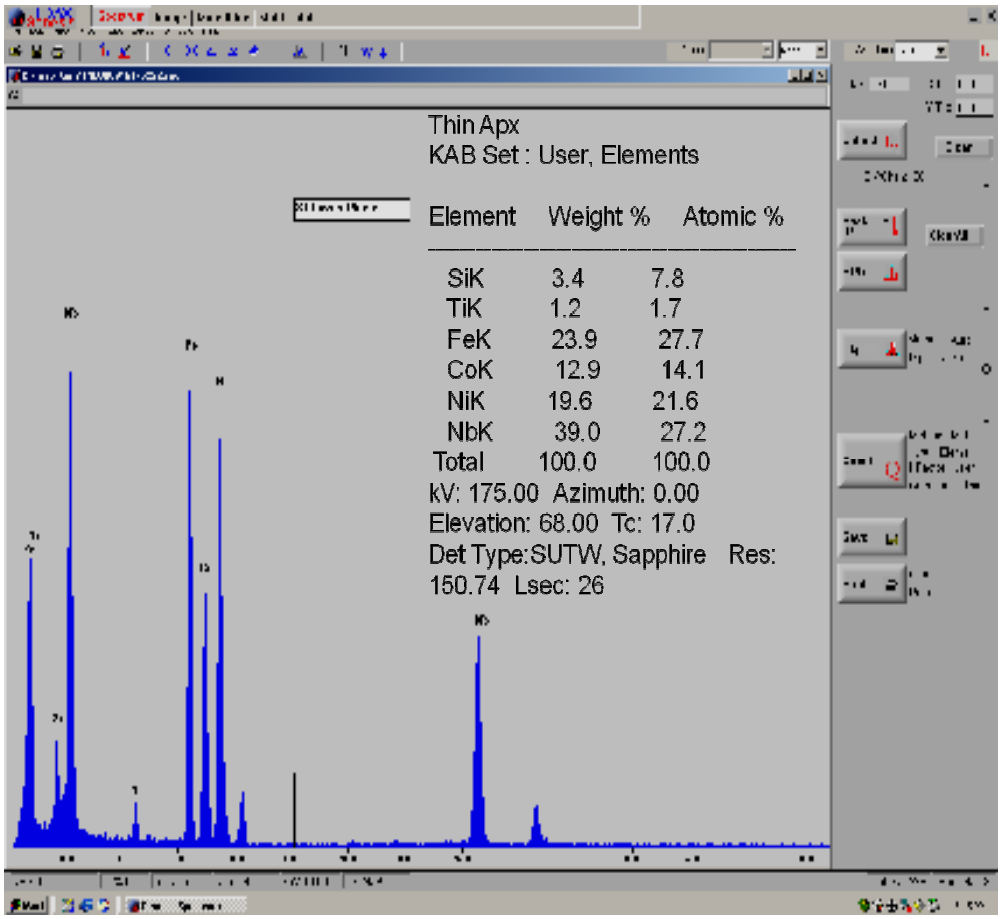

Figure 4-6 TEM-EDS Laves Phase at solution treated condition of Incoloy 909

4.2.2 Microstructure of Incoloy 909 at higher solution treatment temperature

The optical and SEM micrographs shown in Fig 4-7 and Fig 4-8 respectively reveal large grain growth in alloy 909 when solution treated at 1080°C, which is about 100°C over the recommended solution treatment temperature of 982°C. When compared to the microstructure after commercial recommended solution treatment as shown in Figs 4-2 – 4-3, it is evident that only a small amount of Laves phase is retained after the higher solution treatment temperature causing abrupt grain growth consistent with earlier reports. Massive grain growth is deleterious, as it can result in a sudden drop in failure strength, although improving creep rupture properties.

Differential scanning calorimetry (DSC) is often used for studying the precipitation and its melting characteristics on various materials, to measure the temperature and heat flows associated with transitions in materials as a function of time and temperature. A solution treated Incoloy 909 sample was heated at the rate of 2.5K/ min to 1300°C and the heat flows were monitored as a function of temperature to corroborate the Laves phase dissolution temperature. It is evident from Fig 4-9 that DSC chart shows the dissolution of Lave phase began about 1050°C, which is consistent with the microstructure obtained after heat treatment at 1080°C as shown in Figs 4-7 and 4-8. However, DSC studies on Incoloy 909 precipitation kinetics are lacking in the literature. The microstructure of the sample of the DSC run is as shown in Fig 4-10. As expected, the large grain growth was accompanied by complete dissolution of second phases.

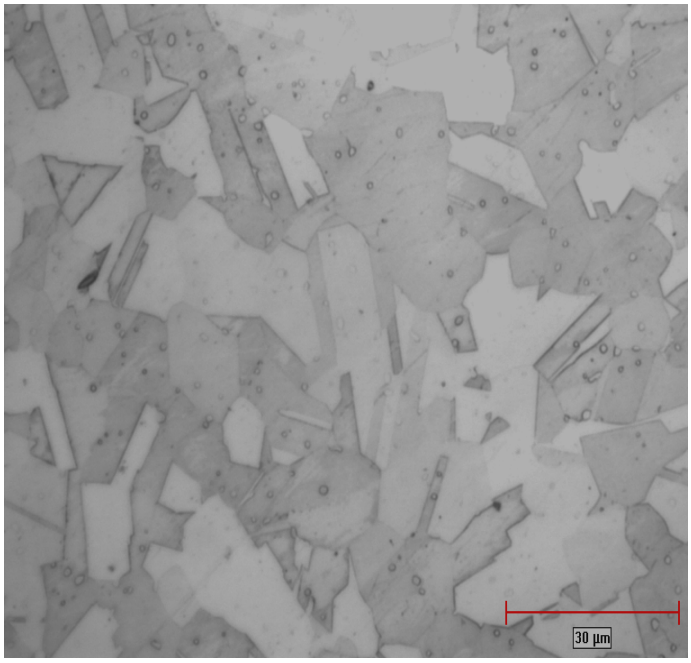

Figure 4-7 Optical micrograph of Incoloy 909 solution treated at 1080°C for 60 minutes

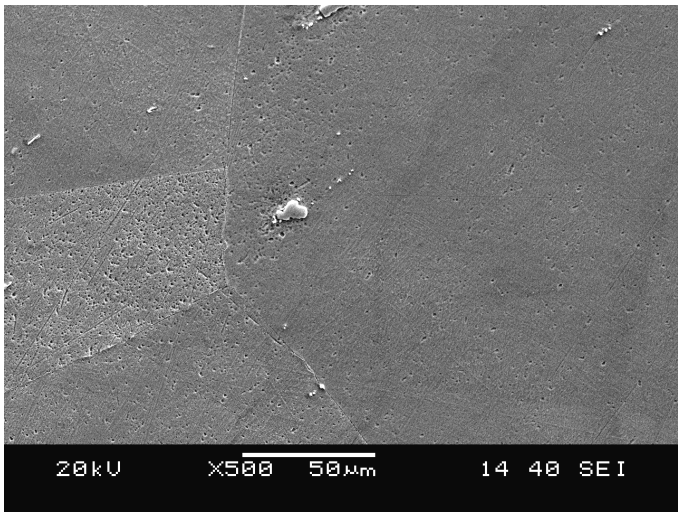

Figure 4-8 SEM micrograph of Incoloy 909 solution treated at 1080°C for 3 hours

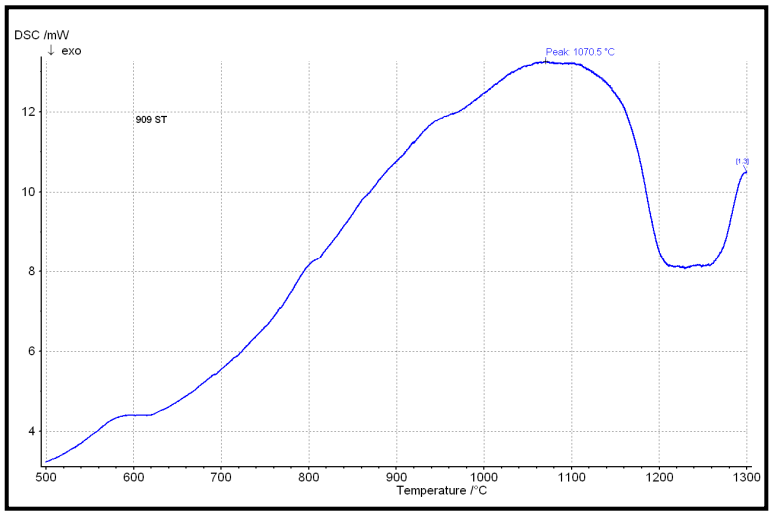

Figure 4-9 DSC run of Incoloy 909 in ST condition

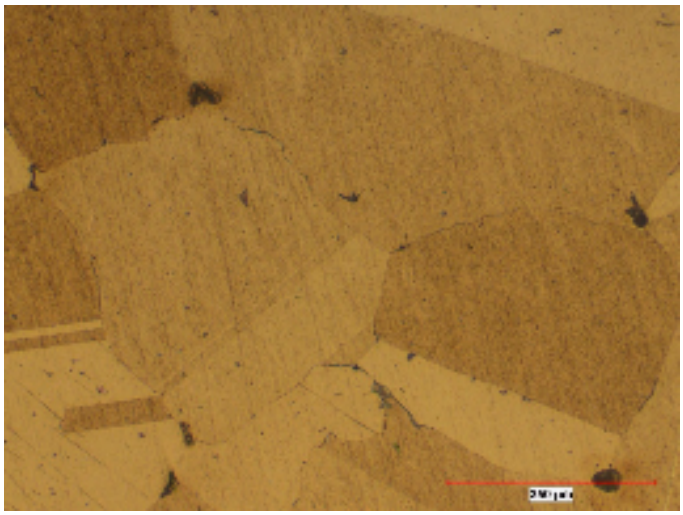

Figure 4-10 Optical micrograph of 909 solution treated after DSC run to 1300°C then argon cooled to ambient temperature

4.2.3 Grain growth study

As part of this research, grain growth characteristics of this alloy were studied by subjecting specimens to various annealing temperature and times as indicated in Chapter 3. Grain size and its coarsening characteristics are important from a manufacturing aspect, as processes such as forming, forging etc., require proper grain size optimization and control to prevent defects. The grain size of this alloy was analyzed at different temperatures with various holding times. Grain growth at various conditions was analyzed assuming that it follows the power law equation,

$$D = Kt^n$$

Where,

D is the mean grain size,

K is a temperature dependent rate constant,

t is the time at temperature and

n is the grain growth exponent related with kinetics.

The samples for microstructure examination were prepared using standard metallographic techniques as detailed in the experimental section. The grain sizes were determined by the standard linear intercept method by manually measuring the average of the grain size. The plot of average grain size as a function of annealing time(t) for Incoloy 909 is shown in Fig 4-11(a).

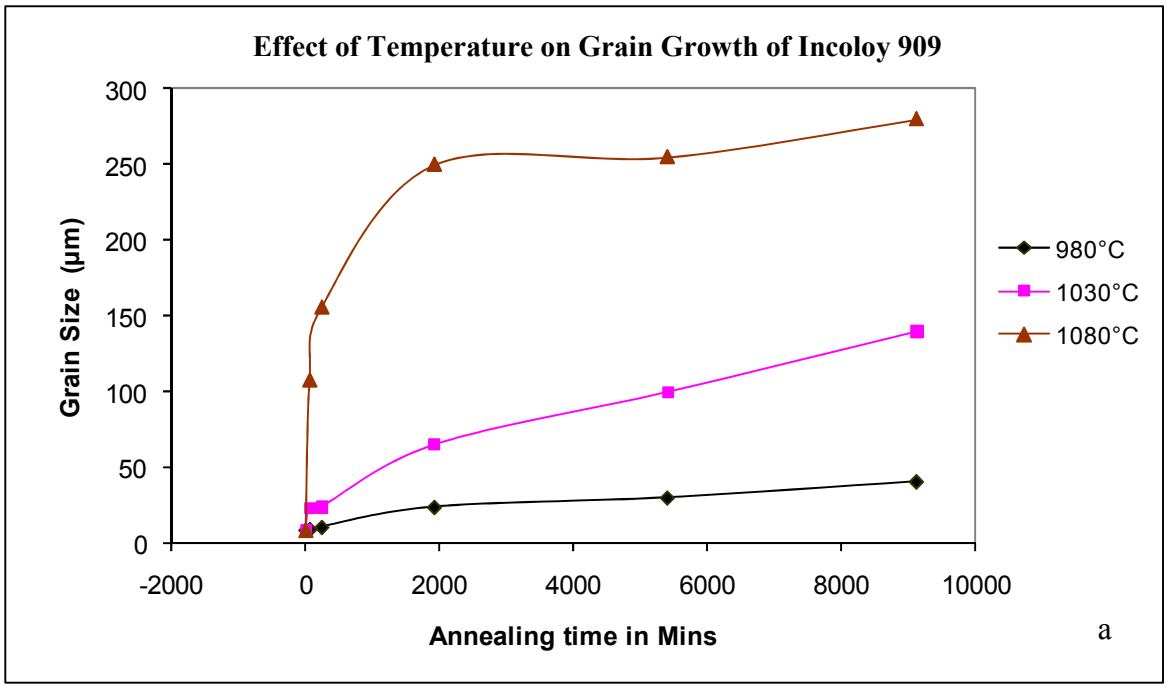

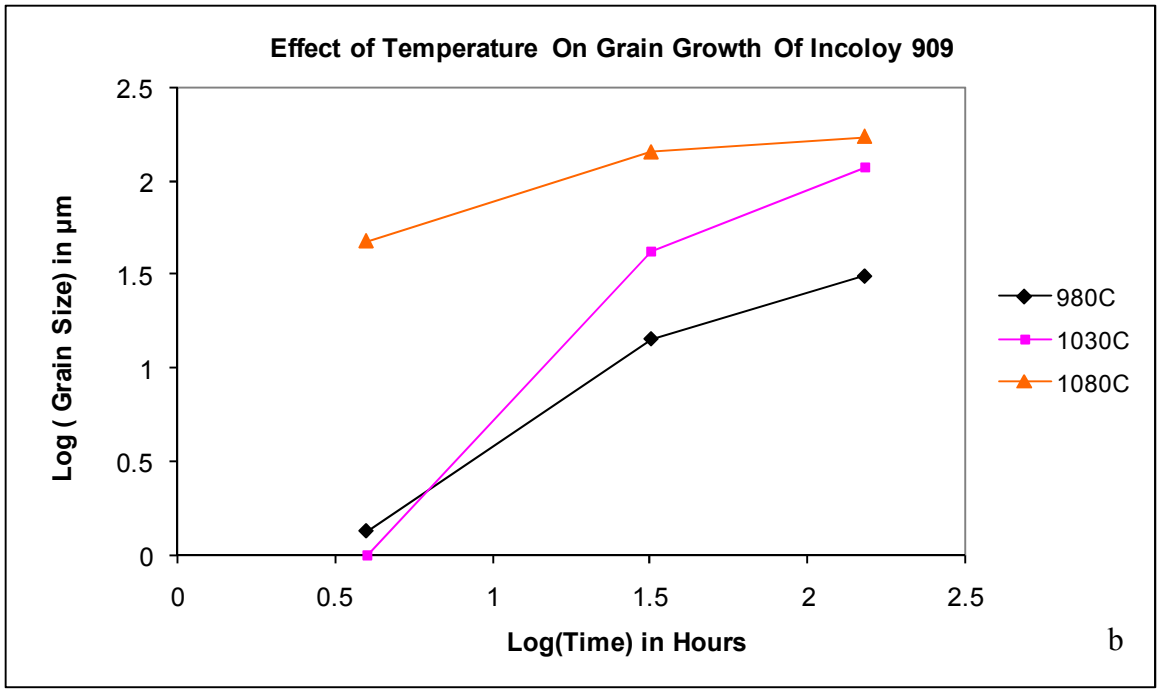

Figure 4-11 (a) Plot of Grain size (µm) as a function of annealing time (minutes) for Incoloy 909
(b) Plot of Log of Grain size (µm) as a function of Log of annealing time (Hours) for Incoloy 909

It can be observed that the grain size in Fig 4-11(a) increases with increasing annealing temperature. Also, the grain size at 1080°C increased greatly during the initial 60-120 minutes of the holding period. However, with further continuation of holding at this temperature resulted a slower increase rate in grain growth with a saturation effect coming in to play much earlier when compared with the lower annealing temperatures. It is reported by numerous researchers that dispersed second-phase particles inhibit grain growth due to exertion of a pinning force on migrating grain boundaries at elevated temperature conditions. The driving force for grain growth varies with the starting grain size; grain growth will take place until it reaches a limiting value, whereupon the driving force is balanced by the pinning force. This effect is known as Zener pinning as it was first postulated by Zener in the 1940s [Nijdam et al., 2008].

The large grain growth during the initial few hours at 1080°C can be attributed to dissolution of Laves phase above about 1050°C based on the present research and other reports in the literature [Heck et al., 1988]. The slope obtained from log (D) vs. log (t) (Fig 4-11(b)) was plotted against annealing temperature in Fig 4-12. It can be seen that the grain growth exponent increases with increasing temperature varying from 0.19 to 0.59. The 'n' value usually is close to 0.5 for pure metals, the values obtained in the present investigation are based on an alloy with the presence of secondary phases such as Laves phase which acts as a grain growth barrier at temperatures below 1040°C.

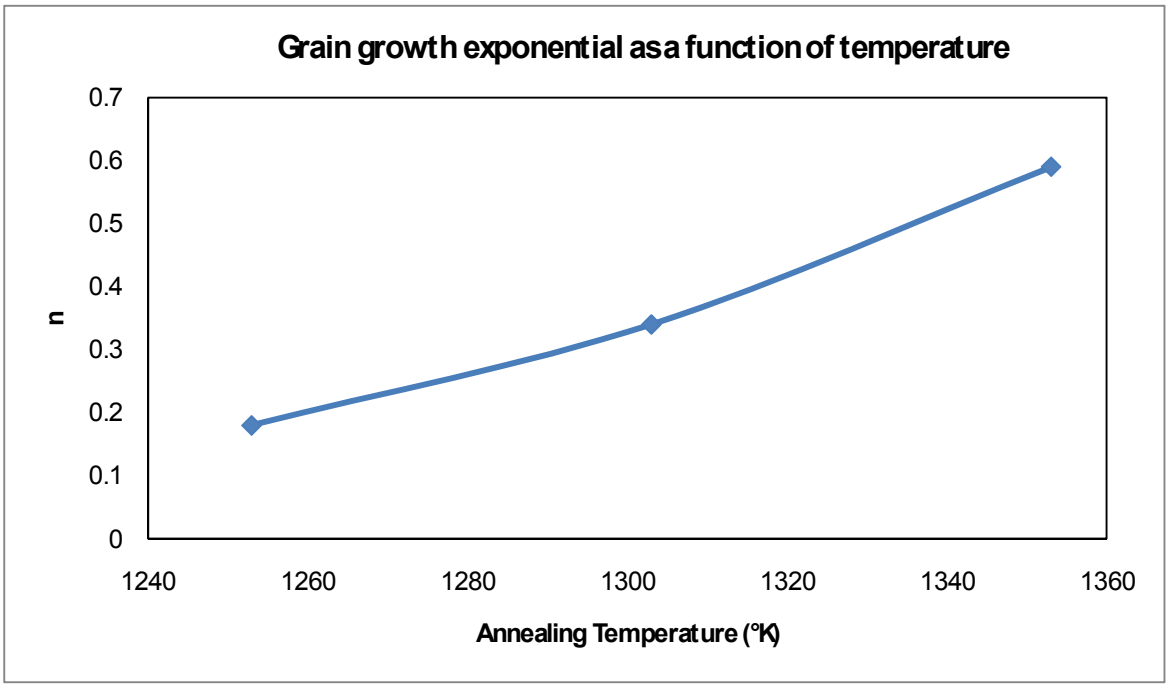

Figure 4-12 Grain growth exponents as a function of annealing temperature

4.3 Microstructure of Incoloy 909 in Solution Treated and Aged condition

4.3.1 Commercial Aged condition (STA)

The microstructure in the solution treated and aged condition was examined using optical, scanning and transmission electron microscopes as shown in Figs 4-13 through 4-19. The optical micrographs in Fig 4-13 and 4-14 at lower and higher magnification showing Laves Phase and twinned grains. The scanning electron micrographs in Fig 4-15 and Fig 4-16 show uniform dispersion of Laves Phase in the matrix with better clarity than the optical micrographs. The transmission electron micrograph shown in Fig 4-17 is a typical micrograph with finely dispersed gamma prime particles and globular Laves particles in the matrix and Fig 4-18 shows an unusual needle or platelet like formation. These individual platelets are made up of numerous nano-sized particles oriented in a Widmanstatten like configuration. This formation was also reported by another researcher, while studying the transitioning of gamma prime phase to needle or platelet phase [Guo et al., 2001]. Previous researches [Heck et al., 1988; Chen et al., 1993] in a non-standard heat treatment have shown the presence of platelet precipitates(ε phase) in the aged condition, however, the current investigation did not find any platelet like phase in the commercial STA condition, except transitioning gamma prime, a rare feature in the microstructure.

The high resolution TEM image in Fig 4-17 shows the presence of fine dense spherical particles, as reported by various researchers [Heck et al., 1988; Kusubiraki et al., 1997; Chen et al., 1993; Larker et al., 1992] to be A_3B, $L1_2$ type, where A represents Ni (also some Co

and Fe) and B represents Ti (also smaller amounts of Nb). The γ' was reported to precipitate between 540-760°C [Chen et al., 1993; Larker et al., 1992].

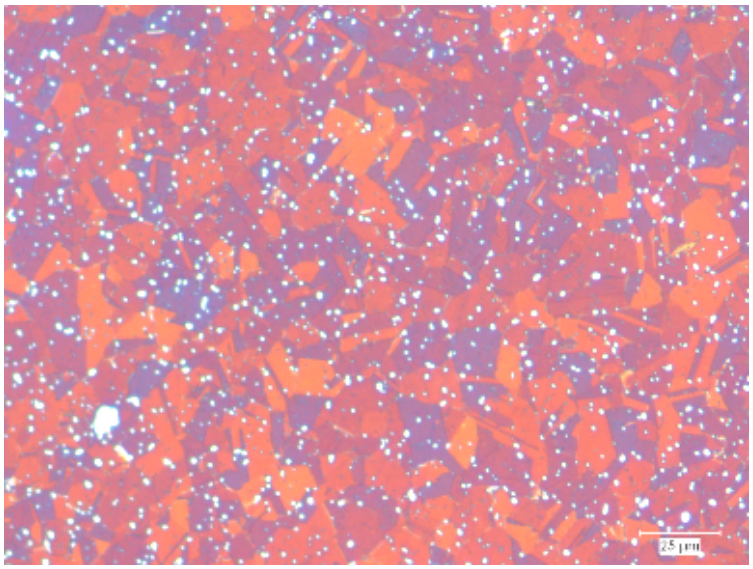

Figure 4-13 Optical micrograph of Incoloy 909 in STA condition

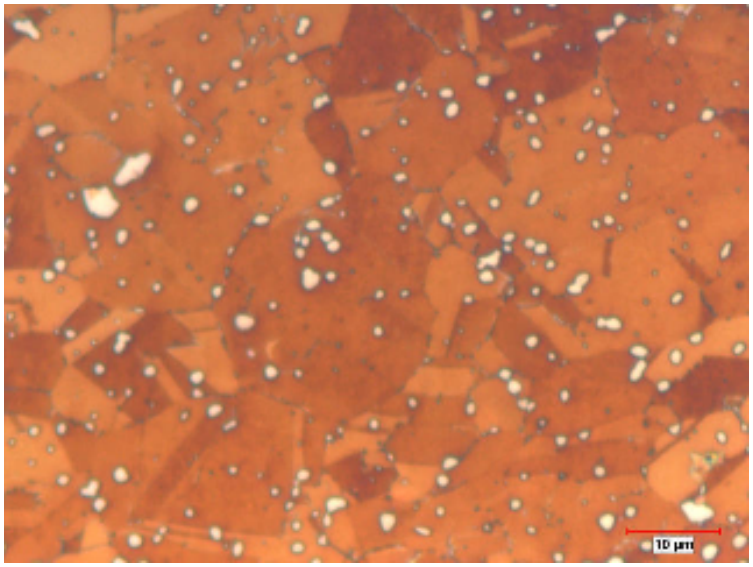

Figure 4-14 Optical micrograph of Incoloy 909 in STA condition

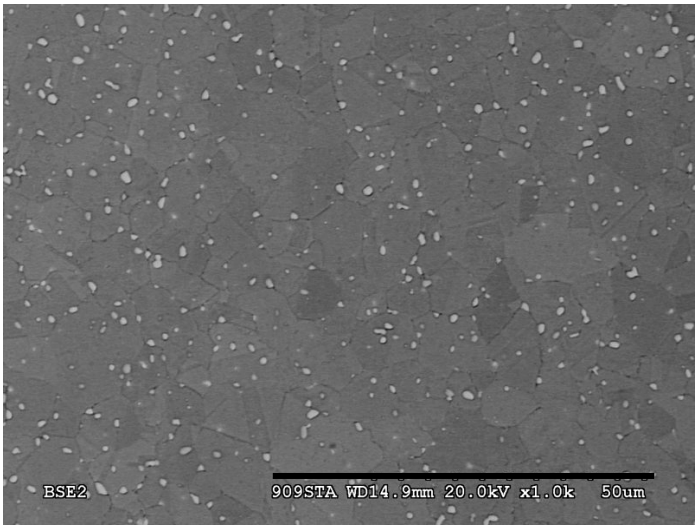

Figure 4-15 SEM micrograph of Incoloy 909 in STA condition

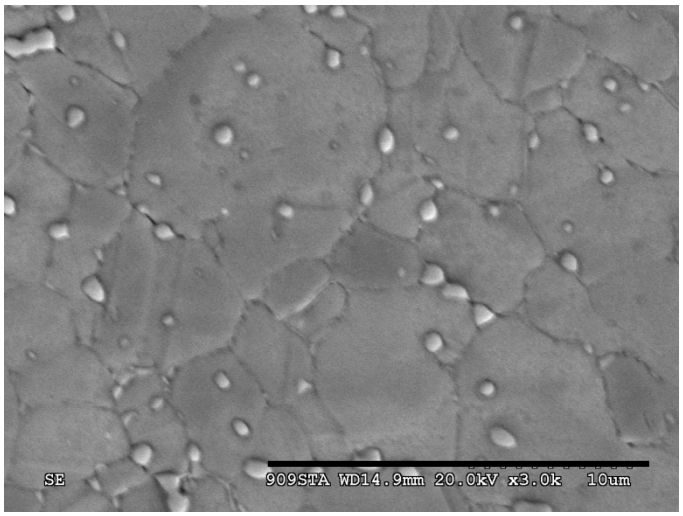

Figure 4-16 SEM micrograph of Incoloy 909 in STA condition

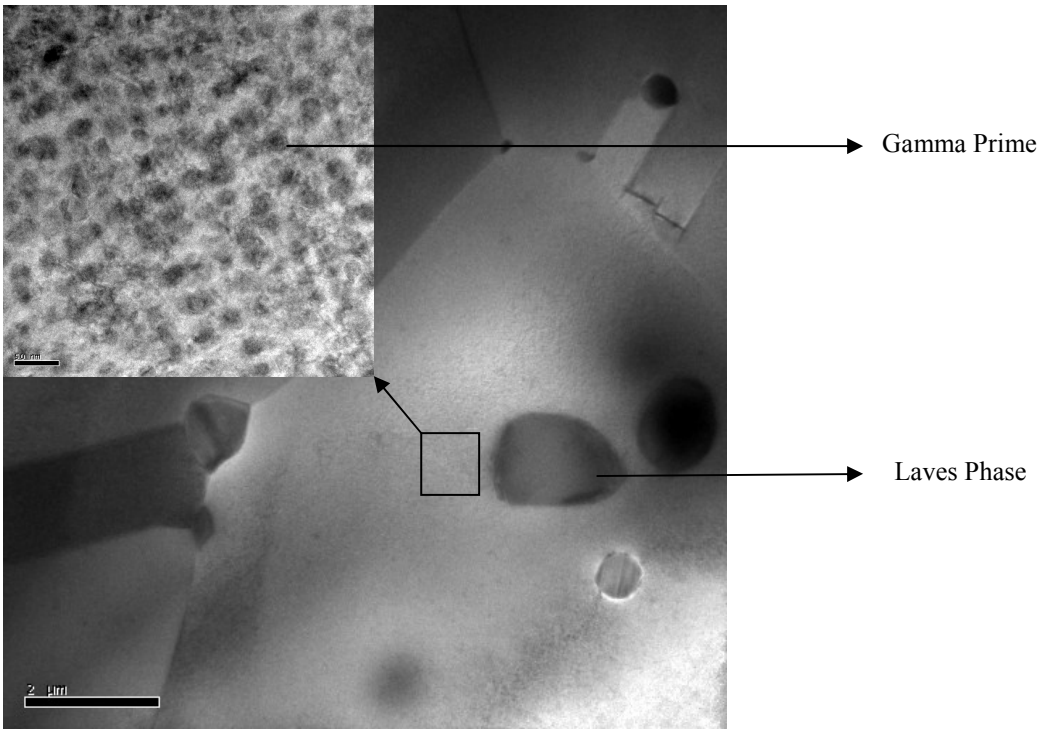

Figure 4-17 A typical TEM micrograph of Incoloy 909 in STA condition (Inset scale marker 50nm)

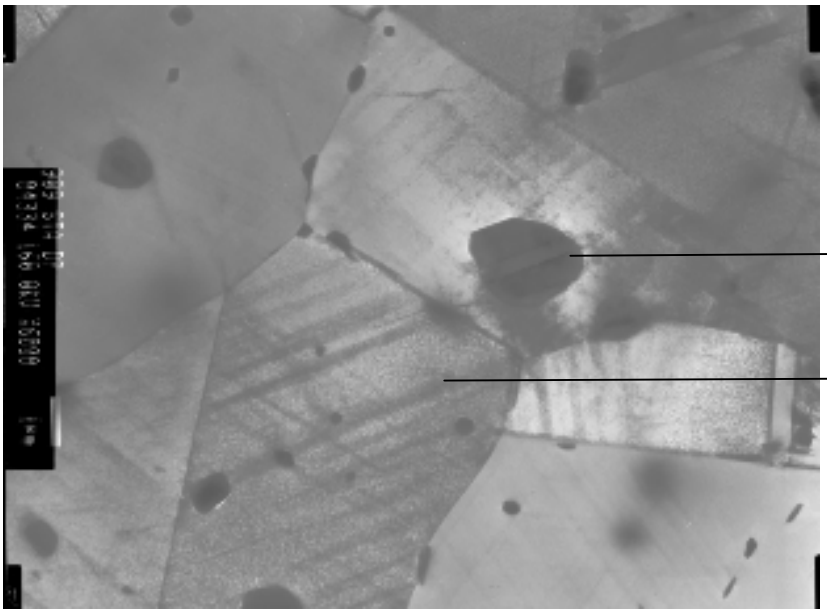

Figure 4-18 A TEM micrograph of Incoloy 909 in STA condition

The γ' phase in Incoloy 909 is known to be metastable, and can transfrom into a more stable platelet type phase with increasing temperature. The fine spherical particles are observed to coarsen with time at temperature and are reported to increase the hardness until the diameter reaches about 20nm, with further coarsening causing reduction in hardness. Based on this report, it is evident that commercial aging heat treatment results in optimal hardness based on the γ' size shown in Fig 4-19 (a) and (b), is about 20nm. The SAED patterns for the γ' particles corresponding to <110> and <111> zone axis are shown in Fig 4-19 (c) and (d).

A high Ti/Al ratio and a low amount of aluminum is cited to be one of the reasons for the metastable nature of the γ' precipitate, which is often the cause of formation of cellular η phase in Ni-Fe alloys [Larker et al., 1992]. The major ordered BCT precipitate γ" (Ni_3Nb), the primary strengthener in niobium containing Superalloy such as Inconel 718 is not found in this alloy. The presence of sufficient cobalt is reported to suppress the formation of γ" in this alloy. Overall, the current investigation did not consistently find the presence of needle or platelet phase in STA condition, except rarely as observed in Fig 4-18 that shows γ' particles likely ready to transforming into platelet phase,l occurring γ'–> ε" –> ε, as γ' particles can be seen oriented in needle or platelet like fashion but not per say, platelet precipitate. Figs 4-20 (a) and (b) show bright field image and SAD patterns for HCP Laves phase. The information detailed in ST condition is also applicable here to the STA condition for Laves Phase, except that the precipitation treatment increases the size and abundance of Laves Phase.

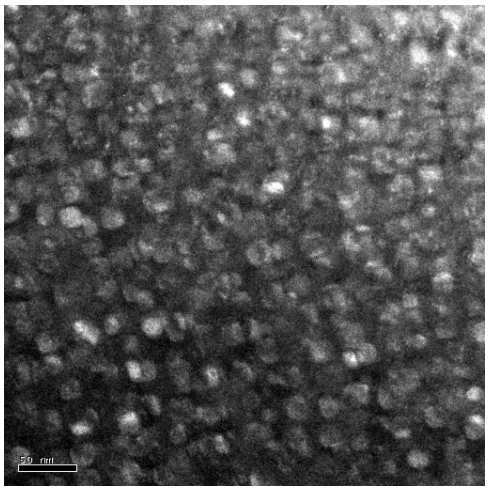

(a)

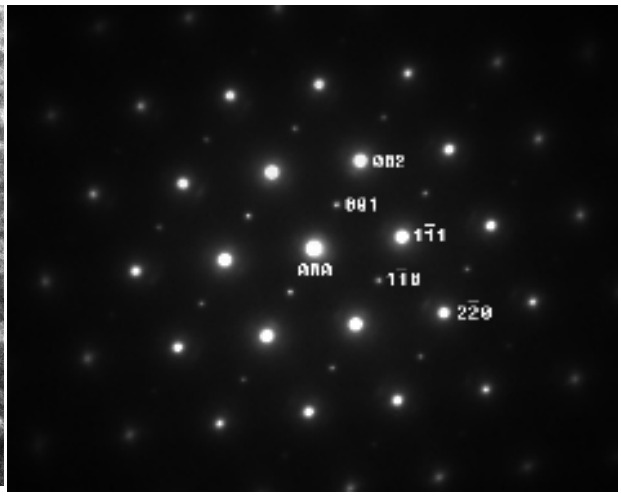

(c)

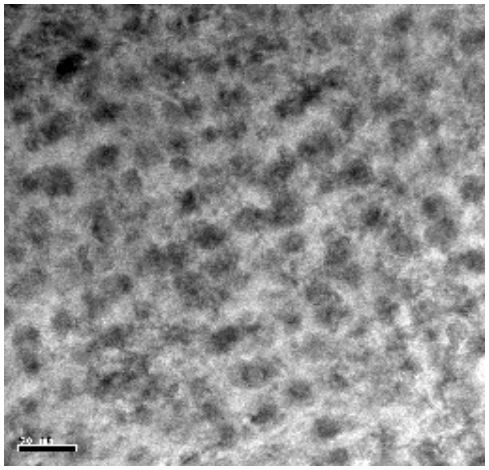

(b)

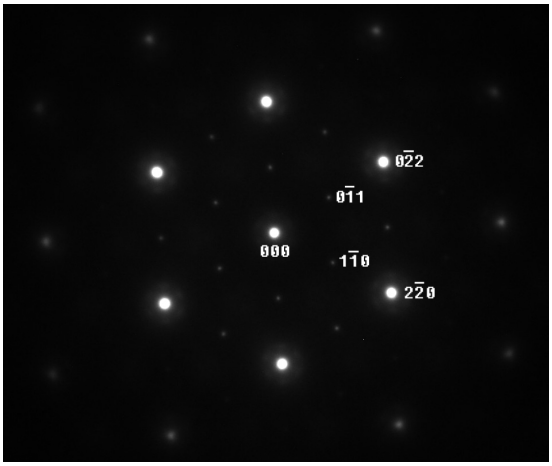

(d)

Figure 4-19 (a)TEM bright field (scale marker 50nm) and (b) dark field image of nano sized γ' particles in STA condition (scale marker 50nm) (c): <110> and (d): <111> zone SAED patterns of the $L1_2$ γ' phase in STA condition. [Help from Dr.Tang, former post doctoral is gratefully acknowledged]

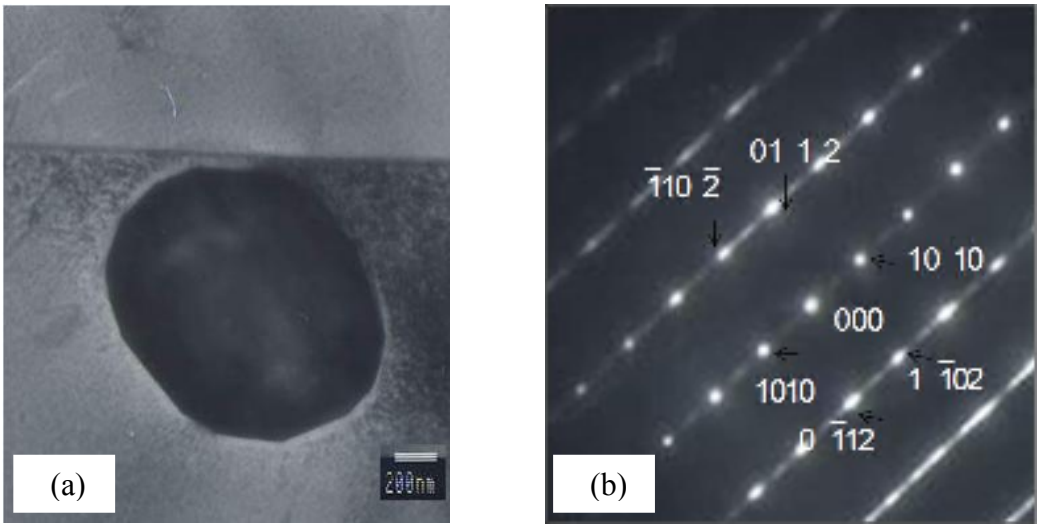

Figure 4-20 (a) TEM bright field image of Laves phase from STA treatment with SADP (b) of Laves phase in the direction parallel to the zone axis [$\bar{2}$4 $\bar{2}$3] [Help from Dr.Vishwakarma, post doctoral fellow is gratefully acknowledged]

4.3.2 Solution Treated and Over Aged condition (STOA)

The optical micrographs in Fig 4-21 provide little information about the phases present except a distinct fine grained structure with dark and bright grains. However at higher magnification, Fig 4-22 shows some variations relative to the commercial aged condition, especially with the presence of copious amounts of platelet like precipitates present in intragranular and intergranular locations. The SEM micrograph shown in Fig 4-23 and the TEM micrograph shown in Fig 4-24 provides a more detailed view of the needle or platelet precipitates arranged in Widmanstaten type structure that are extensively distributed throughout the matrix, with some globular Laves phase particles scattered around.

TEM investigation (Fig 4-24) proved the absence of the nano-sized spherical phase in the matrix after this overaging treatment. Hence, it can be ascertained that complete transformation of γ' phase to ε phase took place, or alternatively, ε phase could have directly precipitated during this over aging heat treatment. This is consistent with previous findings in the literature [Kusubiraki et al., 1999] which suggests that with time at temperature the system would favor the formation of more stable ε phase. It is believed at aging temperatures above about 770°C, the platelet precipitates (ε) directly precipitated out of the supersaturated gamma matrix [Heck et al., 1988].

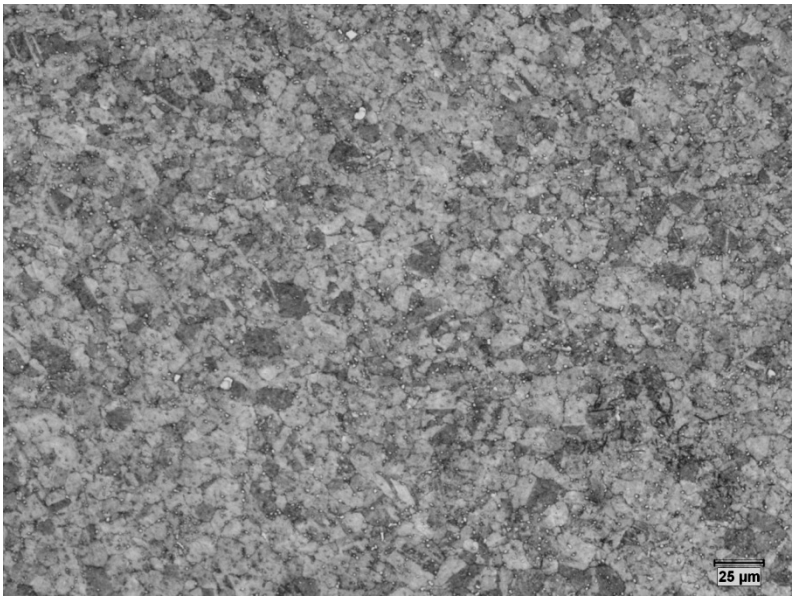

Figure 4-21 Low magnification optical micrograph of Incoloy 909 in STOA condition

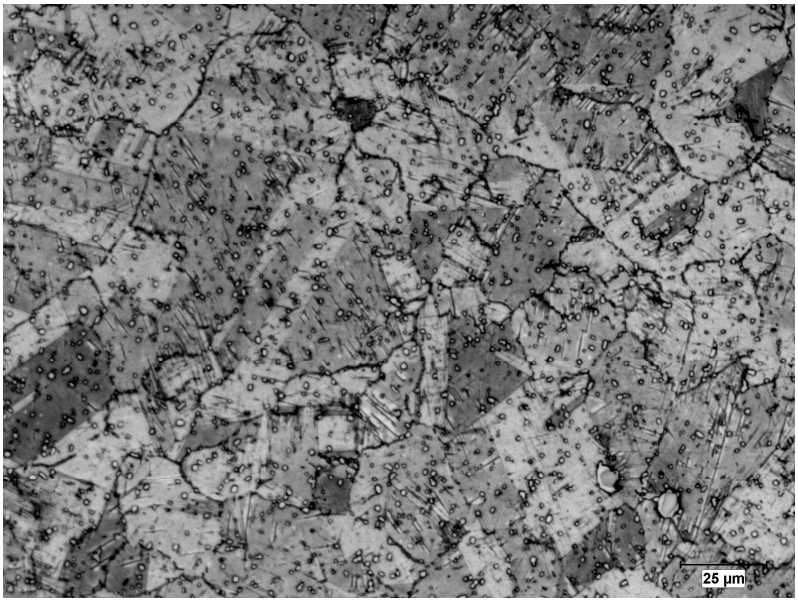

Figure 4-22 Higher magnification optical micrograph of Incoloy 909 in STOA condition

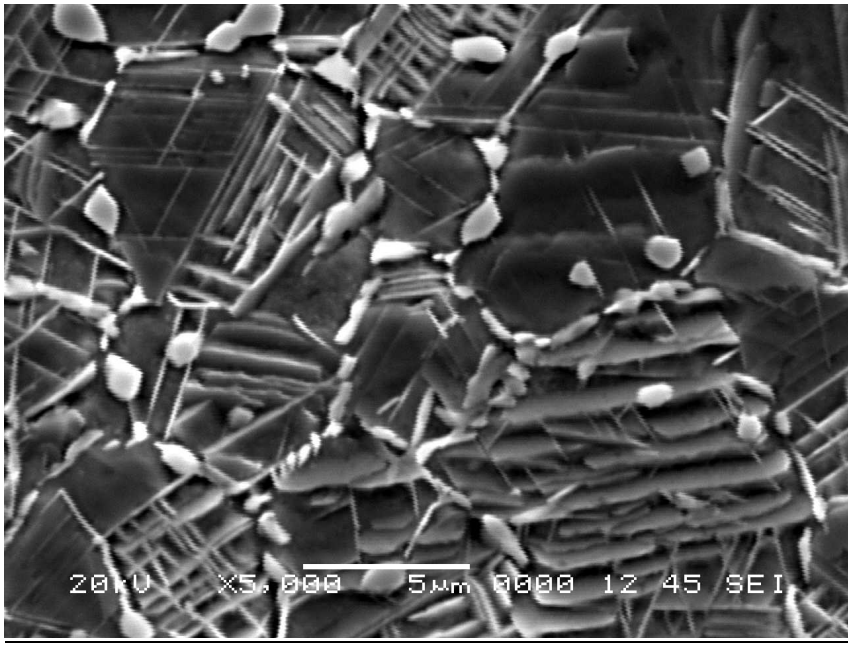

Figure 4-23 Higher magnification optical micrograph of Incoloy 909 in STOA condition

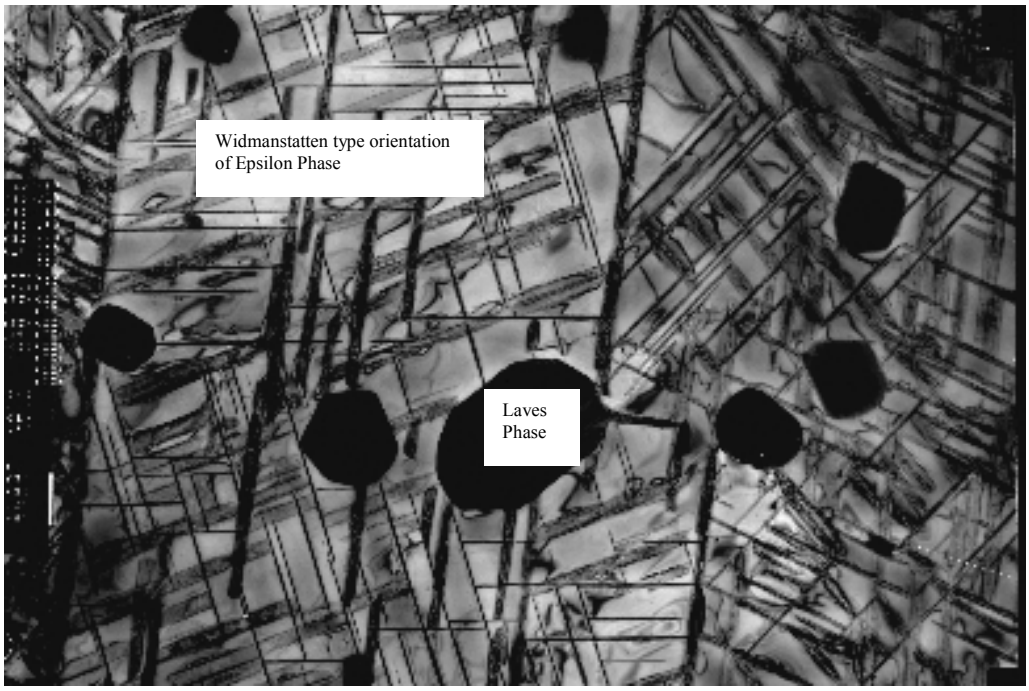

Figure 4-24 Higher magnification optical micrograph of Incoloy 909 in STOA condition

It is likely that at the lower precipitation temperature range that the advantage of the elevated chemical free energy change associated with the formation of the platelet phase was offset by the much smaller activation barriers associated with the nucleation of (more metastable) γ' phase. However, at higher temperature this is not valid, resulting in the precipitation of epsilon phase directly from the supersaturated austenite similar to the formation of delta phase in Inconel 718 reported in the literature [Sunderaraman et al., 1988]. However, the ε phase also is not a very stable phase, as with time and temperature the phase can transform into the cellular closed packed η type phase. These cellular type precipitates forms after very long exposure (>1000 Hrs) at intermediate temperatures [Heck et al., 1988, Kusabiraki et al., 1997]. The η phase is similar to Ni_3Ti, a topologically closed pack structure of type Do_{24} was not found in this heat treated condition.

The strain energy plays an important role in deciding the shape and size of the precipitates formed in the matrix. The orientation of these phases, mismatch, and shape often are considered as important parameters. It has been shown [Jena et al., 1984] that a strain energy mismatch of less than 0.4%, usually results in spherical precipitates. A mismatch between 0.4 to 1% results in cubic precipitates and a mismatch of over 1% results in cellular phases. Hence, as the precipitates grows, strain energy increases, and this results in morphological changes to the precipitates during the initial stages of the precipitation.

In Fig 4-25, a high resolution TEM micrograph shows a Laves phase particle measuring about 1μm lying along with Widmansttaten type platelet precipitates. In Fig 4-26, TEM

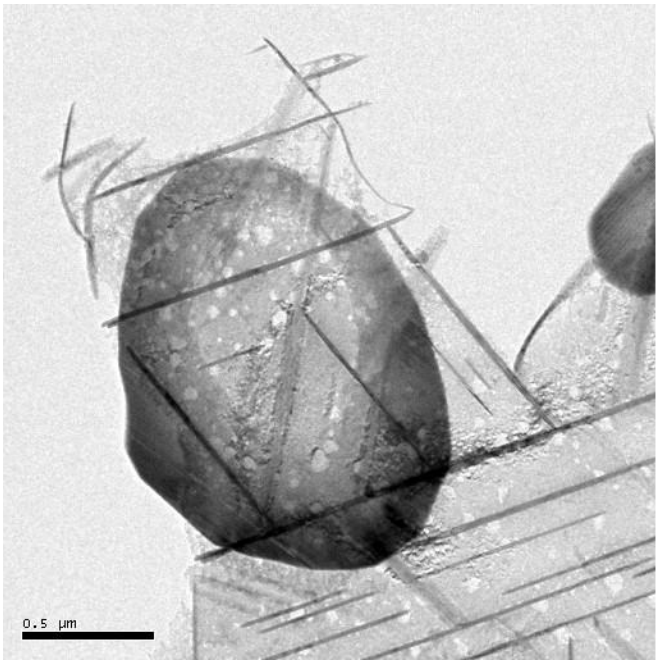

Figure 4-25 HRTEM micrograph of Incoloy 909 in STOA condition (scale marker 0.5μm) [Help from Dr.Tang, post doctoral fellow is gratefully acknowledged]

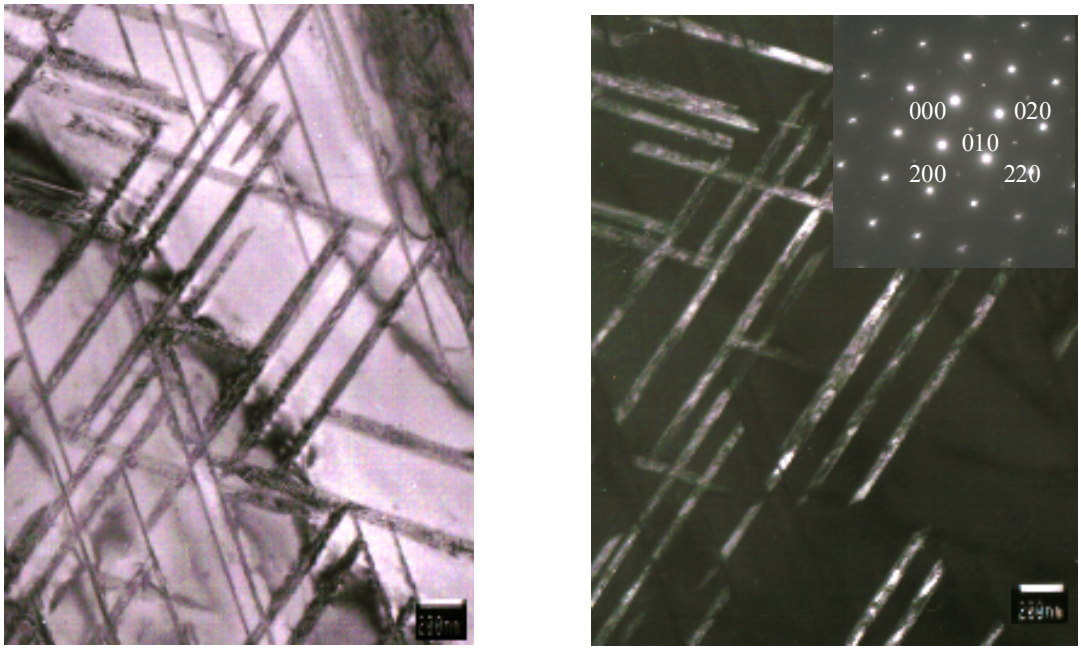

Figure 4-26 (L) Bright and (R) Dark field TEM micrograph (scale marker 200nm) with selected area electron diffraction pattern, beam along [001] gamma showing Superlattice reflections pertaining to epsilon phase [Help from Dr. Vishwakarma, postdoctoral fellow is gratefully acknowledged]

micrographs of epsilon phase in bright and dark field are given, the dark field micrograph also contains a SAD pattern, with the beam along [001] gamma, showing superlattice reflections from the epsilon phase. The SAD analysis indicated that the ε phase conforms to Hexagonal close pack (HCP) structure [Guo et al., 2001] and not orthorhombic [Chen et al., 1993]. These ε platelets intersect with each other forming a typical Widmanstatten like morphology. In the literature [Heck et al., 1988] existence of an ε″ phase is mentioned. This ε" phase is reported as another platelet type precipitate present along with the ε phase. They conducted X-ray diffraction studies on both ε and ε″, which indicated that lattice constants of ε were: a = 0.518 nm and c = 0.426 nm, while the lattice constants of ε" were a = 0.5177nm and c = 0.4196 nm. However, no conclusive crystallographic structural differences between the ε and ε" were reported. No further detailed crystallographic studies on ε"

in Incoloy 909 is available in the literature, except by Heck and Smith [Heck et al., 1988; Heck 1990], who have shown TEM DP of ε" is similar to FCC γ' <001>. It is not known if previous researchers considered the transition phase between γ' to ε.

Due to the presence of anti phase boundaries (APB) in the ε platelets as shown in Fig 4-27, it is likely that these APBs contribute to strengthening of alloys similar to gamma prime in many nickel based alloys [Baither et al., 2002]. Anti phase boundaries are reported to occur in ordered alloys, due to crystallographic defects. If the ordering is ABABAB, an anti phase boundary will result in the form, for example, ABAABA. Information is available in the literature [Zhang et al., 2002] on such antiphase boundaries, due to various factors. These APBs are said to be formed in γ' and other closed packed phases in many alloys, few reasons that are thought to promote APB formation are (a) misarrangment of the local ordered atoms occur within a precipitate, (b) dislocation cutting into the precipitate and (c) matrix dislocation.

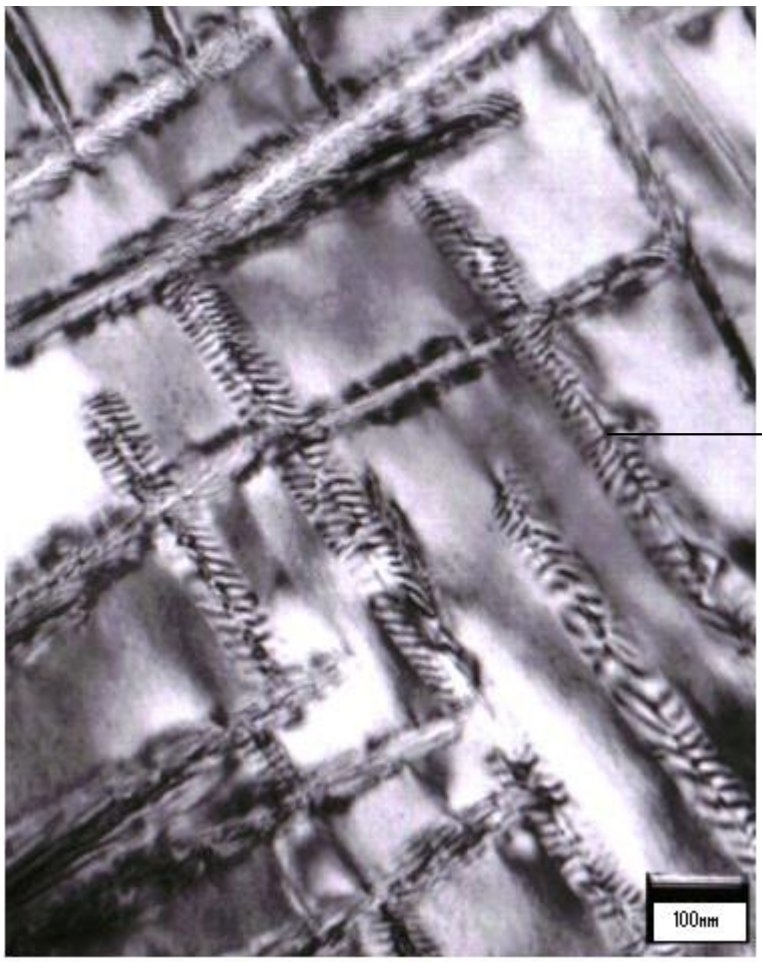

Figure 4-27 Bright field TEM micrograph with selected area electron diffraction pattern, beam along [001] gamma showing Superlattice reflections pertaining to epsilon phase [Help from Dr.Krutika Vishwakarma, postdoctoral fellow is gratefully acknowledged]

Conflicting reports exist on beneficial effects and deleterious effects of ε precipitates. This study shows that with growth of ε precipitates there is a marked reduction in short-term tensile strength, as shown in the Table 4-5, tensile data for the solution treated (ST), solution treated and aged (STA) and solution treated and over aged (STOA) conditions presented in the subsequent sections (4.6) of this Chapter.

4.4 Composition of precipitates in various conditions

The precipitates present in this alloy, structure, morphology and composition type are presented in Table 4-2. It should be noted that the metastable γ' transitions to ε, which again transitions to a relatively stable η phase. In this study, the transitioning from ε to η was not studied, but details can be found elsewhere in the literature [Kusabiraki et al., 1997].

Heat treated conditions and the corresponding precipitates present in Incoloy 909 are presented in Table 4-3. As discussed earlier, the solution heat treatment take all the precipitates except Laves into solution. The precipitation hardening treatment results in gamma prime precipitation and Laves Phase. The over aging heat resulted in Epsilon phase and Laves Phase.

Chemical composition of various precipitates and the matrix for 909 in various heat treated condition is presented in Table 4-4. The TEM-EDS composition of gamma prime (γ') precipitate was not analyzed due to extremely small size, but this intermetallic compound is one of the well known precipitates occurring in several other nickel based Superalloys is extensively characterized, reported to confirm to A_3B (3:1) type composition. In this research and also based on reports in literature [Heck et al., 1988, Chen et al.,1993] the ε phase confirms to about $(FeCoNi)_3(NbTiSi)_{1,.}$ Hence, it is observed to confirm to A_3B (3:1) type composition similar to γ'. It is expected that the overall composition of epsilon phase is similar to γ', although the morphology and the crystal structure are different. This kind of chemical composition relationship can also be observed with $\gamma'' \rightarrow \delta \rightarrow \eta$ in Alloy 718.

Table 4-2: Precipitates, their structure, morphology and composition type in Incoloy 909

Precipitate	Structure	Morphology	Composition Type
Laves Phase	HCP	Globular	$(Fe,Ni)_2Nb$
γ'	FCC	Spherical	$Ni_3(Ti,Nb)$
ε	HCP	Platelet	Ni_3Nb

Table 4-3: Heat treat conditions and corresponding precipitates present in that condition for Incoloy 909

Condition	Precipitates
Solution Treated (ST)	Laves Phase
Solution Treated and Aged (STA) (Commercial Process)	Laves Phase, Gamma Prime, rare occurences of transitioning γ ′
Solution Treated and Over Aged (STOA)	Laves Phase, Platlet/needle epsilon Phase

Table 4-4: Chemical composition in Atomic % of precipitates and matrix for Incoloy 909

Phase	**Fe**	**Co**	**Ni**	**Si**	**Ti**	**Nb**
Laves [Heck et al.,1988] STA XRD	18	14	38	5	3	18
Laves (present) STA TEM EDS	14.5	13.6	40.3	5	1.9	20.5
Laves (present) STOA TEM EDS	14.7	13.5	41.5	6.1	1.8	22.4
Epsilon [Heck et al., 1988] XRD	11	16	50	2	4	18
Epsilon [Heck et al., 1988] XRD	11	16	50	2	4	18
'Platelet' Chen et al, aged 750°C/30 hrs. TEM/EDX	12.9	11.5	52.5	0	7.5	15.6
Epsilon (present) STOA TEM/EDX	11.3	12.9	52.7	1.6	8.6	12.8
Matrix (present) STA TEM/EDX	41.1	13.3	40.5	0.3	1.7	3.1
Matrix (present) STOA TEM/EDX	47.7	12.6	37.6	0.3	0.7	1.2

4.5 Black and White grain analysis

The so called “Black” and “White” grains are noticed in all conditions to varying degrees as shown in Fig 4-28 - 4-30. Several conflicting reports exist in the literature on the possible mechanisms of formation of black grains. Smith et al., [Smith et al., 1991] pointed out that presence of black grains would reduce the strength and ductility of the alloys. Another research group [Heck 1990] suggested that the black grain is formed due to unrecrystallized grains present prior to aging and related with presence of ε phase particles. They also suggested other possible mechanism involving generation of stacking faults in low stacking fault energy matrix. These sites then could act as nucleation sites for precipitates such as ε phase coherent with the faults in the FCC matrix or embryonic γ’.

Guo et al., [Guo et al., 2000] have shown that a possible mechanism could be due to orientation relationship between ε and γ matrix. They thought the relative orientation of ε plates to polish plane might make some of the grains to appear as black similar to pearlite appearing black under an optical microscope. They pointed out that black grains did not form when aging temperature exceeded 850°C. However, in the present thesis, depending upon the etching time and etchants used, varying results were obtained with the contrast between white-black grain to varying degree. It implied that this is likely related with etching artifacts or grain orientation effects rather than to do with differences in chemistry between the grains.

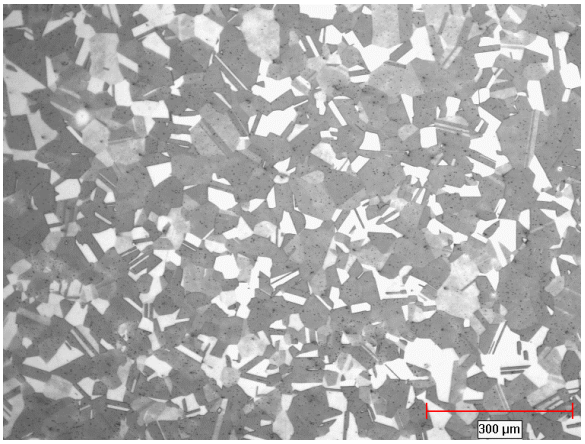

Figure 4-28 Microstructure of Incoloy 909 solution treated at1065°C for 20 minutes

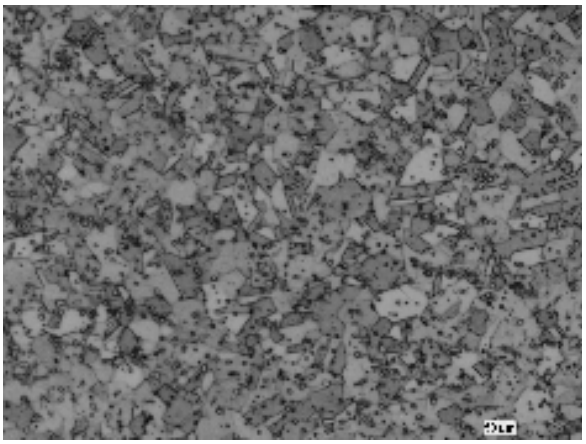

Figure 4-29 Microstructure of Incoloy 909 solution treated at 982°C for 30 minutes

Figure 4-30 Microstructure of Incoloy 909 solution treated and over aged condition

4.6 Mechanical and microstructural properties of Incoloy 909

4.6.1 Tensile Properties of Incoloy 909

It is of interest to study the role the ε phase has on the yield strength of the alloy relative to the γ ′phase. The tensile properties of Incoloy 909 in various heat treated condition is presented in Table 4-5. The difference in the yield strength between STA and ST is 689 MPa and the difference between STOA and ST is 163 MPa. In other words, the effect of the ε phase at a ΔYS of 162MPa is considerably less than that of the γ ′phase at 689 MPa. However, it can be seen that the ε phase still has a significant effect on the yield stress relative to the ST condition.

The anti-phase domains (Fig 4-27) being formed by a nucleation and growth process, can strengthen alloys containing ordered Superlattices [Davies et al., 1963]. Thus the copious amount of ε phase present in the matrix contributed to the yield stress over and above that of the ST condition as shown in Table 4-5. Comparisons of metallographic observations on anti phase boundaries (APB) present in epsilon phase and yield strength confirms that a strong correlation exists between yield stress and precipitation of epsilon phase in STOA phase. These boundaries are known to form where anti-phase domains meet which have the wrong neighbours resulting in an anti-phase boundary with a higher energy than the surrounding matrix [Stoloff et al., 1968]. It was also reported that there is a presence of a highly ordered anti-phase boundary type structure in the ε phase in the over aged condition [Guo et al., 2002].

Table 4-5: Tensile properties of Incoloy 909 in various heat treated conditions

Heat treatment	Yield stress, MPa	U.T.S. MPa	Elongation %
ST	555	944	41
STA	1247	1344	19
STOA	717	1034	22

4.6.2 Fractographs of Incoloy 909 in ST, STA and STOA conditions

The SEM fractrographs for all the three heat treated conditions are as presented in Figs 4-31 through 4-33. All the fractrographs reveal a more or less ductile cup and cone failure with some variations.

The solution treated condition produced the classic cup and cone fracture surface as depicted in Fig 4-31 indicating excellent ductility in this condition. Also from section 4.6.1, we know the elongation percentage at this condition is about twice that compared to STA and STOA conditions. In the solution treated and aged condition, the examination of fracture surface again showed the presence of a ductile cup and cone fracture, as shown in Fig 4-32. However, when compared to solution treated condition, the dimple sizes were smaller and there were also indications showing a smaller extent of intergranular fracture caused due to likely presence of larger sized globular Laves Phase. In the solution treated and over aged condition, examination of fracture surface as shown in Fig 4-33 indicate presence of generally smaller dimple sizes, but the shape varied with a smaller area indicating about 10% intergranular fracture. The increase in brittleness in STOA condition is likely due to the presence of copious amounts of platelet type precipitates. The transformation of beneficial spherical gamma prime strengthening in STA condition to relatively poor strengthening of platelet like epsilon phase in STOA condition is evident from the differences observed in the fracture surfaces.

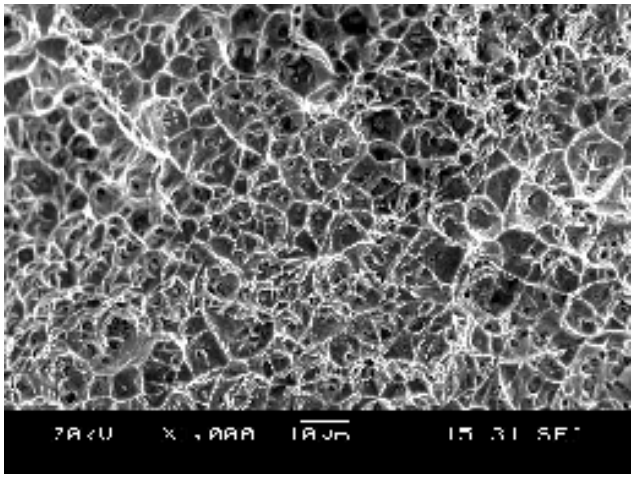

Figure 4-31 Fracture surface of Incoloy 909 in ST condition

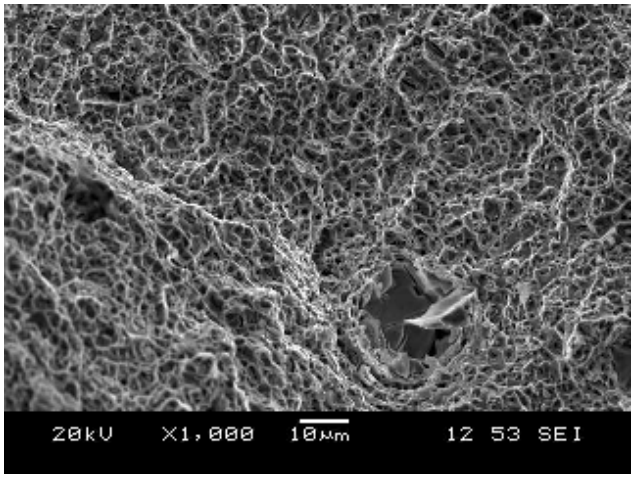

Figure 4-32 Fracture surface of Incoloy 909 in STA condition

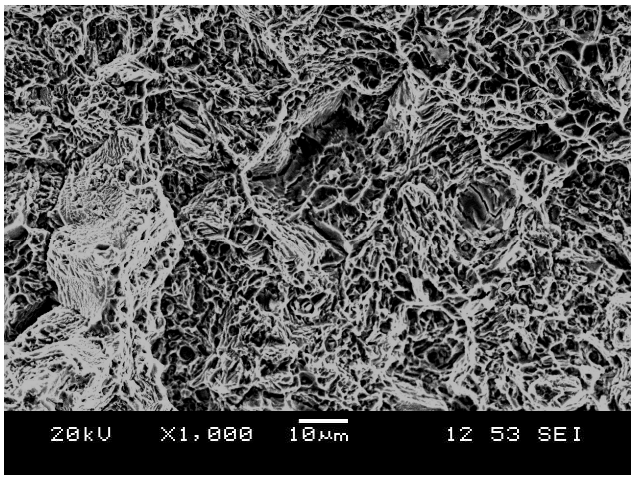

Figure 4-33 Fracture surface of Incoloy 909 in STOA condition

4.6.3 Hardness Results

The hardness of Incoloy 909 at ST, STA and STOA were obtained using Vickers micro hardness measurements, ten readings were taken from each polished sample and the average hardness is reported in Table 4-6. It can be seen that the hardness readings of the various heat treated conditions are related to the tensile properties reported in Table 4-5. The STA sample with superior gamma prime strengthening precipitates yielded the highest average hardness 482 HV, while the solution treated sample with only Laves precipitates yielded the lowest average hardness 276 HV. The STOA sample with excessive platelet or needle shaped ε phase is considered to be inferior to spherical or cubical shaped precipitates for strengthening, yielded an average hardness of 338 HV. The differences in hardness in relation with ST condition data showed that STA was superior with almost 206 points higher, while the STOA was higher by 62 points compared to the base line. The absence of γ' phase and excessive amounts of ε phase results in a drop of 143 points in STOA condition compared to the optimal STA condition.

Table 4-6: Hardness of Incoloy 909 in various heat treated conditions

Condition	Hardness (HV500)	ΔHardness (difference from ST)
ST	276±5.3	0
STA	482±7.5	205.8
STOA	338±8.5	62.4

4.7 Welding

As a part of studying the fabrication characteristics of Incoloy 909, gas tungsten arc welding and electron beam welding joining process were used to study the alloys, susceptibility to weld cracking. Solution heat treated coupons were welded by electron beam welding using bead on plate methodology, the parameters used were 79 μA Current, 44kV Voltage, sharp focus and 150 cm/min traverse speed. The weld trials were carried out in the ST condition at an average grain size of 10μm and 250μm as shown in Fig 4-34 and Fig 4-35 respectively.. The material was not found to be susceptible to HAZ cracking, likely due to fine grain size in the as received material condition. Microfissuring was observed only when the grains were grown over 250 μm, with a HAZ with cracks as shown in Fig 4-35.

The TIG weld trials were carried out in ST condition at an average grain size of 250μm as shown in Fig 4-36 and Fig 4-37 at two different amperage rates of 75A and 100A respectively. The microstructure revealed heat affected zone cracking with incidence of back filling from fusion zone. However, weld cracking with a large grain structure is somewhat expected and moreover, materials with such a microstructure is seldom used in fabrication shops. Welding metallurgy needs to be studied in depth, as the predecessor alloy Incoloy 903 was found susceptible to HAZ cracking [Nakkalil 1993], however this was not the main focus of this research.

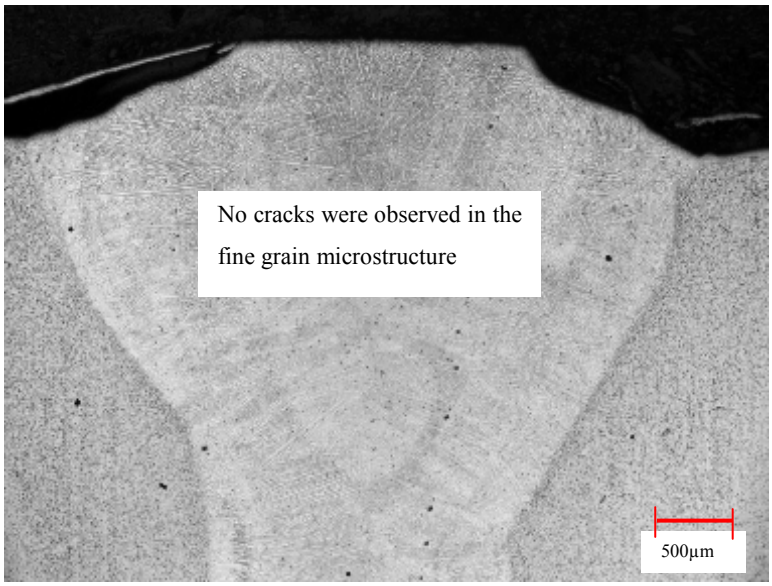

Figure 4-34 Electron beam welded Incoloy 909 solution treated at 982°C for 30 minutes

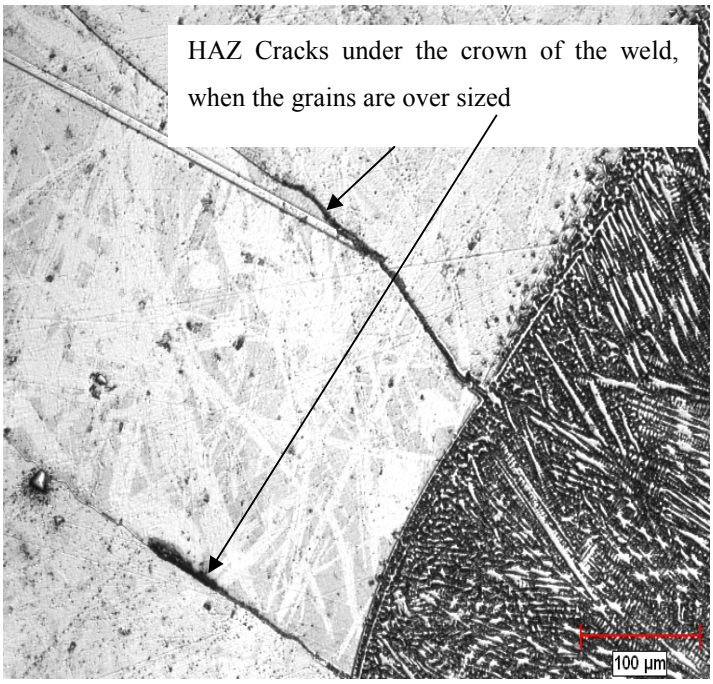

Figure 4-35 Electron beam welded Incoloy 909 solution treated at1080°C for 8 hours

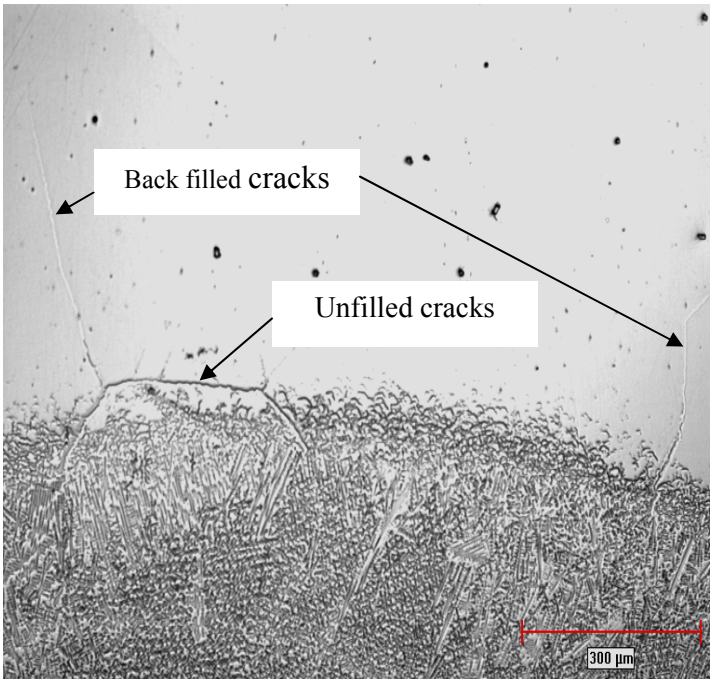

Figure 4-36 TIG welded (75A) Incoloy 909 solution treated at1080°C for 8 hours

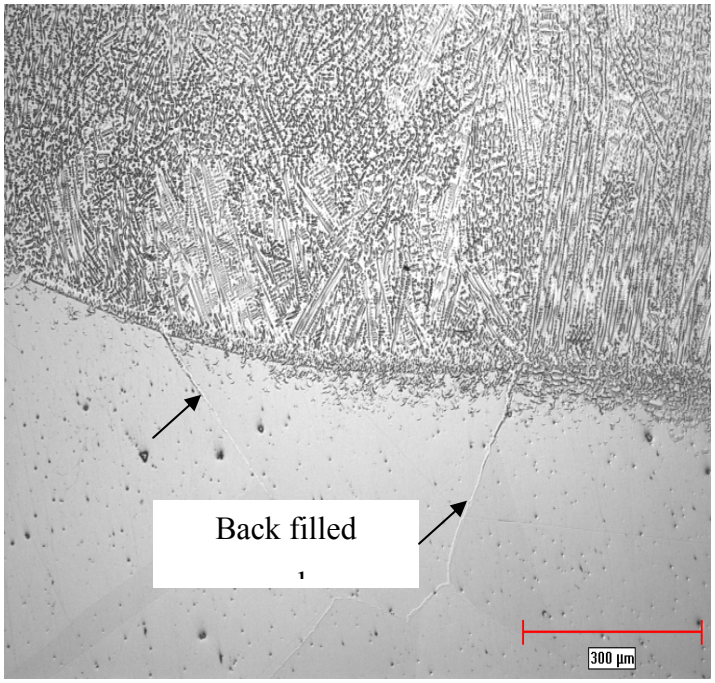

Figure 4-37 TIG welded (100A) Incoloy 909 solution treated at1080°C for 8 hours

4.8 Oxidation

To evaluate the high-temperature oxidation behavior of Incoloy 909 and to compare it with Inconel 718 with and without coatings, the test coupons were exposed to an isothermal furnace heat treatment in air (furnace atmosphere without flowing air) and cyclic oxidation cycles using burner test rig for specified time and temperature ranges in the experimental section in Chapter 3. The morphologies, compositions, and growth of the scales formed during oxidation at these conditions were investigated and presented in the following sections.

4.8.1 As sprayed condition

4.8.1.1 Bare Alloys

The bare solution treated test coupon bars of Incoloy 909 and Alloy 718 were prepared using standard metallographic preparation; the optical micrographs are presented in Fig 4-38 and Fig 4-39 respectively. It can be seen that there are no prior oxide scales present on the surface of both the alloys, hence, it can be concluded that all the prior heat treatment in vacuum did not result in any scale formation. Earlier research reports indicated that even a short time exposure at elevated temperature results in sufficient scale formation in Incoloy 909 [Kusubiraki et al., 1997; Srivastava 1992], while Alloy 718 is reported to exhibit relatively slower oxide scale growth during short time exposure at elevated temperature [Jian et al., 2000].

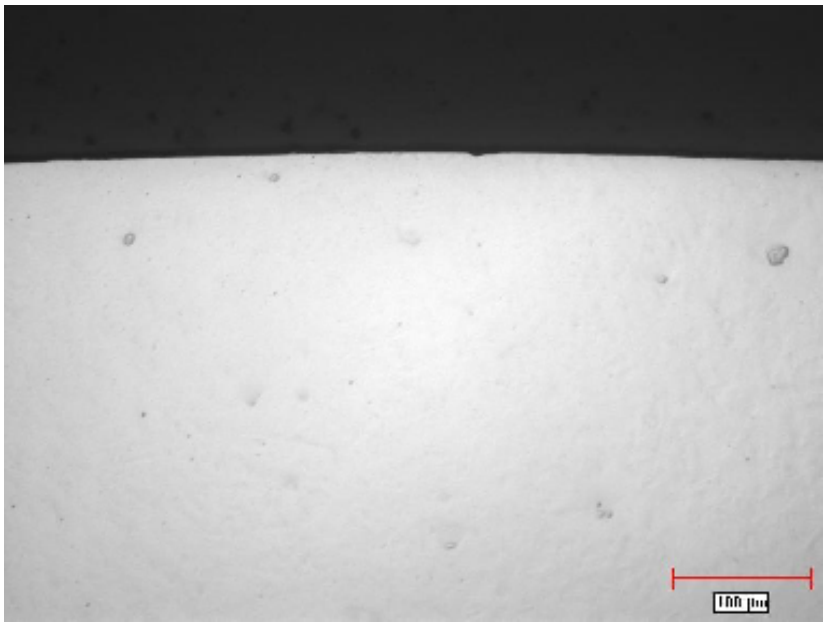

Figure 4-38 Bare In 909 (Prior to oxidation test)

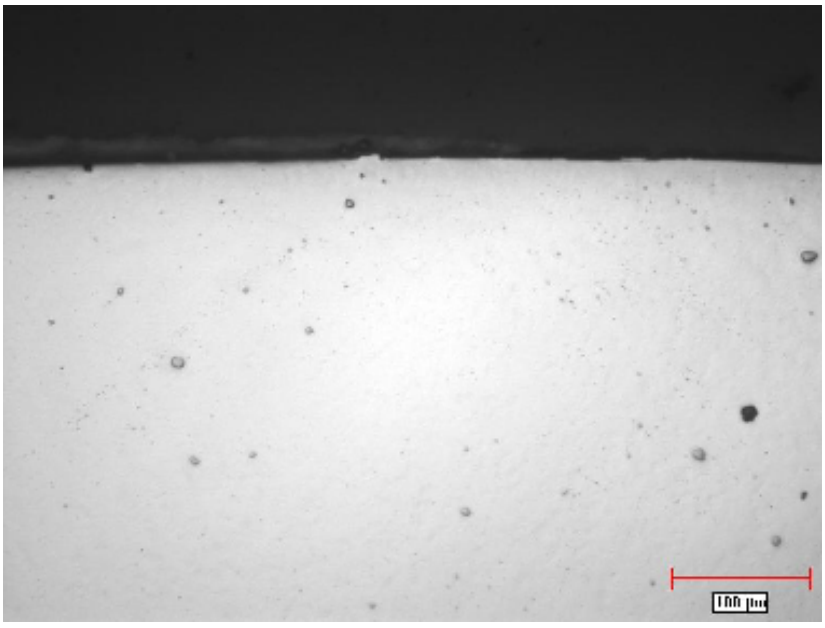

Figure 4-39 Bare In 718(Prior to oxidation test)

4.8.1.2 As Coated Incoloy 909 and Inconel 718

Fig 4-40 shows a SEM micrograph of gas atomized CoNiCrAlY powder used in this study, the morphology of these particles being spherical with the presence of satellites. The HVOF sample coated CoNiCrAlY showed extensive coating debonding to approximately 50% of the circumference of the rod. An optical micrograph showing one such field containing a completely separated coating is shown in Fig 4-41. It is reported in literature that thermally sprayed coatings with high residual stresses are more prone to micro cracking that may result in separation of the coating from the substrate thus resulting in exposing the underlying substrate to the service environment[Knight et al., 1993; Stokes et al., 2008]. However, HVOF coatings are reported to exhibit excellent bonding due to extensive compressive stresses produced due to high impacting kinetic energy employed during coating deposition process, akin to shot peening [Sampath et al., 2004; Lyphout et al., 2008].

High residual stresses are said to be generated within the coatings sprayed on substrates using the thermal spray process [Sampath et al., 2004]. This can be aggravated when the CTE between the coating and the substrate material is different, as it can result in stresses at the interface due to differential expansion and contraction characteristics. Among the thermal spray process types, HVOF spraying results in coatings with lower residual stresses due to high kinetic energy involved during deposition of particles. It is known that CoNiCrAlY coatings are ductile at high temperatures (800°C) but brittle at lower temperatures [Taylor et al., 1996], but it is likely not a reason for debonding as this type of coatings are extensively used as a bond coat for thermal barrier type coatings on several Superalloys without any coating separation problems.

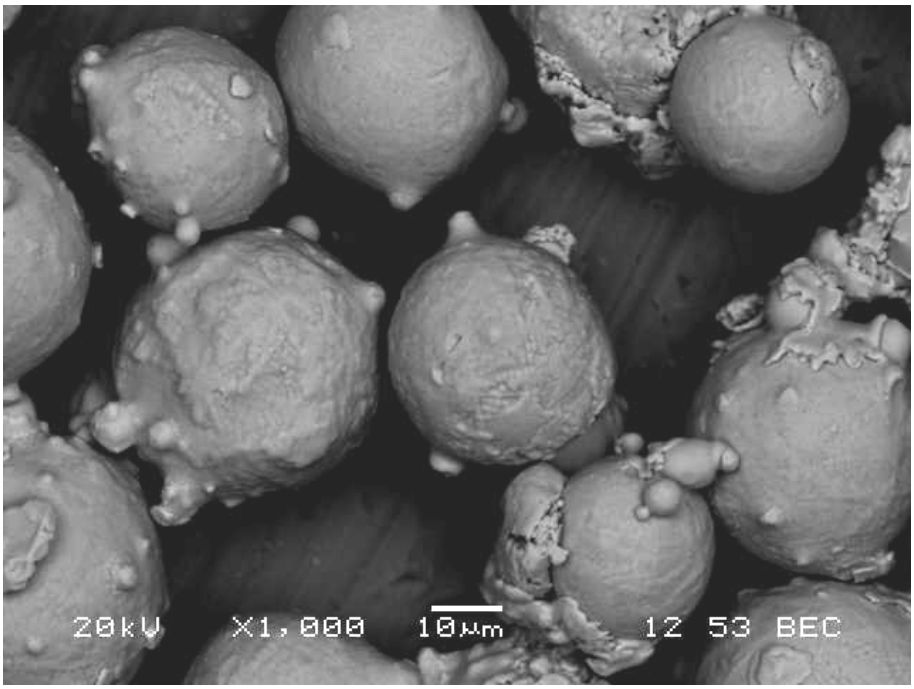

Figure 4-40 SEM micrograph of gas atomized CoNiCrAlY powder prior to spray deposition

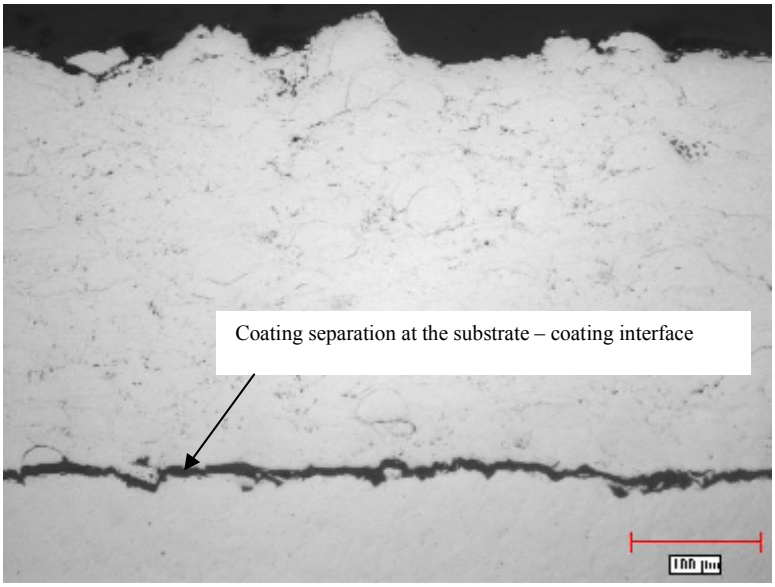

Figure 4-41 As sprayed Incoloy 909 with CoNiCrAlY coating

The coating-surface interface adhesion depends on the coating morphology and inter-particle bonding of the sprayed powders as well as other factors such as residual stresses. The roughness of the grit blasted substrate surface is known to play a role in enhancing the adhesion in many thermally sprayed coatings [Day et al., 2005]. It is evident from Fig 4-41 and Fig 4-42 the interface roughened by aluminum oxide grit blasting step were carried out as a preparation step during the spray deposition process. The amount of embedded grit is minimal, as only few grains of aluminum oxide grit are observed in the micrographs shown in Fig 4-41 and Fig 4-42 at the coating-substrate interface. The CoNiCrAlY coating itself exhibits a uniform coating microstructure with less than 1% porosity confirming to typical high quality HVOF coatings similar to other reports in the literature [Itoh et al., 2000].

It should be noted that the spray parameters used in the HVOF process for this study was optimized using standard stainless steel test coupons for microstructure, hardness and bond strength prior to spraying this test coupons. The spray parameters used also resulted in a coating with negligible amounts of globular or unmelted particles due to excellent splat formation and inter-bonding between the splats. The presence of oxides and oxide stringers were also found negligible in this coating again typical in a good HVOF sprayed MCrAlY coating [Lugscheider et al., 1998]. However, it is known that HVOF coatings consists of finely dispersed oxide within the coating akin to oxide dispersed Superalloys (ODS) as the inflight particles during the spray deposition process gets oxidized on the surface prior to depositing onto the substrate, such oxides are not visible in the optical micrographs. It has been pointed out that the combined effect of Al_2O_3 and Yttrium oxide dispersions within the MCrAlY coatings promotes faster transformation of undesirable meta-stable alumina to

α- Al_2O_3. It is desirable to promote formation of α- Al_2O_3 within the coating as it helps in reducing the oxidation rate [Toma et al., 1999].

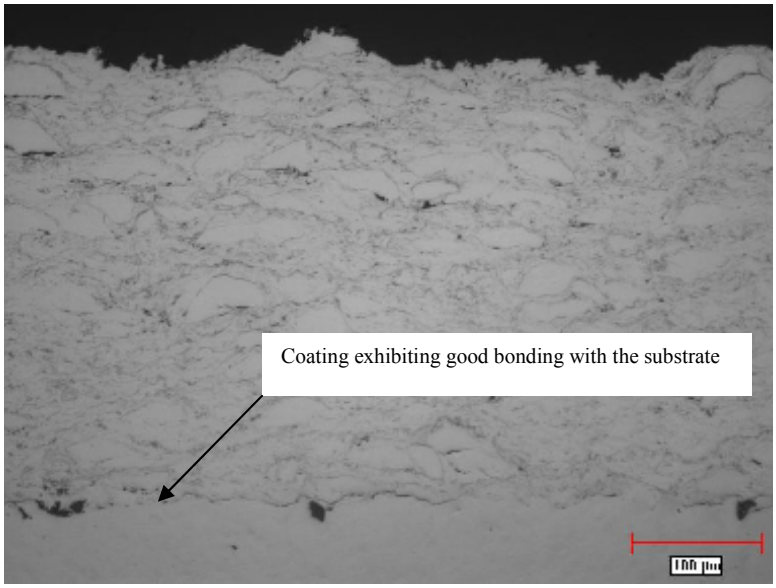

Figure 4-42 As sprayed 718 coating on Incoloy 909 substrate

The 909 alloy coated with 718 coating exhibited coating separation but relatively to a lesser extent of separation compared to CoNiCrAlY coating. An optical micrograph showing a field with a good interfacial bonding is shown in Fig 4-42 and poor coating integrity with coating separation in Fig 4-43.

The 718 alloy coated with CoNiCrAlY and 718 coating did not show any evidence of extensive separation as observed on 909 substrate.

While both the coatings on alloy 909 exhibited dense void free microstructure, the 718 coating exhibited some oxidation especially on the splat interfaces and splat flattening was relatively poor compared to the CoNiCrAlY coating.

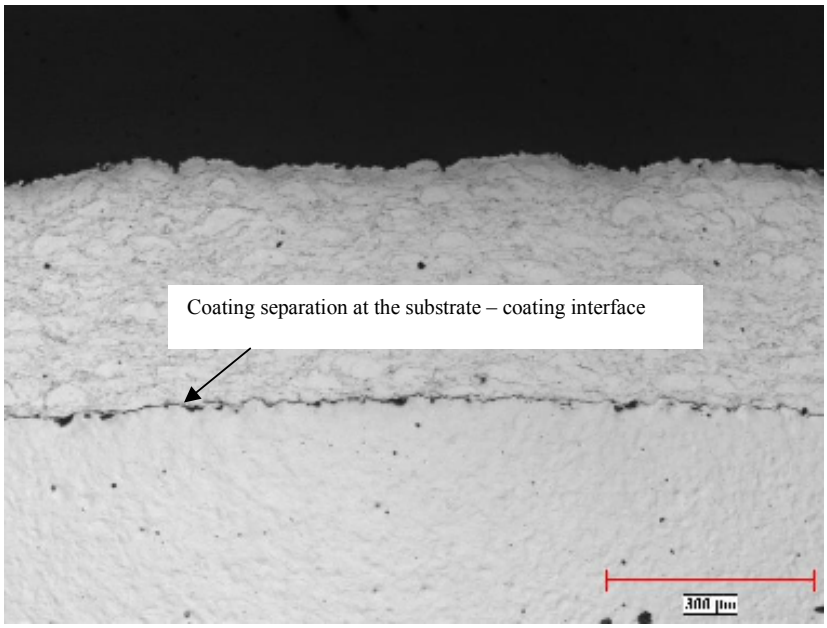

Figure 4-43 As sprayed 718 coating on Incoloy 909 substrate

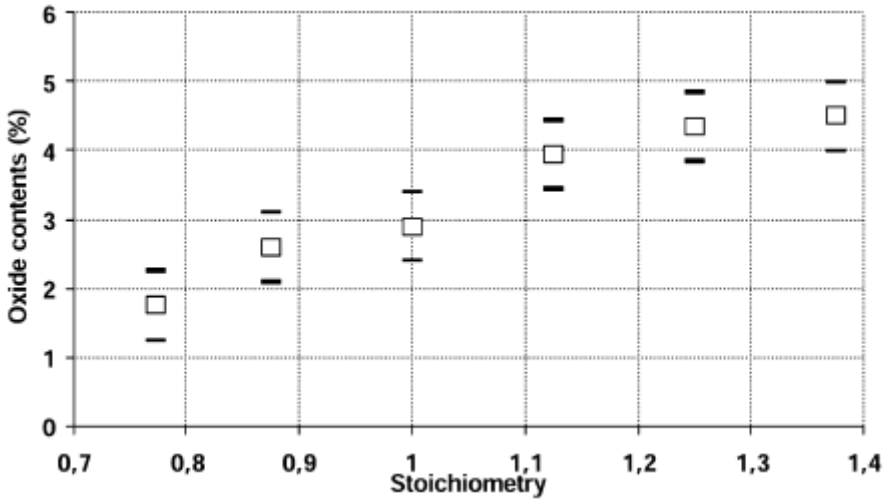

Figure 4-44 Oxide content vs. Stoichiometry (oxygen:fuel ratio) in HVOF sprayed 718 coating . [Planche et al, 2002] (Reproduced with permission from Elsevier)

Most gas turbine manufacturers limit such oxide stringers by imposing a maximum length for coating acceptance, but the coatings microstructure observed in this research are not classified as oxide stringers, since these oxides are characterized by narrow width and short length. The melting range for 718 is typically between 1260-1335°C [Tellkamp et al., 1997]. The HVOF spraying process is capable of producing a combustion temperature of about 2000-2500°C, but the actual heating time of the powder will be a fraction of a second. Due to the short heating time, only smaller particles will likely be fully melted or soft enough to flatten completely on impact with the target substrate. The larger particles will be melted on the surface and due to unmelted core may not form completely flattened splats. A schematic of the heated particle depending upon the size will consists of various zones: a fully molten, liquid shell (L), a solid, unmelted core (UM) and a semi-solid region (SS) caused during the in flight melting process as detailed in Chapter 2 [Zhang et al., 2003]. It can be reasoned that the splats that are oxidized prior to impinging against the coated surface are expected to have poor wetting characteristics [Sobolev et al., 1999] and exhibits higher thermal resistance, which leads to increased splat thickness and porosity within the inter-splat area.

It can also be observed that CoNiCrAlY coating resulted in better coating microstructure compared to the 718 coating microstructure in terms of lower oxidation and relatively lower amount of globular particles. This effect can be attributed to relatively smaller particles size distribution of CoNiCrAlY powder compared with 718 powders. Evidence of fine extremely dense coatings with hardly any globular particles were reported to be obtained by using finer

powder size distribution in air plasma spray process due to complete melting of the powder prior to deposition [Varacalle et al., 1995].

Planche et al., [Planche et al., 2002] reported an increase in oxide content with increase in oxygen / fuel ratio for HVOF sprayed 718 coating as shown in Fig 4-44. In the present study, the fuel is Kerosene compared to natural gas used by Planche, hence variations are expected. The stoichiometry used in this study is 1:1 and the oxide content is 2-3%, which is in good agreement with the results published by Planche et al., even though the fuel and the equipment are different. In general a fine balance between optimum velocity and combustion temperature are vital to get good quality coating.

The alloy 718 coated with CoNiCrAlY and 718 coating on Alloy 718 as shown in Fig 4-45 and Fig 4-46 (a: Low magnification and b: High magnification optical micrograph) respectively does not show any evidence of separation when compared to poor integrity exhibited by the coatings on 909 substrate. It is likely that similar coefficient of thermal expansion of the substrate and the coatings contribute to the good integrity of the coatings on alloy 718 substrate.

`

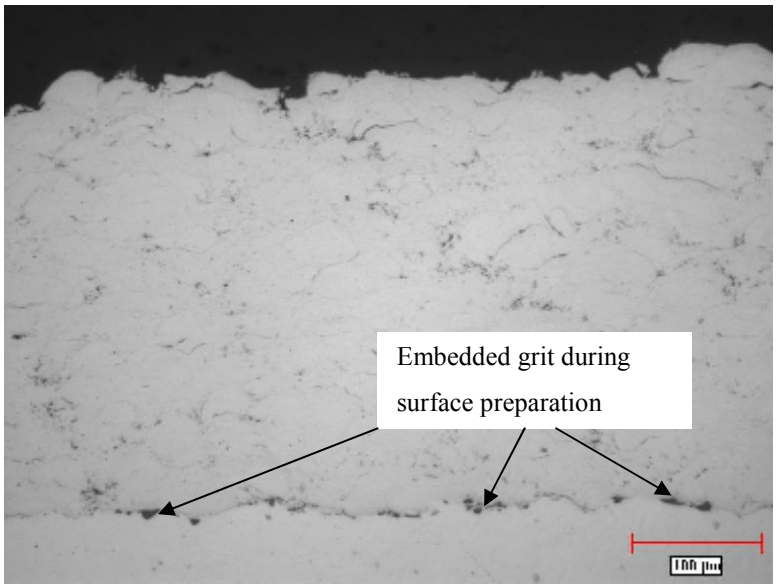

Figure 4-45 As sprayed Alloy 718 with CoNiCrAlY coating

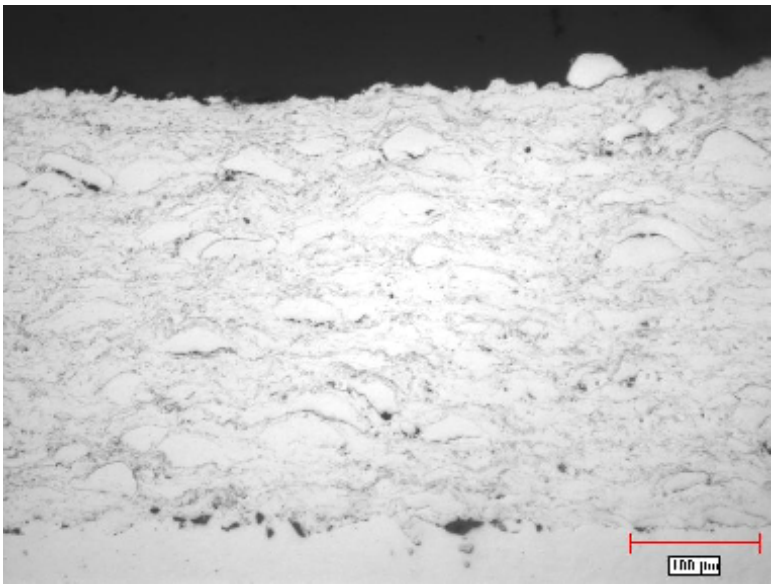

Figure 4-46 As sprayed Incoloy 718 with 718 coating

4.8.2 Isothermal oxidation test

4.8.2.1 704°C for 250 Hours

The oxide scale morphology of bare Incoloy 909 was examined in detail by observing the cross section of the oxidized specimens under an optical microscope at low and high magnification as shown in Fig 4-47 (a: Low magnification and b: High magnification optical micrograph). The oxide scale was continuous consisting of both internal and external scale. Even at 250 hours hold time there is evidence of spallation of the loosely held external scale. It can be clearly observed that the oxide scale consists of two distinguishable colors, the outer scale being dark with hardly any bright phases, while the relatively adherent internal scale is observed to consist of bright metallic color indicating presence of phases yet to be oxidized completely. The external scale was observed to be cracked and about to spall off. The thickness of the dark and bright phase scales are almost of equal thickness with each layer measuring about 30 μm. The morphology of the scale was similar to the one in found in the literature [Kusabiraki et al., 1997] except Kusabiraki et al., studied the oxidation characteristics in flowing Argon and water vapor atmosphere. The internal scale grew by the diffusion of oxygen into the alloy as the oxidation progresses. An external scale grew by the diffusion of metallic elements toward the atmosphere. The morphology of these scales are observed to similar to the scale formed in Ni-Fe alloys found in the literature [Menzies et al., , 1971; Tomlinson et al., 1978].

Bare alloy 718 exhibits negligible oxide scales as observed in Fig 4-48 and Fig 4-49 . This is consistent with the reports in literature [Jian et al, 2000] as the presence of chromium in

alloy 718 offers excellent oxidation resistance within the normal service temperature range of 500-700°C.

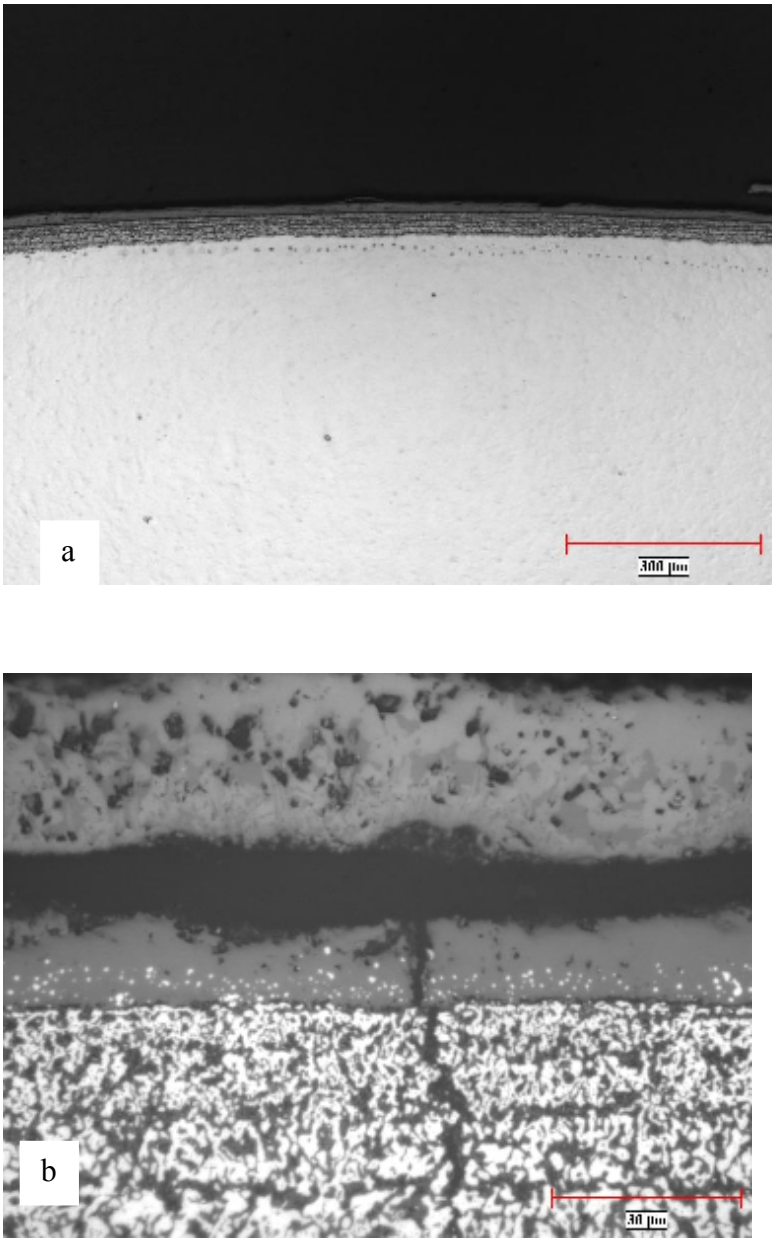

Figure 4-47 (a) Low magnification and (b) High magnification optical micrograph of furnace exposed bare 909 at 704°C for 250 hours

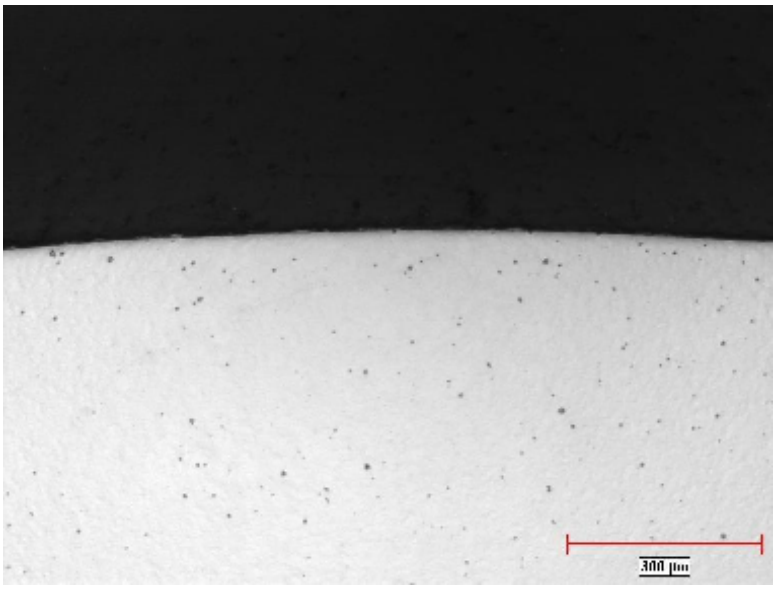

Figure 4-48 Furnace exposed bare 718 at 704°C for 250 hours

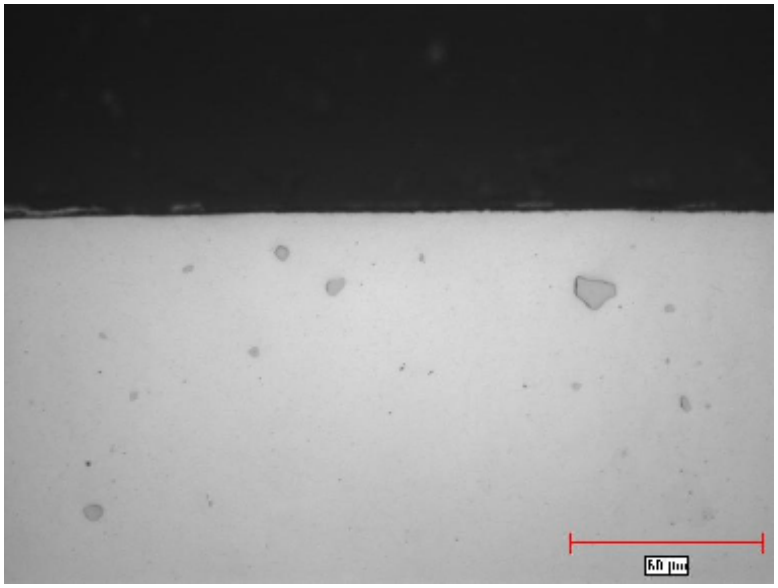

Figure 4-49 Furnace exposed bare 718 at 704°C for 250 hours

The HVOF CoNiCrAlY coating on alloy 909 substrate showed extensive coating separation to approx. 50% of the circumference of the rod. An optical micrograph showing one such field containing completely separated coating is shown in Fig 4-50 (a: Low magnification and b: High magnification optical micrograph).

The HVOF 718 coating on alloy 909 substrate also exhibited coating separation but relatively lesser extent of separation compared with the CoNiCrAlY coating. An optical micrograph showing a field with a good interfacial bonding is shown in Fig 4-51 (a: Low magnification and b: High magnification).

The HVOF CoNiCrAlY coating and 718 coating on alloy 718 substrate as shown respectively in Fig 4-52 (a: Low magnification and b: High magnification optical micrograph) and Fig 4-53 did not show any evidence of separation as observed on the 909 substrate. The identical nature of chemical composition of the coating and substrate could be a likely factor for the excellent compatibility between 718 coating and 718 substrate. Other important factors such as thermal expansion characteristics and adhesion characteristics are likely to play a beneficial role in the compatibility between the 718 coating and alloy 718 substrate.

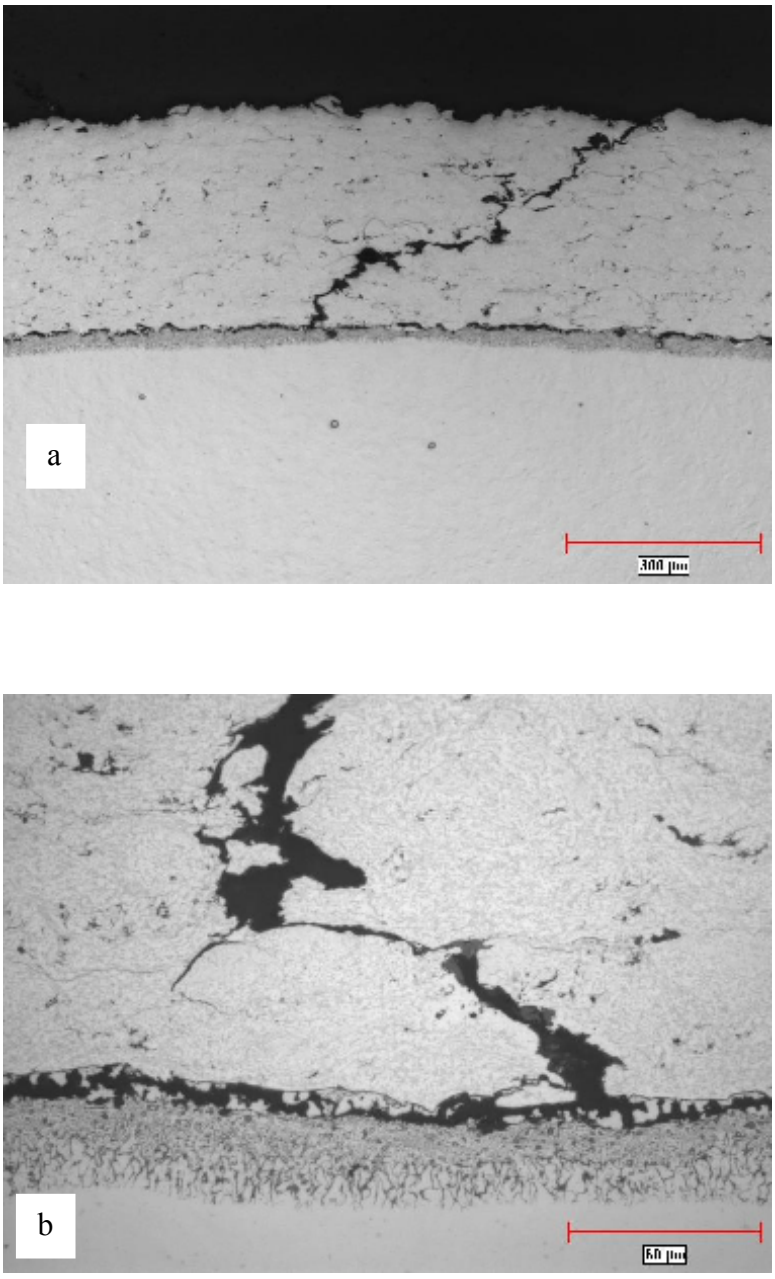

Figure 4-50 (a) Low magnification and (b) High magnification optical micrograph of furnace exposed CoNiCrAlY coated 909 at 704°C for 250 hours

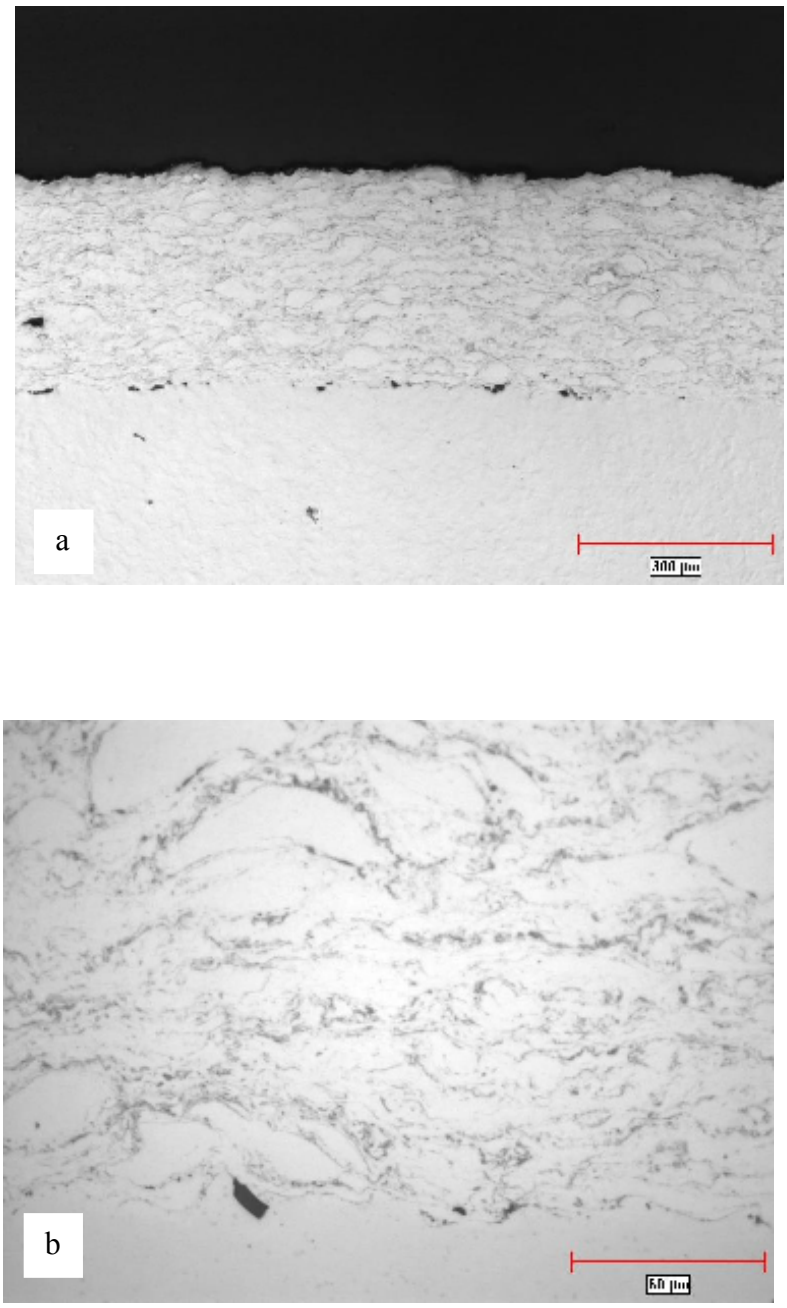

Figure 4-51(a) Low magnification and (b) High magnification optical micrograph of Furnace exposed 718 coated on 909 at 704°C for 250 hours

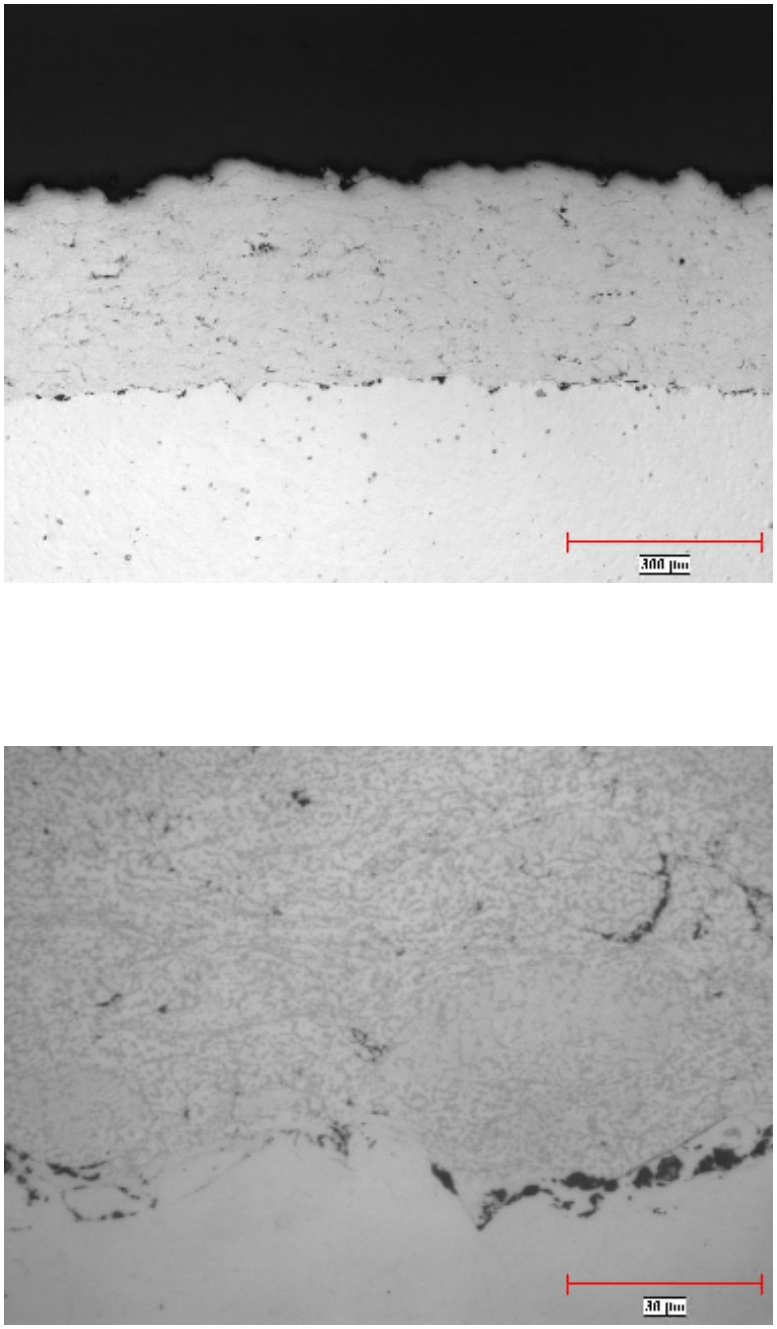

Figure 4-52 (a) Low magnification and (b) High magnification optical micrograph of furnace exposed CoNiCrAlY coated 718 at 704°C for 250 hours

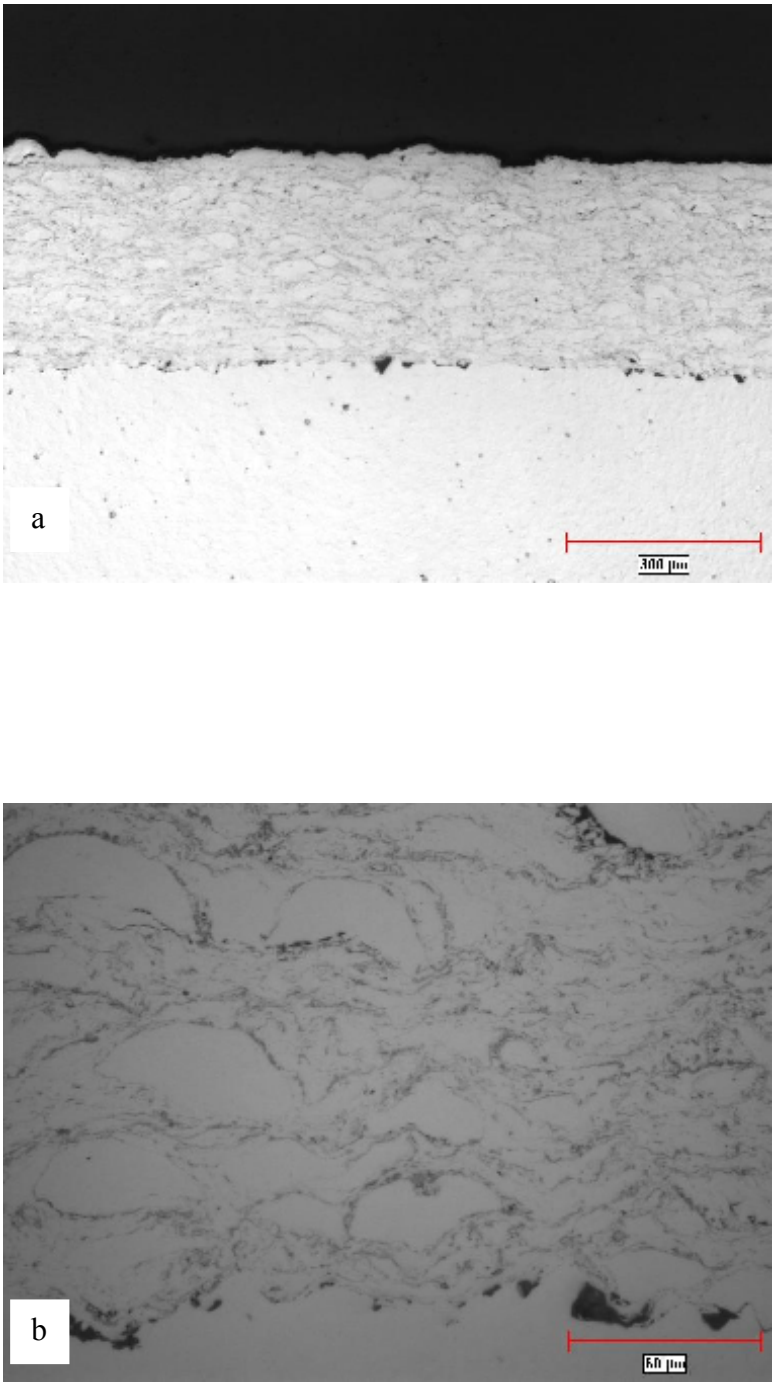

Figure 4-53 (a) Low magnification and (b) High magnification optical micrograph of furnace exposed 718 coated 718 alloy at 704°C for 250 hours

4.8.2.2 704°C for 500 Hours

The oxide scale morphology of bare base alloy 909 was examined by observing the cross section of the oxidized specimen under the optical microscope as shown in Fig 4-54. It is evident from that Fig 4-54, that the oxide scale is continuous, and is observed to have grown thicker compared to the 250 hours exposure time. The oxide scale consisted of both internal and external scale. The dark and bright phase scales are almost of equal thickness with each layer measuring about 40 μm, compared to about 30 μm each with 250 hours exposure time. This oxide scale growth further confirms that the scale does not act as an effective barrier against further internal and external oxidation. The morphology of the scale was observed to be similar to that observed in 250 exposure time. The morphology of these scales are observed to similar to the scale formed in Ni-Fe alloys found in the literature [Menzies et al., 1971; Tomlinson et al., 1978].

The cross section of the bare 718 alloy is shown in Fig 4-55. It is evident that this extended furnace exposure of 500 hours hold time results in negligible amount of oxide scale, and was difficult to identify under the optical microscope. Wang et al., [Wang et al., 2006] observed depletion of Aluminum on the surface which resulted in the formation of the γ phase during investigation of cyclic oxidation characteristics of a coated Inconel 718 at 1100°C after 240 cycles. The likely reason for absence of such dealloyed zone in this research is due to the substantially lower temperature of 704°C used in this research compared to 1100°C used in the literature [Wang et al., 2006].

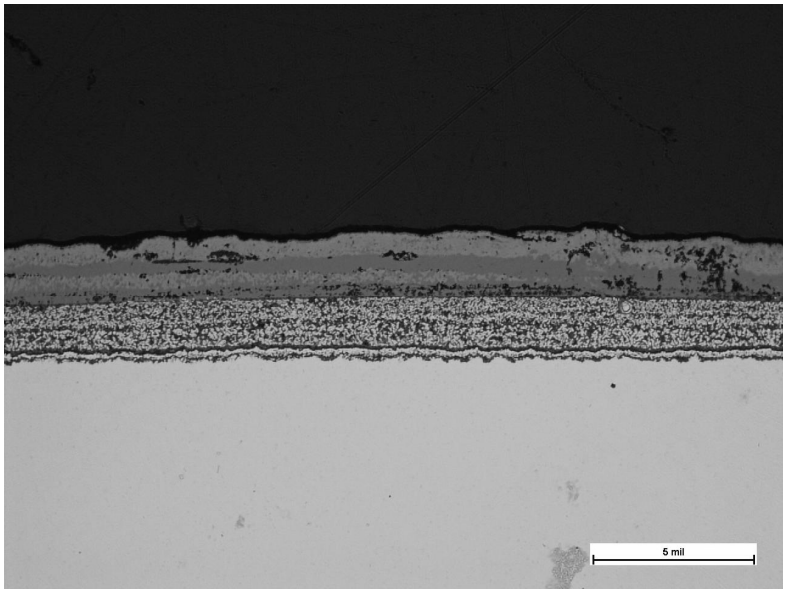

Figure 4-54 Furnace exposed 909 bare alloy at 704°C for 500 hours(Scale 127μm)

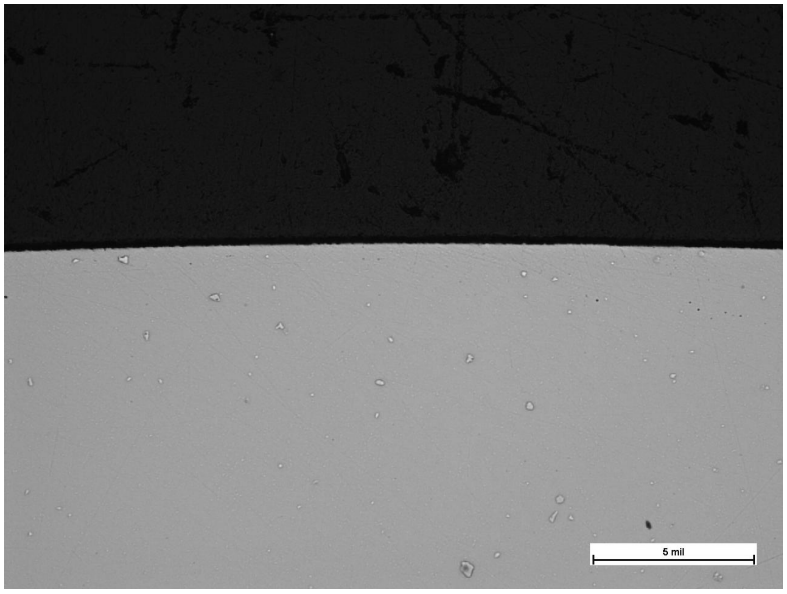

Figure 4-55 Furnace exposed 718 bare alloy at 704°C for 500 hours(Scale 127μm)

The presence of negligible amounts of oxide scale on 718 exposed to elevated temperature in this study confirms with earlier observation by Jian et al [Jian et al., 2000].

It is evident from Fig 4-56 that CoNiCrAlY coating is separated and cracked thereby exhibiting poor integrity on the alloy 909 substrate. It can be seen that the substrate oxidized via the crack through the coating to the substrate coating interface, thereby offering little barrier protection to the surface of the substrate. Alloy 909 with poor coating integrity results in formation of both internal and external oxidation. The presence of a relatively thicker oxide scales on the substrate confirms that coating cracks and separation occurred even prior to furnace exposure. Locations where the coating was found adhering to the substrate were however found well protected with little evidence of any oxide scales.

It can be observed from Fig 4-57 that although 718 coating demonstrates some coating separation, it was found to exhibit better integrity than the CoNiCrAlY coating on alloy 909 substrate. This coating provides partial protection, as the thickness oxide scale on the 909 substrate is less compared to the thicker oxide scale present in the case of CoNiCrAlY coating on the 718 substrate. It can be ascertained that the HVOF sprayed coatings exhibited excellent bonding on Alloy 718 substrate for both CoNiCrAlY and 718 coating as shown in Fig 4-58 and 4-59 respectively. The possible factors for such excellent integrity is likely due to factors (i) CTE of the substrate and the coating are similar and (ii) 718 does not get easily get oxidized on the surface when exposed to heat thereby the wetting characteristics for the coating and substrate may not be affected due to the thin oxide scale .

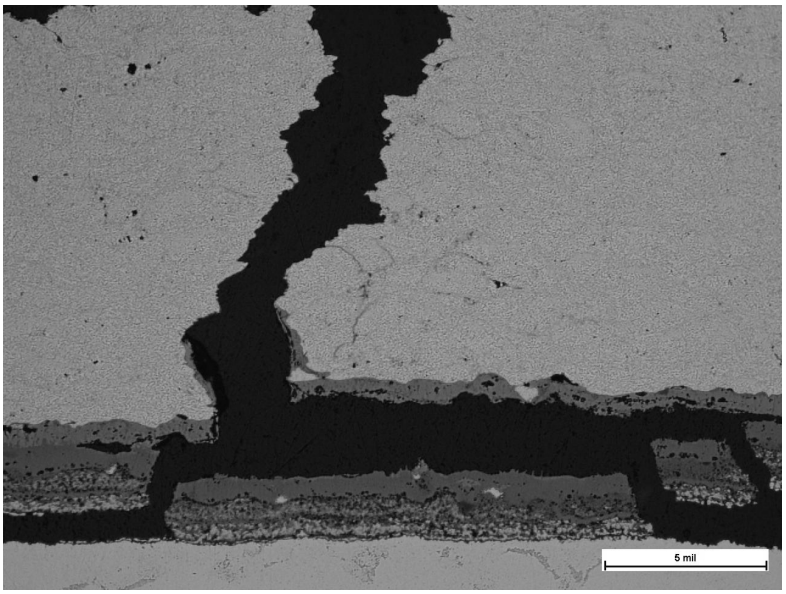

Figure 4-56 Furnace exposed 909 with CoNiCrAlY coating at 704°C for 500 hours(Scale 127μm)

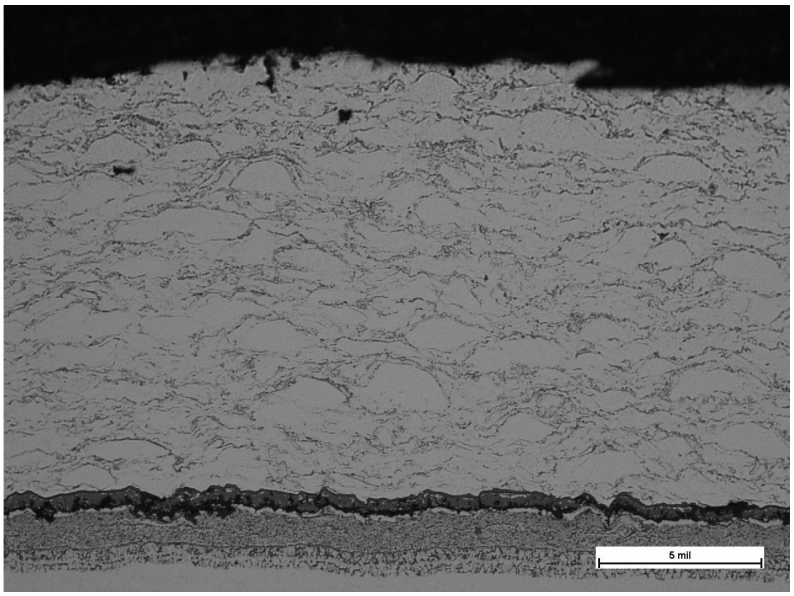

Figure 4-57 Furnace exposed 909 with 718 coating at 704°C for 500 hours(Scale 127μm)

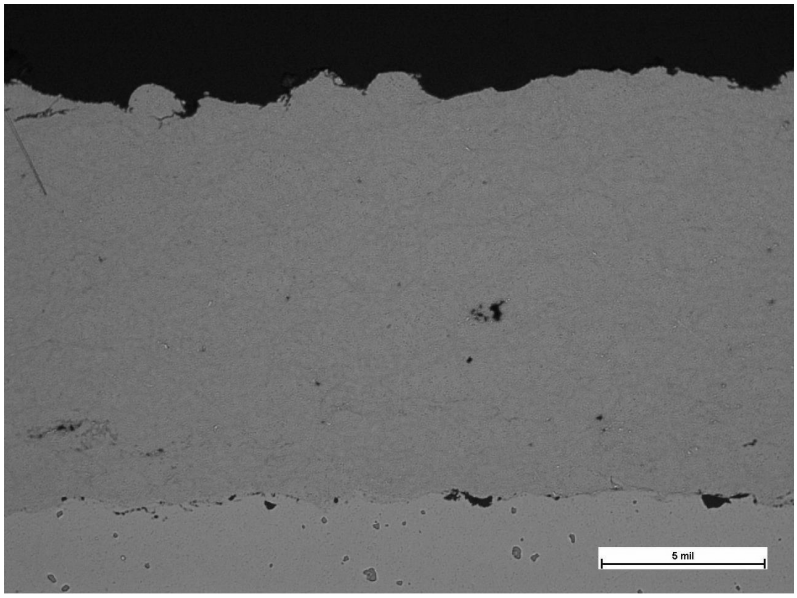

Figure 4-58 Furnace exposed 718 with CoNiCrAlY coating at 704°C for 500 hours(Scale 127μm)

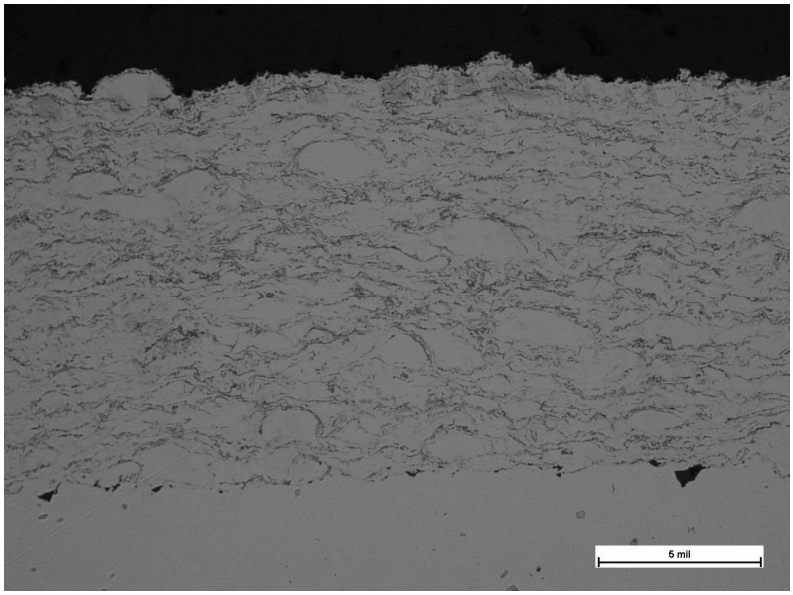

Figure 4-59 Furnace exposed 718 with 718 coating at 704°C for 500 hours(Scale 127μm)

4.8.2.3 704°C for 750 Hours

The cross section details of an oxidized bare alloy 909 specimen exposed for a duration of 750 hours in a furnace at 704°C is shown in Fig 4-60. This micrograph reveals that a portion of the external oxide scale has started spalling. The relatively thicker oxide scale growth further confirms that the barrier properties of this scale is poor and also the external scale was observed to exhibit poor adhesion characteristics. As detailed in the literature review section, previous research have shown that absence of Cr, Al and Si in sufficient amounts in Incoloy 909 increased the susceptibility to elevated temperature oxidation. The CoNiCrAlY coating separated and cracked on the alloy 909 substrate as observed in Fig 4-61 resulting in poor protection of the substrate. The oxide scale can be observed between the coating and the substrate as the cracks allow free access of oxygen to the interface region providing little barrier to prevent formation of oxide scales on alloy 909 substrate surface. The separation and cracking of this CoNiCrAlY coating were found to be similar with preceding furnace exposed conditions.

An optical micrograph of 718 coated on alloy 909 is shown in Fig 4-62 (a: Low magnification and b: High magnification optical micrograph). The coating exhibited good bonding and integrity on the 909 substrate. However in the previous condition (500 hours), it can be seen that 718 coating exhibited poor integrity on 909 substrate. It is also apparent that the magnitude of separation and cracking of 718 coating is relatively less than CoNiCrAlY coating on 909. Both the coatings (CoNiCrAlY and 718) were found to reveal excellent integrity on alloy 718 substrate similar to previous conditions.

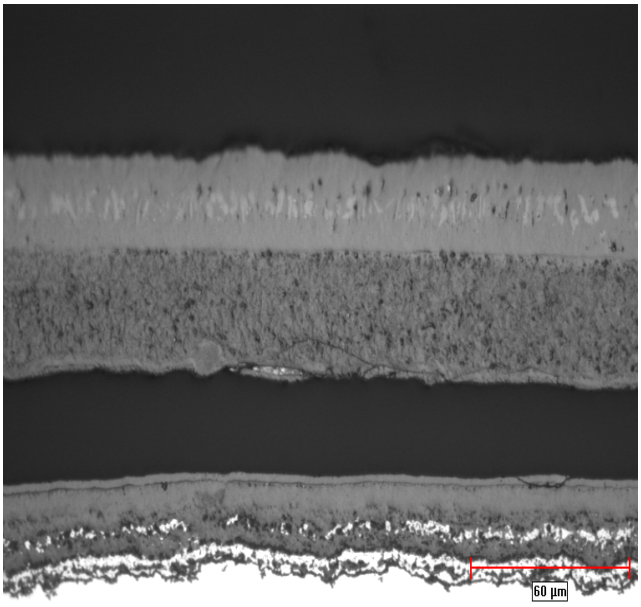

Figure 4-60 Furnace exposed bare 909 at 704°C for 750 hours

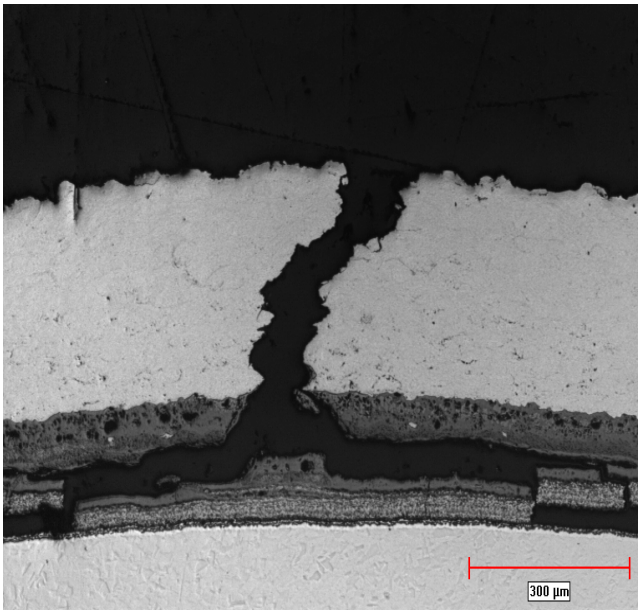

Figure 4-61 Furnace exposed 909 with CoNiCrAlY coating at 704°C for 750 hours

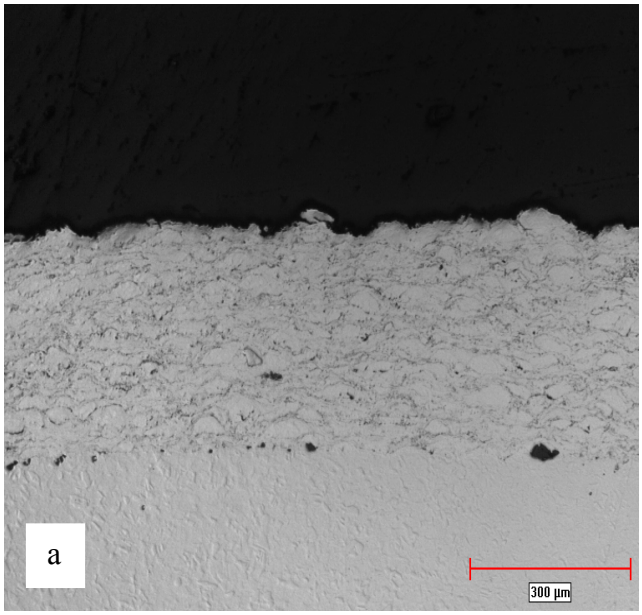

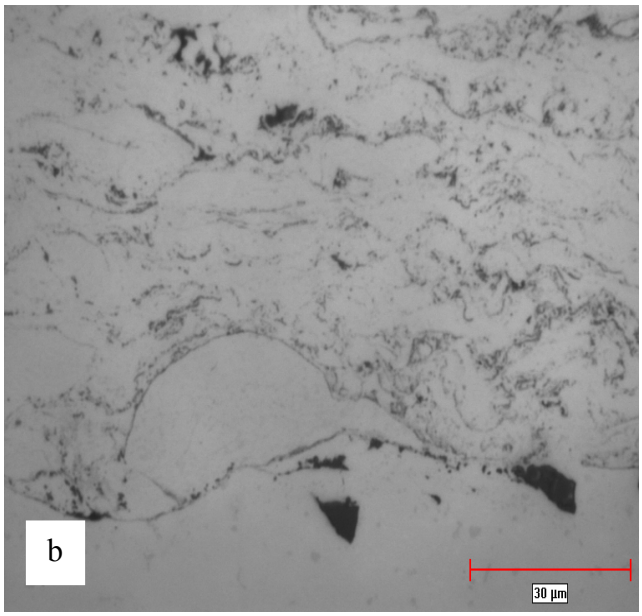

Figure 4-62: (a) Low magnification and (b) High magnification optical micrograph of furnace exposed 909 with 718 coating at 704°C for 750 hours

4.8.2.4 704°C for 1000 Hours

The oxide scale morphology observed in optical micrograph of bare alloy 909 (Fig 4-63) consisted of internal and external oxidation, very similar to the heat treatment at shorter times. In line with the previous observations, the scale growth takes place unimpeded with increasing exposure time, with the external and internal oxide thickness each measuring about 60μm.

The bare alloy 718 specimen even after 1000 hours furnace exposure did not show appreciable amount of external or internal oxidation (Fig 4-64 and Fig 4-65), which is consistent with previous conditions and finding of Jian et al [Jian et al., 2000]. The cracked and separated CoNiCrAlY coating on the alloy 909 substrate exhibits poor adhesion similar to previous conditions (Fig 4-66). It can be ascertained that CoNiCrAlY coating consistently failed to exhibit good integrity on the alloy 909 substrate confirming its incompatibility. The coating does not provide oxidation barrier properties due to poor integrity leading to oxidation of the alloy 909 substrate. To understand the exact mechanism behind this failure, further investigation on ductility, CTE of the substrate and coating, coating bond strength, effect of residual stresses with increase in coating thickness and presence of any oxide scales on the substrate surface prior to coating deposition are required. The results of these factors are presented in the later part of this dissertation.

The 718 coating as shown in Fig 4-67, did not separate or crack thereby exhibiting comparatively better integrity than CoNiCrAlY coating on the alloy 909 substrate. Overall, the compatibility of 718 coating is relatively better than the CoNiCrAlY coating on the alloy 909 substrate. The HVOF sprayed coatings exhibited excellent bonding on the alloy 718 substrate for both CoNiCrAlY coating and 718 coating as observed with previous conditions.

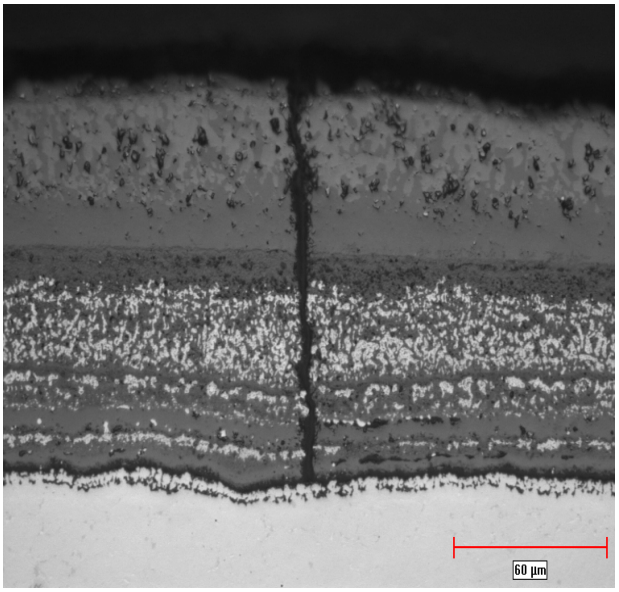

Figure 4-63 Furnace exposed 909 bare alloy at 704°C for 1000 hours

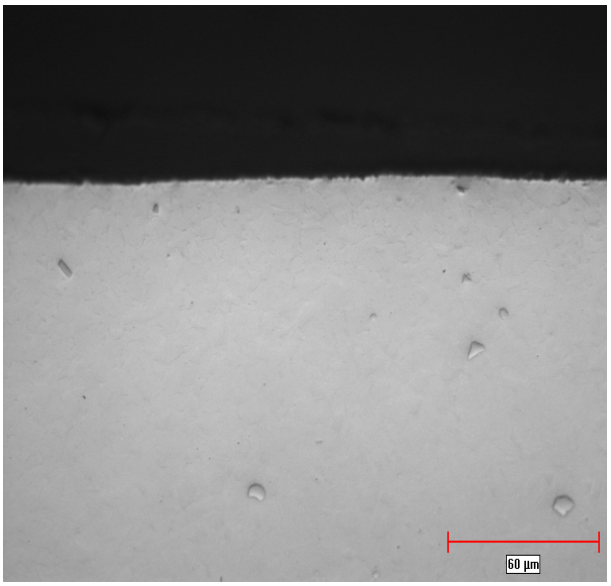

Figure 4-64 Furnace exposed 718 bare alloy at 704°C for 1000 hours

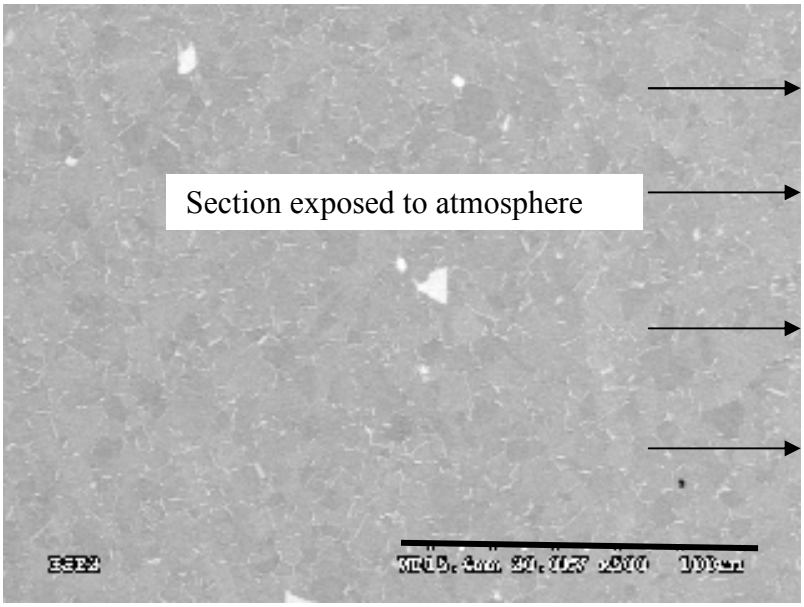

Figure 4-65 Bare Alloy 718 after exposure at 704°C for 1000 Hrs

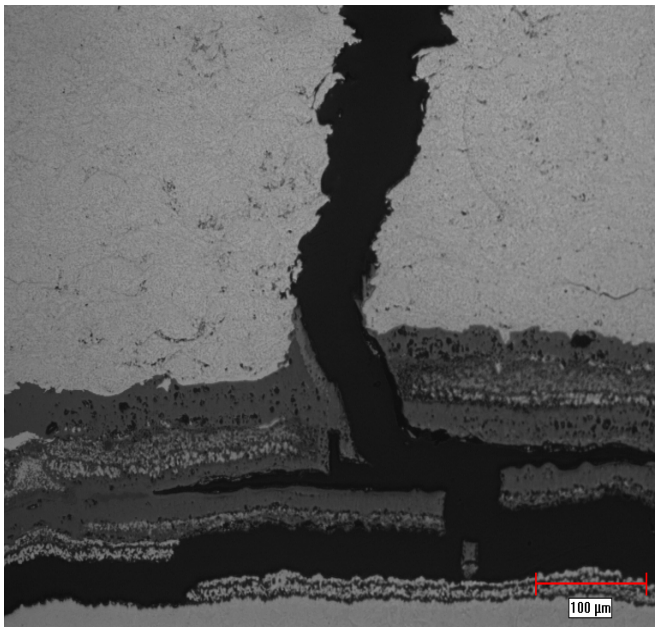

Figure 4-66 CoNiCrAlY coating exposed at 704°C for 1000 hours

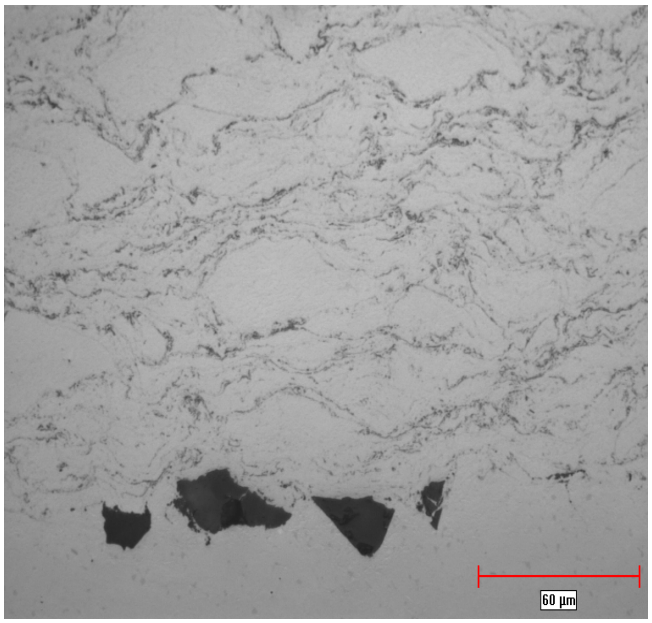

Figure 4-67 Alloy 909 with 718 coating exposed to 704°C for 1000 hours

4.9 SEM-EDS Analysis

4.9.1 Incoloy 909 exposed at 704°C for 1000 Hours

The cross section of a furnace oxidized bare alloy 909 for a hold time of 1000 hours at 704°C was investigated using SEM-EDS analysis. X-ray mapping was performed on the entire area of cross section as shown in Fig 4-68 and elemental maps in Fig 4-69. It is evident from this micrograph that the oxidized region is composed of intergranular oxidation, intragranular oxidation and external scale composed of an ash white region and grey scales from the alloy surface outwards to the atmosphere. In Fig 4-70, the elemental composition is plotted from locations 1 to 9 as identified in Fig 4-68.

The external scale in the outermost layer on the atmosphere side is found to be rich in Fe and Co from Fig 4-68. It is well known [Kusabiraki et al., 1998] that the external scale growth occur in Ni-Fe alloys due to diffusion transfer of metallic elements (Fe and other elements) towards the outer region exposed to atmosphere. The outer scale is likely composed of Fe_2O_3, and CoO. Fe_2O_3. The internal portion of the external scale is observed to be rich in Fe and Nb. This is likely composed of FeO, Fe_2O_3, Nb_2O_5 and minor amounts of Si and Ti oxides. The intragranular portion of the scale is observed to be rich in Ni, Ti, Si but depleted in Fe and Co. This is likely due to outward diffusion of Fe and Co towards the outermost oxide layer leaving the internal scale depleted in Fe and CO but rich Ni. Hence, the inter and intragranular oxides are likely composed of NiO, Nb_2O_5 and minor amount of titanium oxide.

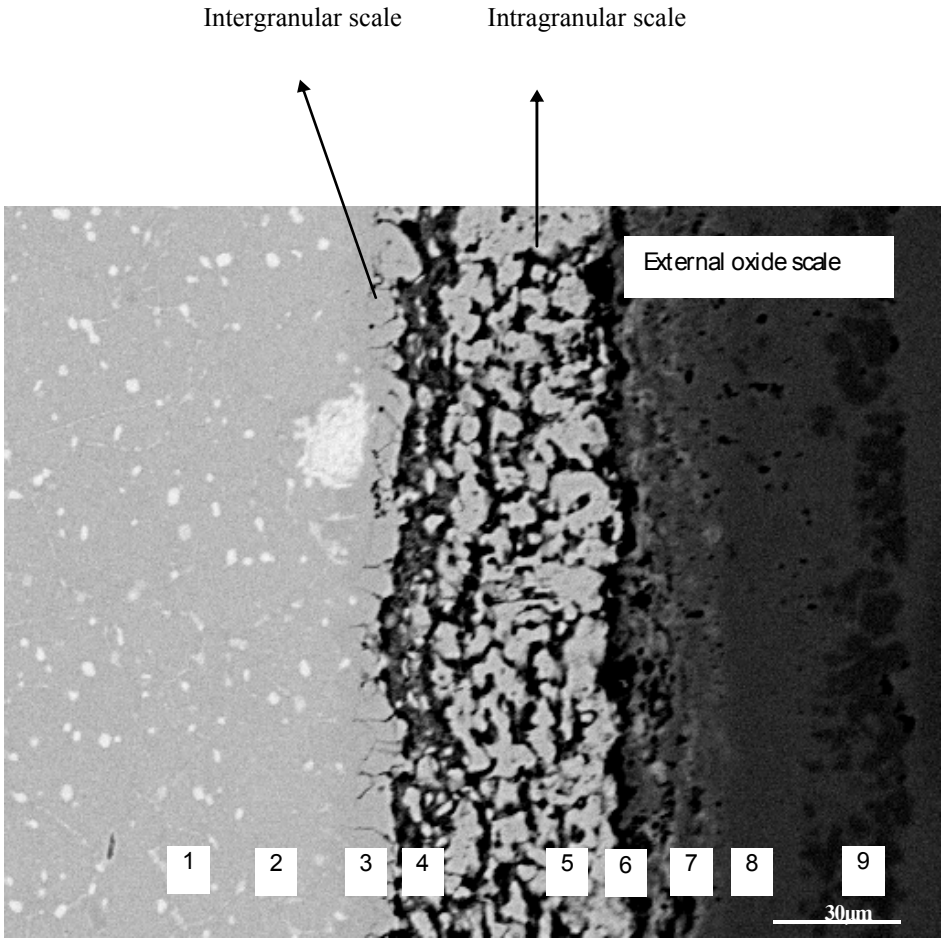

Figure 4-68 Furnace exposed 909 bare alloy at 704°C for 1000 hours

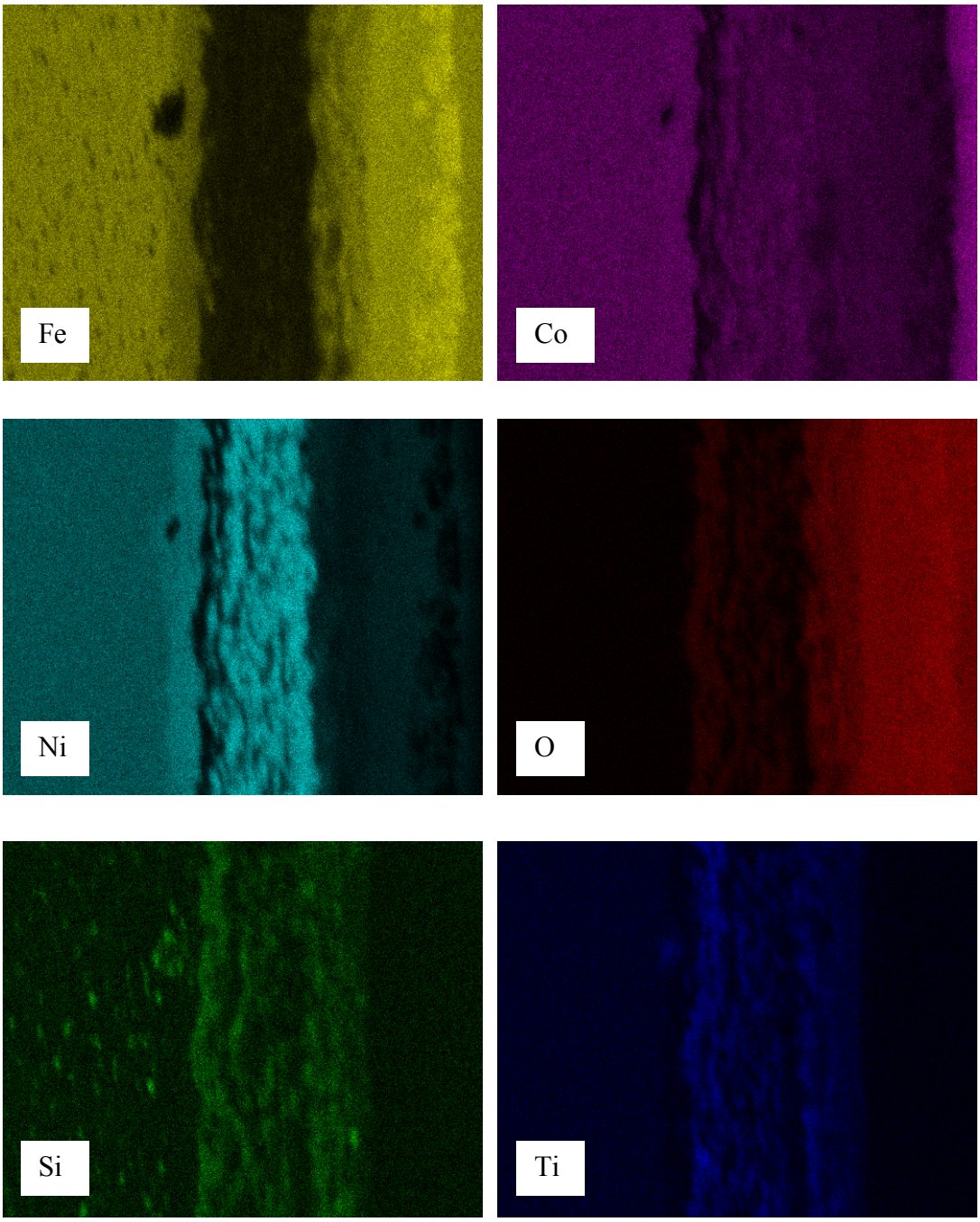

Figure 4-69 Elemental maps for the oxidized alloy shown in previous figure

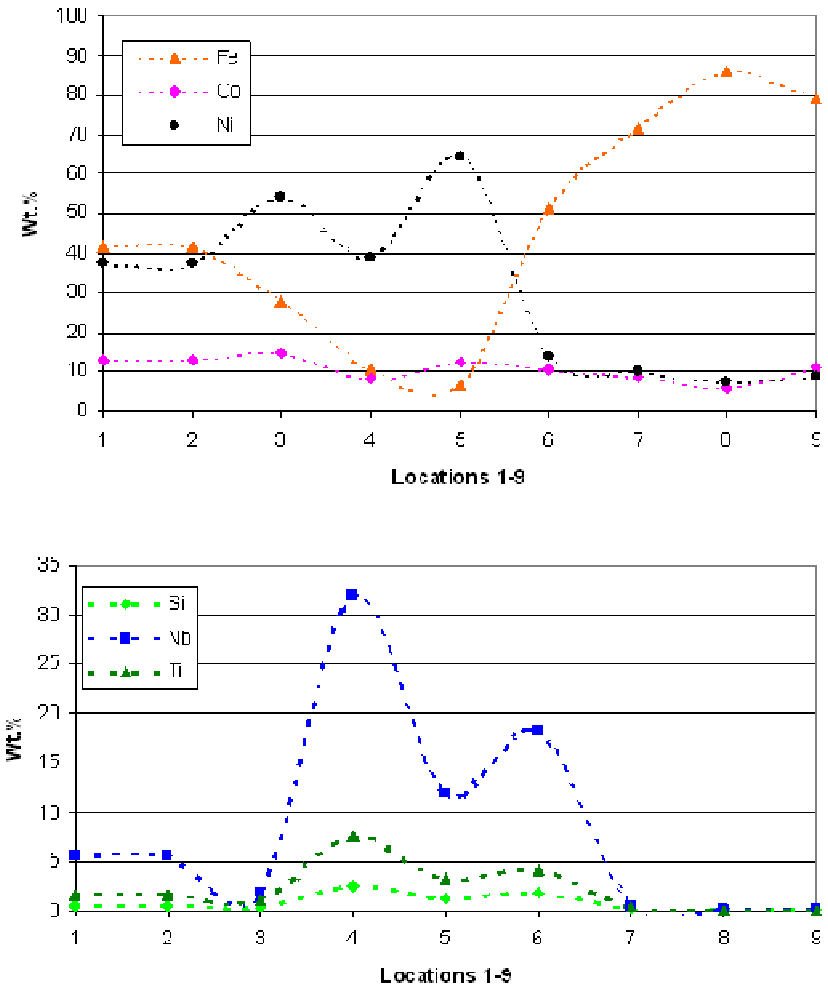

Figure 4-70 (A: Fe, Co, Ni and B: Si, Nb, Ti) Composition of elements at locations 1-9 as shown in Fig 4-69

4.10 Burner Rig Cyclic oxidation

Cyclic oxidation or burner rig testing is used to assess thermal fatigue resistance as this method can closely simulate the actual service conditions due to its rapid heating and cooling exerted on the test coupons. Test methods using burner rigs are often used by researchers for accelerated testing of coatings and substrates to study the behavior of the materials under thermal fatigue environment. In this research cyclic oxidation testing is conducted to compare the bare and coated alloy 909 and 718 with the isothermal furnace oxidation tests.

Fig 4-71 ((a) Low magnification and (b) High magnification optical micrograph) shows the cross section of a of burner rig exposed bare 909 at 704°C for 1000 cycles. A continous oxide scale comprising external and internal oxidized regions can be observed from the higher magnification optical micrograph. The internal oxide is observed to be mostly of intragranular oxidation with the depth ranging about 5 – 15 µm. The external scale is observed to be lighter and darker shades of grey phase with thickness of about 15 µm. The total oxide thickness is observed to be thicker compared to isothermal exposure condition especially considering the actual time at temperature is only 50 hours and total test time including the heating and cooling time is less than 90 hours. The thickness of the oxidized region is likely to be a conservative value, as some amount of scale might have been lost during the impact of the high velocity flame and blowing cooling air. It should be noted that during this heating and cooling cycles a considerable amount of stress is created between the scale and the substrate due to the difference in coefficient of thermal expansion between the oxide scale and the substrate.

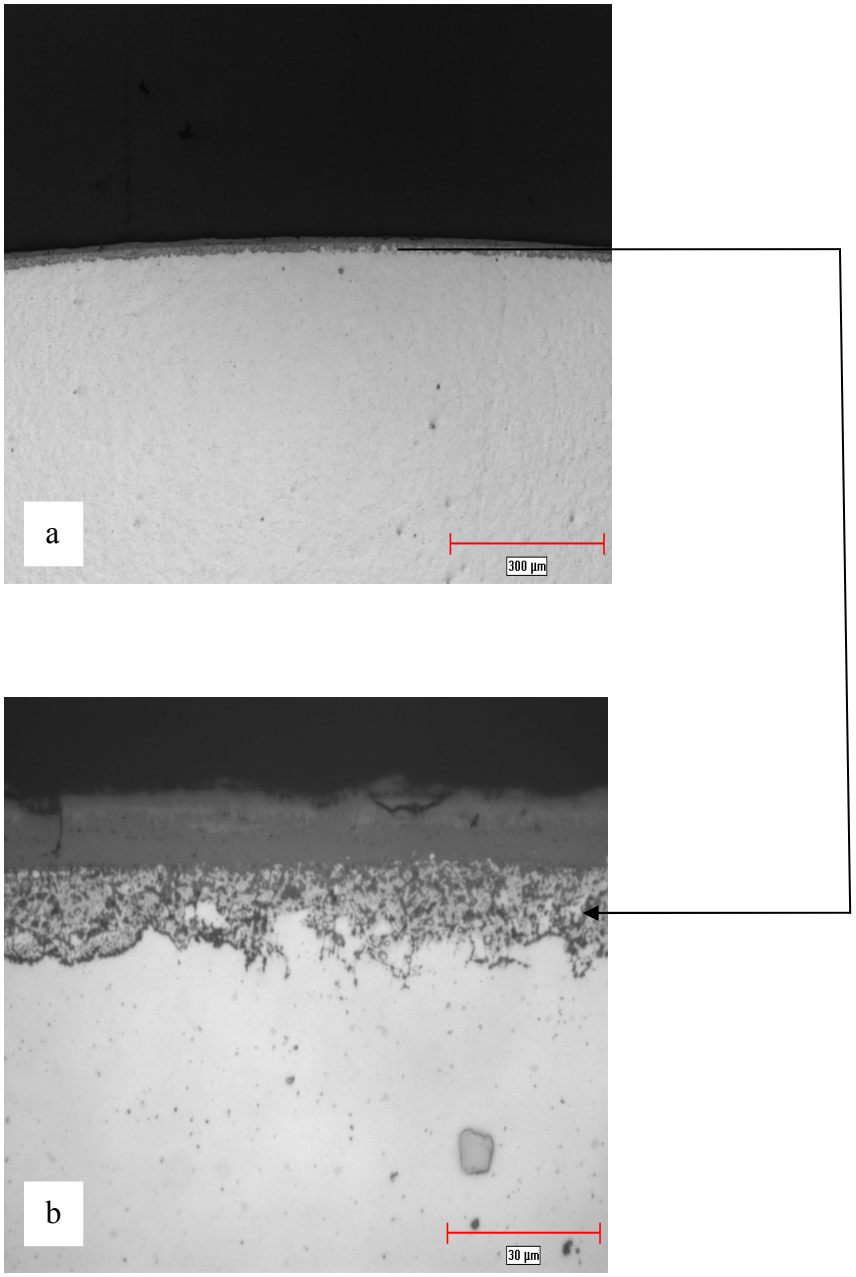

Figure 4-71 (a) Low magnification and (b) High magnification optical micrograph of burner rig exposed bare alloy 909 at 704°C for 1000 cycles

Fig 4-72 ((a) low magnification and (b) high magnification optical micrographs) shows the cross section of a burner rig exposed bare alloy 718. It is remarkable to find a negligible amount of oxide scale even with the cyclic oxidation as most Superalloys exhibit susceptibility to cyclic oxidation due to higher probability of oxide cracks and spallation thereby exposing the underlying substrate to further oxidation. This confirms the robustness of alloy 718 to cyclic oxidation for temperatures up to 704°C for 1000 cycles.

Fig 4-73 ((a) Low magnification (cracks and separation) and (b) High magnification (separation) optical micrographs)shows the cross section of alloy 909 coated with the CoNiCrAlY coating that exhibits cracks and separation as observed in as sprayed condition and isothermal exposure conditions. The optical micrograph clearly shows indication of oxidation on the substrate surface but the thickness of the oxidized region is limited compared to the bare alloy 909.

Similar results exhibiting coating cracking and separation was also observed with 718 coating on alloy 909, but not as extensive as exhibited by CoNiCrAlY coating on this alloy. Fig 4-74 ((a) Low magnification (cracks and separation) and (b) High magnification (cracks and separation) optical micrographs) shows the cross section of alloy 909 coated with 718 coating after burner rig exposure at 704°C for 1000 cycles. The optical micrograph clearly shows indication of oxidation on the substrate surface but the thickness of the oxidized region is limited compared to the bare alloy 909.

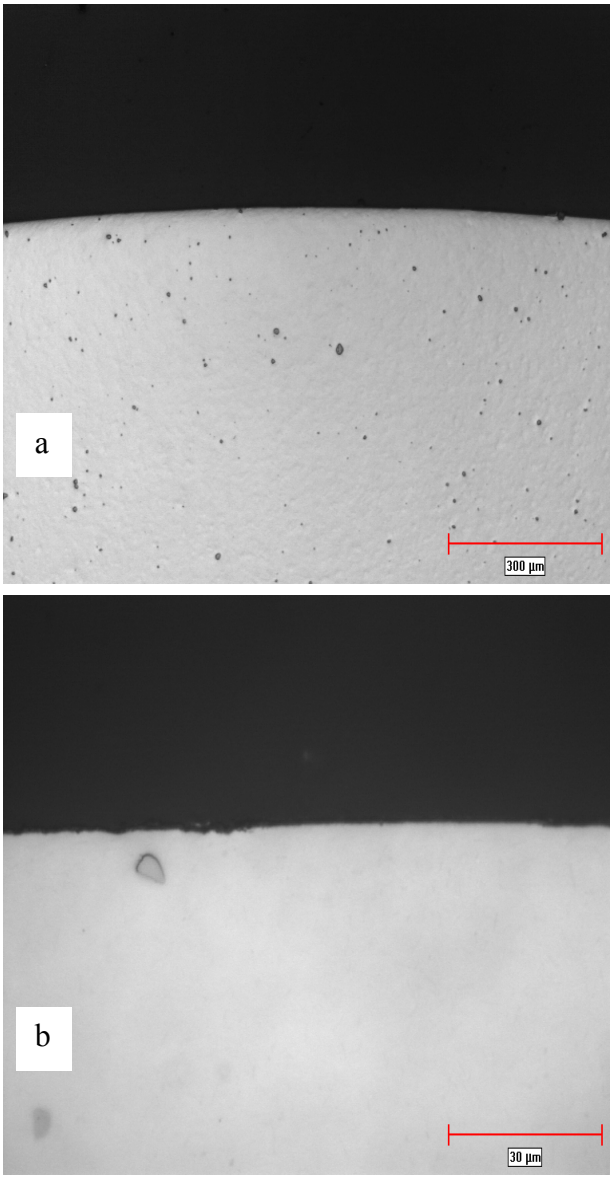

Figure 4-72 (a) Low magnification and (b) High magnification optical micrograph of burner rig exposed bare 718 at 704°C for 1000 cycles

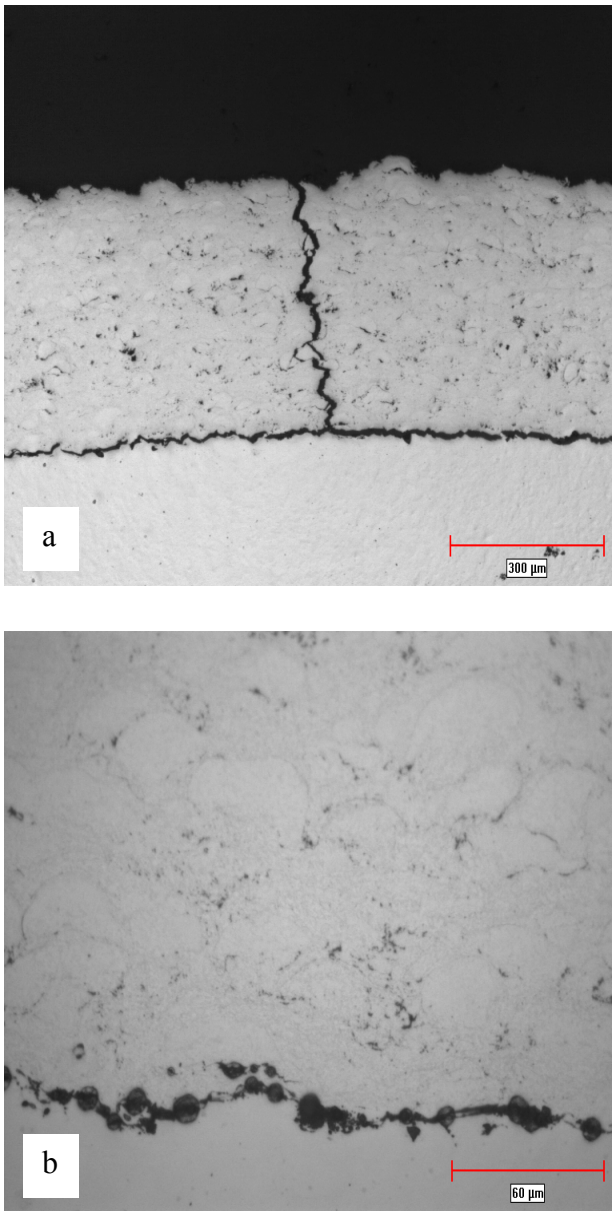

Figure 4-73 (a) Low magnification(cracks and separation) and (b) High magnification (separation) optical micrograph of burner rig exposed 909 with CoNiCrAlY coating at 704°C for 1000 cycles

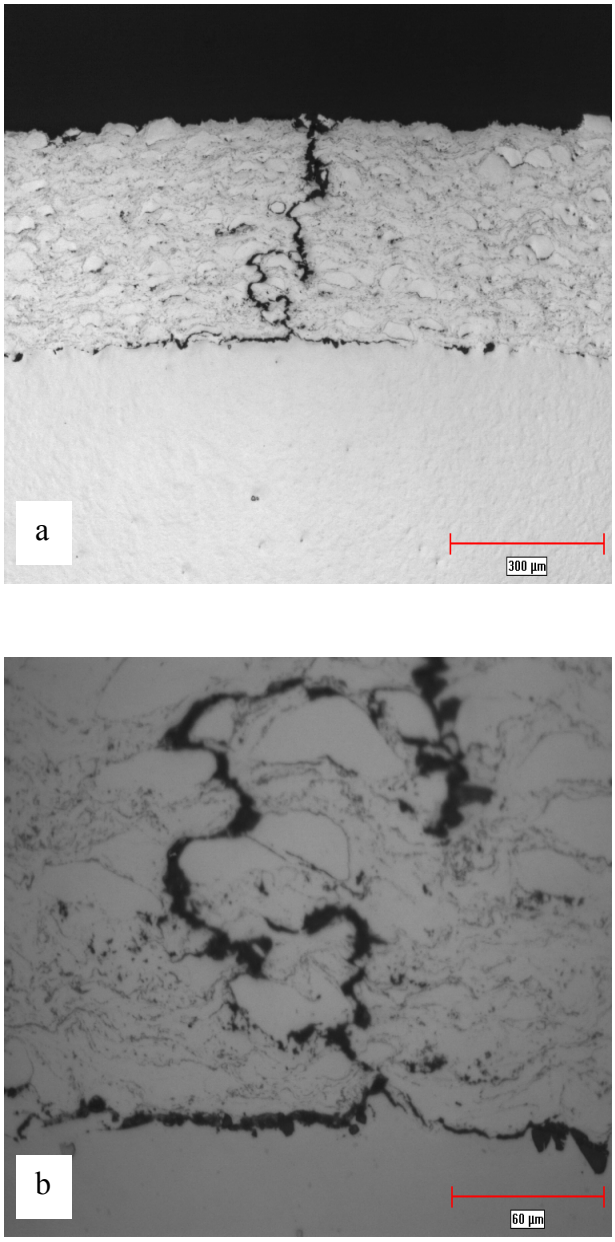

Figure 4-74 (a) Low magnification(cracks and separation) and (b) High magnification (cracks and separation) optical micrograph of burner rig exposed 909 with 718 coating at 704°C for 1000 cycles

Fig. 4-75 ((a) Low magnification and (b) High magnification optical micrographs) shows the cross section of alloy 718 coated with CoNiCrAlY coating that exhibits excellent coating integrity with no indication of separation or cracking as observed in previous conditions. The optical micrographs (a) Low magnification and (b) High magnification clearly shows the absence of oxidation on the substrate or on the coating after burner rig testing at 704°C for 1000 cycles. Very similar results were also observed with 718 coating on alloy 718. Fig 4-76 ((a) Low magnification and (b) High magnification optical micrographs) shows the cross section of alloy 718 coated with 718 coating. It is observed to exhibit excellent coating integrity after burner rig testing with no indication of separation or cracking when compared to the previous condition.

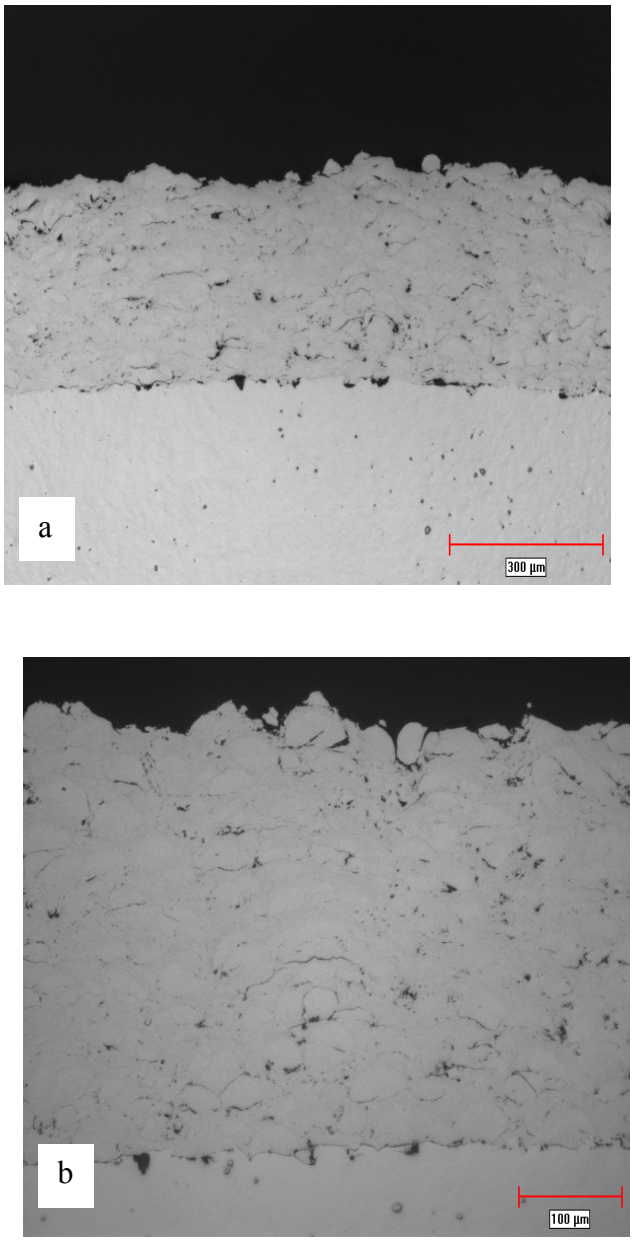

Figure 4-75 (a) Low magnification and (b) High magnification optical micrograph of burner rig exposed 718 with CoNiCrAlY coating at 704°C for 1000 cycles

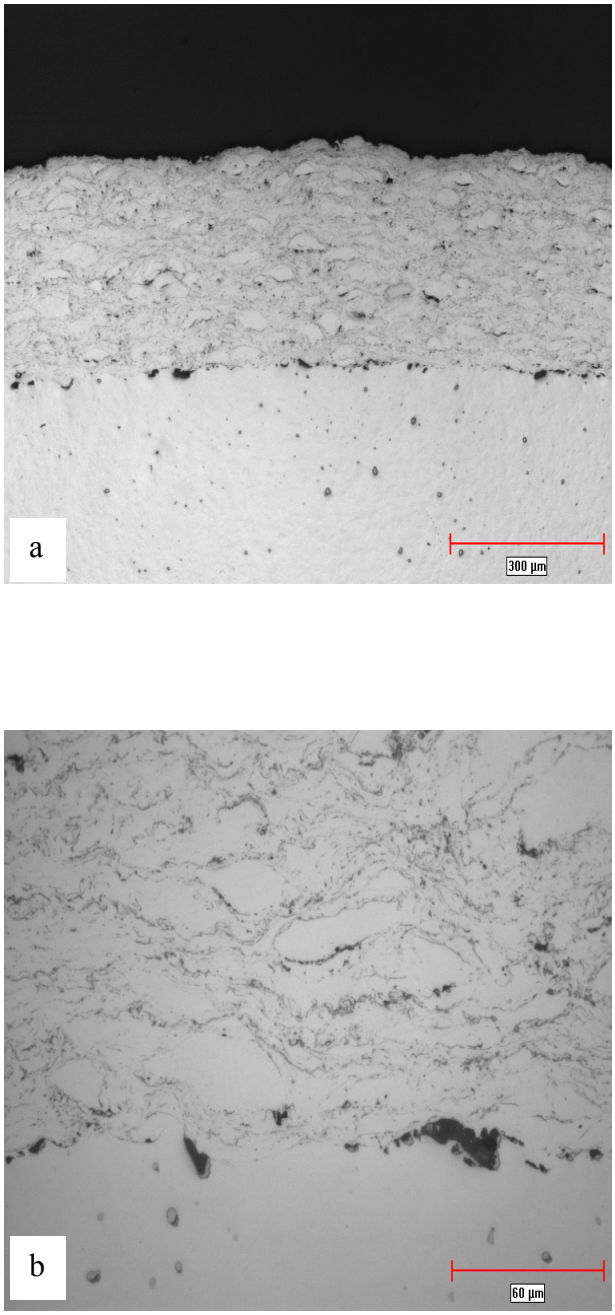

Figure 4-76 (a) Low magnification and (b) High magnification optical micrograph of burner rig exposed 718 with 718 coating at 704°C for 1000 cycles

4.11 Effect of various factors affecting coating compatibility with substrate

Based on the results in preceding sections on as coated condition, isothermal furnace oxidation and cyclic oxidation tests, it is evident that the CoNiCrAlY and 718 coatings tend to separate from the alloy 909 substrate in the as coated condition, while they exhibit excellent compatibility on alloy 718 substrate irrespective of the conditions. The CoNiCrAlY coating was observed to exhibit consistent incompatibility with alloy 909 substrate compared to the 718 coating. On the other hand, 718 coating on 909 substrate tend to exhibit both acceptable and unacceptable coating integrity leading to mixed results. However, when the coating is found to exhibit good integrity on alloy 909, excellent protection to oxidation is observed thereby effectively preventing any oxide scale formation. The reason for the mixed results exhibited by 718 coating on alloy 909 substrate is not clear but confirms that substrate factors do have a bearing on coating compatibility. Hence, it is important to gain an understanding of the underlying factors that play a vital role in the compatibility between the coatings and the substrate. The factors that were investigated are as follows.

Coefficient of thermal expansion of coatings versus substrate.

Comparison of residual stresses of CoNiCrAlY and 718 coatings

Effect of oxidation of the substrate during HVOF spray process

Comparison of adhesion and ductility of CoNiCrAlY and 718 coatings

Comparison of adhesive tensile bond strengths of the coatings

4.11.1 Coefficient of thermal expansion of the coatings

The linear coefficient of thermal expansion " α "is defined as the change in length from the original for each degree of temperature increase, it is represented by the equation:

$$\alpha = \frac{dl}{l \times dT}$$ [Kamasa et al., 2004]

where, dl = the change in length of material in the direction being measured

l = overall length of material in the direction being measured

dT = the change in temperature over which dl is measured

The thermal expansion is basically related to fundamental physics, materials tend to expand with increase in temperature as it causes a greater amplitude of thermal vibration of the atoms in a material, and this translates into an increase in mean inter-atomic distances as shown in Fig 4-77. The CTE is in many instances is specified for a certain temperature range or for a specific temperature. When the CTE is specified for a wide temperature range, it should noted that the value represents an average and may not represent the thermal expansion characteristics at extremes of the range as physical changes accelerated due to phase transitions causing exponential changes to thermal expansion properties [Kamasa et al., 2004]. Several researchers [Sampath et al., 2004, Sanatana et al., 2006] have reported the deleterious effects of residual stresses that is contributed by thermal stresses arising due to difference between the coatings and/or between the coating and the substrate thermal expansion characteristics. Fig 4-78 shows various sources or contributors to the residual stress in thermal spray coatings.

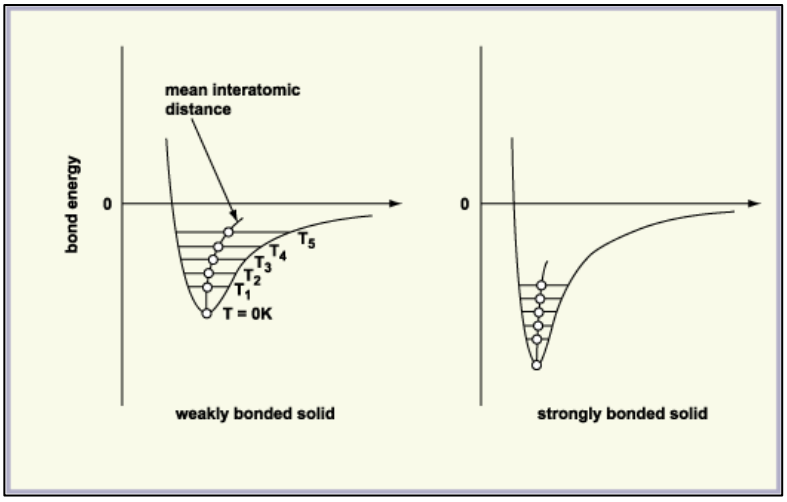

Figure 4-77 Illustration of effect of increase in temperature on mean inter atomic distances for a weekly and strongly bonded solid http://www.ami.ac.uk/courses/topics/0197_cte/index.html

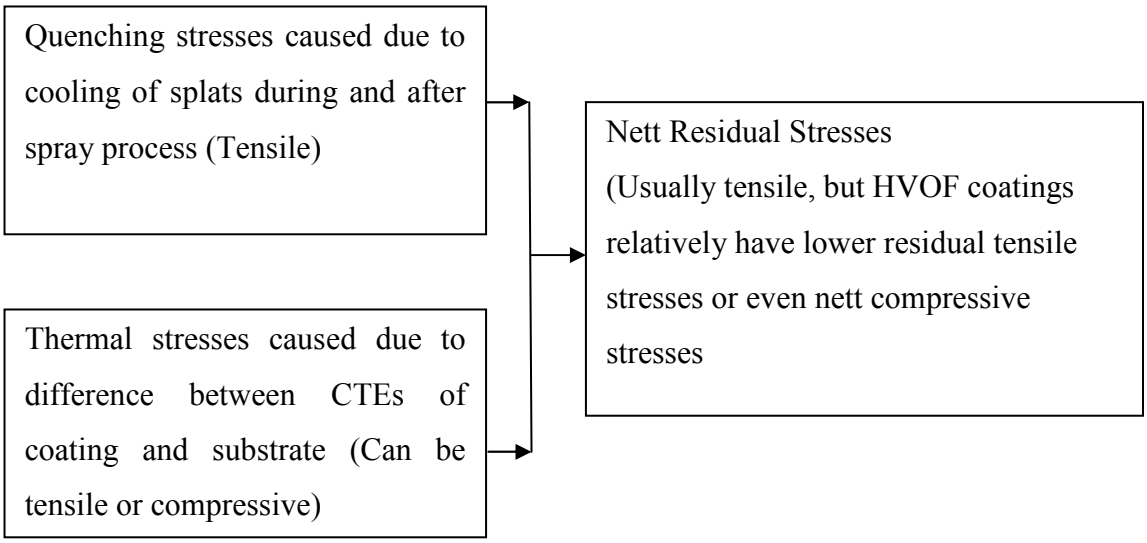

Figure 4-78 Illustration of various sources of residual stresses in thermally sprayed coatings [Illustration base on the theory in Santana et al., 2006]

The expansion and contraction at the interface between the coating and the substrate or between bond and top coat imposes a negative effect on the adhesion forces that keep the coating bonded to its substrate (substrate can be a coating in the case of two layered coatings). This is further undermined by the continuous formation of a brittle oxide layer in the interface between bond and top coat of thermal barrier coating referred to as "TGO" (Thermally grown oxide). This "TGO" layer is extremely brittle thereby resulting in inability to accommodate any thermal stresses causing separation or spalling of the ceramic coating.

The coefficient of thermal expansion were calculated based on instantaneous expansion data at 200°C, 400°C, 600°C and 700°C for 718 (wrought), CoNiCrAlY (sintered), 909 (wrought) from dilatometry data at Dalhousie University, while the NiAl CTE data was derived using the JMatpro software at the University of Manitoba. The CTE data were plotted against the temperature as shown in Fig 4-79. It is evident that 909 exhibits the lowest and NiAl (95% Ni 5% Al, also called by trade name Diamalloy™ 4008 coating) the highest coefficient of thermal expansion in the temperature range of 200 – 700°C. It can be observed that among the four materials plotted in Fig 4-79, except 909, all other materials exhibits CTEs similar to nickel base Superalloys in the temperature range of 200-700°C.

While the low coefficient of thermal expansion characteristics of Incoloy 909 is advantageous from a gas turbine engine design perspective, this factor may severely undermine the coating compatibility as most coating materials used in improving oxidation resistance exhibits higher coefficient of thermal expansion rates there by leading to higher compressive residual stresses in the coating especially during cooling.

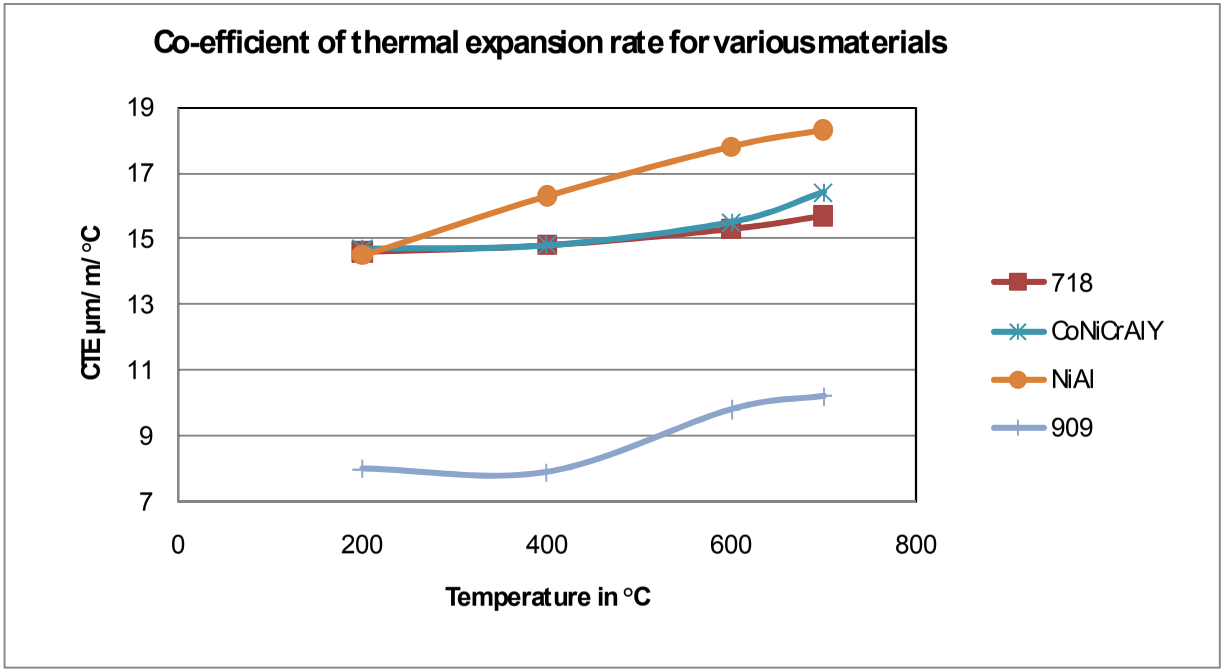

Figure 4-79 Coefficient of thermal expansion for 718, CoNiCrAlY, NiAl and 909
[909 data from Special metals technical data sheet, NiAl data from J Matpro]

4.11.2 Indirect measure of residual stresses of the coatings

Residual stresses are known to have significant effect on the interface bonding between the coating and substrate. This is especially true as the coating thickness increases, since the residual stresses also increases when it exceeds a threshold value and the coating tends to crack, separate from the substrate. In this study a simple methodology has employed in which coated Almen strips were used to qualitatively discriminate coatings based on the amount of deflection measured. An illustration of typical Almen strip and coated Almen strip exhibiting arc deflection height is shown in Fig 4-80. In other words, a change in the curvature of a standardized specimen is used to indirectly compare the net stresses of various coatings.

In this research two coatings, 718 and CoNiCrAlY, were sprayed on standard grit blasted Almen N strips at three different thicknesses (0.13mm, 0.25mm, and 0.38mm) with blowing cooling air and without any cooling (also referred to as "NC" representing no cooling in the chart legend). The deflections after grit blasting were subtracted from the arc deflection measurements after coating to reflect the stress state pertaining only due to coatings. It is evident from Fig 4-81 that 718 coating exhibits higher residual stresses compared to CoNi-CrAlY coating at all coating thickness conditions. In general, increase in coating thickness within the tested range (0.13mm to 0.38mm) resulted in increased stresses, except for 718 coating with cooling air exhibiting saturation over 0.25mm coating thickness. When coatings are sprayed without blowing cooling air, the increased heat input from HVOF process is believed to cause a stress relaxation effect on both the coatings and the substrate.

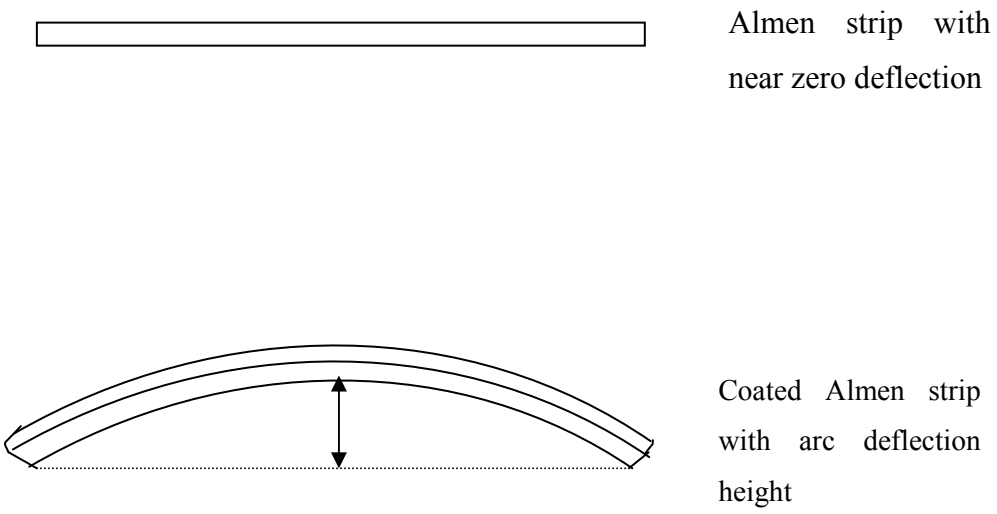

Figure 4-80 Schematic of Almen strip before and after coating to illustrate arc deflection showing presence of residual tensile stresses within the coating

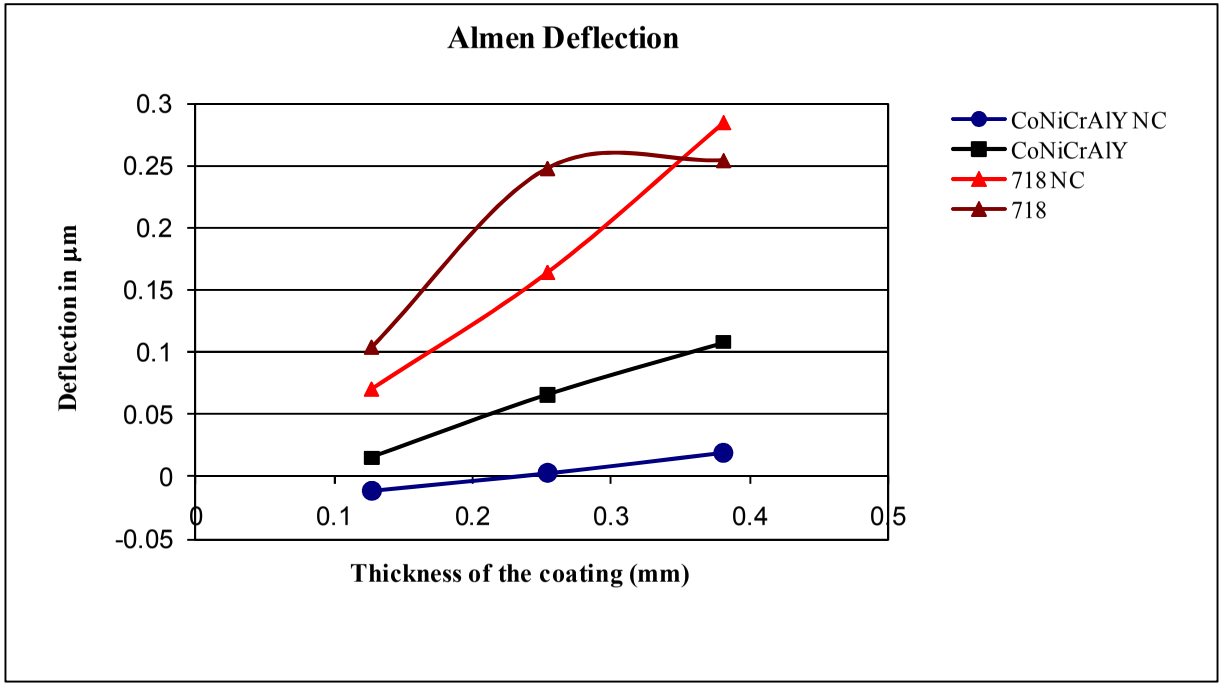

Figure 4-81 Almen deflection for various coatings and thicknesses with air cooling and no cooling (NC)

4.11.3 Secondary Ion Mass Spectrometry (SIMS) – Depth profiling

The Fig 4-82, 4-83, and 4-84 shows the intensity and sputtering time charts for 718 test coupons representing 10 passes of HVOF flame, 1 pass of HVOF flame, and as polished with no exposure to HVOF flame respectively. It can be observed that oxygen concentration (counts per second) on the surface increases with increase in HVOF flame exposure. When 718 coupon is exposed to 10 passes, it can be seen that the oxygen concentration drops from 10^6 to 10^5 but it takes few hundred seconds sputtering time before attaining a plateau, while the 718 without any flame exposure takes less than a minute before attaining a plateau and maintaining the same trend with further sputtering time.

Figs 4-85, 4-86, and 4-87 shows the intensity and sputtering time charts for 909 test coupons representing 10 passes of HVOF flame, 1 pass of HVOF flame and as polished with no exposure to HVOF flame respectively. It can be observed that oxygen concentration on the surface increases with increase in HVOF flame exposure. When a 909 coupon is exposed to 10 passes, it can be seen that the oxygen concentration drops slowly from surface to core and it takes almost 1000 seconds of sputtering time prior to attaining a plateau. A similar trend can also be seen with Ti concentration when the 909 test coupon is exposed to maximum HVOF exposure. It can be seen that alloy 909 is more susceptible to forming a thin oxygen enriched surface layer when compared to 718 for the same test conditions due to lack of a Cr addition.

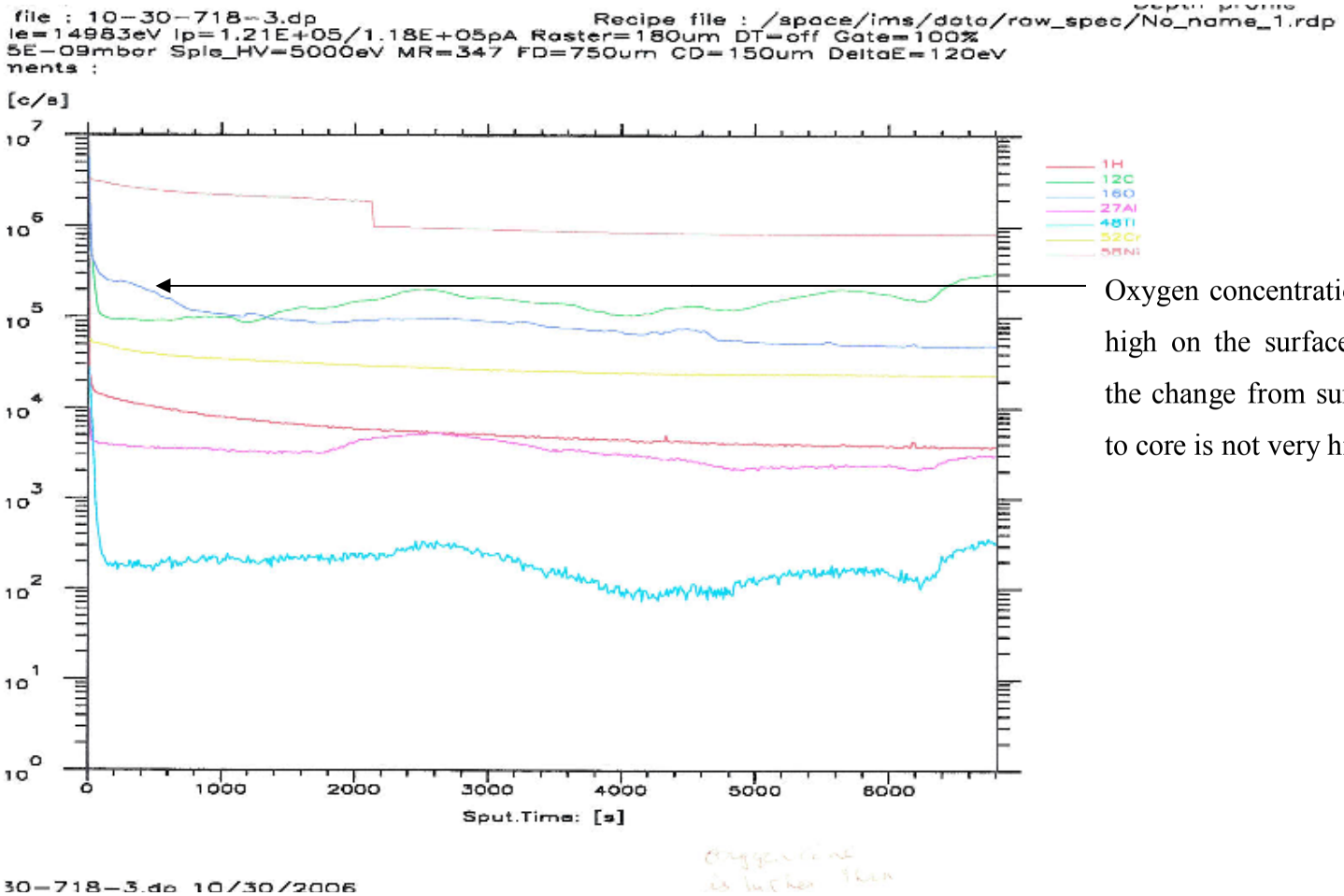

Oxygen concentration is high on the surface but the change from surface to core is not very high.

Figure 4-82: Alloy 718 coupons with 10 passes of HVOF Flame

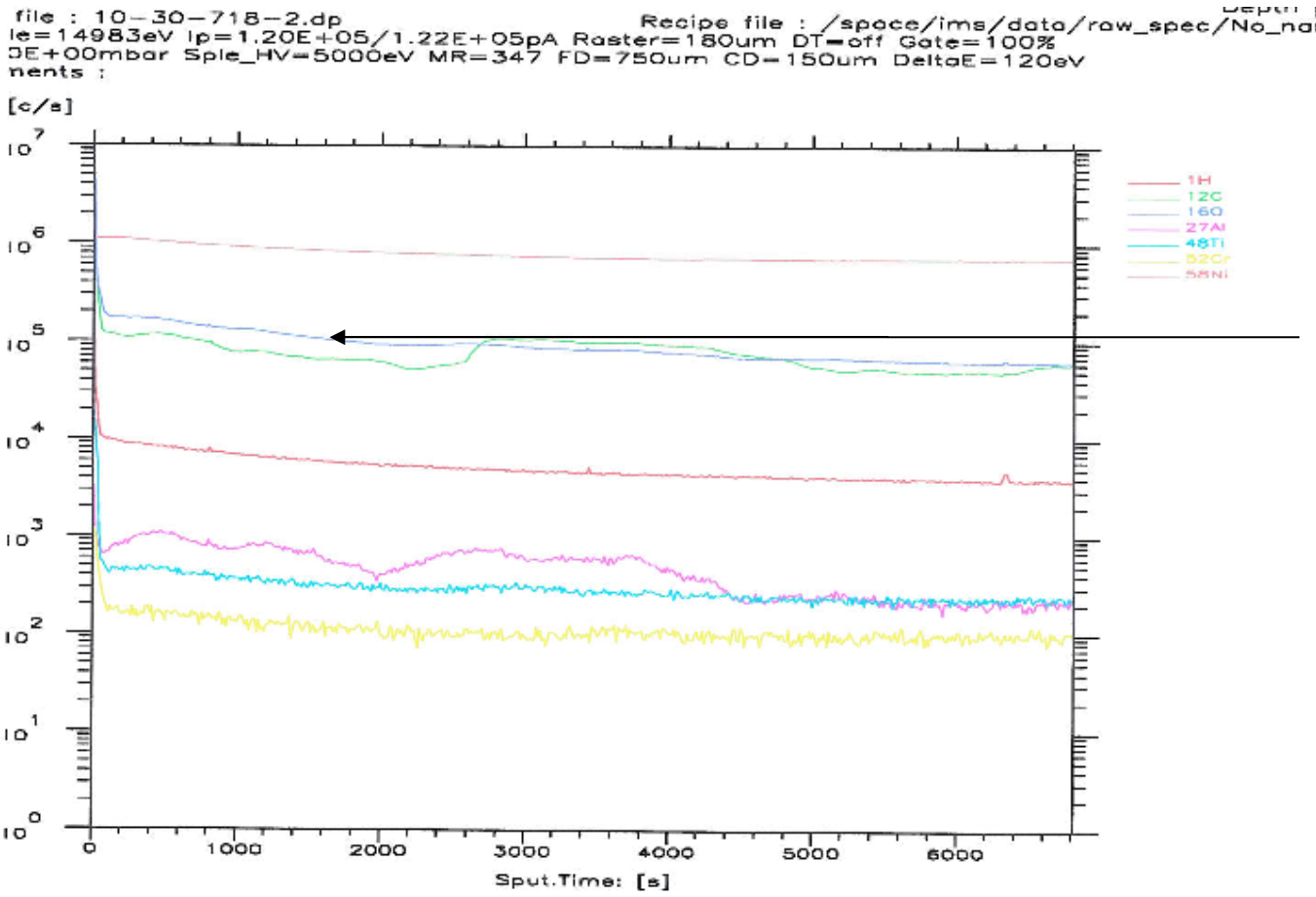

Oxygen concentration very high on the s indicating negligible pr of oxide film

Figure 4-83 Alloy 718 coupons with one pass of HVOF Flame

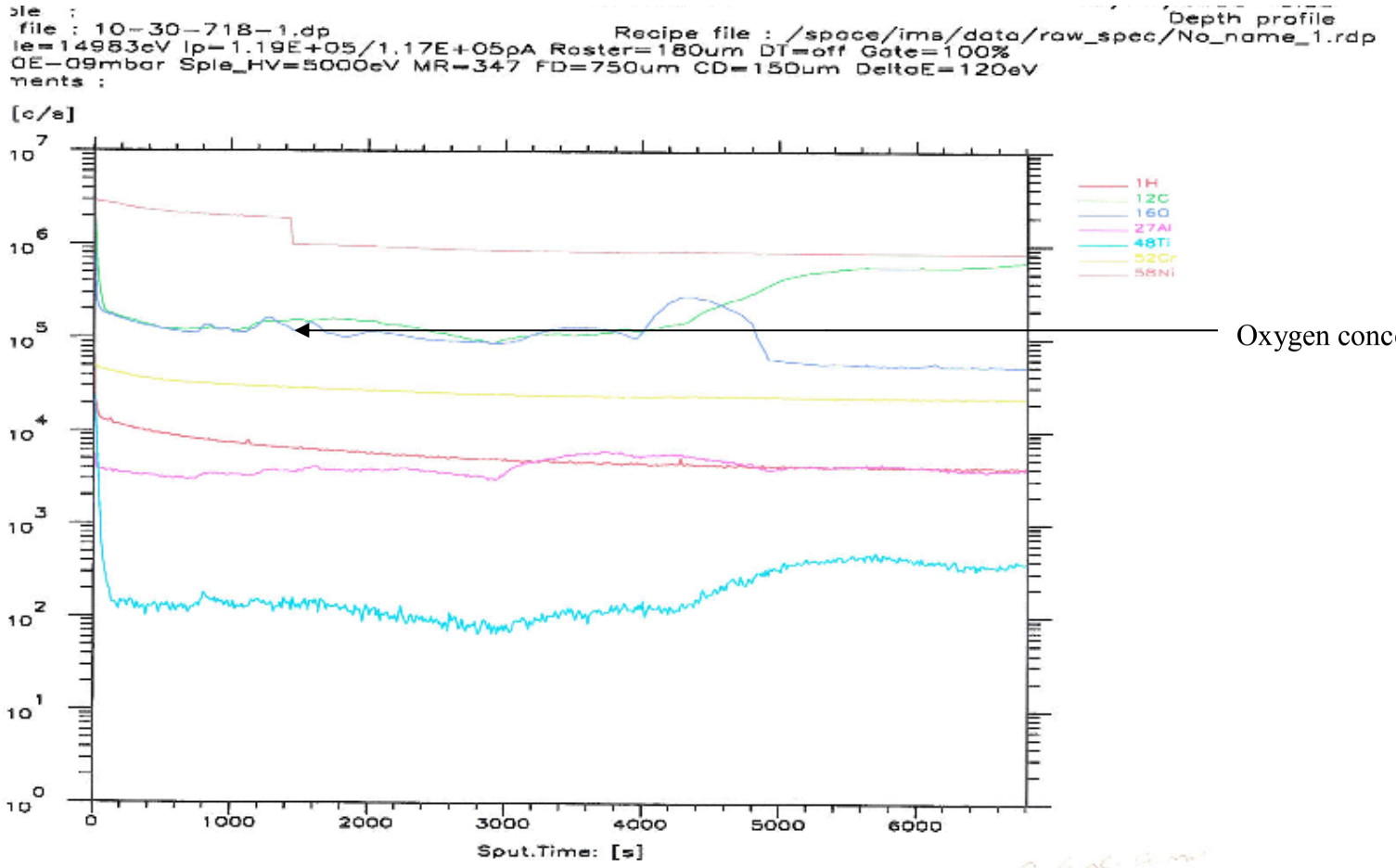

Figure 4-84 Alloy 718 coupons without any exposure to HVOF Flame

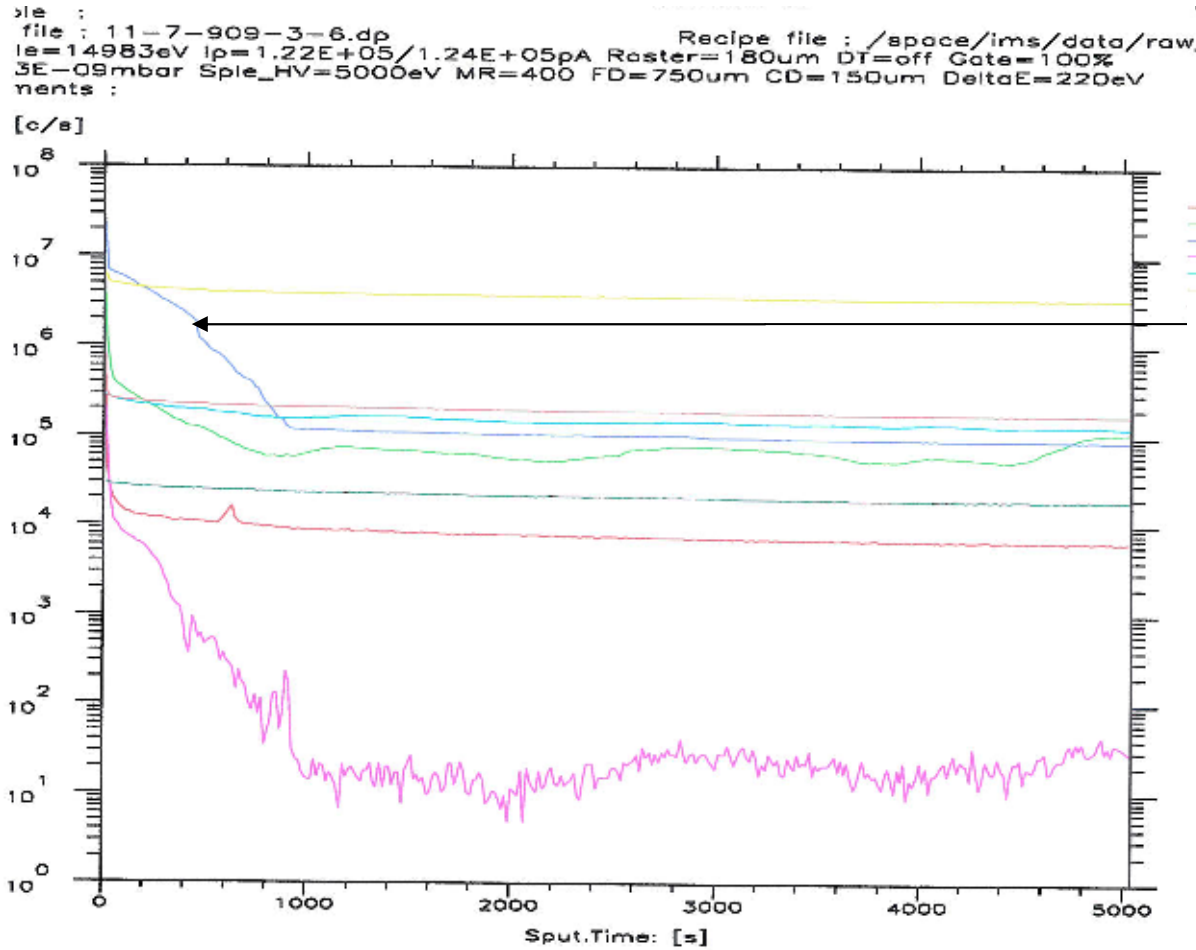

Oxygen concentration is high on the surface and gradually decreasing for about 1000 seconds thus indicating presence of thicker oxide film compared to 718 alloy subjected to identical condition.

Figure 4-85 Incoloy 909 coupons with 10 passes of HVOF Flame

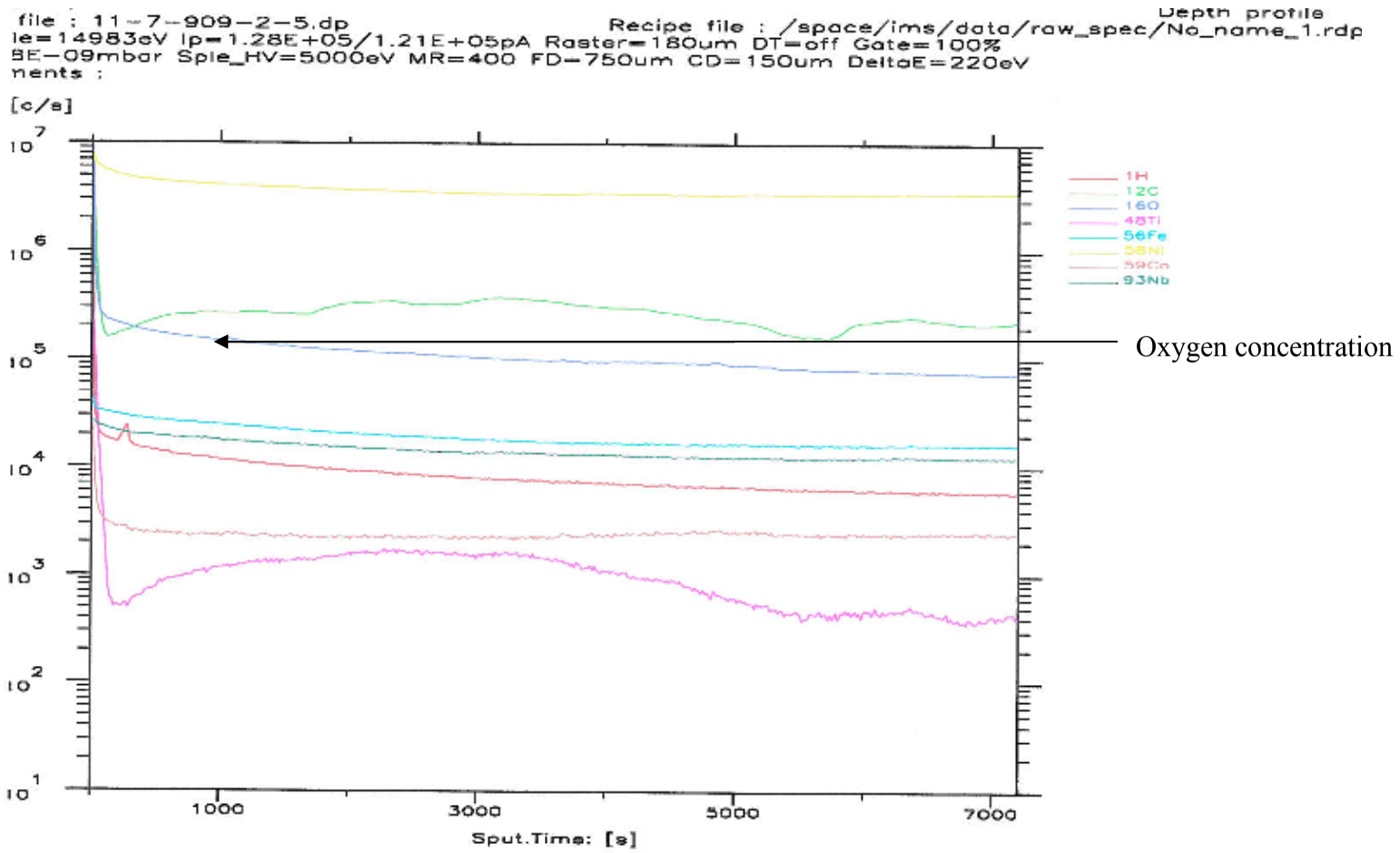

Figure 4-86 Incoloy 909 coupons with one pass of HVOF Flame

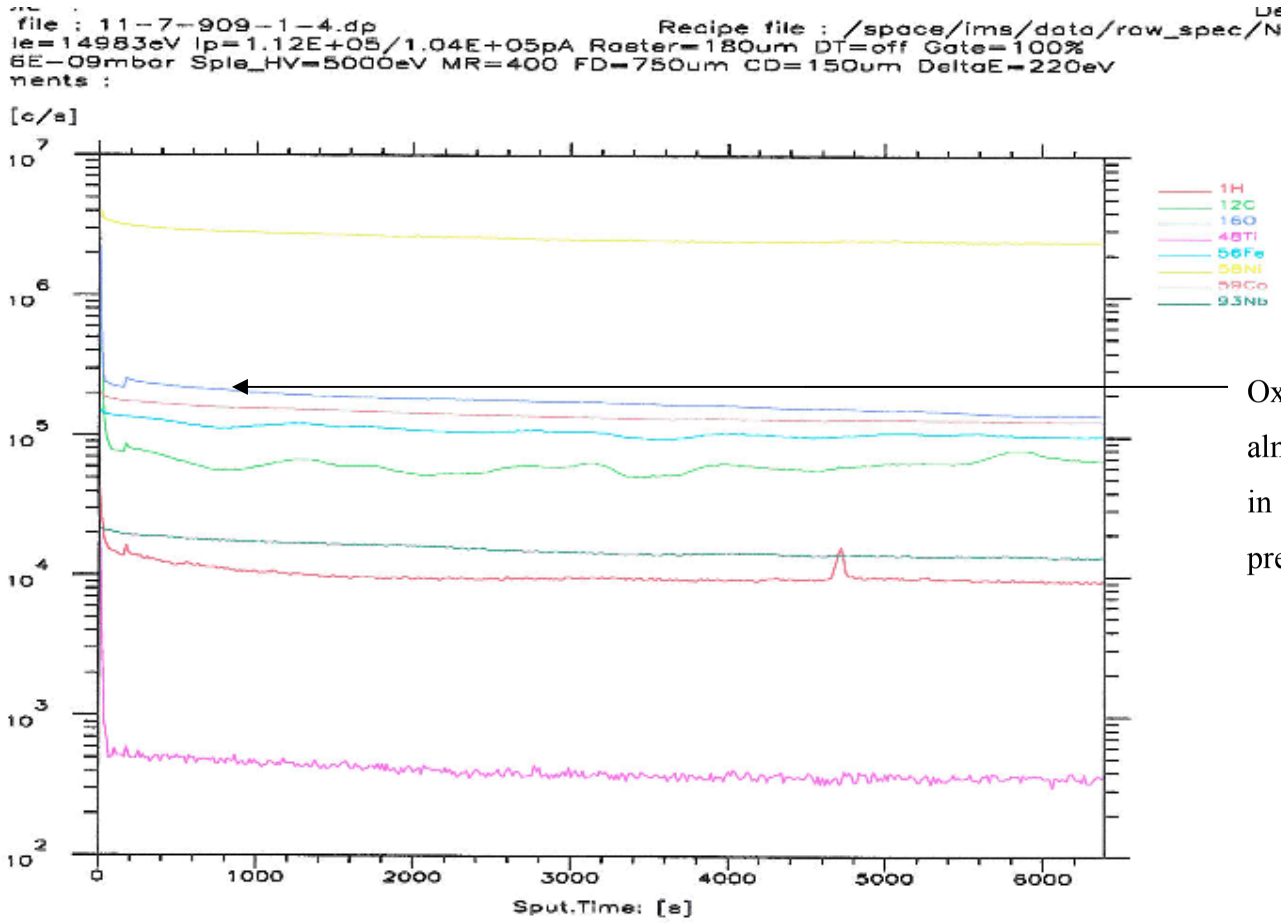

Oxygen concentration remains almost same with the increase in depth indicating negligible presence of oxide scale

Figure 4-87 Incoloy 909 coupons without any exposure to HVOF Flame

4.11.4 Coating ductility test results using 4 point bend test

The bending fracture stress and strain values were calculated in the direction perpendicular to the coating, with the coating being subjected to tensile stress during testing. It is known that the fracture stress is minimum in the direction perpendicular to the coating deposition direction due to anistropic nature of thermals spray coatings [Powlowski., 1995]. The stress strain charts for 718 coating on the Al 6061 substrate for three coating thicknesses 125µm, 254µm and 381µm are shown in Fig 4-88, 4-89 and 4-90 respectively. It can be seen that during testing the bending stress and strain increases until the coating fractures giving rise to a sharp drop in stress value. Since, the substrate test coupons used are identical for all the test coupons and Al 6061 being a ductile material was chosen for better differentiation of coating fracture as a function of load. It can be observed that the average fracture stress decreases from about 650MPa to 425 MPa and the average fracture strain decrease from 0.014 to 0.010 for coating thickness from 125 µm to 381µm for the 718 coating. It can be seen an inverse correlation exist between coating thickness versus both fracture strength and fracture strain. This suggests that increasing coating thickness can be deleterious to coating adhesion and can accelerate coating spallation or debonding at the coating-substrate interface especially under application of external stress during service conditions.

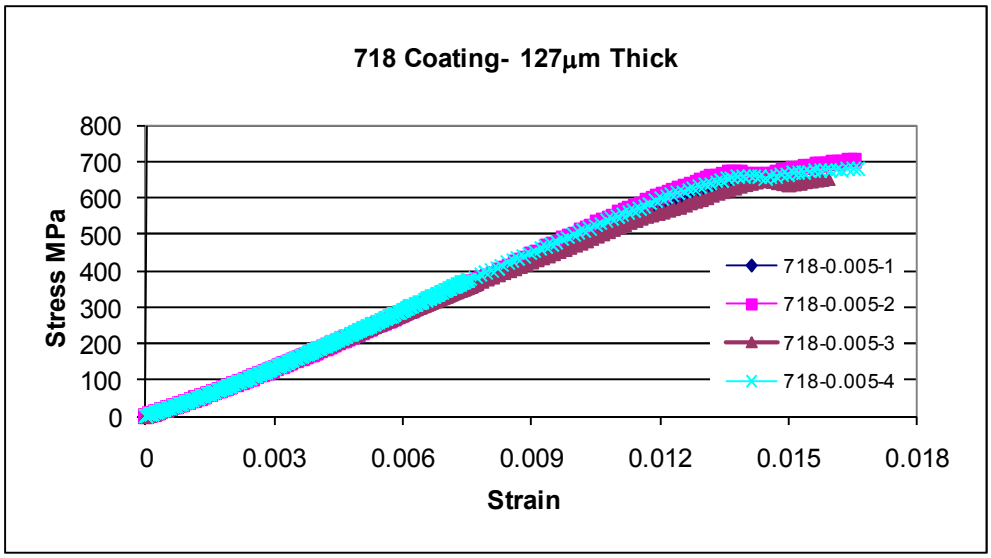

Figure 4-88 Stress vs. Strain curves of 6061 aluminum plate coated with 718 coating (127µm Thick)

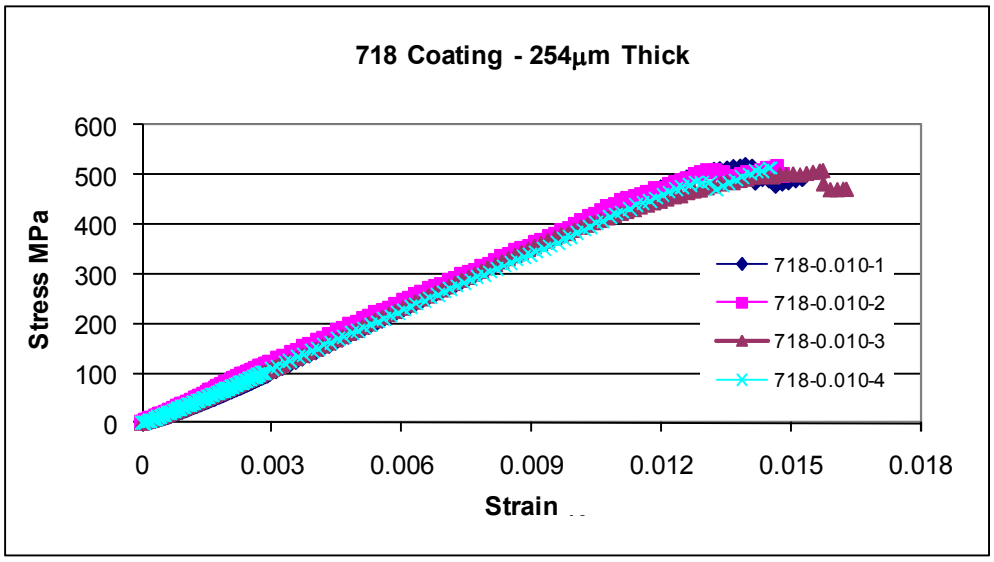

Figure 4-89 Stress vs. Strain curves 6061 aluminum plate coated with 718 coating (254µm Thick)

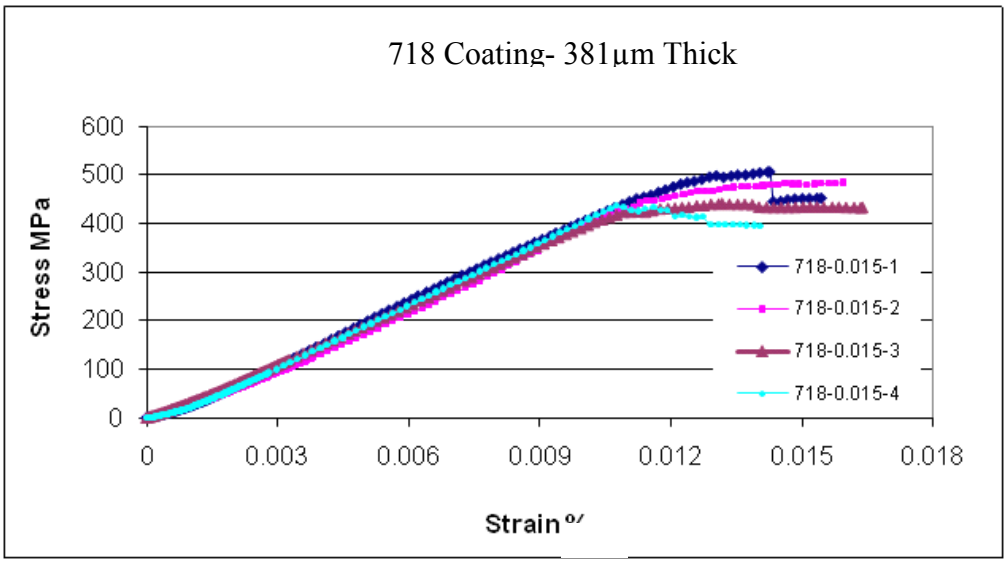

Figure 4-90 Stress vs. Strain curves 6061 aluminum plate coated with 718 coating (381µm Thick)

The stress strain charts for CoNiCrAlY coating on Al 6061 substrate for three coating thicknesses 125µm, 254µm and 381µm are shown in Fig 4-91, 4-92 and 4-93 respectively. It can be observed that the average fracture stress decreased from about 550MPa to about 350 MPa and fracture strain decrease from 0.014 to 0.012 when the coating thickness increased from 125 µm to 381µm for the CoNiCrAlY coating. It is evident that CoNiCrAlY coating exhibit relatively lower average coating fracture strength compared to 718 coating. However, both the coatings exhibited about ~35% decrease in average fracture stress with the coating thickness increasing from 125µm to 381µm. It should be noted that previous research [Wiklund et al, 1997] had used similar test method to differentiate the coating cracking resistance of TiN (brittle) and CrN (ductile) PVD (physical vapor deposition) coatings.

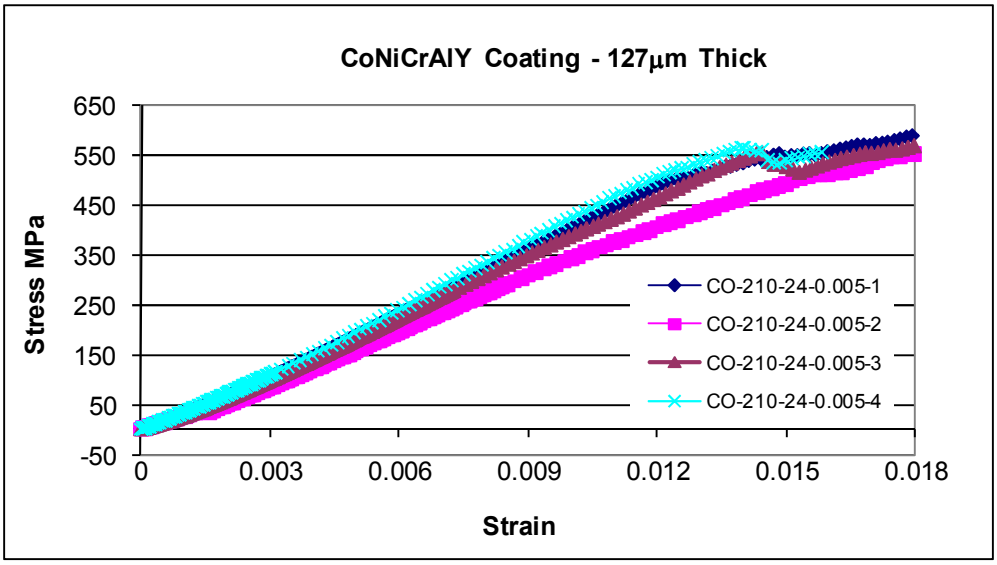

Figure 4-91 Stress vs. Strain curves 6061 aluminum plate coated with CoNiCrAlY coating (127µm Thick)

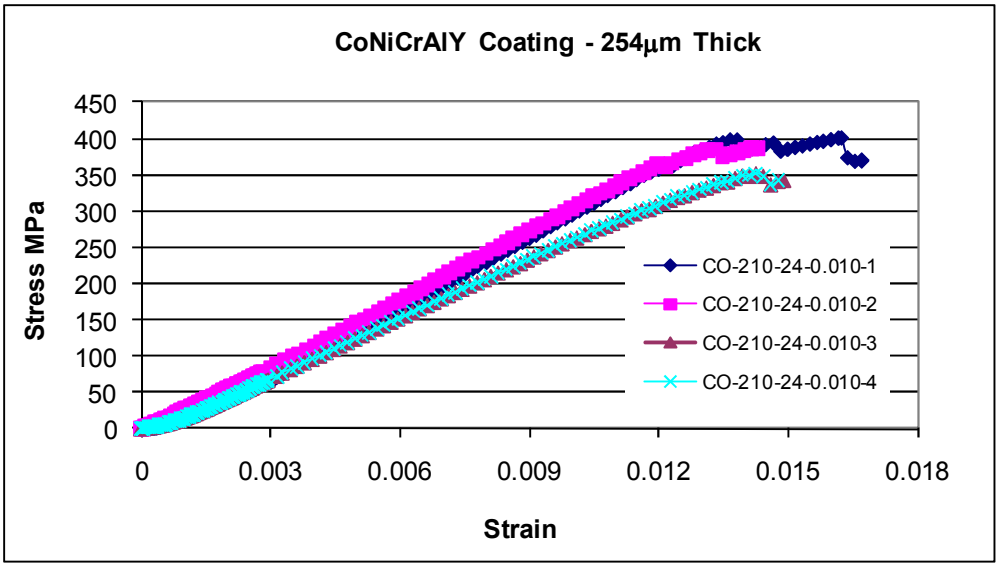

Figure 4-92 Stress vs. Strain curves 6061 aluminum plate coated with 718 coating (254µm Thick)

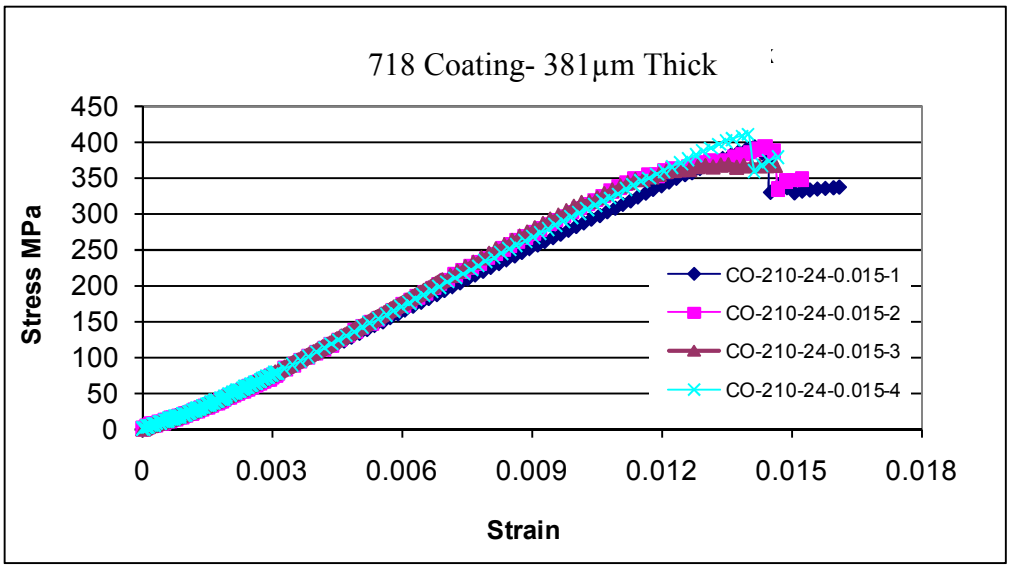

Figure 4-93 Stress vs. Strain curves 6061 aluminum plate coated with 718 coating (381µm Thick)

4.11.5 Bond Strength of coatings

The tensile bond strength results for two coatings (CoNiCrAlY and 718) on 909 and 718 substrates are as shown in Fig 4-94 and Fig 4-95 respectively.

4.11.5.1 Incoloy 909 Substrate with CoNiCrAlY coating

Among the two coatings, CoNiCrAlY coating exhibited the lowest average bond strength irrespective of coating thickness. The bond strength of this coating, as expected decreased with increasing coating thickness. The average coating bond strength varied from 52 MPa to 40 MPa for coating thickness of 0.13mm to 0.38 mm as shown in Fig 4-94. The increase in coating thickness especially for 0.25 and 0.38mm caused the coating to fail at the coating and substrate interface region confirming that coating bond strength is relatively lower than the glue bond strength (~70Mpa). This result also concurs with the earlier metallographic results, where the coating tend to separate at the substrate interface region. The range of bond strength for this coating at highest thickness was relatively wide, indicating presence of pre-existing interface separation but varying amounts leading to variation of tensile bond strength between the individual test coupons.

4.11.5.2 Incoloy 909 Substrate with 718 coating

Among the two coatings, 718 coating exhibited excellent bond strength at 0.13mm and 0.25mm coating thickness, indicating that variation in coating thickness within a limited range does not affect the tensile bond strength. However, at the maximum coating of

thickness 0.38mm, it is evident from Fig 4-94 that there is a substantial drop in average tensile bond strength from ~68Mpa to ~51MPa. The average coating bond strength varied from 69 MPa, 68 MPa, and 51 MPa for coating thickness of 0.13mm, 0.25mm and 0.38 mm respectively from Fig 4-94. The failure location in coatings with 0.13mm thickness exhibited an adhesive failure due to epoxy film, often referred to as glue failure. The HVOF sprayed coatings are characterized with excellent bond strength, sometimes the coating strength exceeded the strength of the epoxy film (~70MPa) used to prepare the tensile test coupon. The failure location for coating with 0.25mm coating thickness were mixed (both glue and at coating substrate) but at 0.38mm, all the test coupons failed at coating substrate interface. The tensile bond test results were in good agreement with the earlier metallography results in the 'as sprayed' condition. The bond strength results were better than CoNiCrAlY coating on the 909 substrate.

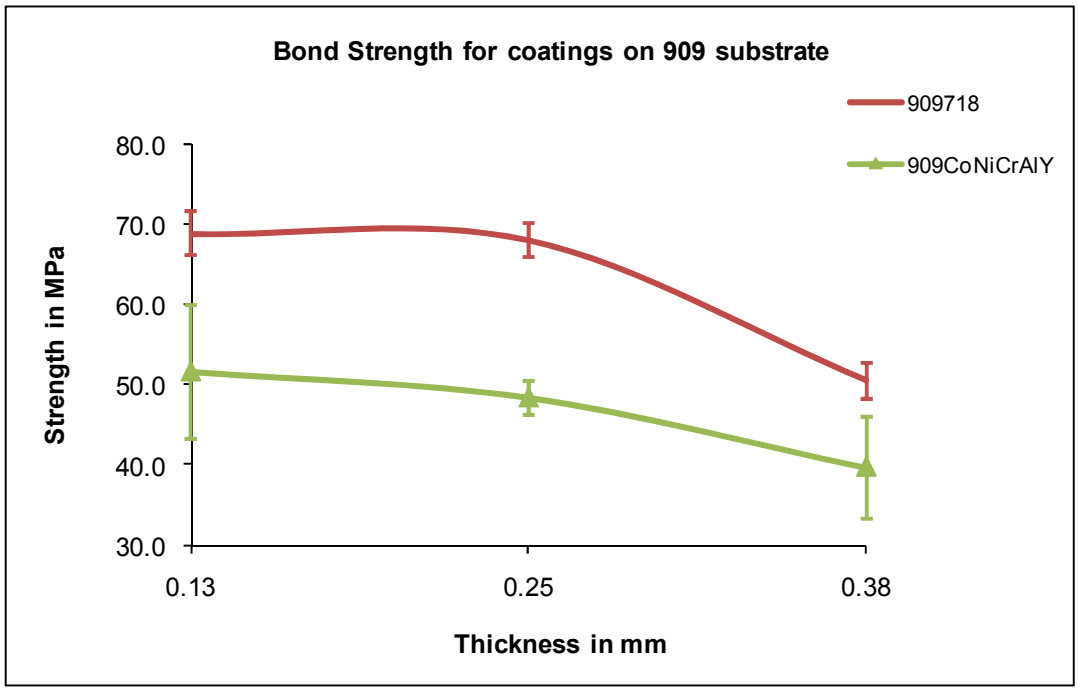

Figure 4-94 Bond strength of 718 and CoNiCrAlY coatings on 909 Substrate at various coating thicknesses

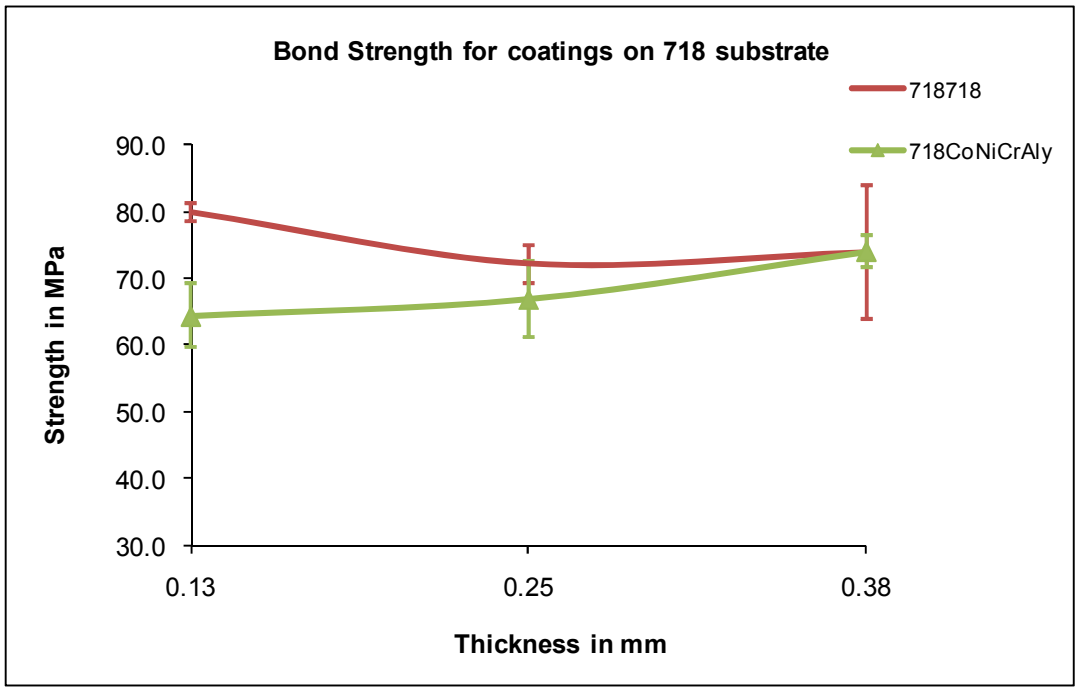

Figure 4-95 Bond strength of 718 and CoNiCrAlY coatings on 718 Substrate at various coating thicknesses

4.11.5.3 718 Substrate with CoNiCrAlY coating

From Fig 4-95 the CoNiCrAlY coating exhibited similar bond strength as 718 coating on this substrate especially at the maximum coating thickness. The average bond strength seems to imply a direct correlation with the coating thickness, while the general expectation is decrease in adhesion strength with increase in coating thickness. However, it should be noted that all the failures occurred at the glue instead of the coating substrate interface. Hence, it can be concluded the bond strength was excellent for all the tested coating thicknesses; the variation in glue strength (65~74MPa) is the cause for the contrarian trend. From Fig 4-95, the average coating bond strength varied from 64.3 MPa, 66.9 MPa to 74 MPa for coating thickness of 0.13mm, 0.25mm and 0.38 mm

respectively. The tensile bond strength results were found to be in good agreement with the metallographic analysis at the as sprayed condition, which also exhibited good interfacial conditions between the coating and the substrate.

4.11.5.4 718 Substrate with 718 coating

From Fig 4-95 the 718 coating exhibited the highest average bond strength at 0.13mm, and 0.25mm coating thickness, and the bond strength at the maximum coating thickness was in proximity to the highest bond strength exhibited by CoNiCrAlY coating. However, at all conditions the failure location was limited to the adhesive failing rather than in the coating making it difficult to distinguish the superiority of 718 coating. It is likely that the identical nature of the coating and the substrate contributed for the excellent adhesive bond strength in this condition. The average coating bond strength varied from 80 MPa, 72 MPa and 74 MPa for coating thickness of 0.13mm, 0.25mm and 0.38 mm respectively. The microstructure also exhibited good interfacial bonding between 718 coatings on 718 substrate of the as sprayed condition showing excellent agreement with the bond strength results.

4.12 Investigation of Ni-Al coating on Alloy 909 Substrate

Based on the results obtained in the previous sections, it was thought that lack of ductility and adhesion of the coating could be a significant factor for the coating failures on Incoloy 909 substrate as any resultant stress due to differential CTE could likely be accommodated by a coating that exhibits better adhesion to the substrate and also strain

tolerant. In order to substantiate this view, a common aerospace ductile bond coating material Ni-5wt%Al [Diamalloy 4008, Technical Data Bulletin, Sulzer Metco] was sprayed using HVOF process on Incoloy 909 and 718 coupons. The nickel aluminide coating formed a very dense microstructure as shown in the optical micrograph in Fig 4-96 and scanning electron micrograph in 4-97. It is significant to note that the Ni-Al coating resulted in excellent bonding on both of the substrates, Incoloy 909 and Inconel 718 without showing any substantial coating separation. Various reports [Sampath, 1989; Sampath et al., 2004; Hearley et al., 2000; Deshpande et al., 2006; Culha et al., 2008; Mahesh et al., 2009] supports that thermally sprayed Ni-Al coatings are versatile and provide excellent high temperature oxidation resistance on variety of substrate materials. They reported excellent coating contact with the substrate, leading to better adhesion strength (~85 MPa by Culha et al., 2008), with the porosity ranging from 1-3% [Sampath et al., 2004; Culha et al., 2008]. Hence to further investigate the compatibility exhibited by NiAl coating on both Inconel 718 and Incoloy 909 substrates, more testing was carried out by conducting Almen arc deflection test, 4 point bend test, tensile bond test and isothermal oxidation test with particular interest on Incoloy 909 substrate as other substrate (Inconel 718) used in this research was found to exhibit excellent compatibility with all the three coatings used in this research. The test results of NiAl coatings are presented and discussed in the subsequent sections.

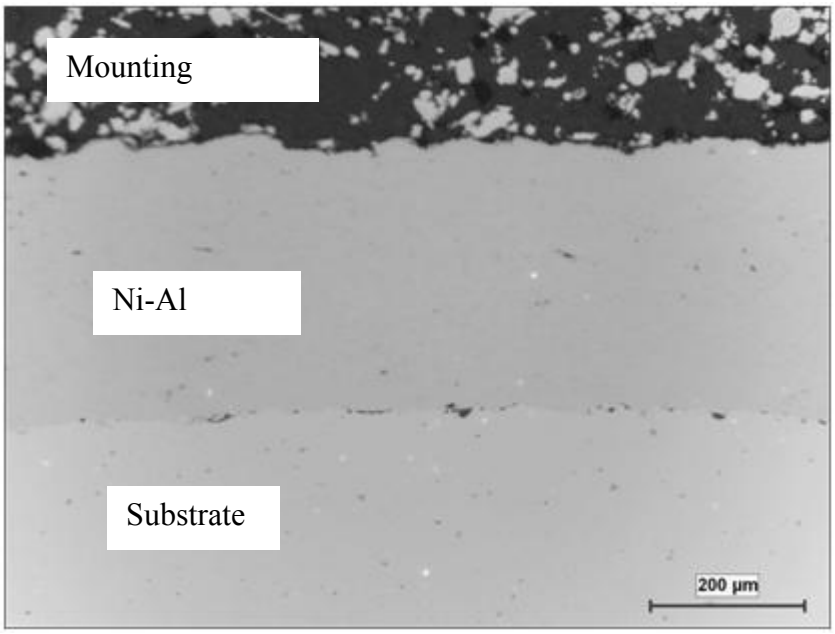

Figure 4-96 As sprayed micrograph of Incoloy 909 with Ni-Al coating

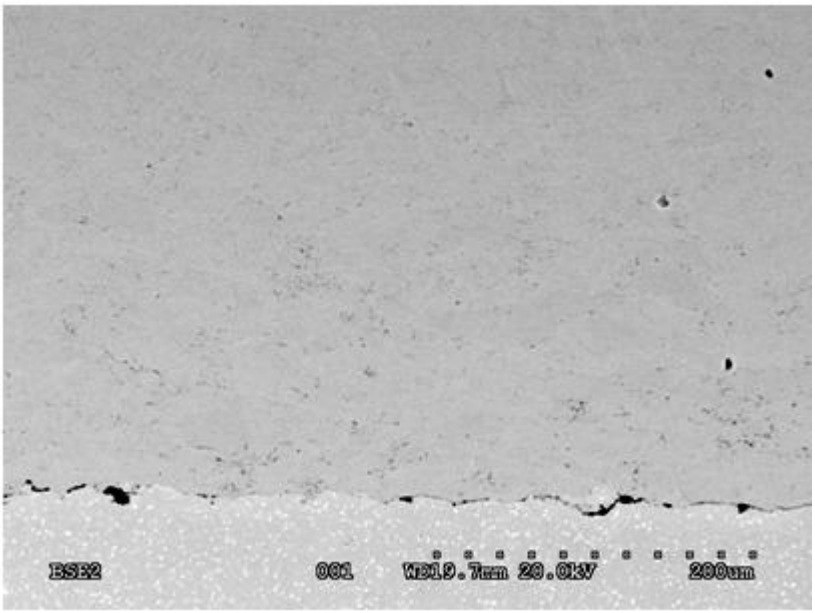

Figure 4-97 As sprayed SEM micrograph of Incoloy 909 with Ni-Al coating

4.12.1 Incoloy 909 Substrate with NiAl coating

Among all the coatings, NiAl coating exhibited the best average bond strength irrespective of coating thickness as shown in Fig 4-98. The bond strength of this coating was excellent at all coating thicknesses. All test coupons failed at glue upto 0.25mm coating thickness, while the failures were mixed (both glue failure and coating failure) at 0.381mm coating thickness. The average coating bond strengths were 70.5 MPa, 69.4 MPa and 67.8 MPa for coating thickness of 0.13mm, 0.25 mm and 0.38 mm respectively. It is evident that the bond strength results are in excellent agreement with as sprayed microstructural evaluation exhibiting very little interface separation between the coating and substrate.

4.12.2 718 Substrate with NiAl coating

The Ni-Al coating also exhibited similar results on alloy 718 substrate like with alloy 909. The bond strength at all coating thicknesses were excellent. From Fig 4-98, the average coating bond strengths were 70.7 MPa, 69.3 MPa, and 68.7 MPa for coating thickness of 0.13mm, 0.25mm and 0.38 mm respectively. The microstructure also exhibited good interfacial bonding between NiAl coating on 718 substrate in as sprayed condition showing excellent agreement with bond strength results. All test coupons failed at glue interface. The NiAl is the only coating among the three coatings to exhibit good bond strength on both 909 and 718 substrates.

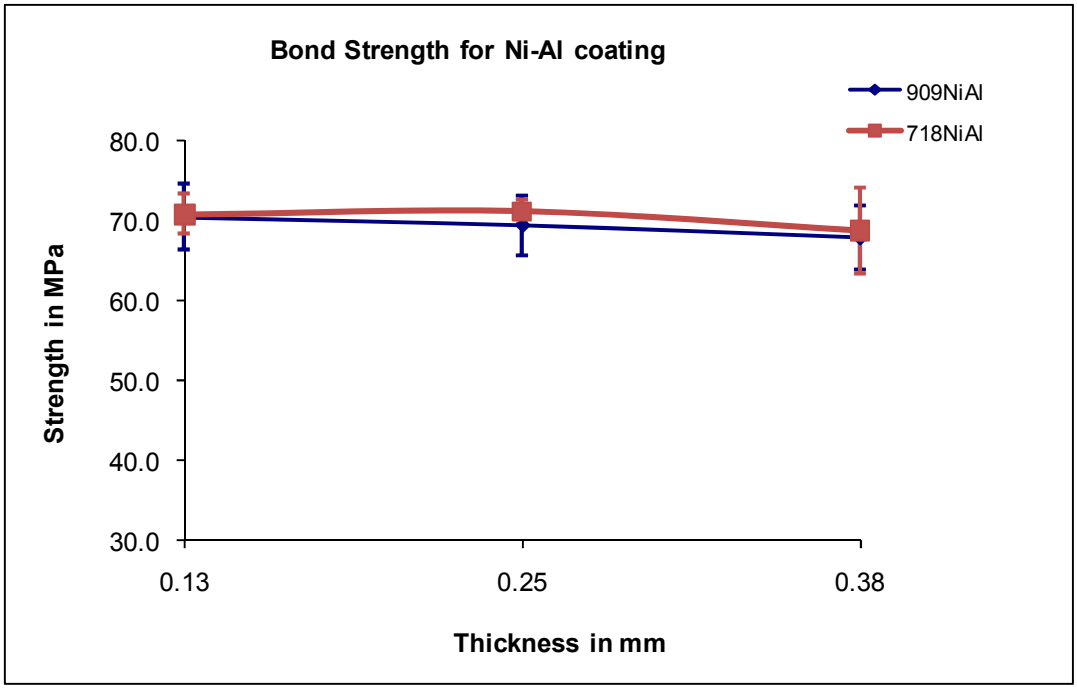

Figure 4-98 Tensile strength results for Ni-Al coating on Incoloy 909 and Inconel 718 substrate for various coating thickness

4.12.3 NiAl Coating ductility and adhesion test results using four point bend test

NiAl coated Al 6061 panels were tested using 4 point bend test as previously used for CoNiCrAlY and 718 coatings to compare the bending fracture strength and fracture strain results. NiAl coating exhibited superior bending fracture strength (adhesion and better fracture toughness) and fracture strain (ductility) than CoNiCrAlY and 718 coatings especially with the increasing coating thickness. The test results are detailed in the last section of this chapter and presented in Table 4-7.

4.12.4 Almen deflection test using NiAl coatings

To qualitatively study the effect of residual stresses, NiAl coatings were sprayed at 0.127, 0.254 and 0.376 mm, with cooling and with no cooling air (NC) on Almen N strips. As shown in Fig 4-99, residual tensile stresses increased with coating thickness, similar to CoNiCrAlY and 718 coatings. Also the effect of cooling and no cooling made negligible difference in the arc deflection height of NiAl sprayed panels. It is expected that the coating deposition without cooling (NC: No cooling) to exhibit slightly higher arc deflection height as the contribution from quenching stresses will be higher. However, the lower arc deflection height (also lower residual stresses) with no cooling (NC) observed in this research is a contrarian effect caused likely due to the stress relaxation effect accompanied with the higher coating deposition temperature The details on comparison with coatings are presented towards the end of this Chapter (Paragraph 4.13).

4.12.5 Isothermal furnace oxidation

NiAl coated Incoloy 909 test coupons were subjected to isothermal furnace exposure at 704°C for 1000 hours to study any effect of oxidation on the coatings and/ or substrate. The coated area showed presence of thin adherent greenish scale after elevated temperature exposure. The optical and SEM micrographs of the cross section of this coupon are shown in Fig 4-100 and Fig 4-101 respectively. Fig 4-100 shows excellent coating

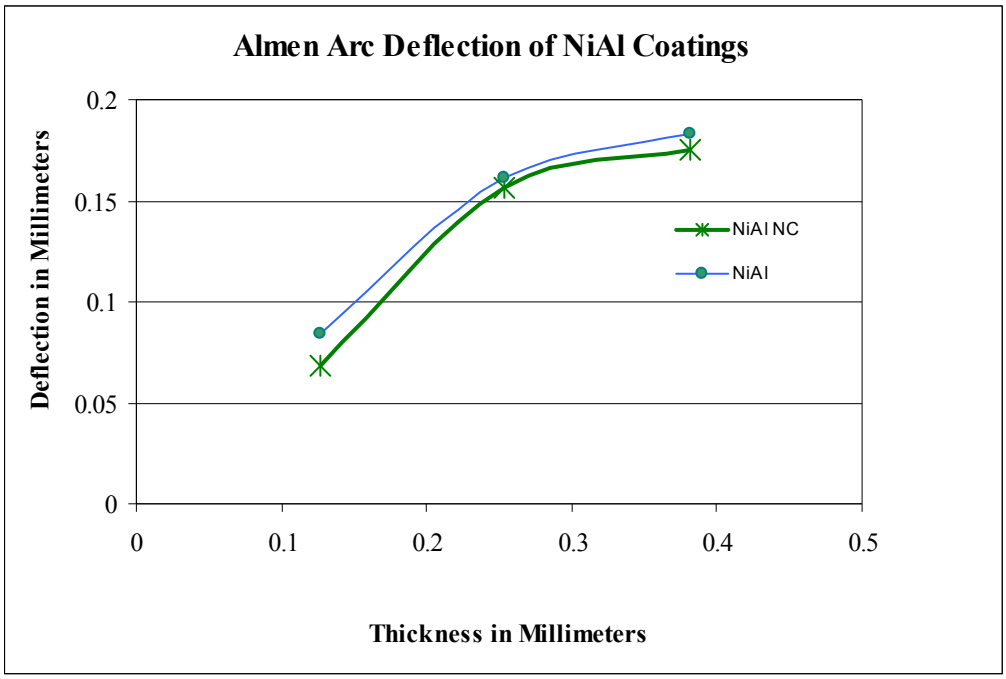

Fig 4-99 Almen arc deflection height for NiAl coating with cooling and without cooling air blast (NC)

integrity even after the furnace exposure, while Fig 4-101 presence of negligible amounts of thin discontinuous scale on the surface of the coating formed after isothermal oxidation testing. Due to the very thin scale, EDS characterization was difficult, the thin green oxide scale are likely nickel oxide, as aluminum oxide formation is favored only at higher temperatures i.e., above 1000°C. Previous research in the literature confirms that 95Wt.%Ni Al coatings at lower temperature favor formation of Nickel oxide and at elevated temperatures favor formation of alumina scales [Deshpande et al., 2006].

In Fig 4-102 NiAl coating on 909 substrate SEM micrograph and associated elemental maps are shown. In Fig 4-102 it can be seen that the Ni and Al is uniformly distributed within the coating. Thus as long as any of the coatings used in this study exhibits good integrity, the protection against oxidation of even oxide scale forming Incoloy 909 can be protected effectively in its service temperature range (~650°C). It can be further noticed that the microstructure of NiAl coatings shown in Fig 4-100 and Fig 4-101 consists of well bonded splats with negligible presence of unmelted or globular particles, this observation concurs well with the previous research reports [Sampath et al., 2004; Culha et al., 2008]. This excellent splat to splat bonding and also splat to substrate bonding ensures in the formation of dense coating that provides an excellent barrier to oxidation of the underlying substrate.

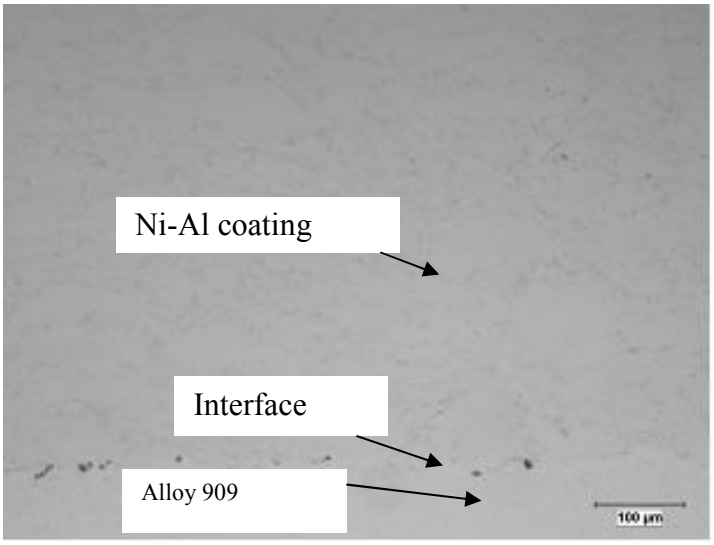

Figure 4-100 Optical Micrograph of Incoloy 909 with Ni-Al coating T=704°C, t=1000Hrs

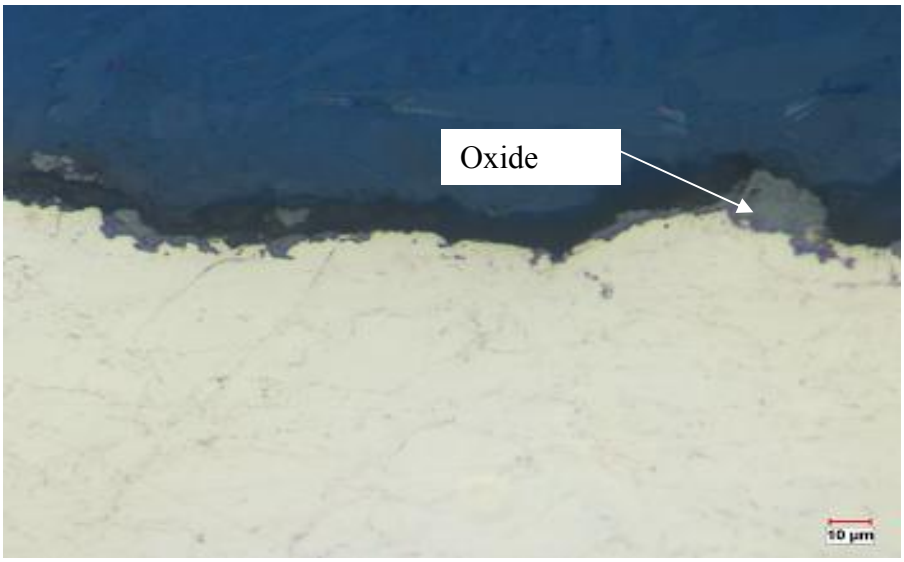

Figure 4-101 Optical Micrograph of Incoloy 909 with Ni-Al coating T=704°C, t=1000Hrs with thin oxide scale

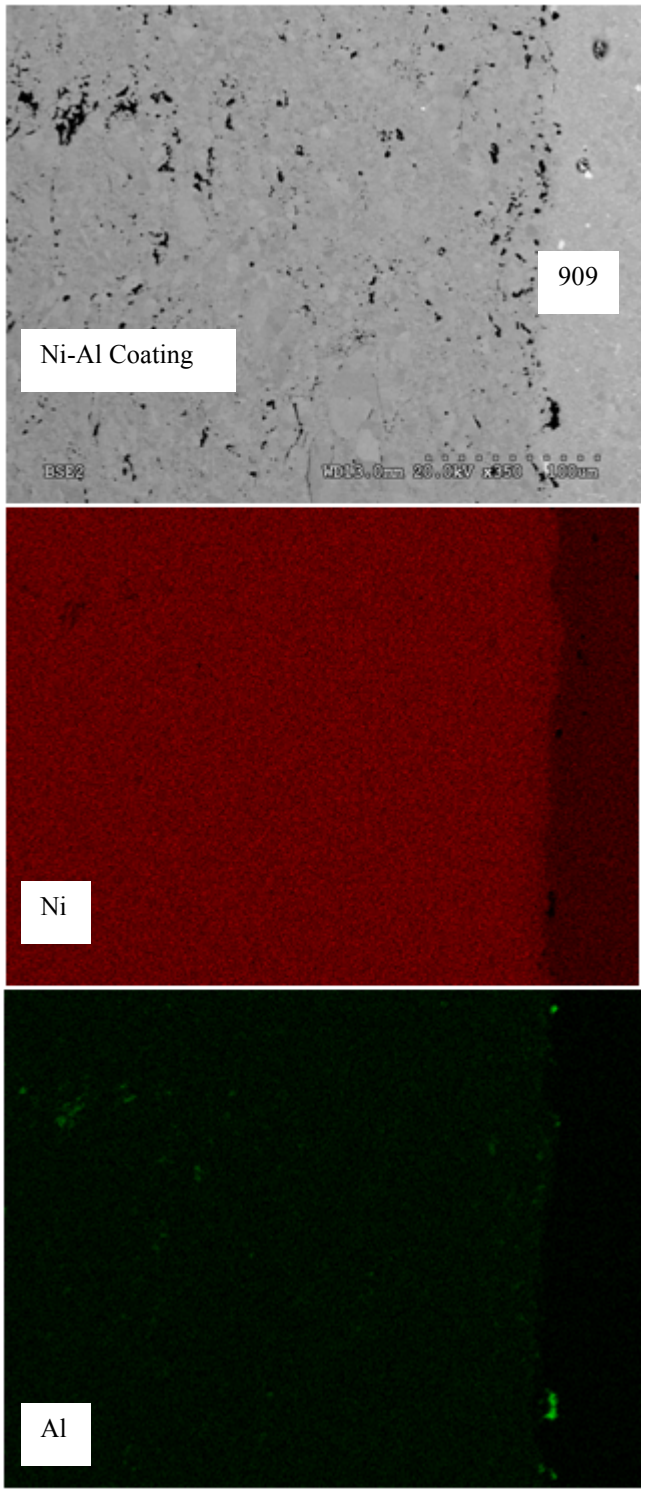

Figure 4-102 SEM micrograph and EDS maps Ni-Al coated alloy 909 Elemental mapping of nickel, aluminum and oxygen in the plasma sprayed Ni–5 wt.%Al deposit

4.13 Ranking of factors that play a role in coating separation on alloy 909 substrate

As indicated earlier, various factors that play a role in determining the compatibility between the coatings and the Incoloy 909 substrate were investigated, the various factors and their impact on coating integrity is discussed:

a.Residual stresses of the coatings

b.Effect of oxidation of the substrate during HVOF spray process

c.Adhesive bond strengths of the coatings

d.CTE of the coatings versus substrate.

e.Adhesion and ductiltiy of the coatings

4.13.1 Residual stresses of the coatings

The Almen arc deflection height represents the residual stresses caused due to quenching, or deposition stress caused due to quenching of splats and the cooling stress during post deposition contributed due to thermal mismatch between substrate. From Fig 4-103, it is evident that Almen arc deflection height increases with increase in the coating thickness for all coatings. It is known that the increase in coating thickness increases the residual stresses, as shown in the literature [Lyphout et al., 2008]. The rate of increase in curvature or arc deflection height, however decreases with increasing coating thickness as exhibited by the 718 coating as, also reported in the literature [Seiji Kuroda et al., 2001]. It can be seen that all the coatings exhibit more or less similar characteristics, with 718 and NiAl coatings exhibits slightly higher arc deflection heights compared to

the CoNiCrAlY coating. The residual stresses calculated based on simple beam theory as discussed in literature [Kirk, 1999], using equation,

$$\sigma = Etd/2L^2$$

Where E = Elastic modulus (Pa); t = thickness (m); d = measured deflection (m); L =length of curved beam (m).

and also using Stoney's equation,

$$\sigma = Et^2\kappa/6t_c \quad \text{[Stokes et al., 2008]}$$

Where E = Elastic modulus of substrate (Pa); t =thickness of substrate (m); κ =curvature constant; t_c = thickness of coating

provides an approximate uniformly distributed stress range of 13 – 30 MPa, assuming the coating as a homogenous material with E(Young's Modulus) =200GPa exhibiting excellent adhesion to the substrate. The stress value calculated from Almen deflection height is an approximate average residual stress and it cannot be compared with the values calculated by location specific XRD or Neutron diffraction methods. Previous research [Kuroda et al., 1995] reported residual stresses in the order of 50 MPa in ceramic coatings, that have inherently lower stresses due to presence of numerous microcracks within the coatings. The same researchers have indicated that metallic coatings, similar to the coatings used in this research can exhibit residual stresses as high as 100-300 MPa. Stokes [Stokes et al., 2008] used various methodologies to calculate residual stresses based on previous literature with the coating thickness 0.2mm, substrate thickness 1mm, E ~200GPa, Poisson's ratio ~ 0.3 and reported residual stresses ranging from -4.84 GPa (compressive) to 26.7 GPa (tensile). Residual stresses however likely play a role in the compatibility of the various coatings also as shown by previous re-

search [Sampath et al., 2004] for the NiAl coating evaluated by neutron diffraction analysis. They measured a range of residual stresses values from -500 MPa near to the substrate coating interface and -50 MPa, 1.5mm away close to the coating surface. Due to the inherent presence of defects such as oxides, voids and other defects are present in the coatings, hence, the residual stresses can vary extensively within the coating. The Almen method used in the present research only gave an average value rather than specific values at specific porosity in the coating. So based on the information from the results from this research residual stresses does not play an important role in coating failures on alloy 909. However, residual stresses measured by neutron diffraction method [Sampath et al., 2004] can vary and potentially can contribute to the coating interface separation..

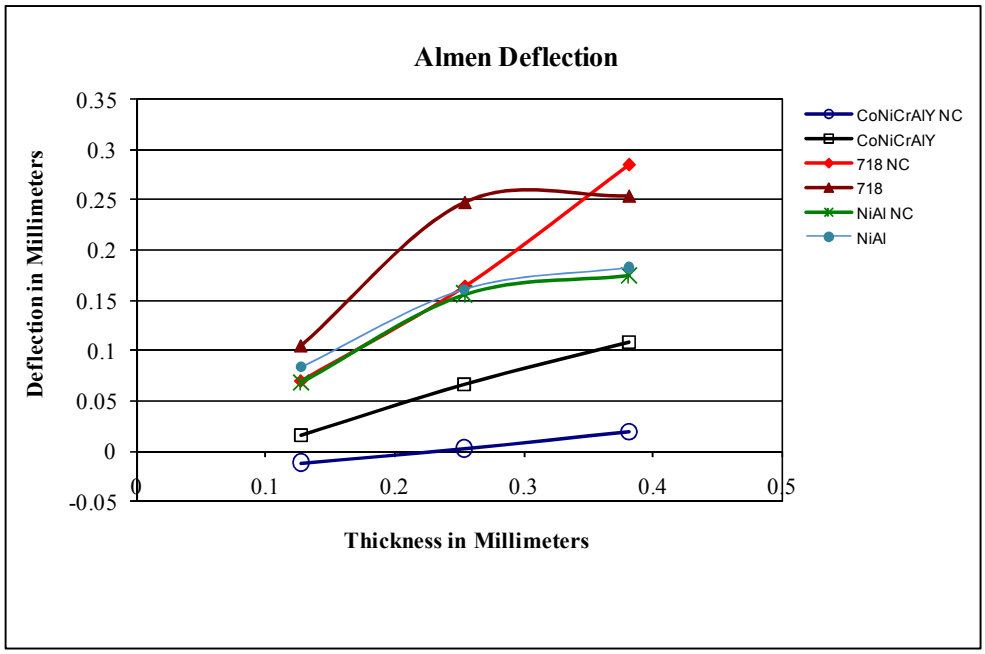

Fig 4-103 Almen deflection of CoNiCrAlY, 718, and NiAl coatings

4.13.2 Effect of oxidation of the substrate during HVOF spray process

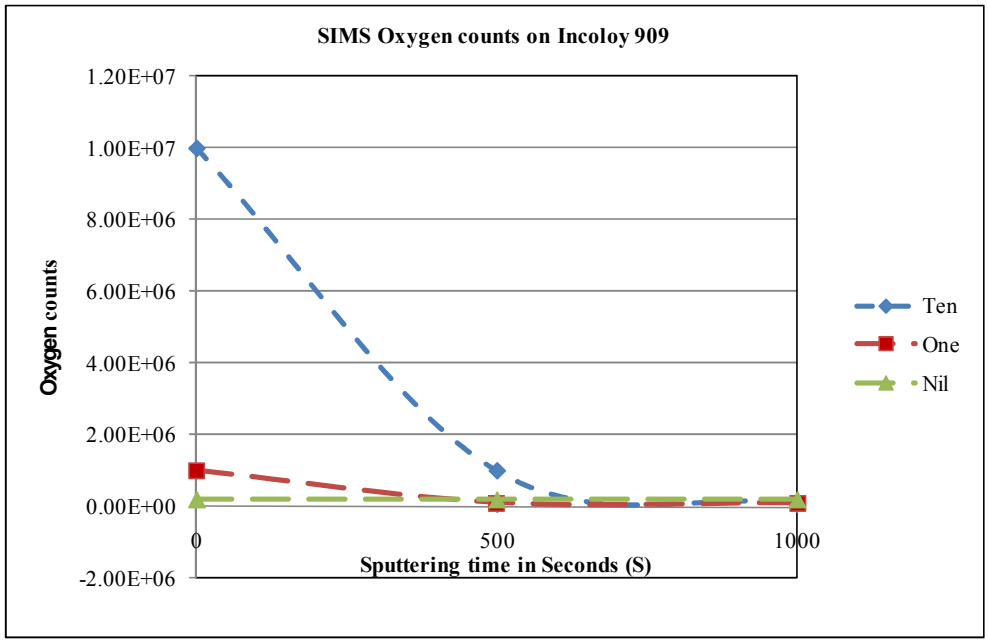

Fig 4-104 Oxidation counts (SIMS) on the surface of Incoloy 909 test coupons after ten passes, one pass, and without exposure to high velocity flame

As shown in Fig 4-104, alloy 909 was found susceptible to form an extremely thin oxygen enriched scales after 10 passes of HVOF flame using secondary ion mass spectroscopy results. At the same time, with one pass of HVOF flame and with no exposure to HVOF flame, there is negligible presence of oxygen enriched surface layer detected by secondary ion mass spectroscopy results. However, during a practical coating deposition process, the substrate surface will be exposed to elevated temperatures and air only during the application of the first layer of coating. During subsequent coating passes, the oxygen supply to the substrate is effectively cut-off due to barrier effect exhibited by the first layer of the coating on the substrate surface. Hence, formation of thin oxide scale is unlikely and it does not play a major role in causing coating separation or debonding from alloy 909 substrate..

4.13.3 Adhesive bond strength of the coatings

As shown in Fig 4-105, the tensile bond strength results from lowest to highest were in the order CoNiCrAlY, 718 and NiAl, especially at the maximum coating thickness of 0.38mm. Also, Diamalloy 4008 (NiAl) coating exhibited excellent bond strength as earlier observed in the optical and scanning electron micrographs. The excellent bond strength of NiAl coating at the maximum coating thickness on Incoloy 909 confirms that this coating exhibited better adhesion strength than CoNiCrAlY and 718 coatings on this substrate. As the reason behind the superior adhesion mechanism of NiAl coating over CoNiCrAlY and 718 coating on 909 substrate was not part of the present research, the adhesion mechanism is unknown and needs further investigation.

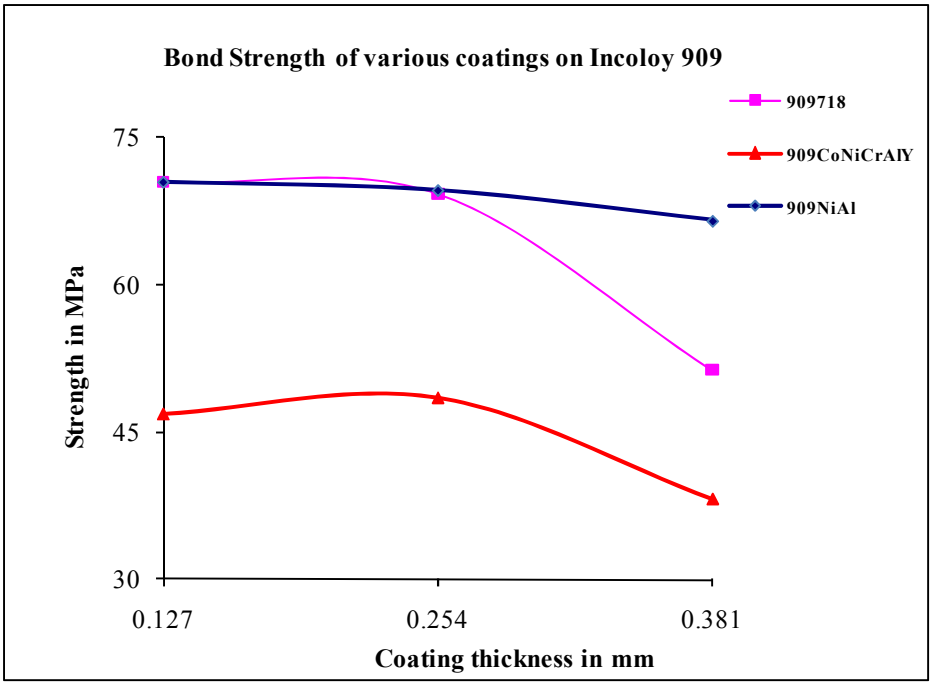

Figure 4-105 Bond strength of 718 and CoNiCrAlY coatings on 909 Substrate at various coating thicknesses

4.13.4 CTE of coatings versus substrate.

As shown in Fig 4-79, it can be ascertained that alloy 909 exhibits the lowest CTE characteristics, while 718, CoNiCrAlY, and NiAl exhibits higher but similar CTE characteristics to CoNiCrAlY and 718.

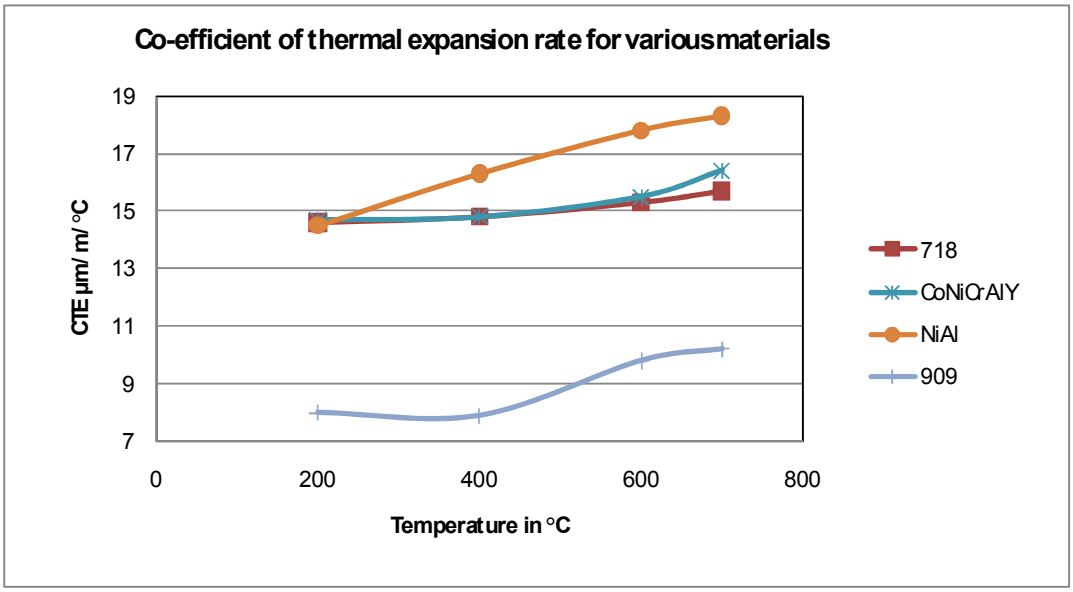

Figure 4-106 Coefficient of thermal expansion for 718, CoNiCrAlY, NiAl and 909

The wide difference between the CTE characteristics certainly plays a major role in the incompatibility of CoNiCrAlY and 718 coating on the alloy 909 substrate. However, NiAl coating even though exhibits higher CTE characteristics, still exhibited excellent compatibility on the alloy 909 substrate. This anomalous outcome suggests that adhesion and ductility of the coating are vital, especially when the CTE difference between the coating and substrate are wide apart from each other.

4.13.5 Adhesion and ductility of the coatings

It can be inferred from Table 4-7 that the ductility characteristics of CoNiCrAlY and 718 coatings are similar, but NiAl coating exhibits superior average bending fracture strength and fracture strain at all coating thicknesses. Diamalloy 4008 (NiAl) coating is well known for its application as a bond coat on a variety of substrates and known for its excellent adhesion on a variety of substrates [Sampath et al., 2004]. Since industrial application involves coating thickness of more than 300µm, it is important to consider the results at the highest coating thickness. The NiAl coating at maximum coating thickness exhibits relatively better ductility based on fracture strain values(~15% better than nearest rival CoNiCrAlY coating). At the maximum coating thickness, the highest combination of bending fracture strength and fracture strain is exhibited by NiAl coating, followed by 718 and CoNiCrAlY coating.

Table 4-7: Bending fracture strength and strain for various coatings

Coating Type	Coating Thickness					
	125µm		251 µm		381 µm	
	Bending strength (MPa)	Bending strain (%)	Bending strength (MPa)	Bending strain (%)	Bending strength (MPa)	Bending strain (%)
CoNiCrAlY	546 ±44	1.4± 0.1	373± 40	1.3±0.1	359± 21	1.2± 0.1
718	647 ± 47	1.4± 0.1	490± 24	1.3±0.1	431± 21	1.1± 0.1
Ni-Al	573 ± 21	1.6± 0.1	497 ±12	1.5±0.1	543± 23	1.4± 0.1

Further using the basic fracture mechanics expression for plane strain fracture toughness (K_{1C});

$$K_{1C} = Y\sigma (\pi a)^{0.5}$$

Where,

Y is a dimensionless parameter dependant upon specimen shape factor;
σ is critical stress for crack propagation;
a represents ½ crack length;

From Table 4-7, it can be inferred that the average fracture strength of NiAl coating at the maximum coating thickness (0.38mm) is ~20% higher than the 718 coating and ~30% higher than the CoNiCrAlY coating at the same coating thickness. Based on the plane strain fracture toughness expression, it is evident that K_{1C} is directly proportional to σ, since Y and "a" can be assumed to identical for all the three coatings. Hence, it can be concluded that the NiAl coating exhibits superior fracture toughness compared to the other coatings used in this research. It is evident that better coating adhesion and ductility can improve the coating substrate compatibility, as it can better accommodate the stresses arising from the wide difference between CTEs between the coating and the substrate.

4.14 Summary of the coating test results

Previous research [Taylor et al., 2006] has shown that the compatibility between Superalloy substrate and CoNiCrAlY type coatings is generally good due to similar CTE

characteristics, but they did not consider Superalloys such as Incoloy 909 used for low CTE applications. It is evident that the combination of low ductility and wide CTE difference between the substrate and coating were observed to be deleterious, resulting in coating separation or debonding as observed with CoNiCrAlY and 718 coatings on Incoloy 909 substrate. However, on Inconel 718 substrate, the CTE difference between the coatings and the substrate is negligible, thereby leading to better coating compatibility with the substrate.

Based on the above it can be concluded that coating adhesion and ductility are primary factors, for NiAl coating to exhibit excellent compatibility with Incoloy 909 substrate. The CTE differences between the coatings (CoNiCrAlY and 718) and the alloy 909 substrate and the poor coating adhesion are thought to be the primary contributor for the coating failures on alloy 909. Note that the combination of factors such as CTE, coating ductility, residual stresses and coating thickness can all contribute to coating incompatibility on the alloy 909 substrate.

5. SUMMARY AND CONCLUSION

5.1 Microstructure of Incoloy 909

When the material used in this study was solution treated (commercially recommended cycle) at 982°C, the Laves phase did not completely go into solution, Laves phase began going into solution at a treatment temperature of above 1050°C as shown by the DSC and metallographic evaluation. The Laves phase in the Incoloy 909 provides a grain pinning effect at elevated temperature thus preventing a higher rate of grain growth; however, at temperatures in excessive of 1050°C, the majority of the Laves phase goes into solution, with the absence of effective grain growth inhibiting mechanism, resulting in massive grain growth.

In the as received solution treated and aged condition, the material exhibited a fine-grained structure. The precipitates present in the material were fine gamma prime, intergranular Laves phase, and intragranular Laves phase. Epsilon phase was absent except for gamma prime precipitates orienting in a platelet ready to transform into epsilon phase.

In the solution treated and over aged condition, the precipitates present were intergranular Laves phase, intragranular Laves phase, and a copious amount of Widmanstatten type epsilon phase. The complete absence of gamma prime phase in STOA condition agree with earlier findings in the literature that the epsilon phase would have directly precipitated out of the gamma matrix at aging temperature above about 760°C.

The bright and black grains present in STA and STOA condition are likely caused due to grain orientation rather than due to difference in densities of epsilon precipitates as proposed by Heck et al [Heck et al., 1988]. In STA condition, the alloy showed higher tensile yield and ultimate strength than STOA condition. This confirms that precipitation of Widmanstatten like epsilon phase in Incoloy 909 results in considerable reduction in strength.

5.1.1 Effect of Coatings on Incoloy 909 and Inconel 718

Bare Incoloy 909 was found to be susceptible to elevated temperature oxidation, leading to oxide scale formation in air, even when held at a temperature of 704°C, due to the absence of chromium and aluminum in this alloy. The oxidized scales on Incoloy 909 were composed of internal and external scales when exposed to temperatures between 538 – 700°C for varying periods. The internal scale composed of both inter and intragranular oxidation, while, bare Inconel 718 oxidized to a negligible extent when exposed to identical isothermal and thermal cyclic conditions.

As expected the rate of oxidation increases with temperature and exposure time. Coated substrates of Incoloy 909 and Inconel 718 did not show presence of oxide scales irrespective of the type of coating. Incoloy 909 exhibited oxidation scales only in the areas where the coating was cracked or separated from the substrate interface. This allowed free oxygen transportation to the underlying Incoloy 909 substrate leading to oxidation. Both the HVOF sprayed coatings CoNiCrAlY and 718 exhibited interface separation and

cracking on Incoloy 909 substrate in the as sprayed condition, while both coatings met acceptance quality requirements on Inconel 718 substrate when sprayed with the same process parameters.

Several factors that can potentially cause coating interface separation in Incoloy 909 substrate were investigated, i.e., CTE, residual stresses, oxidation of substrate during coating deposition, ductility, fractured toughness and tensile bond strength of the coatings. Among these factors are: i) coating ductility and superior adhesion based on 4 point bend test results and ii) difference in CTE between coating and substrate based on thermal expansion characteristics were observed to contribute to a major extent, while oxidation, was observed to play a minor role. Residual stress levels evaluated via the Almen tests only give an average value, while the data of Sampath et al, 2004, using neutron diffraction using the same process and coating showed large compressive residual stress levels. Thus future work should evaluate this point more closely possibly using XRD.

6. SUGGESTIONS FOR FUTURE WORK

Microstructure characterization of Incoloy 909 should be investigated beyond the overaging condition used in this study for a more comprehensive information on over aging characteristics of this alloy at long aging times.

The oxidation characterization of Incoloy 909 should be examined further with thermo-gravimetric analysis at various temperatures and the oxide scales should be further evaluated using electron probe micro analysis (EPMA) and X ray diffraction (XRD) for composition and residual stress evaluation.

A more detailed coating compatibility testing should be carried out on Incoloy 909 using other coating materials and coating processes than used in this research. In this research, all the coated Incoloy 909 test coupons were in solution treated and aged condition, other heat treatment conditions of the substrate needs to investigated in detail.

Interactive effect of various factors that can affect the coating substrate compatibility including some fundamental characteristics such as wetting characteristics needs to be further researched for understanding the superior adhesion characteristics of NiAl coating and poor adhesion characteristics of CoNiCrAlY coating on Incoloy 909.

Modeling with further experimental data using techniques such as Finite Element Modeling (FEM) can be attempted which will be extremely useful for design engineers while choosing appropriated coatings for variety of substrate surfaces.

REFERENCES

Aerospace structural materials hand book, Center for information and numerical data analysis and synthesis, Purdue University, Indiana, USA.

H. V. Atkinson,"A review of the role of short-circuit diffusion in the oxidation of nickel, chromium, and nickel-chromium alloys", Journal Oxidation of Metals, Oct 1985, Vol 24, No. 3-4, p 177-197.

D. Baither, C. Rentenberger, H.P. Karnthaler and E. Nembach, "Three alternative experimental methods to determine the antiphase-boundary energies of the precipitates in superalloys", Philosophical Magazine A, Jun 2002, Vol 82, No.9, p 1795-1805.

P.Bansal, P.H.Shipway and S.B.Leen, "Effect of particle impact on residual stress development in HVOF sprayed coatings", Journal of Thermal Spray Technology, Dec 2006, Vol 15,No. 4, p 570-5.

U. Bardi, S.P. Chenakin , F. Ghezzi , C. Giolli , A. Goruppa e, A. Lavacchi , E. Miorin , C. Pa-gura and A. Tolstogouzov ," High-temperature oxidation of CrN/AlN multilayer coatings", Applied Surface Science, 2005, Vol 252 , p 1339–1349.

S.N. Basu and G.J.Yurek, "Effect of alloy grain size and silicon content on the oxidation of austenitic Fe-Cr-Ni-Mn-Si alloys in pure O_2", Oxidation of Metals, Oct 1991, Vol 36, No.3-4, p 281-315.

N.Birks, G.H.Meier and F.S.Pettit, "Introduction to the High Temperature Oxidation of Metals", 2nd Edition, Cambridge University, April 2006.

S.Bose, "High Temperature Coatings (Hardcover)", 1st Edition, Butterworth-Heinemann, Jan 2007.

O.C.Brandt, “Mechanical properties of HVOF coatings”, Journal of Thermal Spray Technology, June 1995, Vol 4, No.2, p 147-52.

R.H.Bricknell and D.A.Woodford, “Grain Boundary Embrittlement of the Iron-Base Superalloy In903”, Metallurgical transactions, A Physical metallurgy and materials science, Sep 1981, Vol 12 , No.9, p 1673-1680.

W.F. Brown, C.Gibson and C.Y. Ho, “Center for Information and Numerical Data Analysis and Synthesis (CINDAS)”, Code:4103 (Inconel 718), Aerospace Structural Metals Handbook, 1998, Vol 4, 1998.

J.A.Browning, “Highly conc supersonic liquefied material flame spray methol and apparatus” ,US Patent 4416421, Jul 1981.

Z. Chen, J.W. Brooks and M.H. Loretto; ‘Precipitates in Incoloy 909’, Materials Science and Technology, Aug. 1993, Vol 9, No. 8, p 647-53.

T.W.Clyne and S.C.Gill, “Residual stresses in thermal spray coatings and their effect on interfacial adhesion: A review of recent work”, Journal of Thermal Spray Technology, v 5, n 4, p 401-418, Dec 1996.

J. P. Collier, S.H. Wong, J. K. Tien and J.C. Phillips, “The effect of varying AI, Ti,and Nb content on the phase stability of INCONEL 718”, Metallurgical and Materials Transactions A, Jul 1988, Vol 19, No.7, p 1657-1666.

O.Culha, E.Celik, N.F.Ak Azem, I.Birlik, M.Toparli and A.Turk, “Microstructural, thermal and mechanical properties of HVOF sprayed Ni-Al-based bond coatings on stainless steel substrate”, Journal of Materials Processing Technology,Aug , Vol 204, No 1-3, p 221-230.

K.Cushnie, J.A.E.Bell and G.D.Smith, "Thermal barrier coatings on Incoloy 909",Thermal Spray Research and Applications, Proceedings of the Third National Thermal Spray Conference, May 1990, p 539-544.

J.R. Davis & Associates, "Handbook of thermal spray technology", ASM International, 2004.

R.G. Davies, N.S. Stoloff , "Work hardening in Fe_3Al", Acta Metallurgica, Oct 1963, Vol 11, No. 10, p 1187-1189.

J. Day, X. Huang and N. L. Richards, "Examination of a grit-blasting process for thermal spraying using statistical methods", Journal of Thermal Spray Technology, Dec 2005, Vol 14, No.4, p 471-479.

D.L. Deadmore and C.E. Lowell, "The effect of ΔT (oxidizing temperature minus cooling temperature) on oxide spallation", Oxidation of Metals, April 1977, Vol 11, No.2, p 91-106.

Y.Ding, D.O.Northwood and A.T.Alpas, "Microstructure and mechanical properties of Ni-Al composite coatings for tribological applications", Surface Engineering, 1997, Vol 13, No 1, p 31-36.

M.J. Donachie, "Superalloys: a technical guide", 2nd ed., ASM International, 2000.

D.L.Douglass, "Critique of internal oxidation in alloys during the post-wagner era", Oxidation of Metals, Aug 1995, Vol 44, No. 1-2, p 81.

J. Doychak, J. H. Westbrook and R. L. Fleischer, "Intermetallic Compounds: Principles and Practice", John Wiley & Sons Inc, Dec 1994, Vol 1, p 977-1016.

H. J. T. Ellingham, “Reducibility of oxides and sulphides in metallurgical processes”, J. Soc. Chem. Ind., 1944, 125.

H.E.Evans and R.C.Lobb, “Conditions for the initiation of Oxide-Scale cracking and spallation”, Corrosion Science, 1984, Vol 24, No. 3, p 209-222.

S. Fantassi, M. Vardelle, P. Fauchais, and C. Moreau, “Investigation of the splat formation versus different paniculate temperatures and velocities prior to impact,” in: Proc. of 13th Internat. Thermal Spray Conf., 1992, p. 755–760.

S.Fantassi, M.Vardelle, A.Vardelle, and P.Fauchais, “Influence of the velocity of plasma sprayed particles on the splat formation”, Thermal Spray Coatings: Research, Design and Applications, Thermal Spray Coatings: Research, Design and Applications, 1993, p 379-384.

A.Feuerstein, J.Knapp, T.Taylor, A.Ashary, A.Bolcavage and N.Hitchman,“Technical and economical aspects of current thermal barrier coating systems for gas turbine engines by thermal spray and EBPVD: A review”, Journal of Thermal Spray Technology, Jun 2008, Vol 17, No. 2, p 199-213.

G. A. Greene and C. C. Finfrock, “Oxidation of Inconel 718 in Air at High Temperatures”, Oxidation of Metals, June 2001, Vol 55 , No. 5-6, p 505-521.

X.Guo, K.Kusabiraki and S.Saji, “Intragranular precipitates in Incoloy Alloy 909”, Scripta Materialia, 2001, Vol 44, No.1, p 55-60.

Y.Han, P.Deb and M.C. Chaturvedi, “Coarsening behaviour of γ"- and γ'-particles in Inconel alloy 718”, Metal Science, Dec 1982, Vol 16, No 12, p 555-561.

L.L.Harner, “Selecting controlled expansion alloys”, Carpenter Alloys, August 1994.

K.A. Heck, “The Effects of Silicon and Processing on the Structure and Properties of Incoloy Alloy 909”, Physical Metallurgy of Controlled Expansion Invar-Type Alloys, TMS, 1990, p 273-282.

K.A. Heck, D.R Smith, J.S. Smith, D.A. Wells, and M.A. Holderby: ‘The Physical Metallurgy of a Silicon-Containing Low- Expansion Superalloy’, Superalloys 1988, Conf. Proc, TMS- AIME; 1988, p 151-160.

G.R. Heath and R.J. Du Mola, “Practical experience of with the new generation of low cost port-able HVOF”, Proceedings of International Thermal Spray Conference, 1998, p 1-6.

J.A.Hearley, J.A.Little, and A.J.Sturgeon, “The effect of spray parameters on the properties of high velocity oxy-fuel NiAl intermetallic coatings”, Surface and Coatings Technology, Jan. 2000,Vol 123, No. 2-3, p 210-18.

X. Huang, “A microstructural study of heat affected zone microfissuring of electron beam welds in cast Alloy 718”, Ph.D. Thesis, University of Manitoba, 1993.

K.Ishikawa, M.Seki, S.Tobe, “Application of thermal spray coatings to prevent corrosion of construction in Japan”, Proceedings of 5th National Thermal Spray Conference, ASM International, 1993, p 679-684.

Y. Itoh, M. Saitoh, and M. Tamura, “Characteristics of MCrAlY Coatings Sprayed by High Velocity Oxygen-Fuel Spraying System”, Journal of Engineering Gas Turbines Power, Jan 2000, Vol 122, No. 1, p 43-50.

A. K. Jena and M. C. Chaturvedi, “The role of alloying elements in the design of nickel-base superalloys”, Journal of Materials Science, Oct 1984, Vol 19, No.10, p 3121-3139.

L. Jian, C. Y. Yuh and M. Farooque, “Oxidation behavior of Superalloys in oxidizing and reducing environments”, Corrosion Science, September 2000, Vol 42, No.9, p 1573-1585.

P. Kamasa, P. My li ski and J. Sta kiewicz, “Instantaneous Coefficient of Thermal Expansion Determined by Temperature-modulated Dilatometry”, Czechoslovak Journal of Physics, Dec 2004, Vol 54, No.4, p 627-630.

R. Knight and R.W. Smith, “Residual stress in thermally sprayed coatings”, Thermal Spray Coat.: Res , Design Appl , Proc. Natl. Spray Conf , Jun 1993, Vol 7, No.11, p 607-12.

Y.S.Korobov, “Comparative analysis of supersonic gas-flame methods of coating application”, Metallurgist, March 2006, Vol 50, No. 3-4, p 158-162.

G.R.Krishna, D.K.Das, V.Singh and S.V.Joshi, “Role of Pt content in the microstructural devel-opment and oxidation performance of Pt-aluminide coatings produced using a high-activity aluminizing process”, Materials Science & Engineering A (Structural Materials: Properties, Microstructure and Processing), Aug. 1998, Vol A251, No 1-2, p 40-47.

K.Kusabiraki, E.Amada and T.Oaka, “Precipitation and growth of γ′ phase in an Fe-38Ni-13Co-4.7Nb Superalloy”, ISIJ International, 1996, Vol 36, No. 2, p 208-214.

K.Kusabiraki, E.Amada, T.Ooka and S.Saji, “Epsilon and Eta Phases Precipitated in an Fe-38Ni-13Co-4.7Nb-1.5Ti-0.4Si Superalloy”, ISIJ International, 1997, Vol 37, No.1, p 80-86.

K.Kusabiraki, H.Tsujino and S.Saji, “Effects of Tensile Stress on the High-temperature Oxidation of an Fe–38Ni–13Co–4.7Nb–1.5Ti–0.4Si Superalloy in Air”, ISIJ International, 1998, Vol 38, No.9, p1015-1021.

K. Kusabiraki, H. Toda, H. Komatsu and S. Saji, "Precipiation sequences of γ', ε and η phases in Fe-Ni-Co-Nb based Superalloys", Proceedings of the international conference on solid-solid phase transformations, May 1999, Vol 84, No.9, p 1645-1648.

R. Larker, K. Anevik, S. Kristiansson and Bengt Loberg, "Heat treatments of the low-expansion superalloy incoloy 909 for application in ceramic/metal joints and in metal matrix composites", Materials & Design, 1992 ,Vo1 3, No. 1, p 11-15

J.A.Legoux, L.Leblanc, V.Bouyer and C.Moreau, "Evaluation of four high velocity thermal spray guns using WC-10% CO-4% Cr cermets", Journal of Thermal Spray Technology, March 2002, Vol 11, No.1, p 86-94.

C.-J. Li, A. Ohmori, and Y. Arata: "Effect of Spray Methods on the Lamellar Structure of Al_2O_3 Coatings", Thermal Spray, Current Status and Future Trends, Japan High Temperature Society, 1995, pp. 501–06.

C.Li and W.Li "Effect of sprayed powder particle size on the oxidation behavior of MCrAlY materials during high velocity oxygen-fuel deposition", Surface & Coatings Technology, Jan. 2003, Vol 162, No.1, p 31-41.

W. Lin, "A methodology for quantifying heat-affected zone liquation cracking susceptibility", Ph.D. Thesis, Ohio University, 1991.

C.K.Lin and C.C.Berndt, "Measurement and analysis of adhesion strength for thermally sprayed coatings", Journal of Thermal Spray Technology, Mar 1994, Vol 3, No.1, p 75-104.

D. M. Lipkin, D. R. Clarke, H. Schaffer and F. Adar, "Lateral growth kinetics of a-alumina ac-companying the formation of a protective scale on (111) NiAl during oxidation at 1100 °C", Appl. Phys. Letter, May 1997, Vol 70, No.19, p 2550-2552.

E. Lugscheider, C. Herbst and Z. Lidong, “Parameter studies on high-velocity oxy-fuel spraying of MCrAlY coatings”, International Conference on Metallurgical Coastings and Thin Films No25, Surface & coatings technology, 1998, Vol 108-09, No.1-3, p. 16-23.

C. Lyphout, P. Nyle´n, A. Manescu and T. Pirling, “Residual Stresses Distribution through Thick HVOF Sprayed Inconel 718 Coatings” Journal of Thermal Spray Technology, 2008, Vol 17, No. 5-6, p 915-923.

Material Data Sheet of Incoloy 909, “Special Metals Corporation, Publication Number SMC-077”, available at http://www.specialmetals.com/documents/Incoloy%20alloy%20909.pdf, 1992.

R.A.Mahesh, R.Jayaganthan and S.Prakash, “Microstructural characterization and hardness evaluation of HVOF sprayed Ni-5Al coatings on Ni- and Fe-based superalloys”, Journal of Materials Processing Technology, Apr 2009, Vol 209, No.7, p 3501-3510.

S.Mannan, S.Patel, and J. deBarbadillo, “Long term thermal stability of Inconel Alloys 718, 706, 909, and Waspaloy at 593ºC and 704ºC”, Superalloys , TMS, 2000, p 449-458.

P.J.McLellan, “A differential-algebraic perspective on nonlinear controller design methodolo-gies”, Chemical Engineering Science, Vol 49, No.10, p 1663-1679.

I. A. Menzies and J. Lubkiewicz, “Oxidation of an Fe-12% Ni alloy in oxygen at 700–1000°C”, Oxidation of Metals, Jan 1971, Vol 3, No.1, p 41-58.

R.Nakkalil, “Microstructural characterization of Incoloy 903 weldments”, Ph.D. Thesis, University of Manitoba, 1993.

J.R.Nicholls, K.J.Lawson, A.Johnstone and D.S.Rickerby, “Low thermal conductivity EB-PVD thermal barrier coatings”, Materials Science Forum, 2001, Vol 369-372, No.2, p 595-606.

T.J. Nijdam and W.G. Sloof, “Microstructural evolution of a MCrAlY coating upon isothermal annealing”, Materials Characterization, Dec 2008, Vol 59, No.12, p 1697-1704.

L. Pawlowski, “The Science and Engineering of Thermal Spray Coatings”, 1st edition, John Wi-ley & Sons, 1995.

M. P. Planche, B. Normand, H. Liao, G. Rannou and C. Coddet, “Influence of HVOF spraying parameters on in-flight characteristics of Inconel 718 particles and correlation with the electro-chemical behaviour of the coating”, Surface and Coatings Technology Aug 2002, Vol 157, No.2-3, p 247-256.

P.Poza and P.S.Grant, “Microstructure evolution of vacuum plasma sprayed CoNiCrAlY coatings after heat treatment and isothermal oxidation”, Surface & Coatings Technology, Dec. 2006, Vol 201, No. 6, p 2887-96.

P.R.Roberge, “Handbook of Corrosion Engineering”, McGraw-Hill Professional, 2000, ISBN 0070765162, 9780070765160

W.Rusch, “Comparison of Operating Characteristics for Gas and Liquid Fuel HVOF Torches”, Equipment Engineering, Sulzer Metco, 1101 Prospect Ave., Westbury, NY 11590.

Y.Y. Santana, J.G. La Barbera-Sosa, M.H. Staia, J. Lesage, E.S. Puchi-Cabrera, D. Chicot and E. Bemporad, “Measurement of residual stress in thermal spray coatings by the incremental hole drilling method”, Surface and Coatings Technology, Oct 2006, Vol 201, No.5, p 2092-2098.

S. Saeidi, K.T. Voisey, and D.G. McCartney,"The Effect of Heat Treatment on the Oxidation Be-havior of HVOF and VPS CoNiCrAlY Coatings", Journal of Thermal Spray Technology, June 2009, Vol 18, No. 2, p 209-216.

S.Sampath, "Rapid solidification during plasma spraying", Ph.D. Dissertation, 1989, State University of New York.

S.Sampath, X.Y.Jiang, J.Matejicek, L.Prchlik, A.Kulkarni and A.Vaidya "Role of thermal spray processing method on the microstructure, residual stress and properties of coatings: an integrated study for Ni–5 wt.%Al bond coats", Materials Science and Engineering, Jan 2004, Vol 364, No.1-2, p 216-231.

Y.Y. Santanaa, J.G. La Barbera-Sosaa, M.H. Staiaa, J. Lesageb, E.S. Puchi-Cabreraa, D. Chicotb and E. Bemporadc, "Measurement of residual stress in thermal spray coatings by the incremental hole drilling method", Surface and Coatings Technology, Oct 2006, Vol 201, No.5, p 2092-2098.

K. Sato and T. Ohno, "Development of low thermal expansion superalloy", Journal of Materials Engineering and Performance, 1993, Vol 2, No.4, p 511-516.

M.Schütze, "Corrosion and Environmental Degradation", 1st Edition, Wiley-VCH, 2000, ISBN 3527295054, 9783527295050.

C.T.Sims, N.S.Stoloff and W.C. Hagel, "Superalloys II", Wileys and Sons, 1987, p 327 – 384.

T.S.Sidhu, S.Prakash and R.D.Agrawal, "Studies on the properties of high-velocity oxy-fuel thermal spray coatings for higher temperature applications ", Journal of Material Science, Nov 2005, Vol 41, No.6, p 805-823.

H. Singh, S. Prakash and D. Puri, “Some observations on the high temperature oxidation behaviour of plasma sprayed Ni3Al coatings”, Materials Science and Engineering: A, Jan 2007, Vol 444, No.1-2, p 242-250.

R.Sivakumar Krishna and B.L.Mordike, “High temperature coatings for gas turbine blades: A review”, Surface and Coatings Technology, April 1989, Vol 37, No.2, p 139-160.

J.L.Smialek, G.H.Meier, “Superalloys II--High Temperature Materials for Aerospace and Industrial Power”, Wiley and Sons, 1987, pp. 293-326

D.F. Smith, and M.A. Holderby, “Process sensitivities in Incoloy alloy 909”, Heat resistant materials, Sep 1991, p 285-292.

D.F.Smith and J.S. Smith, “A history of controlled expansion superalloys”, Physical Metallurgy of controlled expansion invar type alloys, 1989, p 253-272.

G. D. Smith, “Thermal Barrier Characteristics of Partially Stabilized Zirconia Coatings on INCOLOY Alloy 909 (A Controlled Expansion Alloy)”, Journal of Engineering for Gas Turbines and Power , January 1991,Vol 113, No.1, p 113-135.

V. V. Sobolev and J. M. Guilemany, “Flattening of droplets and formation of splats in thermal spraying: A review of recent work—Part 1”, Journal of Thermal Spray Technology, Mar 1999, Vol 8, No.1, p 87-101.

S.K. Srivatsava, “Mechanical properties, oxidation resistance and their interaction for two gas turbine seal ring alloys”, ASME, International Gas Turbine and Aeroengine Congress and Exposition, , Cologne, Jun 1992, Vol 37, No.6 p 1992.

F. Stein, M. Palm and G. Sauthoff, “Structure and stability of Laves phases. Part I. Critical assessment of factors controlling Laves phase stability”, Intermetallic and Advanced Metallic Materials, Sep 2004, Vol 12, No. 7-9, p 713-720 .

K.H. Stern, “Metallurgical and ceramic protective coatings”, 1st Edition, Chapman and Hall, 1996, ISBN 0 412 54440 7

N.S. Stoloff and R.G. Davies, “The mechanical properties of ordered alloys Progress”, Materials Science, 1968, Vol 13, p 1-84.

J. Stokes and L. Looney, “Predicting Quenching and Cooling Stresses within HVOF Deposits”, Journal of Thermal Spray Technology, Dec 2008, Vol 17, No. 5-6, p 908-914.

J.Stokes and L.Looney, “Residual stress in HVOF thermally sprayed thick deposits”, Surface & Coatings Technology, Jan 2004, Vol 177-178, p 18-23.

M. Sundararaman, P. Mukhopadhyay and S. Banerjee, “Precipitation of the δ-Ni3Nb phase in two nickel base superalloys”, Metallurgical and Materials Transactions A, Mar 1988, Vol 19, No. 3, p 453-465.

C.H. Symonds, D.F. Smith and D.J. Tillack, “The Effect of Stress and Environment on Low-Expansion Superalloys”, Proceedings on High Temperature Alloys for Gas Turbines and Other Applications 1986, Vol 2, p 979-988.

Y. Tamarin, “Protective coatings for turbine blades”, ASM International, 2002.

T.A. Taylor and D.F. Bettridge, “Development of alloyed and dispersion-strengthened MCrAlY coatings”, Surface and Coatings Technology, Dec 1996, Vol 86-87, No.1, p 9-14.

T.Taylor and J.Foster, “Thermal expansion of Tribomet MCrAlY coatings”, Surface & Coatings Technology, Dec. 2006, Vol 201, No.7, p 3819-23.

V.L. Tellkamp, M.L. Lau, A. Fabel and E.J. Lavernia, “Thermal spraying of nanocrystalline in-conel 718”, Nanostructured Materials, 1997, Vol 9, No.1-8, p 489-492.

M.L.Thorpe, “Thermal spray. Industry in transition”, May 1993, Advanced Materials and Proc-esses, Vol 143, No 5, p 50-61.

M.L. Thorpe and H. J. Richter, “A pragmatic analysis and comparison of HVOF processes”, Journal of Thermal Spray Technology, June 1992, Vol 1, No.2, p 161-170.

D. Toma, W. Brandl and U. Köster, “Studies on the transient stage of oxidation of VPS and HVOF sprayed MCrAlY coatings”, Surface and Coatings Technology, Nov 1999, Vol 120-121, p 8-15.

W. J. Tomlinson and I. A. Menzies, “Oxidation of an Fe—19 wt. % Ni alloy in CO_2 at 700–1000°C”, Oxidation of Metals, Jun 1978, Vol 12, No.3, p 215-225.

V.B. Trindade, U. Krupp, Ph. E.-G. Wagenhuber and H.-J. Christ, “Oxidation mechanisms of Cr-containing steels and Ni-base alloys at high-temperatures Part I: The different role of alloy grain boundaries”, Materials and Corrosion, 2000, Vol 56, No. 11, p 785 – 790.

Y.C.Tsui and T.W.Clyne, “Analytical model for predicting residual stresses in progressively deposited coatings”, Part 1: Planar geometry Source: Thin Solid Films, Aug 1997, Vol 306, No. 1, p 23-33.

A. Vardelle, P. Fauchais and N.J. Themelis, “Oxidation of Metal droplets in Plasma sprays”, Surface Engineering, 1995, Vol 12, No. 2, p 171.

C. Wang and S. Chen, “Microstructure and cyclic oxidation behavior of hot dip aluminized coating on Ni-base superalloy Inconel 718”, Proceedings of the 33rd International Conference on Metallurgical Coatings and Thin Films - ICMCTF 2006, The 33rd International Conference on Metallurgical Coatings and Thin Films, Surface and Coatings Technology, Dec 2006, Vol 201, No.7, p 3862-3866.

E.A. Wanner and D.A. DeAntonio, “ Development of a new controlled thermal expansion Superalloy with improved oxidation resistance”, Proceedings of conference “Superalloys 1992”, p 237-246.

E.A. Wanner. D.A. Deantonio, D.F. Smith, and J.S. Smith, “The Current Status of Controlled Thermal Expansion Superalloys”, Journal of Materials, 1991, Vol 43, No. 3, p 38–43.

B.M.Warnes and D.C.Punola, “Clean diffusion coatings by chemical vapor deposition”, Surface and Coatings Technology, Oct. 1997, Vol 94-95, No.1-3, p 1-6.

D.P.Whittle,“High temperature oxidation of superalloy”, High Temp Alloys for Gas Turbines, Proc of a Conf, Sep 1978, p 109-123.

D.A.Woodford and R.H.Bricknell, “Grain boundary penetration of oxygen in nickel and the effect of boron additions”, Metallurgical Transactions A (Physical Metallurgy and Materials Science), Aug. 1981, Vol 12A, No.8, p 1467-75.

P. K. Wright and A. G. Evans, “Mechanisms governing the performance of thermal barrier coatings”, Current Opinion in Solid State and Materials Science, June 1999, Vol 4, No.3, p 255-265.

G.Xiping, K.Kusabiraki: ‘Aging an Fe-Ni-Co-Nb-Ti-Si Superalloy under tensile stress’, Zeitschrift fur Metallkunde, July 2000, Vol 91, No. 7, p 601-606.

D. Zhang, S. J. Harris and D. G. McCartney, “Microstructure formation and corrosion behaviour in HVOF-sprayed Inconel 625 coatings”, Materials Science and Engineering A, Mar 2003, Vol 344, No. 1-2, Pages 45-56.

J. Zhang, T. Jin, Y. Xu, Z. Hu and X. Wu, “Antiphase boundary strengthening in a single crystal nickel-base superalloy”, Cailiao Kexue Yu Jishu (Journal of Materials Science & Technology) , Mar 2002, Vol 18, p 159-162.

CONTRIBUTIONS

The author acknowledges contributions from Dr.R. Ding, Dr.B. Tang, and Dr.K. Vishwakarma (all previous post doctoral fellows at the University of Manitoba) in Transmission electron microscope investigation of alloy 909 and Dr.R.Liu for SIMS analysis at Department of Geological Sciences, University of Manitoba. The author also would like to acknowledge the support from Dr. P.Bishop in characterization of coefficient of thermal expansion properties using Dilatometry (Dalhousie University), and Dr. D.Akindale for JMat Pro support. The support for using various testing equipment at Bristol Aerospace (Magellan Aero) and Standard Aero are also gratefully acknowledged.

JOURNAL PUBLICATIONS FROM THE PRESENT WORK:

Balachander M.A., Vishwakarma, K.R., B. Tang, and Richards, N.L.; Microstructure Characterization of solution treated (ST) and solution treated & aged (STA) Incoloy 909" to Materials Science and Technology, Materials Science and Technology, Accepted, in the press for publication (Jan, 2010).

Balachander M.A., Vishwakarma, K.R., and Richards, N.L.; Microstructure Characterization of solution treated & over aged (STOA) Incoloy 909" to Materials Science and Technology, Materials Science and Technology, In the process of submission (Jul, 2010).

Publication in Conference Proceedings

Balachander M.A., Ding. R, Richards N.L..; Microstructural characterization of commercially heat treated Incoloy 909, 47th Int. Conf. of Metallurgists, Metallurgical Society of CIM, 361–366.Winnipeg, Canada COM 2008.

Conference Presentations

Balachander M.A., Shanker K., Richards, N.L.; Comparison of HVOF sprayed CoNiCrAlY coating on Incoloy 909 and Inconel 718", The Materials Science & Technology 2008 Conference and Exhibit (MS&T '08), October 5-9, 2008, Pittsburgh, Pennsylvania.

Balachander M.A., Shanker K., Richards, N.L.; Comparison of HVOF Sprayed MCrAlY Coating and Nickel-Aluminum on a Low CTE Superalloy (Alloy 909) , The Materials Science & Technology 2008 Conference and Exhibit (MS&T '09), October 25-29, 2009, Pittsburgh, Pennsylvania.